CHARACTERISTICS OF SOLAR FLARE HARD X-RAY EMISSIONS: OBSERVATIONS AND MODELS

A DISSERTATION
SUBMITTED TO THE DEPARTMENT OF PHYSICS
AND THE COMMITTEE ON GRADUATE STUDIES
OF STANFORD UNIVERSITY
IN PARTIAL FULFILLMENT OF THE REQUIREMENTS
FOR THE DEGREE OF
DOCTOR OF PHILOSOPHY

Wei Liu
December 2006

I certify that I have read this dissertation and that, in my opinion, it is fully adequate in scope and quality as a dissertation for the degree of Doctor of Philosophy.

(Vahé Petrosian) Principal Adviser

I certify that I have read this dissertation and that, in my opinion, it is fully adequate in scope and quality as a dissertation for the degree of Doctor of Philosophy.

(Philip Scherrer)

I certify that I have read this dissertation and that, in my opinion, it is fully adequate in scope and quality as a dissertation for the degree of Doctor of Philosophy.

(Peter Sturrock)

Approved for the University Committee on Graduate Studies.

Abstract

The main theme of this thesis is the investigation of the physics of acceleration and transport of particles in solar flares, and their thermal and nonthermal radiative signatures.

The observational studies, using hard X-rays (HXRs) observed by the *RHESSI* mission, concentrate on four flares, which support the classical magnetic reconnection model of solar flares in various ways. In the X3.9 flare occurring on 11/03/2003, there is a monotonic upward motion of the loop top (LT) source accompanied by a systematic increase in the separation of the footpoint (FP) sources at a comparable speed. This is consistent with the reconnection model with an inverted-Y geometry. The 04/30/2002 event exhibits rarely observed two coronal sources. The two sources (with almost identical spectra) show energy-dependent structures, with higher-energy emission being close together. This suggests that reconnection takes place within the region between the sources. In the 10/29/2003 X10 flare, the logarithmic total HXR flux of the FPs correlates with the mean magnetic field. The two FPs show asymmetric HXR fluxes, which is qualitatively consistent with the magnetic mirroring effect. The M1.7 flare on 11/13/2003 reveals evidence of evaporation directly imaged by *RHESSI* for the first time, in which emission from the legs of the loop appears at intermediate energies. The emission centroid moves toward the LT as time proceeds, indicating an increase of density in the loop.

The theoretical modeling of this work combines the stochastic acceleration model with the NRL hydrodynamic model to study the interplay of the particle acceleration, transport, and radiation effects and the atmospheric response to the energy deposition by nonthermal electrons. We find that low-energy electrons in the quasi-thermal portion of the spectrum affects the hydrodynamics by producing more heating in the corona than the previous models that used a power-law spectrum with a low-energy cutoff. The Neupert effect is found to be present and effects of suppression of conduction are tested in the presence of hydrodynamic flows.

Acknowledgement

One of the most rewarding parts of the long journey of pursuing a PhD is probably writing this section. First of all, I would like to give my special thanks to my adviser, Prof. Vahé Petrosian. Without his continuous motivation, invaluable support, intellectual guidance, and help of various kinds, this dissertation could barely be accomplished. I would like to thank Prof. Peter Sturrock for discussions of solar flares and solar physics in general. I thank Profs. Tsuneyoshi Kamae and Robert Wagoner for their critical comments that helped improve this dissertation. I would like to acknowledge my wife, Li Jin, and my parents, who have provided me with love and a great deal of support over years.

I would like to thank Dr. Siming Liu and (soon to be Dr.) Yanwei Jiang for their indispensable contributions to my research, which came in many critical discussions of solar flares, plasma physics, and occasionally C++, IDL, and Latex. I thank William East for his latest contributions to the *$\mathcal{F}$lare* code. I thank Michael Dorris, Drs. Chi Yung (Stephen) Ng and David Sowards-Emmerd for their Linux help.

I would like to acknowledge Dr. John Mariska for generously providing his hydrodynamic code and for his timely help with flare simulations; I also thank Dr. Peng Li for discussions in this regard. I would like to thank Dr. Gordon Hurford for helpful discussions on imaging techniques and to Dr. Brian Dennis for suggestions on studying the Neupert effect as well as various help on *RHESSI* software issues. I thank Prof. Robert Lin for his leadership that ensured a successful *RHESSI* mission. I am also grateful to Drs. Sam Krucker, Jim McTiernan, Kim Tolbert, Tom Metcalf, David Smith, Richard Schwartz, Gordon Holman, Linhui Sui, (soon to be Drs.) Amir Caspi and Steven Christe, and other members of the *RHESSI* team for help of various kinds.

I am indebted to Prof. Philip Scherrer, my research adviser in my early years at Stanford, who provided me with generous support and a great deal of help in many ways. His critical comments on this thesis on the late stage of writing are greatly appreciated.

I am particularly grateful to Dr. Xue Pu Zhao for his motivation and guidance my CME studies and general heliospheric research. I sincerely thank Prof. S. T. Wu for his advice and motivation for numerical MHD simulations of CMEs; I thank Drs. Tianxi Zhang and Weiping Guo for their help with technical aspects of that study. I thank Drs. Yang Liu and Todd Hoeksema for help with analyzing *SOHO*/MDI data and enlightening discussions. I also thank Drs. Junwei Zhao, Sasha Kosovichev, Laurent Gizon, Aaron Birch, Tom Duvall, and Jesper Schou for discussions of helioseismology and various help (particularly on IDL); I thank Keh-Cheng Chu and Jeneen Sommers for their help with computing issues; I thank Dr. Simon Plunkett for help with analyzing *SOHO*/LASCO data; I thank Dr. Henrik Lundstedt for discussions on CME predictions and analysis of magnetic field time series; I thank Dr. Nariaki Nitta for discussions on CME observations; I also thank Drs. George Fisher, Janet Luhmann, Yan Li, Yuhong Fan, and Sarah Gibson for helpful discussions on various topics.

I am deeply grateful to Dr. B. C. Low for his motivation for CME modeling and solar MHD in general, as well as his continuous support and help over years. I would like to acknowledge my previous adviser, Prof. You Qiu Hu, who led me into the wonderful field of solar physics and taught me MHD simulation techniques. I also thank Dr. Mei Zhang for her comments and suggestions for my earlier CME modeling.

I am grateful to our administrative staff Dana Volponi, Margaret Stehle, Violet Catindig, Maria Frank, Kathline Guan, and Elva Carbajal for dealing with logistical issues. I would also like to thank Stephen Healey, Cheng Zheng, Adam Mantz, Mustafa Amin, Eric Morganson, Jane Li, and many others, who brought great fun to the astronomy program. I thank my fellow students Dunwei Wang, Zheng Wang, Yanping Pan, Ruixue Liu, Xiuping Xie, Yulin Chen, Zhaohua Yang, Arito Nishimori, Kyungyun Shin, Yao Chen, Zhigang Peng, Xianglei Huang, Yun Chen, Feng Deng, Yan Xu, Tongsheng Xia, Yi Zhou, and many others for their friendship and various help. There are many other people, too numerous to list here, who I would like to thank.

Data analysis in this research used the *RHESSI* software package developed and maintained by the *RHESSI* team members; the map structure developed by Dr. Dominic Zarro was used to produce the heliographic figures presented in this work; we also used many general tools in the IDL *Solar SoftWare* (SSW) package, contributed by the solar physics community at large. This work was supported by NASA grants NAG5-12111 and NAG5 11918-1 and NSF grant ATM-0312344.

Contents

Abstract **v**

Acknowledgement **vii**

1 Introduction **1**

1.1 Solar Flare Observations and Models 1

1.2 Stochastic Particle Acceleration Model 3

1.3 Hard X-ray Observations and *RHESSI* Instruments 5

1.4 Introduction to the Thesis 6

1.4.1 *RHESSI* Observations 6

1.4.2 Combining the Fokker-Planck and Hydrodynamic Codes 8

2 A Statistical Study of *RHESSI* Limb Flares **11**

2.1 Introduction 11

2.2 Data Reduction and Analysis 13

2.2.1 Sample Selection Criteria 13

2.2.2 Imaging 15

2.2.3 Imaging Spectra and Light Curves 16

2.3 Case Study Results 16

2.3.1 Single Loop Flares 16

2.3.2 Multiple Loop Flares 19

2.3.3 Miscellaneous Types 23

2.4 Statistical Results 24

2.4.1 Imaging Spectroscopy 24

2.4.2 Statistics of the Relative Fluxes: FPs vs. LTs 25

2.5 Flare Statistics and Selection Biases 27
2.6 Summary and Discussion 29

3 Flare Reconnection Model & 2003/11/03 X3.9 Flare 31
3.1 Introduction 31
3.2 Observations and Data Analysis 32
  3.2.1 Source Structure and Motion 33
  3.2.2 Imaging Spectroscopy 39
3.3 Summary and Discussion 40

4 Double Coronal Sources and Reconnection Site 43
4.1 Introduction 43
4.2 Observations and Data Analysis 45
  4.2.1 Energy-dependent Source Structure During the First Pulse 45
  4.2.2 Source Structure Evolution Throughout the Flare 49
  4.2.3 Temporal and Spectral Correlation of the Two Coronal Sources . . . 51
4.3 Summary and Discussion 54

5 Asymmetric HXR Footpoints & 2003/10/29 X10 Flare 57
5.1 Introduction 57
5.2 Observations and Data Analysis 58
  5.2.1 Overview of Multiwavelength Observations 58
  5.2.2 General *RHESSI* Observation and Footpoint Motions 59
  5.2.3 Conjugate Footpoints: HXR Fluxes and Magnetic Fields 62
5.3 Footpoint Asymmetry & Magnetic Mirroring 66
  5.3.1 Observational Motivation 66
  5.3.2 Literature Review 68
  5.3.3 Analysis 69
  5.3.4 Discussion 71
5.4 Summary 76

6 Chromospheric Evaporation & 2003/11/13 M1.7 Flare 77
6.1 Introduction 77
6.2 Observations and Data Analyses 80
  6.2.1 Pileup Effects 82

6.2.2 Source Structure and Evolution 83
6.2.3 Spectral Analysis 95
6.2.4 The Neupert Effect 97
6.3 Loop Density Derivation 103
6.4 Summary and Discussion 107

7 Modeling Impulsive Phase Solar Flares 111
7.1 Introduction 111
7.2 Simulation Models 114
7.2.1 Stochastic Acceleration Model 114
7.2.2 Particle Transport and Radiation Model 119
7.2.3 NRL Hydrodynamic Model 121
7.2.4 Combining the Particle and Hydrodynamic Codes 123
7.3 Simulation Result 128
7.3.1 Case R: Reference Calculation 129
7.3.2 Case A: Fiducial Run with SA Model 132
7.3.3 Case B: Variable Electron Spectrum 142
7.3.4 Case C: Harder Electron Spectrum 147
7.3.5 Case D: Smaller Normalization 151
7.3.6 Comparing The Cases: a Summary 154
7.4 Summary and Discussion 156

8 Testing the Neupert Effect 159
8.1 Energy Budget and the Neupert Effect 159
8.2 Case R: Reference Calculation 162
8.2.1 History of Energy Budget 162
8.2.2 Neupert Effect Test 165
8.3 Cases A-D: Combined HD & Particle Calculation 168
8.3.1 Case A: Fiducial Run with SA Model 169
8.3.2 Case B: Variable Electron Spectrum 171
8.3.3 Case C: Harder Electron Spectrum 174
8.3.4 Case D: Smaller Normalization 174
8.4 Summary and Discussion 177

9 Hydrodynamic Simulation of the Decay Phase 181

9.1 Introduction 181

9.2 Simulation Model of Suppression of Conduction and Plasma Heating 182

9.3 Numerical Results 184

9.3.1 Case A: No Heating or Suppression of Conduction 184

9.3.2 Case B: Heating Only 188

9.3.3 Case C: Suppression of Conduction Only 188

9.3.4 Case D: Heating and Suppression of Conduction 191

9.3.5 Comparing Cases A-D 193

9.4 Summary and Discussion 197

10 Concluding Remarks 199

10.1 Summary and Conclusions 199

10.1.1 Hard X-ray Observations 199

10.1.2 Combined Fokker-Planck and Hydrodynamic Modeling 202

10.2 Future Work 204

A *RHESSI* Tools and Tests 207

A.1 *RHESSI* Data Analysis Flow Chart 207

A.2 Technical Notes for Imaging Spectroscopy 211

A.3 *RHESSI* Simulation and Its Applications 213

B Coulomb Loss and Diffusion in Warm Plasmas 215

B.1 Coulomb Loss in Warm Plasmas 215

B.2 Coulomb Diffusion in Warm Plasmas 218

B.3 Implementation of Coulomb Loss and Diffusion 218

B.4 Thermalization Test of Injected Distribution 222

List of Tables

2.1 List of 29 flares in the sample for the statistical study 14

3.1 LT velocities and FP separation speed in the 2003/11/03 X3.9 flare 37

4.1 Spectral indexes of the two coronal sources in the 2002/04/30 flare 54

7.1 Summary of cases in the combined Fokker-Planck & hydrodynamic simulation 154

8.1 Neupert effect test of simulation cases 177

9.1 Summary of cases in the decay phase simulation 184

List of Figures

1.1 Schematic of the reconnecting magnetic field and two examples from flares of 11/03/2003 and 04/30/2002 4

2.1 Heliographic location distribution and histogram of the peak count rate of the sample flares 13
2.2 The 2092002 flare: light curves and hard X-ray images 17
2.3 Hard X-ray images of the 2092002 flare at different energies 17
2.4 νf_ν spectra of the LT and FP sources of the 2092002 flare 18
2.5 Light curves of the individual FP and LT sources in the 12–25 and 25–50 keV energy bands for the 2092002 flare 19
2.6 Light curves and source morphology of the 2080327 flare 20
2.7 *RHESSI* HXR contours at different energies (on *TRACE* EUV image) for the 2080327 flare 21
2.8 Light curves of individual FP and LT sources for the 2080327 flare 22
2.9 Images at different energies of the 2082809 and the 211141 flare 23
2.10 Statistics of LT and FP spectral indexes 24
2.11 Histograms of FP to LP flux ratios at different times and energies 26
2.12 Statistics of *RHESSI* peak count rates 28

3.1 Flare (X3.9) of 11/03/2003: *RHESSI* and *GOES*-12 light curves 33
3.2 Evolution of LT and FP source positions (on *SOHO*/MDI magnetogram) . 34
3.3 History of *RHESSI* light curves and source motion 36
3.4 LT source structure at different energies and its anti-correlation with HXR light curve 38

4.1 Flare of 04/30/2002: *RHESSI* light curves 45

4.2 PIXON images at 08:20:27–08:20:56 UT in different energy bands 46
4.3 Overlay of images in four energy bands 47
4.4 Height above the limb of the centroids vs. energy at four times 48
4.5 Images of three different energies at selected times 50
4.6 History of the centroid heights and HXR fluxes of the two coronal sources . 52
4.7 Imaging spectroscopy of the two sources in the 04/30/2002 flare 53

5.1 Flare (X10) of 10/29/2003: *GOES*-10 light curves 59
5.2 *TRACE* 195 Å images with *RHESSI* 15-21 and 50-100 keV images overplotted at selected times 60
5.3 MDI magnetogram and FP locations 61
5.4 Relative displacement of the two FPs perpendicular and parallel to the neutral line 63
5.5 History of the HXR fluxes of the two FPs and associated magnetic fields . . 65
5.6 Various correlations associated with the HXR fluxes and magnetic fields of the two FPs. 67
5.7 Asymmetry at different energies for the 10/29/2003 event and other flares . 72
5.8 FP photon flux ratio vs. energy for different ratios of the densities in two halves of the loop 75

6.1 Flare (M1.7) of 11/13/2003: *RHESSI* and *GOES*-10 light curves 79
6.2 Mosaic of CLEAN images 81
6.3 Ratio of pileup counts to total counts 83
6.4 Images overlaid with *SOHO*/EIT and MDI maps 85
6.5 Loop model and $(\|, \perp)$ profiles of surface brightness 87
6.6 Evolution of image profiles in three different energy bands 89
6.7 PIXON images at the impulsive peak in four different energy bands 91
6.8 Energy-dependent image profiles in three 24 s time intervals 92
6.9 Centroids of two halves of the loop at different energies 93
6.10 Positions of the centroids of the northern half loop, projected $\|$ and $\perp$ to the loop central arc 94
6.11 Time history of count rates, second moment of emission profile, EM, T, photon spectrum index γ, and low-energy cutoff $E_{\rm cutoff}$ 96
6.12 Bremsstrahlung yield for $E_1 = 20$ keV 98

6.13 Test of the Neupert effect: correlation of $\dot{F}_{SXR}$ and F_{HXR}, and of $\dot{F}_{SXR}$ and $\dot{\mathcal{E}}_e$ 101
6.14 Spatially integrated spectra (νF_ν) for the three 24 s time intervals 106
6.15 Inferred averaged density profiles along the loop during the three 24 s time intervals 107

7.1 Task flow chart for Particle & HD code communication 127
7.2 Initial state of the flare loop for the HD simulation 128
7.3 HD evolution of Case R 130
7.4 History of various quantities at 1 Mm from the LT for Case R 131
7.5 Evolution of electron spectra of Case A 133
7.6 HD evolution of Case A 134
7.7 Evolution of electron flux vs depth for Case A 137
7.8 Evolution of photon spectra of Case A 139
7.9 Evolution of photon emission vs depth of Case A 141
7.10 Evolution of electron spectra for Case B 143
7.11 Evolution of photon spectra for Case B 144
7.12 Evolution of electron & photon fluxes vs distance for Case B 145
7.13 HD evolution of Case B 146
7.14 Evolution of electron & photon spectra for Case C 148
7.15 Evolution of electron & photon fluxes vs distance for Case C 149
7.16 HD evolution of Case C 150
7.17 HD evolution of Case D 152
7.18 Electron & photon spectra and flux spatial distributions for Case D 153
7.19 Comparison of history of various quantities for the five cases 157

8.1 Thermal bremsstrahlung emissivity vs. temperature 161
8.2 History of energy budget and X-ray emission for Case R 163
8.3 Consistency check of energy conservation for Case R 164
8.4 Cross-correlation analysis for Case R at 1.6 keV 165
8.5 Cross-correlation analysis for Case R at 6 keV 166
8.6 History of energy budget and X-ray emission for Case A 168
8.7 Cross-correlation analysis for Case A at 1.6 keV 169
8.8 Cross-correlation analysis for Case A at 6 keV 170

8.9 History of energy budget and X-ray emission for Case B 171
8.10 Cross-correlation analysis for Case B at 1.6 keV 172
8.11 History of energy budget and X-ray emission for Case C 173
8.12 Cross-correlation analysis for Case C at 1.6 keV 174
8.13 History of energy budget and X-ray emission for Case D 175
8.14 Cross-correlation analysis for Case D at 1.6 keV 176

9.1 HD evolution of Case A 185
9.2 Energy evolution for Case A 187
9.3 Energy evolution for Case A: coronal and chromospheric portions 187
9.4 HD evolution of Case B 189
9.5 HD evolution of Case C 190
9.6 HD evolution of Case D 191
9.7 Energy evolution for Case D: the full loop and the coronal portion 192
9.8 Comparison of temperature, density squared n_e^2, and thermal bremsstrahlung emission profiles among Cases A-D 194
9.9 Comparison of decay of various quantities for Cases A-D 196

A.1 Simulated *RHESSI* dynamic range 213

B.1 Function $\psi(x)$ and its derivative. 216
B.2 Coulomb loss rate in a warm plasma 217
B.3 Energy loss and diffusion rates due to Coulomb collisions in a warm plasma 220
B.4 Coulomb loss and diffusion timescales 221
B.5 Thermalization test of an injected gaussian distribution 222

Chapter 1

Introduction

Acceleration of particles and the consequent transport and radiation effects are ubiquitous in astrophysical plasmas, such as those responsible for cosmic ray particles, gamma-ray bursts, and flares on accretion disks near compact objects (e.g., black holes and X-ray binaries). Solar flares serve as one of the most suitable laboratories to study particle acceleration and related high-energy processes, because of the proximity of the Sun and abundant observations available. The primary goal of this research is to understand particle acceleration mechanisms in general, and how these mechanisms operate in solar flares in particular.

1.1 Solar Flare Observations and Models

Solar flares are one of the two most energetic phenomena on the Sun (the other being coronal mass ejections, CMEs), involving up to some 10^{32} ergs or more energy released on a timescale of a few minutes to tens of minutes (cf., solar luminosity of 3.827×10^{33} ergs s^{-1}). The very first flare ever observed was discovered in white-light as an emission burst by R. C. Carrington on September 1, 1859. Since then, flare observations have been accumulated over a century in many other wavelengths, including H_α, radio waves, and X-rays, gamma-rays in recent decades.

Theoretical investigations of solar flares have lagged behind. Among the earliest flare models were those proposed by Carmichael (1964), Sturrock (1966), Hirayama (1974), and Kopp & Pneuman (1976). These 2-D models, in one way or another, involve magnetic reconnection (Sweet, 1958; Parker, 1963; Petschek, 1964) with an inverted “Y”- or an

"X"-shaped topology, in a (vertical) current sheet, which can be produced by a preceding CME or magnetic flux emergence from below the photosphere. Advances in recent decades have improved on these early models, but the basic picture remains the same.

In the currently widely accepted scenario, the basic physical processes involved and the observational signatures are as follows. Magnetic reconnection, as the primary energy release mechanism occurring high in the corona, rapidly heats the plasma and accelerates particles. Some particles escape along the open magnetic field lines into the interplanetary space, with electrons producing various radio bursts and some electrons (Wang, Lin, Krucker, & Gosling, 2006) and ions (Krucker & Lin, 2000) being detected at 1 AU. Other particles escape along the newly reconnected closed magnetic loop to lower layers of the atmosphere. Electrons, while spiring along magnetic field lines, can produce microwave bursts via synchrotron radiation. These electrons, in the meanwhile, lose their energy through Coulomb collisions with the ambient plasma, primarily in the transition region and the chromosphere where the density is sufficiently high, and produce hard X-ray (HXR) emission via bremsstrahlung. This results in the so-called footpoint (FP) emission observed in HXR wavelengths. Accelerated ions, while colliding with background particles, can excite nuclear reactions and produce gamma-ray emission.

The released energy, which is carried by particles and/or thermal conduction and transferred to lower atmospheres, can heat the chromosphere rapidly. The resulting overpressure in the over-heated chromosphere can drive a mass flow upward along the loop at a speed of a few hundred km s^{-1}, which can be observed as blue-shifted chromospheric emission lines. The mass motion fills the flaring loop with a hot plasma, giving rise to the loop structure seen in soft X-ray (SXR) and gradual evolution of SXR flux. This process, termed *chromospheric evaporation* by Neupert (1968), was proposed to explain the empirical temporal relationship of the derivative of the SXR flux and the HXR light curve, i.e., the Neupert effect (Hudson, 1991), which is observed in some (but not all) flares (Dennis & Zarro, 1993).

Consequent energy redistribution in the lower layers of the atmosphere, on the other hand, can produce ribbons seen in H_α and occasionally in white-light for the brightest flares. As time proceeds, reconnection develops to higher altitudes in the inverted-Y shaped configuration, and the two HXR FPs and H_α ribbons are usually seen move away from each other, in a direction more or less perpendicular to the magnetic neutral line. This gives the standard picture of a two-ribbon flare.

1.2 Stochastic Particle Acceleration Model

There are two most important unresolved questions regarding the physics of solar flares. The first is how energy is released, which involves details of the magnetic reconnection process. The other is how particles are accelerated, which is the main goal of this thesis, and we focus on acceleration of electrons here.

In general, there are three types of acceleration commonly quoted in solar flares (and other astrophysical plasmas). (1) **Direct electric field acceleration** (Holman, 1985; Benka & Holman, 1994) can boost a particle to high energies simply via the Coulomb force from the electric field and may operate in the current sheet or in the reconnection site, but it is difficult to maintain a large-scale coherent DC electric field. (2) **Shock or first-order Fermi acceleration** can energize particles by making them repeatedly pass through the shock front back and forth and this mechanism may be present in the fast shock produced by the super-magnetosonic outflow jet from the reconnection region. However, it would be difficult to reflect the particles in the upstream region. (3) **Stochastic (second-order Fermi) acceleration** by turbulence or plasma waves is the most likely mechanism (Petrosian, 1994, 1996) for solar flares, compared with the shortcomings of the other two mechanisms (although they may also be operating to some extent).

The **stochastic acceleration (SA)** mechanism has been studied and advanced by many authors for various reasons (e.g. Ramaty, 1979; Ramaty & Murphy, 1987; Hamilton & Petrosian, 1992; Miller et al., 1996; Park et al., 1997; Petrosian & Liu, S., 2004) and for astrophysical environments (e.g. Liu, S. et al., 2004b). The SA model is supported by remote HXR observations and by *in situ* measurements of interplanetary particles. In particular, Liu, S., Petrosian, & Mason (2004a, 2006) have shown that the enhanced ^{3}He over ^{4}He ions observed by the *ACE* spacecraft can be accounted for by the preferential resonance interactions of ^{3}He with turbulence.

In the SA model, the basic picture is as follows. As a consequence of magnetic reconnection, large-scale turbulence or plasma waves (see Figure 1.1) are generated at/near the reconnection region. Turbulence then cascades to small scales, and accelerates particles and heats the plasma via resonance wave-particle interactions in a region near/at the top of the flaring loop. The accelerated particles produce in the acceleration region the thin-target HXR loop-top (LT) source (Masuda 1994), which was one of the major discoveries of the *Yohkoh* mission. Some particles are trapped in the acceleration region due to scattering by turbulence, and some escape and produce the thick-target FP emission in the chromosphere.

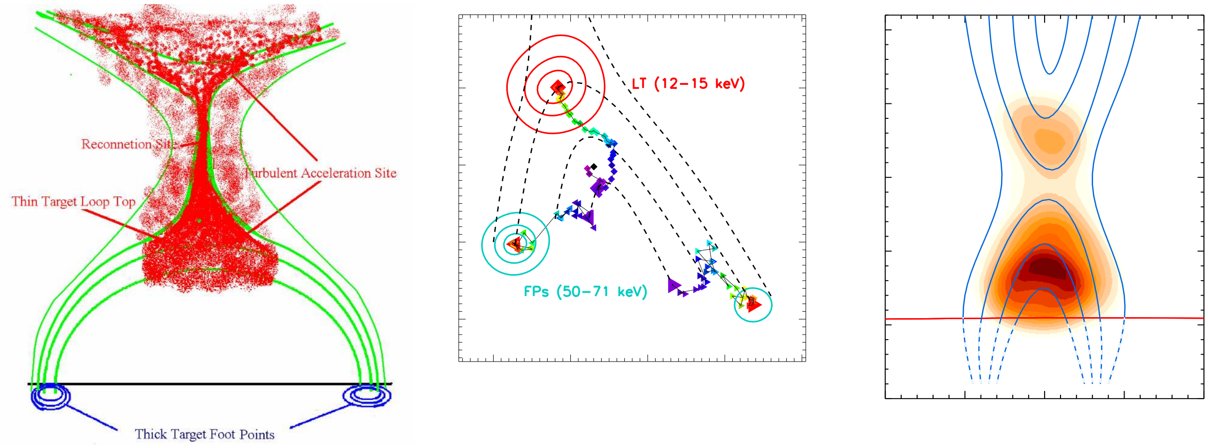

Figure 1.1: *Left:* Schematic of the reconnecting field forming closed loops and coronal open field lines. The red foam represents plasma waves or turbulence (Courtesy of Vahé Petrosian). *Middle:* Temporal evolution of the LT and FP HXR sources of the 2003 November 03 flare (see Chapter 3). The symbols indicate the source centroids and the colors show the time with a 20 s interval, starting from black (09:46:20 UT) and ending at red (10:01:00 UT) with contours for the last time. The dashed curves connect schematically the FP and LT sources for different times showing the expected evolution for the model on the left. *Right:* Image of a flare on April 30, 2002 (see Chapter 4), showing an elongated LT source with two distinct peaks as expected from the model on the left. The red curve indicates the solar limb which occulted the FPs and the blue curves (added by hand) represent the magnetic field lines. Note that both the middle and right panels are rotated from their original orientations for a better visual comparison with the model on the left.

The stochastic acceleration process can be described by the Fokker-Planck equation,

$$\frac{\partial f}{\partial t} = \frac{\partial}{\partial E}\left[D(E)\frac{\partial f}{\partial E}\right] + \frac{\partial}{\partial E}\{[A(E) - \dot{E}_L]f\} - \frac{f}{T_{\rm esc}(E)} + Q(E)\,, \tag{1.1}$$

where $f \equiv f(t, E)$ is the electron distribution function, $E = \gamma - 1$ (γ being the Lorentz factor) is the electron kinetic energy in units of $m_e c^2$, $D(E)$ and $A(E)$ are the energy diffusion and systematic acceleration coefficients, $T_{\rm esc}$ is the particle escape time, $Q(E)$ is the total injection flux of electrons into the acceleration region that acts as source term in the equation. $\dot{E}_L = \dot{E}_{\rm Coul} + \dot{E}_{\rm synch}$ is the absolute value of the net systematic energy loss rate, which is a combination of Coulomb loss $\dot{E}_{\rm Coul}$ and synchrotron loss $\dot{E}_{\rm synch}$. The central task of such a model is to determine the resonance condition for a particle (with a given momentum and pitch angle) and a given turbulence spectrum, and thus obtain the coefficients $D(E)$, $A(E)$, and $T_{\rm esc}$.

The subsequent particle transport in the flare loop can be described with a similar diffusion equation, with the addition of the magnetic mirroring effect and pitch angle scattering. A unified code, called $\mathcal{F}lare$, that can calculate the particle acceleration and transport, together with bremsstrahlung radiation, has been developed (Petrosian, Donaghy, & Llyod 2001), on the basis of previous advances accumulated over two decades (Leach, 1984; McTiernan, 1989; Lu, 1989; Hamilton, 1990; Park, 1996). This code was used in the theoretical modeling part of this thesis (see Chapter 7).

1.3 Hard X-ray Observations and *RHESSI* Instruments

HXRs (and gamma-rays) observed during the impulsive phase of flares provide the most direct information on the spectrum of accelerated particles and give us clues to the acceleration mechanisms. A power-law distribution (with an index of δ) of electrons, for example, can produce a power-law HXR spectrum with a photon index of $\gamma \simeq \delta \pm 1$ from a thin- and thick-target sources, respectively.

Observations by instruments on board earlier missions (e.g. *SMM, Hinoatori, C-GRO, and Yohkoh*) have advanced our understanding on this subject (see the review by Aschwanden, 2004). The currently active Reuven Ramaty High Energy Solar Spectroscopic Imager (*RHESSI*) mission with its superior capabilities (Lin et al., 2002) has proven that it can make a more accurate determination of temporal, spectral and spatial evolution of flares (see the *RHESSI* dedicated Solar Physics Vol. 210, 2002 and ApJ Letters Vol. 595, No. 2, 2003).

RHESSI is a NASA small explorer (SMEX) mission, designed to study particle acceleration and energy release in solar flares (and some non-solar science, Lin et al. 2002). It has an array of nine large-volume (300 $\rm cm^3$) coaxial germanium detectors (Smith et al., 2002), with a total collecting area of $\sim 150\,\rm cm^2$. This provides an energy resolution down to $\sim 1\,\rm keV$ and an energy coverage of 3 keV–17 MeV. Its imaging capability is enabled by the Rotating Modulation Collimator (RMC) system and the spacecraft spin at 15 rpm ($\sim 4\,\rm s$ period). Each of the nine subcollimators consists of two grids, 1.55 m apart, with the germanium detector equipped behind the rear grid. During a flare, each photon arriving at the detector is tagged with its arrival time and energy. Then the spatial information is recovered through the image reconstruction procedure at the time of data analysis on the ground, which is realized by Fourier transform of the time series data of energy tagged counts, i.e., the modulation pattern (Hurford et al., 2002). Such a unique imaging system produces an angular resolution of $2.3''$ in its 1° field of view (covering the full Sun). The temporal resolution can reach $\sim 2\,\mathrm{s}$ for detailed images and tens of ms for basic images.

Since its launch, *RHESSI* has provided us with unprecedented details of solar flares, some of which are of serendipity (e.g., Liu, W. et al., 2006) and some of which pose new challenges to theoretical models (e.g., Sui & Holman, 2003; Hurford et al., 2003). We will present some of such observations in this thesis.

1.4 Introduction to the Thesis

The main theme of this thesis is the investigation of the micro and macro physics of the acceleration and transport of particles (electrons[1]) in solar flares, and their thermal and nonthermal radiative signatures. To reach this objective, we took a two-prong attack, using HXR data analysis and theoretical modeling, both couched in the framework of the SA model. Our data analysis concentrated on HXR images and spectra observed by *RHESSI* during the impulsive phase of flares. Our modeling efforts was devoted to combining the SA model and the $\mathcal{F}lare$ code with a hydrodynamic (HD) model (Mariska, Emslie, & Li, 1989) to study the interplay of the particle acceleration, transport, and radiation effects and the atmospheric response to the energy deposition by accelerated electrons.

1.4.1 *RHESSI* Observations

During 1970s and 1980s, HXR imagers on board early missions, such as *SMM* and *Hinoatori*, revealed the FP emission which supports the thick-target model (Brown, 1971; Petrosian, 1973) for solar flares. In early 1990s, the *Yohkoh* mission discovered the HXR LT source (Sakao, 1994; Masuda, 1994), which marked a milestone in flare research and provided further evidence for the stochastic acceleration model (e.g., Hamilton & Petrosian,

---

[1] Acceleration of protons and other ions is another aspect of solar flare energetics, and is beyond the scope of this work.

1992). *RHESSI*, with its superior capabilities, can provide more accurate temporal, spatial, and spectral information of the LT and FP (and other possible) sources and thus help improve theoretical models. Obtaining such information of individual sources and offering appropriate physical interpretations is the main task of the observational part of this thesis.

In the SA model, the LT emission comes directly from the accelerated electrons (thin target) and the FP emission is produced by escaping electrons in a thick target region. The fluxes and spectra of the two sources are related and can thus be used to constrain the SA model parameters. We have carried out a preliminary statistical study of 29 *limb* flares, which have minimal projection effects, and obtained the relative spectra and fluxes of the LT and FP sources. We find a large difference between the average values of the LT and FP spectral indexes, which, together with other statistical results, will be presented in *Chapter 2*. This statistical study have also paved the path to identify four interesting flares for in-depth investigations, each of which presents *evidence* of particular aspects as well as imposes *challenges* for the classical reconnection model of solar flares.

In the classical flare model, as mentioned earlier, magnetic reconnection takes place at lower altitudes first and progresses to higher overlying loops as time proceeds. In this picture, one would expect that the FPs move apart while the LT source moves up with time. We will show in *Chapter 3* an excellent example (the 2003 November 03 X3.9 flare, see Figure 1.1, *middle*) of such a picture. In the following two chapters, we will focus on the LT and the FP emission respectively.

In the common 2-D reconnection picture, outflow jets of high speed plasmas are present in opposite directions along the current sheet. Accelerated particles and heated plasmas are expected to be present in both directions as well. As we can see in Figure 1.1 (*right*), a flare occurring on April 30, 2002 exhibits a double-source structure in the corona, which suggests that reconnection takes place in between. Analysis of the images and spectra of this flare will be presented in *Chapter 4*.

We now turn our attention from coronal (LT) emission to chromospheric (FP) emission. As noted earlier HXR observations can provide useful information about the electron spectrum, while magnetic field measurements of the flare region can give clues to magnetic reconnection development. Combining both observations, if available, can improve our understanding of flares. As we will see in *Chapter 5*, the 2003 October 29 X10 flare, which occurred near the disk center and thus had minimal projection effects for line-of-sight magnetic field measurement, provided us such an excellent opportunity.

In *Chapter 6*, we will, again, examine both LT and FP emissions. The 2003 November 13 M1.7 flare shows some unusual spatial evolution and provides direct evidence for chromospheric evaporation. We find that emission from the legs of the loop dominates at intermediate energies and the emission centroids move from the FPs to the LT as time proceeds. This suggests an increase of loop density, possibly as a consequence of chromospheric evaporation. However, some observed source morphologies and their evolution cannot be accounted for by previous modeling efforts. Therefore, simulations with more realistic physical conditions are required to explain the results as well as the particle acceleration & transport and plasma heating processes.

1.4.2 Combining the Fokker-Planck and Hydrodynamic Codes

Motivated by the *RHESSI* observations mentioned above, we have embarked on an investigation of combining the Fokker-Planck $\mathcal{F}lare$ code with the Naval Research Laboratory (NRL) flux tube hydrodynamic (HD) model (Mariska, Emslie, & Li 1989). Aside from the observational incentive, the theoretical motivation comes as follows.

There are basically two faces of a solar flare — one concerns energetic particles and their transport and radiation effects, and the other concerns the hydrodynamic evolution of the plasma in the flare loop. These two aspects are actually coupled together in a circular chain. Particles, on the one hand, lose their energy via Coulomb collisions and heat the background plasma, which causes chromospheric evaporation that changes the density and temperature distribution in the loop. In turn, such changes affect the particle acceleration and transport processes and influence the spectrum of the accelerated particles. The energy deposition rate (by particles) will also be altered and fed back to the hydrodynamics of the background plasma.

Due to the complexity of the subject, however, people tend to decouple these processes and study one at a time while assuming some simply forms for the others. For particle acceleration and transport, as mentioned earlier, one of the main streams of studies solves the Fokker-Planck equation and keeps tracking of the particle distribution function (e.g., Leach 1984; McTiernan 1989), assuming a *static* background atmosphere. For the hydrodynamics, a majority of efforts (e.g., Fisher et al., 1985c,b) are put into 1-D numerical HD simulations, assuming the plasma can only move along the magnetic field line, which is a valid assumption for a magnetic field dominated (low-β) plasma. In such simulations, some form of a *simple* (e.g., power-law) electron distribution is usually assumed and results from simplified analytical solutions are used to provide the heating rate.

A more realistic and self-contained treatment of both particles and gas dynamics is thus desired. We have started such an investigation and engineered the two codes (as mentioned above) to work together, which possesses the potential to advance our understanding of solar flares significantly. We have used the newly combined code to examine the atmospheric response to the energy deposition of electrons with a spectrum predicted by the SA model (Petrosian & Liu, S., 2004). Our approach and result will be presented in *Chapter 7*.

From the same simulations, we have also examined the empirical Neupert effect with more rigorous (than previous works, e.g., by Veronig et al. 2005) calculations of the energy contents and thermal and nonthermal X-ray radiation. This study will be presented in *Chapter 8*.

As an extension of our studies on the flare impulsive phase, we will present in *Chapter 9* a simulation of the decay phase. The goal here is to test the effects of suppression of conduction and/or heating, presumably produced by turbulence (at a lower level during the decay phase), in the presence of HD *flows*. Our earlier analytical investigation (Jiang et al., 2006) of the problem assumed a hydrostatic atmosphere which is an approximation, and rigorously speaking, not quite realistic. Our result confirms the earlier conclusion that suppression of conduction and/or heating is required to explain the X-ray observations and suggests that an even larger factor of suppression would be needed.

Finally, in the *Appendix*, we will present some technical notes on *RHESSI* data analysis, together with a note on the improvement of the current SA model by inclusion of Coulomb collisions with a warm/hot background plasma.

Before we move on to the body of this work, I would like to acknowledge contributions from the members of our research group. Prof. Vahé Petrosian, my adviser, provided many of the crucial ideas and original motivation to carry out this research. Dr. Siming Liu offered many ideas from a theoretical point of view to the *RHESSI* observations and he originally noted the interesting features in the 2003 November 13 M1.7 flare (Chapter 6). Yanwei Jiang contributed to the spectral fitting in the statistical study of imaging spectroscopy (Chapter 2) and in other flares (Chapters 3 and 6). William East contributed to the programming task of implementing the warm-plasma Coulomb collision into the acceleration portion of the $\mathcal{F}lare$ code (Appendix B).

Chapter 2

A Statistical Study of Limb Flares Observed by *RHESSI* : Imaging and Imaging Spectroscopy

2.1 Introduction

Observations of solar flares by low spectral and spatial resolution instruments can give us only the light curve and a crude spectrum of the whole flare which may consist of many distinct sources with different characteristics. The discovery of distinct looptop (LT) sources (Sakao, 1994; Masuda, 1994) in addition to the normal footpoint (FP) sources, made by the *Yohkoh* satellite, has provided further evidence for the stochastic acceleration model (Petrosian & Donaghy, 1999; Petrosian et al., 2002) which was shown to be consistent with the broadband spectra of several solar flares (Park et al. 1997). As suggested by this and other models, these different sources should have different electron spectra determined by the physical condition at the acceleration site. Statistical studies of FP-to-LT flux ratios have been conducted for *Yohkoh* flares (Petrosian et al., 2002; Tomczak & Ciborski, 2007).

The exceptional imaging spectroscopic capacity of *RHESSI* (Lin et al. 2002), combined with its excellent time resolution, provides us a multi-dimensional picture of solar flares, which can set stringent constraints on the model parameters and will eventually improve our understanding of the relevant physical processes.

One important aspect of such constraints can be obtained from the spectral correlation of the FP and LT sources. In the stochastic acceleration model the LT emission comes directly from the accelerated electrons (thin target) while the FP emission is produced by the escaping electrons in a thick target region. The flux and spectra of the two sources are related. The exact relation depends on various acceleration mechanism and plasma parameters but very roughly the FP to LT X-ray flux ratio at photon energy E can be written as (see Petrosian & Donaghy 1999 and equation 7.23) $I_{FP}/I_{LT} \simeq \tau_{\rm loss}(E)/T_{\rm esc}(E)$, where $\tau_{\rm loss} = E/\dot{E}_L$ is the electron energy loss time at the LT (due to Coulomb collision at low energies and synchrotron loss at high energies), and the energy dependence of the escape time $T_{\rm esc}$ (see, e.g., equation 7.20) depends on the details of the acceleration process in the LT region. This means that the relative spectra can constrain the plasma and acceleration model parameters. At low energies, for example, $\tau_{\rm loss} \propto E^{3/2}$ (since $\dot{E}_{\rm Coul} \propto 1/\beta$, see equation 7.3), and thus the functional form of $T_{\rm esc}(E)$ can be directly obtained from the observed flux ratio.

A statistical study of the relative spectra of different sources is thus required to obtain such observational constraints with sufficient statistical confidence. We carefully selected a sample of 29 limb flares, which may provide some statistical information on LT and FP emissions. A larger sample of events has not been practically doable in the past, given the unstable status (particularly for imaging spectroscopy) of *RHESSI*'s instrument calibration and software development on the early stage of the mission (launched 2002), but we look forward to expanding our sample in the future.

We present in this chapter images, light curves of the LT and FP sources of the sample flares, as well as their imaging spectroscopy. We describe the flare selection criteria and the imaging procedure in §2.2. Results from case studies of typical flare events are given in §2.3. Statistics on various aspects is shown in §2.4 and §2.5. Finally we conclude this chapter with §2.6. Discussions on miscellaneous techniques used in this study are given in §A.2.

2.2 Data Reduction and Analysis

2.2.1 Sample Selection Criteria

We searched through the online *RHESSI* flare list (from February 12, 2002 through April 18, 2004[1]) for appropriate limb flares, using criteria similar to those introduced by Masuda (1994) and used by Petrosian et al. (2002), which are:

- Heliocentric longitude ≥ 70 degrees. This provides sufficient angular separation between FP and LT sources. The heliocentric (x, y) coordinates in the *RHESSI* flare list[2] were converted to heliographic (longitude, latitude) coordinates[3]. For flares whose locations are not available in the list, we obtained the locations by making full disk *RHESSI* images, usually in the 12–25 keV energy channel about the peak time, and used the position of the brightest pixel as the flare location.
- Peak count rate ≥ 30 per second per detector in the 12–25 keV channel, allowing sufficient count statistics and thus good image quality.

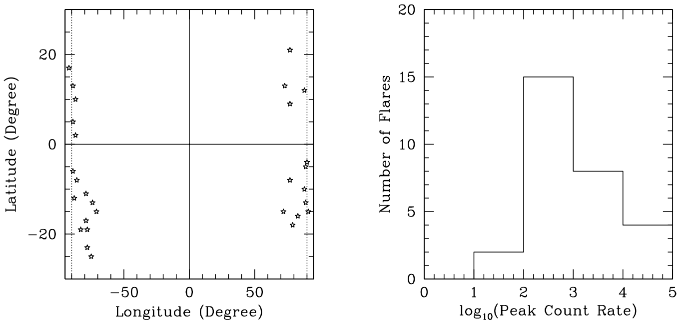

Figure 2.1: The heliographic location distribution (*left*) and the histogram of the peak count rate (*right*) at 12–25 keV of the sample flares. The dotted vertical lines in the left panel marks 90° in longitude

We then carefully examined the sample flares satisfying these criteria and eliminated those with strong particle events, severe pileup or decimation, or poor data quality. There

---

[1] The analysis presented here was initiated back in 2003 using the *RHESSI* software existing then. New flares were added to the latest sample as of April 18, 2004. The software has been improved since then and thus may give slightly different results.

[2] see http://hesperia.gsfc.nasa.gov/hessidata/dbase/hessi_flare_list.txt

[3] We used xy2lonlat.pro in the *Solar SoftWare* package to do the conversion. For flare locations off the limb, the corresponding positions projected back to the limb were used. These flares may have a longitude greater than 90° (see Table 2.1), because the solar pole is not aligned in the plane of the sky.

Table 2.1: List of $(22 + 7 = 29)$ flare events included in this study.

Flare ID (ymmdd#)	Peak time (UT)	Disk position	NOAA AR #	GOES class	Peak Count	Highest E-band (keV)	Image spec. (Y/N)	Notes
2022003	11:06:18	N13W73?	-	C7.5	656	50-100		3 FPs, no LT?
2032819	17:58:18	S04W90	-	C7.6	200	25-50		one source (LT)?
2041509	23:12:26	N21W77	9893?	M1.2	816	25-50		complex^T
2051706	07:38:10	N13E89?	-	M1.5	1328	25-50		2 LTs?
2051909	21:46:22	S23E78	-	C4.7	84	25-50		source not well def.
2062904	09:29:46	S17E79	-	C2.0	352	12-25		single loop
2072301	00:30:06	S13E74	0039	X4.8	57379	800-7000	Y	complex^T
2072307	12:21:42	S19E78	-	C2.9	240	25-50		complex^T?
2080327	19:06:54	S16W83	0039	X1.0	28697	25-50		complex^T
2080602	05:18:18	N17E92	-	C2.1	108	25-50		single loop?
2081203	02:17:18	S08E86	-	C1.4	160	25-50	Y	single loop
2082336	16:10:18	S10W88	-	-	104	25-50		single loop^T
2082418	11:16:10	S05W89	0069?	-	400	25-50		complex (multi-LTs)^T?
2082803	10:59:30	S18W79	0083	C5.7	912	50-100		complex
2082809	18:10:46	N10E87	-	C6.6	784	12-25		one source (LT)
2090309	12:45:42	S08W77	0087?	C1.5	128	25-50		complex
2090608	16:27:02	S06E89	-	C9.2	752	25-50		loop not well def?
2090801	01:39:10	S11E79	0105	M1.5	1072	12-25	Y	complex
2092002	09:26:42	S25E75	0126	M1.8	1520	800-7000	Y	single loop
2111410	11:09:38	S15E71	0195?	C5.5	352	50-100		2 FPs
2112532	21:50:30	S13W89	-	C?	72	25-50		single loop
3021411	09:17:18	N12W88	-	M1.2	1072	25-50		one source
added 05/2004:								
2042101	01:30:30	S15W91	9906	X1.5	59298	800-7000	Y	complex (multi-LTs, 2-FPs)
2090708	17:41:22	S12E88	-	-	240	25-50	Y	complex (multi-LTs, 2-FPs)
3102405	02:35:34	S19E83	-	-	1587	50-100	Y	complex (multi-LTs, 2-FPs)
3110316	09:51:38	N09W77	-	X3.9	13808	300-800	Y	single loop
3110319	15:31:14	S15W72	-	-	3032	25-50	Y	complex (multi-loop, 3-FPs)
3111313	04:59:14	N02E87	0501	M1.7	1328	50-100	Y	single loop
4010604	06:25:30	N05E89	-	-	2288	800-7000	Y	complex (multi-LTs, 2-FPs)

Note — The first 22 events were selected from the period from 12-Feb-2002 through 02-May-2003; the new 7 events were from the period through 18-Apr-2004. (1) Peak counts (counts/s) are in the 12–25 keV energy band. (2) "Image spec." — Y (yes) marks a total of 11 events whose LT and FP spectra have been obtained for spectral index statistics shown in Fig. 2.10. (3) "single loop": 8 events here are of this type. (4) "complex" = complex morphology or multiple loops; 13 events fall into this category. (5) "one source" = only one source was detected; 3 events have this characteristics. (6) Out of the rest 5 events, two do not have a well-defined loop (source) structure, and the other three appear to have either LT or FP (not both) sources. (7) The superscript 'T' denotes those flares with *TRACE* data available in the *RHESSI* FOV.

are 29 flares included in our final sample, which are listed in Table 2.1. The heliographic locations (*left*) and the distribution of the peak count rate (*right*) at 12–25 keV are shown Figure 2.1. For each sample event, we performed imaging spectroscopy and light curve study as follows.

2.2.2 Imaging

At the time of this study, for the purpose of studying spectroscopy and light curves of individual sources using *RHESSI* data, the first step was to reconstruct images in different energy bands and/or time ranges. We describe the key points in our imaging processes below and list the details in the appendix (see § A.1).

(1) **Imaging algorithms**. Among the available *RHESSI* imaging algorithms (Hurford et al. 2002), we used Back-projection and/or CLEAN for preliminary studies, CLEAN for light curve purposes as it is relatively much faster, and used much computationally expensive PIXON for imaging spectroscopy, which because of its excellent photometry is most suitable for this task.

(2) **Time Ranges.** Different time ranges were selected for different purposes. For spectroscopic images, a time range about the peak in the 25–50 keV channel is preferred. For light curve images, we selected a time interval including the rise and decay phase and divided it into a number of time bins (each bin for an image). Each time bin has an appropriate length (a multiple of the spacecraft spin period $\simeq$ 4 seconds) to allow sufficient photon counts for imaging as well as good temporal resolution. All the time bins are selected to be exclude intervals with particle events, with attenuator state changes, or with decimations.

(3) **Energy Bins.** For imaging spectroscopy, the energy ranges were set as follows. The lower limit of the energy range was obtained by the attenuator states: namely, about 6 keV when none of the two attenuators is closed, 10 keV when one is in, and 15 keV when both are in. The upper limit goes as high as there are sufficient signals in the images. Once the energy range was obtained we divided it into logarithmically spaced bins. Two aspects were taken into account for determining the energy bin width. On the one hand, we would like to have as many as possible bins in order to obtain a sufficiently large number of data points for spectral fits, but the smallest bin width (at the low energy end) should not be smaller than 1 keV, the nominal *RHESSI* energy resolution; on the other, we would like to have broad energy bins to increase the photon count rate in each bin for better

statistical S/N in images, but it is not legitimate to construct images with an arbitrarily wide[4] energy range because the instrument response varies with energy and the imaging software only take a mean energy for computing the expected instrument response (Smith et al. 2002). For light curves, we took much broader energy bins, within which images at different energies exhibit common features.

2.2.3 Imaging Spectra and Light Curves

Once images at different energies or times are obtained, we are ready to infer spectra as well as light curves of individual sources. By examining images at various energies and times, we identified FP and/or LT sources. For each source, we selected a box to enclose it and summed over all the pixel values in this box, divided by the width of the energy bin, to get the differential photon flux. If available, images from *Transition Region And Coronal Explorer* (*TRACE*) were used to help distinguish individual sources. Plotting the flux versus energy (time) results in the spectrum (light curve) and in turn the characteristics of the spectrum (light curve) provides clues on the nature of the source. For the events in which we cannot unambiguously identify the magnetic connectivity between corresponding FP and LT sources, we summed the fluxes of all the FPs.

2.3 Case Study Results

We present in this section results from selected events falling in three morphological categories: single-loop, multiple-loop, and miscellaneous types.

2.3.1 Single Loop Flares

Out of the 29 total events, eight appear to be morphologically similar to the canonical Masuda (1994) flare, namely, a LT source connected by a single flaring loop to two FPs. PIXON images of these flares were obtained around the peak time, and other times whenever the count rate was sufficiently large to allow imaging in the 25–50 keV band. We use these images as the input for imaging spectroscopy.

---

[4] Smith et al. (2002) recommended that the size of a energy bin should not exceeds 1/10 of its mean energy for (spatially integrated) spectroscopy. However, this requirement might be too strict imaging spectroscopy, as one usually must use relatively broad energy bins to achieve sufficient count statistics for imaging.

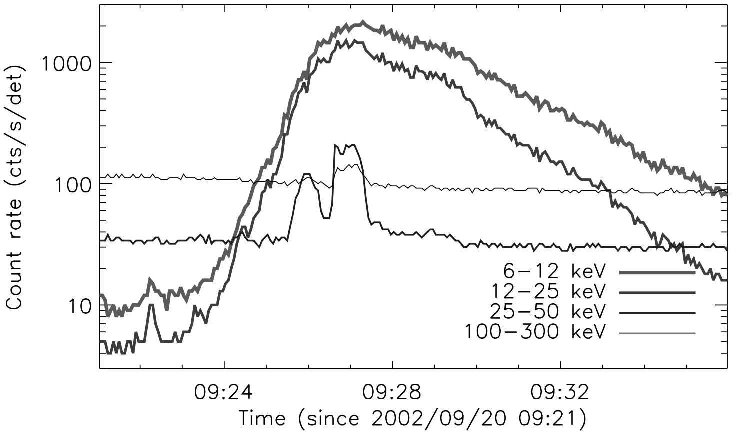

Figure 2.2: *RHESSI* light curves of the 2092002 flare.

Here we describe the 2002 September 20 flare (ID 20920020), which is a *GOES* M1.8 event observed by *RHESSI* up to 800–7000 keV. This event started at 09:22:08 UT, continued rising to a sub-peak at 09:25:59 UT in energy channel between 25 keV and 300 keV, and peaked at 09:26:42 UT nearly simultaneously in the energy channels from 6 keV through 300 keV as can be seen from the light curves in Figure 2.2. We focus on the impulsive phase here. The decay phase of this flare was studied by Jiang et al. (2006).

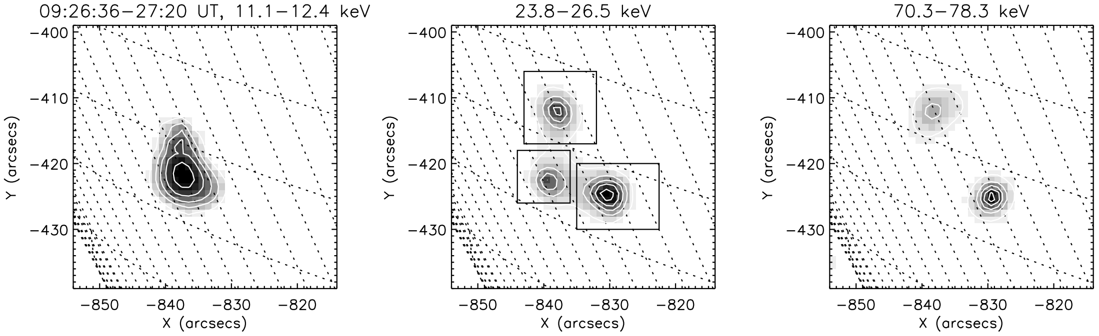

Figure 2.3: Hard X-ray images of the 2092002 flare at different energies. The white contours are at the 10%, 30%, 50%, 70%, and 90% levels of the maximum of each panel. We show in the middle panel three boxes defined to enclose individual sources to infer their spectra and light curves.

The HXR images were reconstructed by the PIXON algorithm using front segments of detectors 3 through 6, and detectors 8 and 9, with a minimal spatial resolution of

7″. Figure 2.3 shows the resulting images in separate energy bands for a time interval [09:26:36, 09:27:20 UT], covering the main peak. It is clearly shown that in the 11.1–12.4 keV image a diffuse source dominates, suggesting a hot LT source. Two FP sources appear in about 23.8–26.5 keV and become more and more dominant at higher energies. Note the southern FP is much brighter than the northern one, which may be due to possible asymmetric convergence of the magnetic loop. That is, the loop may converge more rapidly approaching to the northern FP and this result in a stronger magnetic mirroring effect which suppresses the number of high-energy electrons that reach the chromosphere there. We will address asymmetric FP emission in depth later (see Chapter 5).

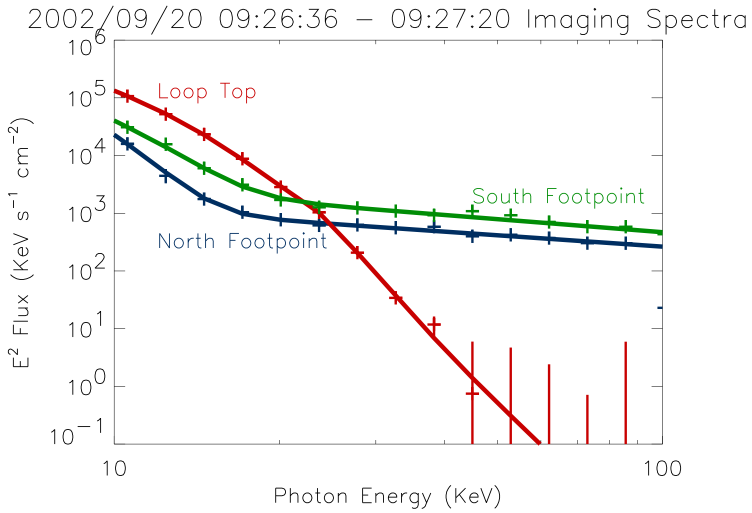

Figure 2.4: νf_ν spectra of the LT and FP sources of the 2092002 flare. The thick lines are fits from a thermal plus power-law model (from Jiang et al., 2003).

We used the boxes shown in Figure 2.3 (*middle*) to define the three sources and integrated the photon flux within each box to obtain the corresponding spectrum, which is shown in Figure 2.4. We (Jiang et al. 2003) then fitted each spectrum with a thermal plus power-law model. The best fit suggests the LT source (fitted within 10–57 keV) has a temperature $k_\mathrm{B}T = 2.22\,\mathrm{keV}$. The two FPs have a weaker thermal component ($k_\mathrm{B}T = 1.31, 1.82\,\mathrm{keV}$) and a stronger power-law component, with an index of $\gamma = 2.65, 2.75$ for the northern and southern one, respectively.

We also used the boxes defined in Figure 2.2 to infer the light curves of individual sources. Figure 2.5 shows such light curves at a cadence of 2 s with about a 4 s integration

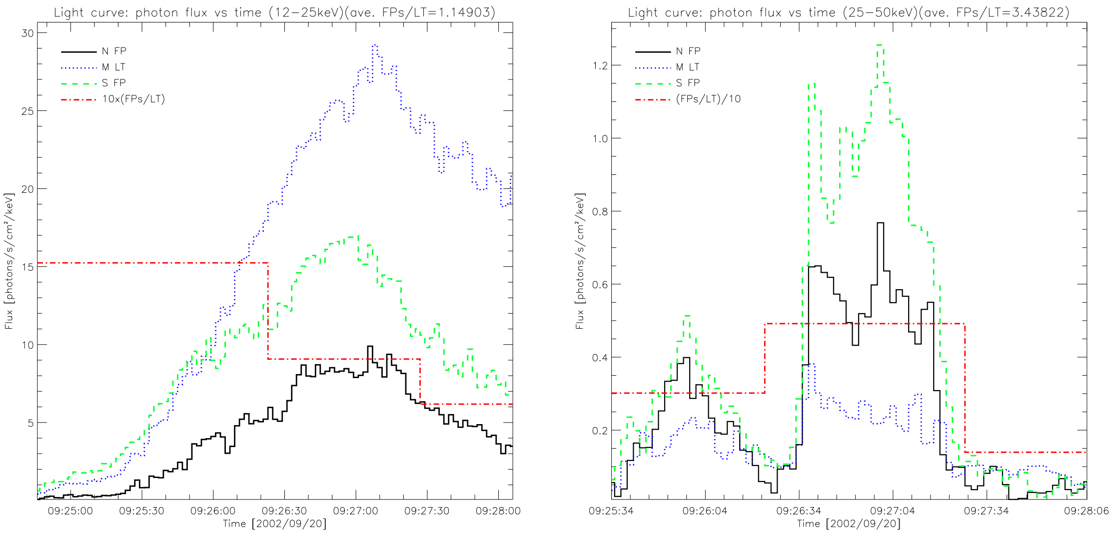

Figure 2.5: Light curves of individual FP and LT sources in the 12–25 keV (*left*) and 25–50 keV (*right*) energy band for the 2092002 flare. The dot-dashed, step-shaped curves show the ratio of flux of the two FPs to the LT sources, averaged over time intervals before, during, and after the peak. "N FP" refers to the northern FP, "M LT" the middle LT, "S FP" the southern FP.

time in the 12–25 keV and 25–50 keV band. The ratio of the fluxes of the two FPs combined to the LT source averaged over the rise, peak, and decay phase, respectively, is shown as the dot-dashed line. We note that the LT source dominates at 12–25 keV and its importance gradually increases with time; in contrast, the FP sources are much brighter in the 25–50 keV channel but it decreases more rapidly after the peak. We note that from the first pulse to the second (as seen at 25–50 keV), the LT emission is essentially constant at 25–50 keV band but increases substantially in the 12–25 keV band. This suggests the LP spectrum undergoes softening.

2.3.2 Multiple Loop Flares

In the sample of flares under study, 13 flares appear to have a more complex morphology, one[5] of which was identified as a multiple-loop event, similar to those studied by Petrosian et al. (2002) during the rising phase of this sunspot cycle. This event (ID 2080327) is an X1.0 class flare, which occurred in AR10039 on August 03, 2002. Figure 2.6 shows the

---

[5] The other complex events require further analysis of light curves and imaging spectroscopy, as well as multiple-wavelength observation to distinguish individual sources.

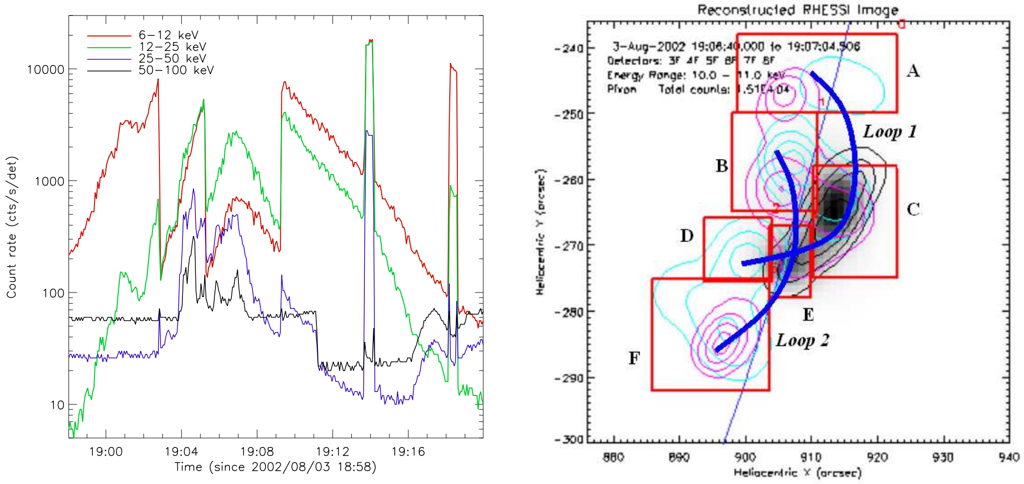

Figure 2.6: The 2080327 flare: light curves (*left*) and PIXON images, together with boxes enclosing individual sources (*right*). The artificial jumps of the count rates (*left*) are due to the changes of the attenuator state. The background map and the contours (of different colors) are images at different energies, same as those shown in Figure 2.7. Two major flaring loops are identified, marked in thick, blue lines, and their corresponding LT and FP sources are assigned a letter, A, B, C, etc.

light curves (*left*), which exhibit a complex history, with multiple pulses appearing at high energies ($\gtrsim 50\,\mathrm{keV}$).

Figure 2.7 shows *RHESSI* image contours at different energies superimposed on a *TRACE* 171 Å image. As is evident, the HXR source morphology is more complex than the 2092002 flare. At high energies, there are several sources (presumably FPs) located inside the limb. At low energies, the structure appears simple, with a single source (LT) appearing above the limb. However, its elongate shape and the existence of many FP sources suggest that this simple appearance could be a projection effect and there are probably more than one LT sources (but not resolved by *RHESSI*). The *TRACE* image was recorded at a later time (19:32:37 UT) during the flare and was selected in order to show the coronal loop structure in EUV, which reveals an arcade of a series of magnetic loops. Two of these loops seem to be cospatial with the *RHESSI* sources, and based on this, we group the HXR sources in two loops, as shown in Figure 2.6 (*right*). Sources A, C, and D are of loop 1, and the others are of loop 2.

Again, we obtained the light curves of the individual sources by integrating fluxes in the boxes (see Figure 2.6, *right*) and show them in Figure 2.8. We note that the two loops

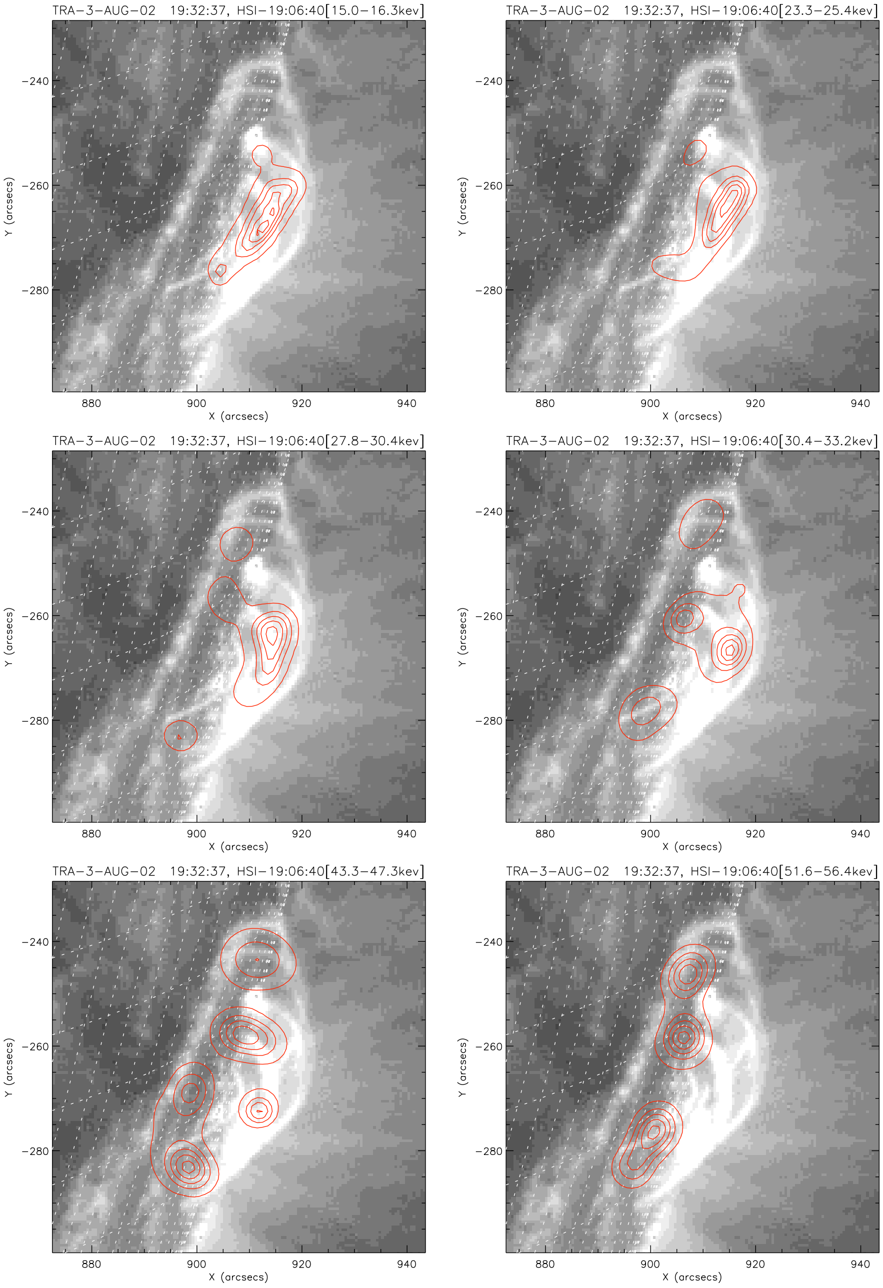

Figure 2.7: *RHESSI* HXR contours at different energies superimposed on a *TRACE* 171 Å images for the 2080327 flare. Heliographic grids (dashed lines) have a 1° spacing in both longitude and latitude.

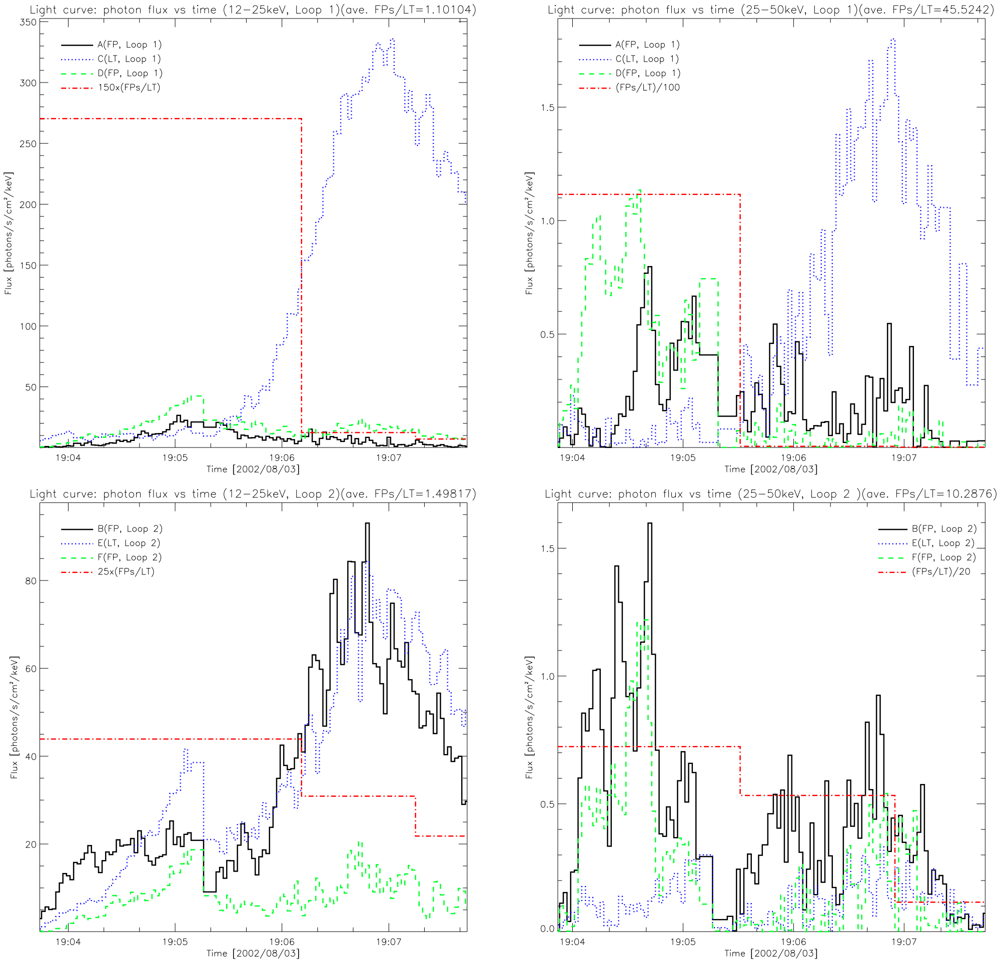

Figure 2.8: Same as Figure 2.5, but for the two loops of the 2080327 flare. The upper panels are for loop 1 (see Figure 2.6, *right*) in 12–25 keV (*left*) and 25–50 keV (*right*); the lower panels are for loop 2.

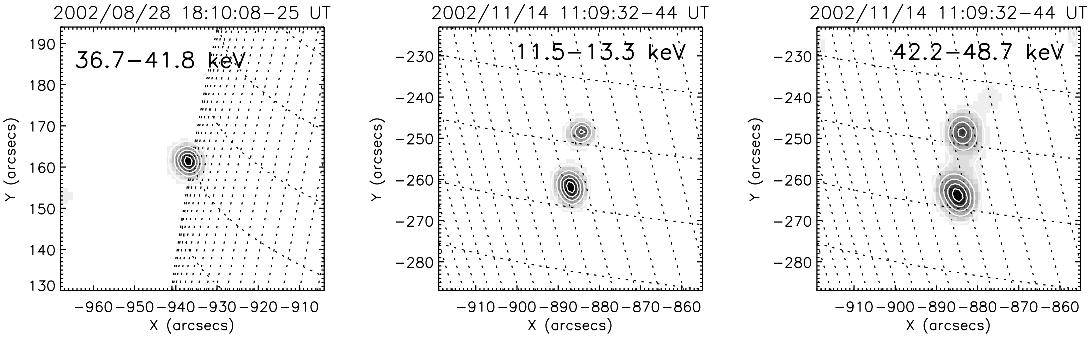

Figure 2.9: Images of the 2082809 flare at 36.7–41.8 keV (*left*) and the 2111410 flare at 11.5–13.3 (*middle*) and 42.2–48.7 keV (*right*).

do not contribute equally to the total emission. In the 25–50 keV band, the total flux of loop 2 is higher during the first pulse but lower in the second than that of loop 1; in the 12–25 keV channel, the LT source of loop 2 is stronger than that of loop 1 by a factor of about 2 during the first pulse (although their total fluxes are comparable at this time) but much weaker (by a factor of 4) in the second (the total flux of loop 2 is lower too). The LT emission from loop 1 dominates over others in the second (major) peak in both energy channels. In the 25–50 keV band, the total flux of loop 1 (2) increases (decrease) from the first peak to the second. This suggests that the burst of loop 1 may be initiated by its interaction with loop 2.

2.3.3 Miscellaneous Types

In six events of this sample, not both LT and FP sources are present. Based on their locations, light curves, and spectra, out of these six flares, we find that three appear to have only a LT source, one seems to have *two* LT sources (beyond the limb), and the other two seem to have only FP sources (see Table 2.1).

Flare 2082809, occurring on August 28, 2002, is a single LT source flare, without FPs detected. In the PIXON images at around the peak time, this event appears as a single source on the limb (see Figure 2.9, *left*) in all the 13 energy bins from 10 to 54.2 keV. CLEAN images at different times also indicate a single source. Fits to the spatially integrated spectrum yield a power law index of 5.0 (steep) and a temperature of 1.9 keV, suggesting this source is a LT, presumably with its corresponding FPs being occulted behind the limb.

Flare 2111410 (November 11, 2002), does not show an appreciable LT source possibly because the LT is too faint to be detected (i.e., out the *RHESSI* dynamic range) and/or the angular separation is not sufficient between the LP and FPs, considering its low heliocentric longitude of 71°, the lowest in this sample of the 29 flares.

2.4 Statistical Results

2.4.1 Imaging Spectroscopy

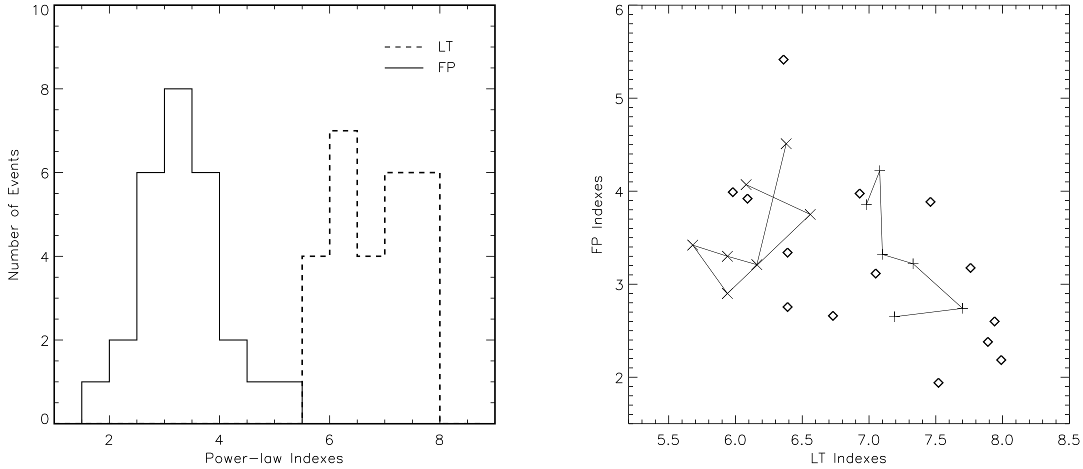

Figure 2.10: *Left*: Histogram of LT and FP spectral indexes during the impulsive peak for a sample of 11 limb flares (see Table 2.1). *Right*: The spectral indexes of the LT vs FP sources for the same sample. The data set also includes the first (*cross*) and second (*plus*) pulses of the 2003 November 03 flare (see Chapter 3), for which the data points are connected by lines.

Figure 2.10 (*left*) shows the histogram of LT and FP spectral indexes from single power-law fits for a set of 11 limb flares (i.e., those marked with "Y" in the "Image spec." column of Table 2.1). Several flares with multiple pulses have multiple entries in the data set. In general, the LT spectra are steeper than those of the FPs. The means of the two distributions are $\bar{\gamma}_{\rm LT} = 6.84$ and $\bar{\gamma}_{\rm FP} = 3.35$ and yield a large difference of $\Delta\bar{\gamma} = 3.49$, which could be expected from the stochastic acceleration model (Petrosian & Liu, S. 2004). Such a large difference is also seen for some of the individual flares as shown in the scatter plot on the right panel for the same flares. Note that Petrosian et al. (2002) obtained

$\bar{\gamma}_{\rm LT} = 6.2 \pm 1.5$ and $\bar{\gamma}_{\rm FP} = 4.9 \pm 1.5$ from broadband *Yohkoh* data. The main difference between our and their results is that our FP spectra are harder, which can be ascribed to the different flare sample selected here and/or the higher energy and spatial resolution *RHESSI* has as compared with *Yohkoh*.

However, one would also expect some correlation between these indexes which does not seem to be present. In this figure we also show the evolution of these indexes for the 2003 November 03 X3.9 flare (see Chapter 3), whenever both the LT and FP sources can be fitted with a power law model. During the first pulse (cross signs) the spectral indexes seem to be correlated weakly, but not during the second pulse (plus signs), which appears to be still in its rising phase (see Figure 3.3) and a weak anti-correlation is seen the index values. The correlation expected from the simple model is clearly not present. But this is not surprising. Firstly, the actual LT and FP spectra and expressions for loss and escape times are more complicated (see Chapter 7). Secondly, the observed LT indexes are more representative of the spectrum at lower energy (where the spectrum is steeper) than those of the FPs. These indicate that we need to carry out more accurate data analysis and use more accurate models than the toy model given earlier.

2.4.2 Statistics of the Relative Fluxes: FPs vs. LTs

For ten of the sample flares, we have obtained the light curves of individual LT and FP sources and their flux ratios. Histograms of the FP-to-LT flux ratio are shown in Figure 2.11, which reveals the following characteristics.

1. Again, we find that the LT sources have softer spectra than the FP sources (see the *lower right* panel). At low energies (≤ 25 keV), the median of flux ratio distribution is very close to one; in contrast, at high energies (≥ 25 keV), the median ratio is much greater than unity and its distribution is much flatter. These results are qualitatively consistent with the theoretical calculations by Petrosian and Liu (2004).

2. At flare peak times, the LT emission dominates at low energies (with the ratio distribution concentrated close to unity) while FPs dominate at high energies (*lower left* panel).

3. During the decay phase of a flare (*upper* panels), the LT source tends to be the major contributor to the total flare emission, especially at low energies (≤ 25 keV).

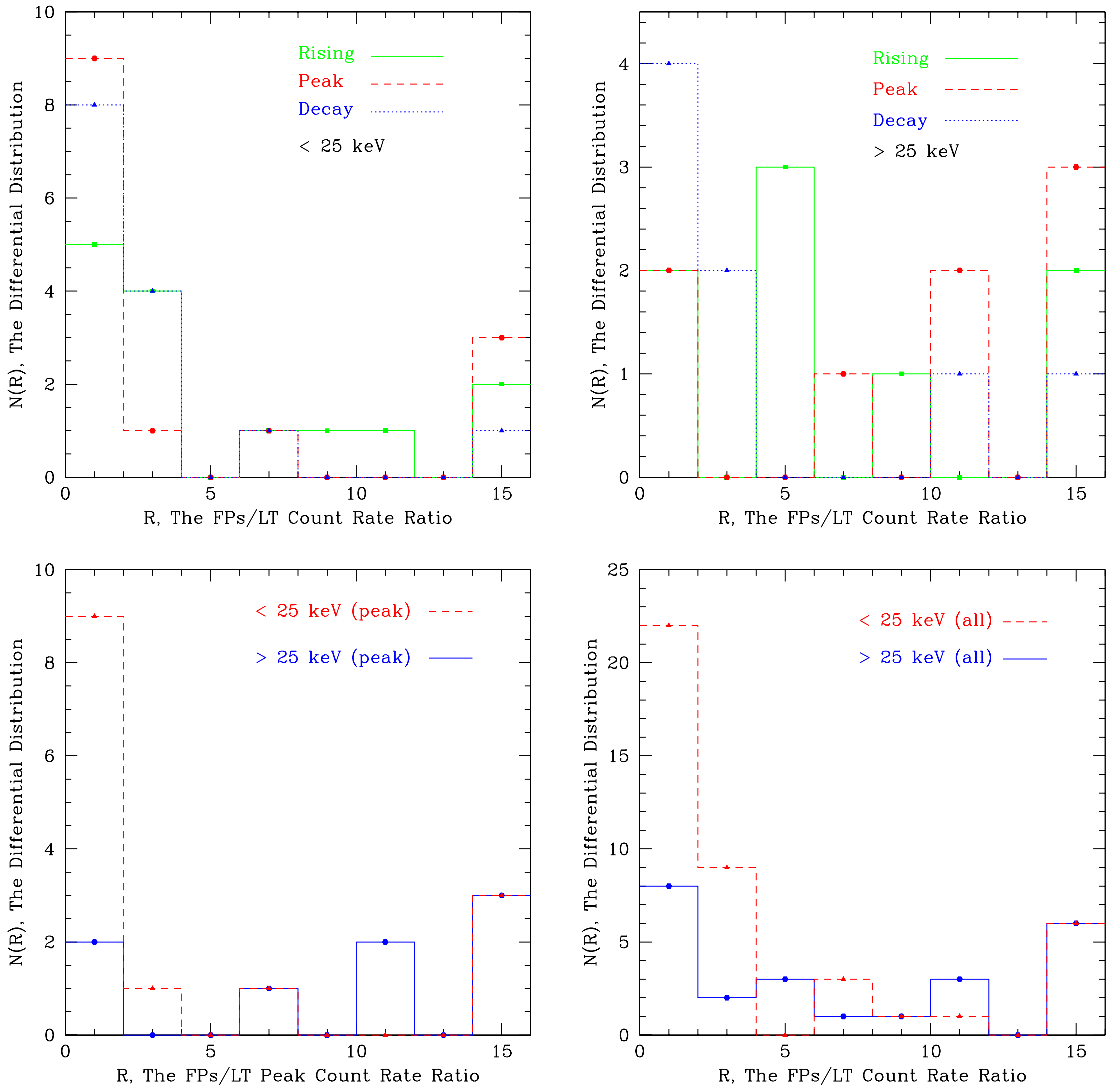

Figure 2.11: Histograms of R, the FPs to LP flux ratios at different times and energies, with a bin size of 2. The upper cutoff is set at 16, about the upper limit of RHESSI images, and any ratio greater than this value is counted to the last bin (note this results in the tail bump at $R = 16$).

4. At high energies ($\leq$ 25 keV), the median of the distribution first increases (from the rise to the peak phase) and then decreases, which translates to that the relative importance of the FP emission has an up-and-down variation. This LT-FP-LT (importance) pattern is correlated with the commonly observed soft-hard-soft variation in the spatially integrated spectrum during the course of a flare, and this suggests such a spectrum variation is (at least partly) contributed by the transition between the spatial variation of the dominant emission.

2.5 Flare Statistics and Selection Biases

The study described above is appropriate for a small sample of flares. To uncover the general characteristics of flares, it is necessary to have statistical studies of the parameters (e.g. peak X-ray flux and duration) for a much larger number of flares. Here we briefly describe the background of this subject and propose an approach for a future study.

Several statistical investigations of distributions, ranges and mean values of relevant parameters, and the correlations between them have been carried out (see, e.g., Lee et al., 1993, 1995; Petrosian et al., 2002) using statistical methods developed by Efron & Petrosian (1992, 1995). Similar statistical studies were done by many others as well (e.g., Dennis, 1985; Crosby, Aschwanden, & Dennis, 1993; Dennis & Zarro, 1993).

One of the most important aspects of this kind of study is proper accounting of the selection biases. The first step here is the careful selection of the sample. The left panel of Figure 2.12 shows a representative distribution of peak count rates of *RHESSI* flares. It clearly suffers from bias at high peak count rates (A) from the effects of the *RHESSI* shutters and at low peak rates (B) due to background variations. A flare usually is identified when its count rate in some channel is more than several sigmas above the background noise. This means that the threshold for detection varies from flare to flare and with the energy band due to different background. The right panel of Figure 2.12 shows the peak count rate versus the threshold count rate of the flares used in the left hand side plot. It is clear that the sample is biased against identification of weaker flares, as shown by the truncation of the data below the diagonal line, when the background level, and hence the count-rate threshold, is higher. Less obvious but no less real is the truncation above a peak rate of about 100 counts $\mathrm{s}^{-1}\mathrm{detector}^{-1}$ due to the insertion of the *RHESSI* shutters for these more intense flares. This kind of biased or truncated data can

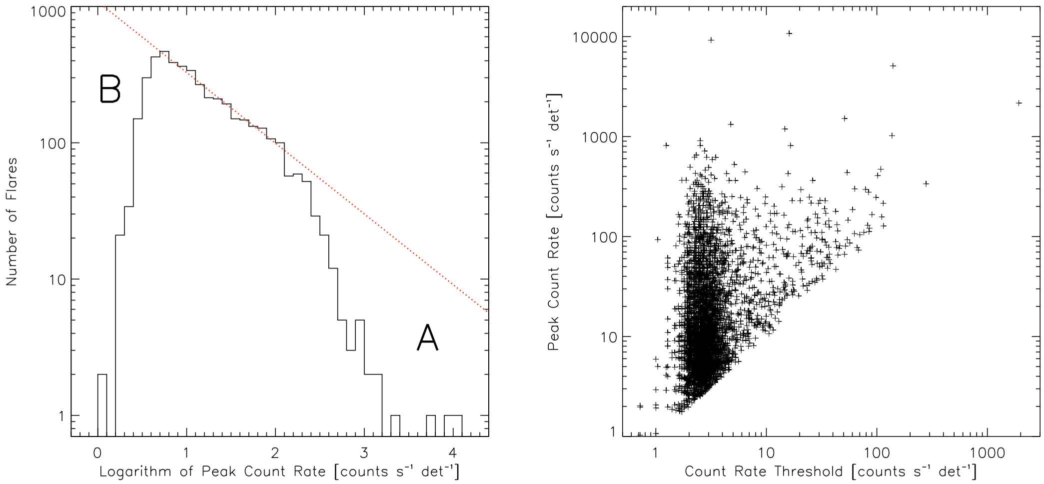

Figure 2.12: *Left*: Distribution of the *RHESSI* flares with peak count rates (in the 12–25 keV channel) greater than 4σ above the background noise and when no shutters were in, which introduces the bias at high count rates in region A that can be corrected. The bias at low count rates (region B) is due to variation of the detection threshold as shown on the *Right*, which shows the peak count rate versus the threshold count rate for these flares. The truncation of the data below the diagonal line is obvious.

be analyzed using our statistical methods (Efron & Petrosian 1992, 1999). Several other characteristics of flare emission, e.g. duration and spectrum, also influence the sample selection process (see Lee et al. 1993, 1995), and will require similar thorough statistical treatment.

Su, Gan, & Li (2006) have recently reported a statistical study on *RHESSI* peak count rates and various (rise, decay, and duration) timescales, using data in the 12–25 keV band which was taken directly from the online flare list without proper corrections. For example, they used a simple, empirical method to account for the different attenuator states. They found a power-law index of 1.80 ± 0.02 for the peak count rates, but this may be subject to improper consideration of the instrument response and selection biases mentioned above.

In the near future, as the *RHESSI* calibration and software are improved and become more stable, we plan to carry out a similar analysis for more flares, carefully correcting various biases. The peak X-ray flux would be the first parameter to be studied. For each flare in the *RHESSI* flare list, one should use the detector response matrix (DRM) to convert the count rate to the incident photon rate nd properly subtract the background, using the OSPEX software package. An automated tool will be developed to perform this analysis. The statistical methods quoted above will be used to correct selection biases. Similar analysis will be applied to other flare parameters, e.g. duration and total counts.

We expect to obtain the intrinsic distribution of these flare parameters and their correlation with much higher accuracy and sensitivity benefiting from the superior capabilities of *RHESSI* , and compare the results with those from earlier missions. This will provide important implications to flare energization and particle acceleration. Examples of such implications include addressing the question that whether numerous small flares play a significant role in coronal heating (Lee et al. 1993).

2.6 Summary and Discussion

We have initiated an investigation of a sample of *limb flares* observed by *RHESSI.* We used X-ray images to infer flaring loop structures and to distinguish between FP and LT sources. We analyzed the light curves and spectra of these individual sources, and presented the statistics of the spectrum indexes, as well as the FP-to-LT flux ratio during different phases of a flare. The preliminary results from a sample of 29 flares are as follows.

1. The averages of the LT and FP spectral indexes are 6.84 and 3.35, respectively, with a large difference of 3.49, which can, in principle, be used to constrain the parameters in the particle acceleration model.

2. An expected correlation between the LT and FP spectral indexes is not present in this study, suggesting that a more accurate statistical study (with a larger sample) is required and a more rigorous prediction from the particle acceleration model is needed as well.

3. At flare peak times, the LT (FP) emission dominates at low (high) energies. During the decay phase, the LT emission becomes more important than the FP emission. The LT-FP-LT variation of relative importance of HXR emission is correlated with the soft-hard-soft variation of the spatially integrated spectrum.

We have also proposed a plan for future statistical studies (in addition to expanding the sample of flares for imaging spectroscopy analysis), in which using proper statistical methods to correct data selection biases is required to uncover the intrinsic distribution of various flare parameters.

The statistical study presented here, in practice, also served as data mining to identify several interesting flares for detailed investigations. Studies of these particular events will be presented in next four chapters.

Chapter 3

Classical Flare Models and New *RHESSI* Observations: the 2003 November 03 X3.9 Flare[1]

3.1 Introduction

Since its launch *RHESSI* has observed several X-class flares and thousands of midclass and small flares. The compactness of microflares limits our access to details of the energy release and particle acceleration processes (Krucker et al., 2002). On the other hand, large and well-resolved flares usually involve multiple loops with complex structures, and the looptop (LT) and associated footpoint (FP) sources are not readily identified and separated (Gallagher et al., 2002; Lin et al., 2003). This makes a direct comparison of theoretical models with observations a challenging task (Alexander & Metcalf, 2002; Sui et al., 2002). This task would be easier for a large flare with a simple morphology, where one can identify source positions and evolutions with certainty (Tsuneta, 1996; Tsuneta et al., 1997).

In late October and early November of 2003, *RHESSI* and other instruments observed a series of X-class flares from solar Active Regions 0486 and 0488 (reminiscence of the 1991 June flares of the previous solar cycle; Schmieder et al., 1994). Among these flares, we studied an event that occurred on November 3 in AR 0488 at heliographic coordinate

---

[1] The majority of the material of this chapter was published in Liu, W., Jiang, Liu, & Petrosian (2004a).

N09°, W77°. Unlike other X-class flares, e.g., the 2002 April 21 flare (Gallagher et al., 2002) and the gamma-ray flare on 2002 July 23 (Lin et al., 2003), this flare shows a surprisingly simple morphology with well-defined one LT and two FP sources.

In this chapter we present a brief description of the spatial evolution of the various emission regions of this flare. As we show, this provides an excellent example of the classical solar flare model of magnetic reconnection and energy release in an inverted Y magnetic field configuration (Kopp & Pneuman, 1976; Forbes & Acton, 1996; Aschwanden, 2002), whereby reconnection in the oppositely directed field lines leads to particle acceleration near the LT. The energy release and particle acceleration processes are not well understood; nevertheless, it is expected that the reconnection will produce closed loops at lower altitudes first and progress to higher overlying loops as time advances. Consequently, the altitude of the LT source and the separation of the two FPs should increase with time. The flare studied here shows this exact behavior.

On the other hand, we also see evidence for deviations from the simplest reconnection models. Our study indicates that the reconnecting fields could be nonuniform and may have a shearing component. In the next section, we present the observations, data analysis, and our results. Their implications are discussed in § 3.3.

3.2 Observations and Data Analysis

The flare under study, classified as a *GOES* X3.9-class flare, was observed by *RHESSI*, *Solar and Heliospheric Observatory* (*SOHO*), etc. Figure 3.1 shows the *RHESSI* and *GOES-12* light curves. In lower energy channels (< 25 keV), the count rates started to rise at around 09:43 UT, peaked about nine minutes later, and then began a monotonic declining phase until 10:01:20 UT when *RHESSI* entered the Earth's night region. The higher energy channel (> 50 keV) light curves exhibit two broad impulsive bursts, each of them consisting of several pulses with a more quiescent part in between, suggesting a persistent but episodic energy release process. Impulsive radio activities were also observed by the Nançay Observatory (N. Vilmer 2003, private communication). A partial halo coronal mass ejection (CME) with a speed of ~ 1375 km s^{-1} was observed by the Large Angle and Spectrometric Coronagraph on *SOHO*.

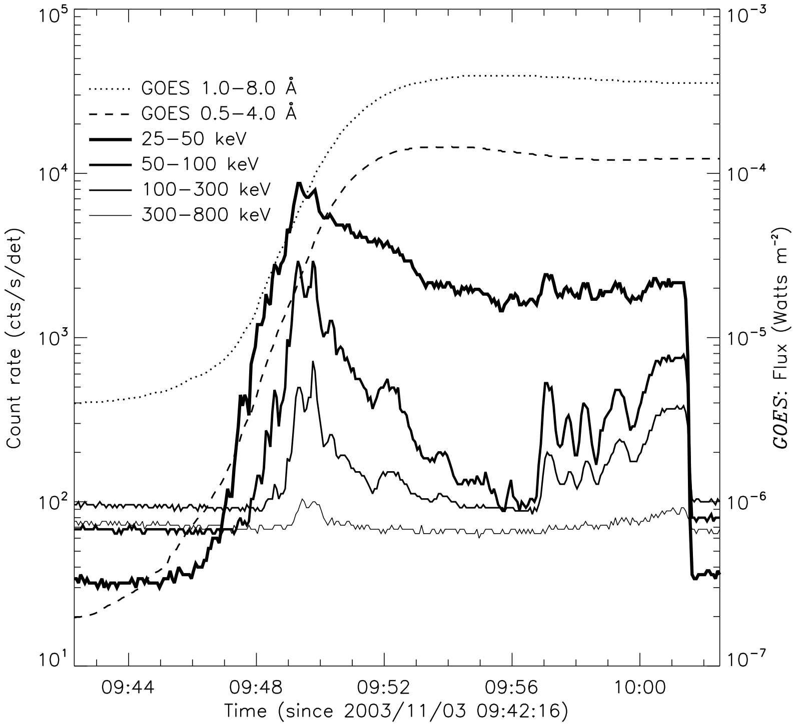

Figure 3.1: *RHESSI* count rates (counts/second/detector, averaged over 4 s intervals) and *GOES*-12 fluxes (in a 3 s cadence).

3.2.1 Source Structure and Motion

To study the hard X-ray (HXR) source motion and structure, we obtained images at different energies in 20 s intervals from 09:46:20 through 10:01:00 UT using the CLEAN algorithm (Hurford et al., 2002) and front segments of detectors 3–8 to achieve a FWHM of 9.″8 with a 0.″5 pixel size. Figure 3.2 shows the HXR emission contours during the two main activity peaks. There are three sources: an LT, a northern FP (N-FP), and a southern FP (S-FP). The LT source dominates at low energies while the FPs dominate at high energies. As evident from the background pre-flare magnetogram obtained with the Michelson Doppler Imager (MDI), the N-FP is around a negative magnetic polarity region while the S-FP remains in a region of positive polarity. Note that early in the event there is a partial overlap between the N-FP and the LT source. Grids with higher spatial resolution will not help for this flare because grid 2 is in a severely degraded condition (Smith et al., 2002) and grid 1 will overresolve the sources (see Schmahl & Hurford, 2003,

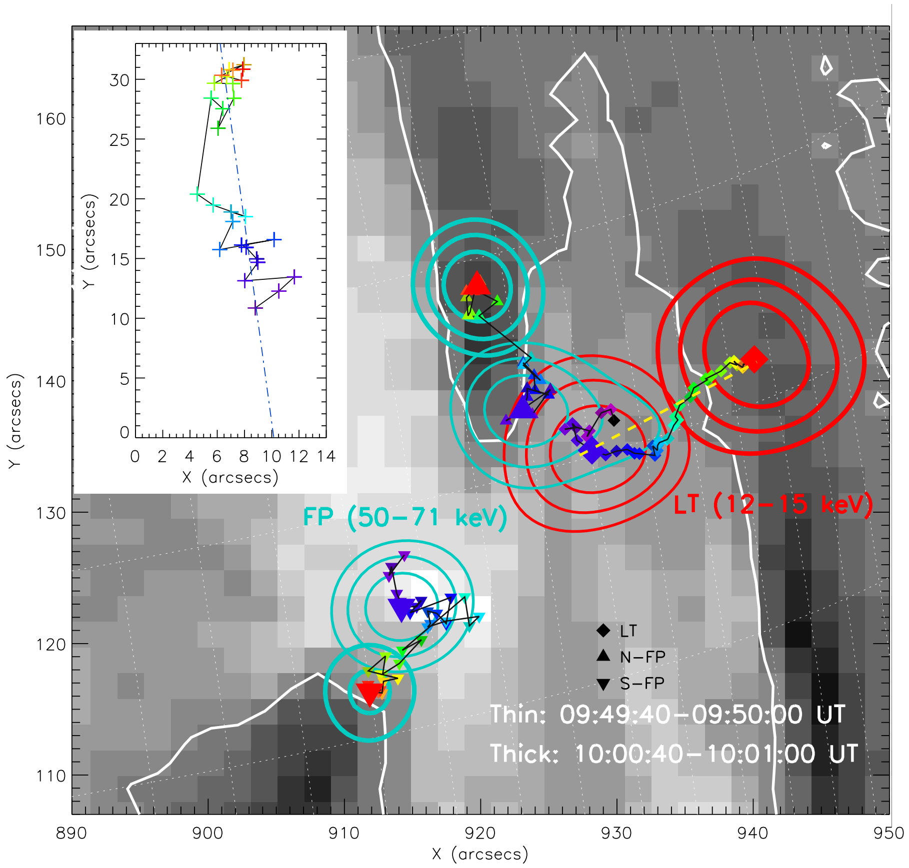

Figure 3.2: Temporal evolution of HXR source centroids, over-plotted on an MDI magnetogram (09:32:30 UT). Black line segments connect the centroids obtained from CLEAN images in successive 20 s intervals chronologically from black (09:46:20 UT) through violet, blue, green, yellow, and to red (10:01:00 UT). The LT (12–15 keV) centroid is the brightness-weighted source center within the 70% level contour, but each FP (50–71 keV) centroid is the peak position obtained with a 3 × 3 pixel parabolic fit around the brightest pixel. The yellow dashed line represents the main direction of motion of the LT source. To estimate the uncertainty in the LT centroid location, we fitted the LT data points with four straight lines within the time intervals, 09:46:20–09:49:40, 09:49:40–09:52:00, 09:52:00–09:55:20, and 09:55:20–10:01:00 UT, respectively. For each interval, following Krucker et al. (2003), the standard deviation of the offset of the data from the corresponding straight line was used as the error in the location. The insert shows the relative positions of the N-FP with respect to the S-FP, which is fixed at the origin. We attribute the motion perpendicular to the straight line to uncertainties in the locations (see text for details). Four HXR images in two time intervals, 09:49:40–09:50:00 (*inner*) and 10:00:40–10:01:00 UT (*outer*), and in two energy channels, 12–15 (*red*) and 50-71 keV (*cyan*), are overplotted as contours (at 55%, 70%, 85% levels of the maximum brightness of the image), which clearly depict the LT and FPs, respectively. The centroids corresponding to these two intervals are indicated with larger symbols. The magnetogram shows the line-of-sight magnetic field in a gray scale ranging from −979 (*black*: pointing away from the observer) to +1004 (*white*) G. The apparent neutral lines are marked in white (from Liu, W. et al. 2004a).

for technical details). A postflare (10:35:43 UT) EUV Imaging Telescope (EIT) 195 Å image (not shown) shows a loop structure that agrees well with the *RHESSI* sources.

As shown in Figure 3.2, the LT and FPs have well-defined and correlated motions, with the symbols indicating their emission centroids at different times. The yellow dashed line represents the main direction of the LT motion, which is roughly at a right angle to the solar limb. We refer to the motion along this direction as changes in altitude. The motion perpendicular to this direction might be due to asymmetry of the reconnecting loops or the LT motion along an arcade. Before the rise of the impulsive HXR emission, there is an apparent downward LT motion. This downward motion could indicate a shrinkage of newly formed loops. It may also be due to the formation of nearby sources (Krucker, Hurford, & Lin, 2003) or to projection effects should the LT source move eastward along an arcade of loops (Sato, 2001). Qualitatively similar features have been seen in several other flares (Krucker et al., 2003; Sui & Holman, 2003), suggesting that this may be a common characteristic of solar flares. However, for the remainder of the flare duration the LT source rises systematically. The apparent separation of the FP sources, whenever detectable, also increases with comparable speed. As emphasized above, this is expected in a simple continuous reconnection process that moves up to the corona, accelerating particles and energizing plasma higher up into overlying larger loops.

To analyze the FP motion quantitatively, one needs to take into account projection effects because any motion and its associated uncertainty in the east-west direction are amplified by a factor of about $\csc 77^\circ \simeq 4.4$. Motions in this direction are highly uncertain, and the motion of both FPs appears to have an east-west component. Magnetic reconnection, on the other hand, is characterized by the change in the size of newly formed loops rather than their absolute motions. Thus one may concentrate on the relative motion of the two conjugate FPs. In the insert panel of Figure 3.2, we illustrate this relative motion by fixing the S-FP at the origin of the coordinates and showing the relative locations of the N-FP. The relative motion is obviously systematic. The fact that the line tracing the location of the N-FP is not exactly aligned with the lines connecting the two FPs shows that there is another component of the relative motion introducing a small rotation of the plane containing the newly formed loop. Because this line is nearly parallel to the longitudinal line, one can ignore the projection affects. We quantify the relative motion along this line, and the standard deviation of the displacement (apparently) perpendicular to this line is used as an upper limit for the uncertainties of this relative motion.

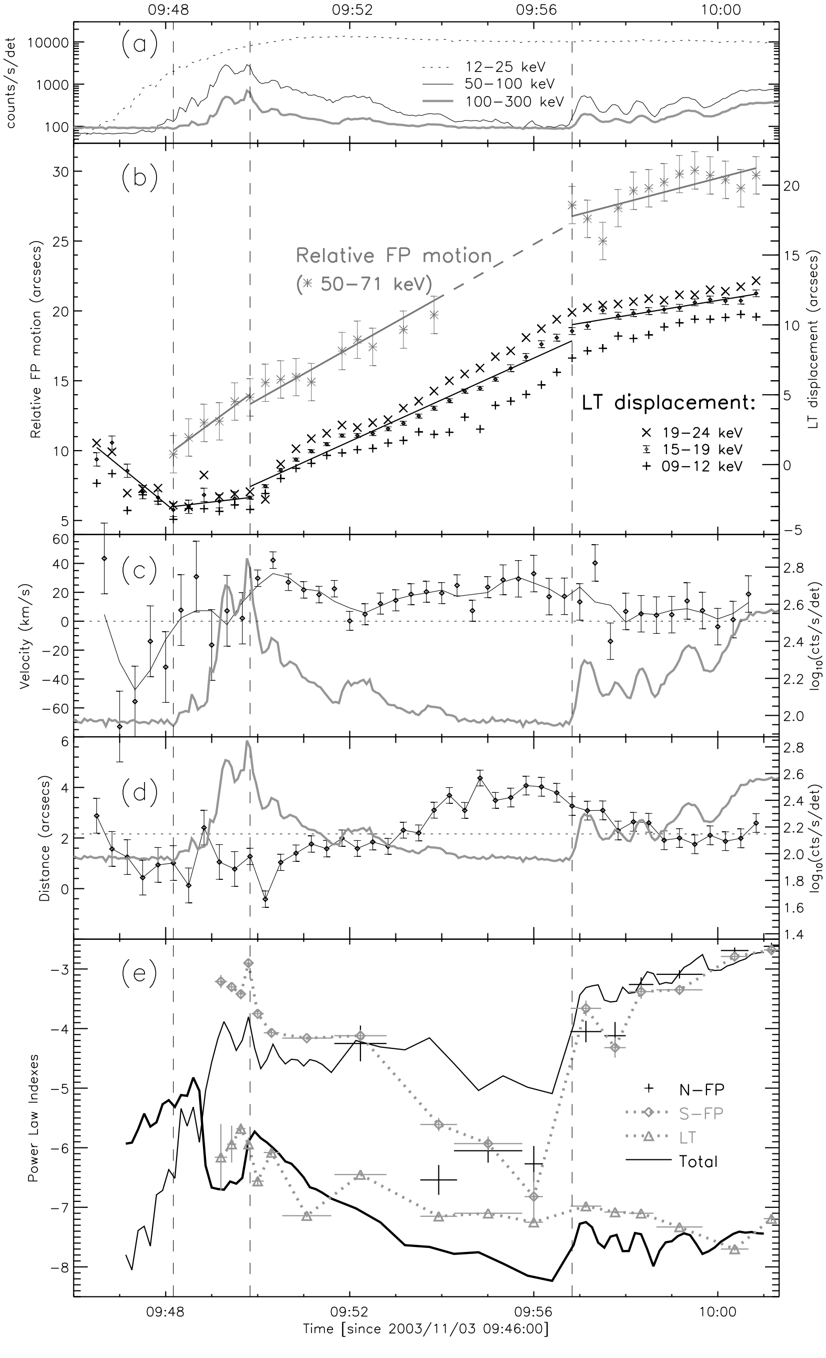

Figure 3.3: (*a*) *RHESSI* light curves. (*b*) Evolution of the displacement of the LT centroid (*right scale*) and the separation of the two FPs (*left scale*). The straight lines are fits to the data (15-19 keV for LT). The vertical dashed lines separate the four phases (see text). (*c*) LT velocity at 15–19 keV (*symbols*) and its value (*thin line*) smoothed over one minute intervals. The thick curve is the logarithmic count rate at 100–300 keV (*right scale*). (*d*) Separation of the LT centroids at 19–24 and 9–12 keV (panel *b*), together with the count rate logarithm (same as *c*), vs. time The dotted line marks their mean. (e) Spectral indexes for various model fits. The thick and thin solid curves give the low and high energy indexes of the spatially integrated spectra. Imaging spectroscopic results are indicated by the points with 1σ vertical error bars. Horizontal error bars represent imaging integration time. (*a–d* from Liu, W. et al. 2004a).

Figure 3.3*b* shows this relative motion of the FPs (at 50–71 keV) along with the location of the emission centroids of the LT source in three energy bands projected onto its main direction of motion that is nearly perpendicular to the solar limb. As evident, the two motions are correlated and the two sets of data points are nearly parallel to each other indicating comparable velocities. To further investigate these motions we divide the observed flare duration into four phases: a preimpulsive phase (before 09:48:10 UT) when there is no significant high-energy HXR emission, a rising phase (from 09:48:10 to 09:49:50 UT), a declining phase (from 09:49:50 to 09:56:50 UT), and a second active phase (from 09:56:50 to 10:01:00 UT). We then fit straight lines to each segment and determine the corresponding average velocities. The results are summarized in Table 3.1. Surprisingly, the LT velocity is highest in the declining phase, when the X-ray emission is relatively weaker (Figure 3.3*c*). In the simplest model of reconnection of *uniform* and oppositely directed magnetic fields, one would expect the opposite correlation, i.e., a higher rate of energy release when the velocity is larger. However, this would be true if the observed HXR flux were actually proportional to the total energy release and if reconnection were indeed occurring in a uniform background plasma, neither one of which is exactly true.

Table 3.1: LT velocities and FP separation speed.

Time range	LT velocities (km/s)				FP speed(km/s)
(UT)	9-12 keV	12-15 keV	15-19 keV	19-24 keV	(50-71 keV)
09:46:20-09:48:10	-18.3 ± 3.7	-22.5 ± 4.6	-32.5 ± 4.1	-30.8 ± 4.7	— — —
09:48:10-09:49:50	3.5 ± 3.3	4.0 ± 3.0	4.7 ± 2.6	4.3 ± 2.7	29.1 ± 11.6
09:49:50-09:56:50	14.6 ± 0.4	16.5 ± 0.2	18.0 ± 0.2	20.9 ± 0.1	22.4 ± 2.5
09:56:50-10:01:00	9.3 ± 0.9	8.6 ± 0.7	6.6 ± 0.7	5.9 ± 0.5	10.4 ± 3.6

Another interesting morphological evolution is the change of the centroid of the LT source with energy. In Figure 3.4 (*left*) we show the *RHESSI* 75% contours and centroids at several energies superposed on an MDI continuum image showing sunspots. Compared with the two FPs, the LT source shows a clear and systematic displacement of the centroid of the higher energy emissions toward higher altitudes, as seen in two other flares (Sui & Holman, 2003; Gallagher et al., 2002).

To investigate what this separation of the LT centroids is related to, we looked for its correlations with other characteristics. We found an anticorrelation between the centroid separation and the high-energy (100–300 keV) count rate, which comes mainly from the FPs (3.3*d*). The continuous curve in Figure 3.4 (*right*) shows their cross-correlation

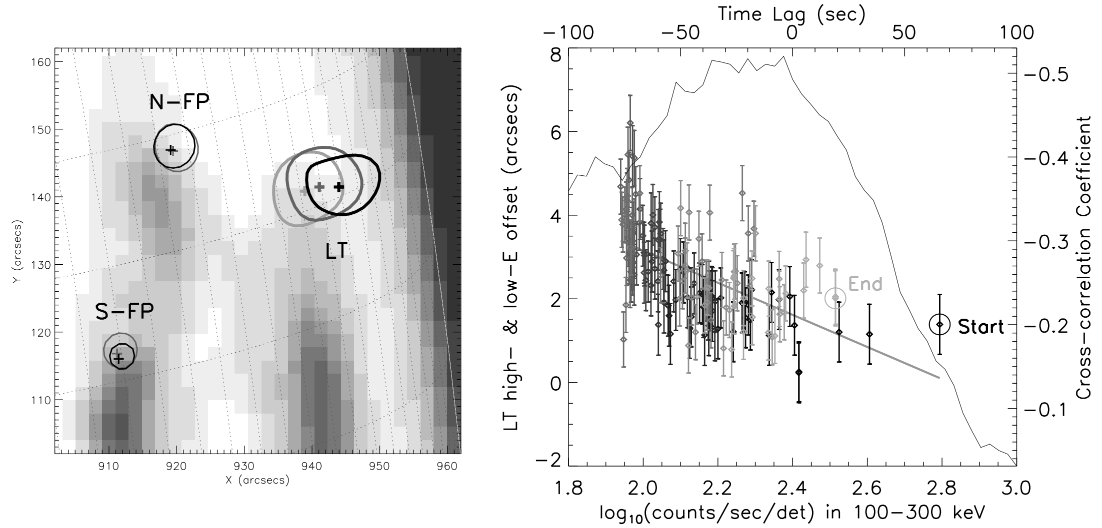

Figure 3.4: *Left: RHESSI* image contours (75%) and the corresponding brightness-weighted centroids (*plus signs*) in the interval 10:01:00–10:01:20 UT. The LT contours are for 12–14 (*light gray*), 18–21 (*gray*), and 27–31 keV (*dark gray*) and the FP contours are for 40–46 (*grey*) and 60–73 keV (*dark gray*). The background is an MDI continuum map taken at 09:36:00 UT. The dark areas inside the limb are three sunspots. *Right:* Correlation between the LT structure and the 100–300 keV (mainly FPs) light curve. The thin curve (with the top and right axis) shows the cross-correlation coefficient of the logarithm of the count rate and the separation between the 19–24 and 9–12 keV centroids of the LT source, showing a 22 ± 39 s delay relative to the light curve. The separation is similar to that shown in Figure 3.3*d* but with a higher time resolution, obtained by imaging at a 4 s cadence (same as the light curve) with an integration time of one spacecraft spin period ($\sim$ 4 s) from 09:49:48 to 10:01:00 UT. We excluded the first two phases of the flare duration when the spatial contamination to the LT source by the N-FP is severe. The diamond symbols (with the bottom and left axis) show the LT separation vs. the logarithm of the count rate shifted by +24 s, corresponding to the peak of the correlation coefficient. The vertical error bars represent the uncertainty in the centroid separation. The darkness of the symbols represents time with the start and end point being circled. The gray thick line is a linear fit to the data with a slope of -3.84 ± 0.34 (from Liu, W. et al. 2004a).

function, which gives a peak correlation coefficient of -0.51 ± 0.08 with a time lag of $\Delta t = -22 \pm 39$ s. The data points (LT separation vs. HXR count rate) used for evaluating the correlation and a straight-line fit are also shown in the same figure.

3.2.2 Imaging Spectroscopy

We also analyzed the spectra of this flare. In most cases, the spatially integrated spectra from 8 to 100 keV can be fitted with a double power law (DPL) model or a thermal plus a power law (ThPL) model with similar reduced χ_s^2. The time history of the DPL parameters are shown by the solid lines in Figure 3.3*e* (The high energy index of the ThPL is nearly identical to that of the DPL). Note that during the first rising phase the spectra change from convex to concave (Holman et al. 2003), as can be seen from the intersection of the low- and high-energy indexes.

For the purpose of imaging spectroscopy we reconstructed CLEAN images (pixel size of $1''$) with detectors 3-6 and 8 (excluding detector 7 because of its poor spectral resolution) at photon energies from 12 keV through 200 keV in 18 time intervals mostly selected at the peaks of the higher energy emission. To get the spectra of individual sources we used the component maps. For a given area, taking into account the over-sampling of the $1''$ pixel size compared to the $\sim 9\overset{''}{.}5$ FWHM resolution (S. Krucker, private communication), the rms fluctuation in the residual map was used to estimate the error of the corresponding source flux. When the FPs and LT are well separated, we successfully obtained the spectra of the LT and two FP sources. Early in the event (between 09:47:48 and 09:51:37 UT) when the LT and N-FP source are partially overlapped, we first obtained the spectrum of the S-FP and the combined spectrum of the LT and N-FP. Then assuming that the two FP sources have the same spectral index and dominate at high energies (> 50 keV), we subtracted the N-FP spectrum (normalized appropriately) from the combined spectrum to obtain the LT spectrum.

In general, the spectra of the two FPs can be fitted by a single power law with very similar indexes and their fluxes are consistent within a factor of ~ 2. The LT spectrum can be fitted by a power law as well and its index is smaller than those of the FPs by > 4 units (Figure 3.3*e*). This difference is larger than that found by Petrosian, Donaghy, & McTiernan (2002) though. On the other hand, as we have shown earlier in Chapter 2, a large difference of 3.49 between the average FP and LT spectral indexes are also found from our preliminary statistical study, which seems to be consistent with the stochastic acceleration model (Petrosian & Liu, S. 2004). (Note that the LT and FP spectra are fitted in the energy range 12-200 keV. However, the FP spectral indexes are mainly determined by data above 30 keV because data points below this energy have relatively large error bars, while most of the contribution to the LT index comes from data below 30 keV as the LT spectrum has comparably large errors above 30 keV.) There also seems to be a weak *anti-correlation* (see also Figure 2.10) between the indexes of the LT and FP sources during the second active phase of the flare. This is not expected from simple solar flare models. Unlike other *RHESSI* flares that we have studied, in this flare a thermal model gives a poor fit to the LT spectra for most of the times (Holman et al. 2003).

The bottom panel of Figure 3.3 shows that the imaging spectroscopic results (without pileup correction which is not yet available for imaging) are roughly consistent with the spatially integrated values (which are corrected for pileup). The primary reason for the difference most likely is due to the presence of extended sources (Schmahl & Hurford 2002) as well as some pileup effects. To investigate the pileup effect on imaging spectroscopy, we fitted the LT spectra in 12-30 keV energy range (Emslie et al., 2003), where the pileup effect is negligible and found that the power-law index changed by 10% in the worst case (livetime $\sim$ 77%) and by less than 5% at all the other times (73% $\leq$ livetime $\leq$ 94%). The pileup correction therefore will not change the imaging spectroscopic results significantly.

3.3 Summary and Discussion

We have investigated the 2003 November 3 X3.9 flare, having a simple morphology with well-defined LT and FP sources. The high flux combined with the simple loop structure allows us to determine the spatial evolution of the LT and FP sources clearly and to compare with the simple reconnection models. Similar studies of flares have been limited to the investigation of the motion of the FPs alone (Sakao, Kosugi, & Masuda 1998; Qiu et al. 2002; Fletcher & Hudson 2002) or have dealt with complex loop structures (Krucker et al. 2003; Qiu, Lee, & Gary 2004), This has made the comparison with models more difficult. Our analysis of *RHESSI* data has yielded several new and interesting results.

1. We observe a systematic rise of the LT source and a comparable increase in the separation of the FPs as the flare proceeds. This agrees very well with the canonical solar flare model of magnetic reconnection in an inverted Y configuration. Similar behaviors have been reported previously using soft X-ray or EUV observations

(Švestka et al., 1987; Tsuneta et al., 1992; Gallagher et al., 2002) during later thermal gradual phases of flares. However, these emissions are not directly related to the impulsive particle acceleration processes (Forbes & Acton, 1996).

2. The LT source seems to move more slowly during the HXR peaks than during the declining and more quiescent phases, in apparent disagreement with reconnection of *uniform* and oppositely directed field lines, where one would expect a correlation between the velocity of the LT source and the energy release rate. However, we note that the HXR flux is not a good proxy for the energy release rate, and the magnetic fields in the reconnection region are likely to be nonuniform. Stronger magnetic fields would require a smaller volume of reconnecting fields and possibly slower motion. However, in an inhomogeneous case other factors such as the geometry and Alfvén velocity variation can also come into play. This problem needs further exploration.

3. The centroid of the LT source appears to be at higher altitudes for higher photon energies. This suggests that the energy releasing process happens above the LT and that harder spectra, implying more efficient acceleration, are produced at higher altitudes. In the stochastic acceleration model by turbulence where the acceleration efficiency depends on the intensity of turbulence, this would indicate a decrease of the intensity with decreasing altitudes, presumably because of decay of turbulence away from its source at a higher altitude (Petrosian & Liu, S., 2004).

4. The above shift of the centroids decreases with the increase of HXR flux from the FPs. Such an anticorrelation will be difficult to produce in simple models. In the above-mentioned model, this would imply a more inhomogeneous distribution of turbulence during more active phases, because a smaller shift means a larger spatial gradient.

5. The spatially integrated spectra are fitted equally well with a double power-law model and a thermal plus power-law model.

6. The imaging spectroscopy study suggests that the LT and FP sources could be purely nonthermal. In the second active phase of the flare, there appears to be an anticorrelation between spectral indexes of the LT and FP sources and their difference can exceed 4.

Another possible explanation, as regard to No. 4 mentioned above, concerns the interplay of the heating/acceleration and cooling processes. Studies of the evolution of loops in the gradual phase indicate that cooling of the plasma confined within closed loops plays an important role in determining the observed emission morphology (Forbes & Acton 1996). If cooling is also important in the impulsive phase, one would expect that loops forming earlier have lower plasma temperatures and contribute mainly to emission at lower energies. Then the motions of the emission centroids at lower energies will be dominated by the cooling process. The motions of centroids at higher energies, however, are presumably determined by the heating/acceleration process, a direct consequence of reconnection. When higher energy sources slow down due to the increase of reconnecting magnetic fields as discussed above, the apparent velocities of lower energy sources do not change significantly until their centroids are determined by emission from hotter plasmas at the reconnection site. The sudden decrease of the 19-24 keV centroid velocity and the relatively smooth transition of the 9-12 keV centroid motion during the onset of the second HXR burst (Figure 3.3*b*) and the delay of the LT centroid separation relative to the light curve (Figure 3.4, *right*) seem to support such a scenario.

A more detailed analysis of this flare including imaging spectroscopy and quantitative comparison with theoretical models will be needed to shed light on the observations presented here and distinguish between the possibilities discussed above.

Chapter 4

Double Coronal Sources and the Reconnection Site: the 2002/04/30 Flare

4.1 Introduction

In the classical 2-dimensional reconnection model, magnetic field annihilates in a current sheet and outflows of high speed plasmas as well as turbulence generated (see Figure 1.1, *left*) are present in opposite directions. Accelerated particles and heated plasmas, believed to be the consequence of the energy release process, are expected to be present in both directions as well. Observational signatures, i.e., HXRs or SXRs produced by these high-energy particles or hot plasmas, are thus expected to be associated with the two outflows too (see Figure 1.1, *right*).

The so-called looptop (LT) source, believed to be near the reconnection site and produced by freshly accelerated particles or heated plasmas, are commonly observed at SXR and HXR energies (e.g., Masuda 1994; Petrosian et al. 2002; Liu, W. et al. 2004). However, observations of two or more distinct XR sources near the reconnection region have been rarely reported. This may be due to limited sensitivity or spatial resolution of the instruments, because one source may be much dimmer than the other, or the small spatial separation can not be resolved.

Sui & Holman (2003) reported a weaker, additional coronal source that appeared above a stronger LT source in the 2002 April 15 flare and Sui et al. (2004) found a similar phenomena in another two homologous flares. They suggested that there was a current sheet existing between the two sources. Veronig et al. (2005) also found an additional coronal source, appearing briefly, in the 2003 November 03 X3.9 flare, which we analyzed and showed in Chapter 3. Recently, Gan & Li (2006) reported another *RHESSI* flare, occurring on 2002 November 02, that shows a similar double source morphology and they interpreted the two sources as thermal emission because no HXR emission was detected above 25 keV and the FPs were occulted. Pick et al. (2005) reported a double-source structure observed in the 2002 June 02 flare with the multi-frequency Nancay Radio-heliograph. Due to the low brightness of the additional coronal source, imaging spectroscopy was not available or has not been studied for the above *RHESSI* events.

We discovered another flare, occurring on April 30, 2002, that exhibits similar signatures of double coronal sources. The upper coronal source is relatively brighter and stays longer ($\sim$ 9 minutes) than that of Sui et al. (2004), which makes it a stronger case and allows more detailed analysis, including imaging spectroscopy of individual sources and tracking their temporal evolution. In addition, the footpoints (FPs) are occulted by the solar limb, and thus spectroscopic analysis of the coronal sources are not contaminated by the FPs at high energies. Analysis of the decay phase of this flare was originally reported by Jiang et al. (2006). Here we extended analysis throughout the whole course of the flare.

Early in the flare, we find that the two coronal sources are closely separated, down to a distance of about $4''$ between their centroids. The source morphology exhibits a double-cusp or “X” shape, indicating where magnetic reconnection takes place. The two sources gradually separate from each other as the flare evolves. We also find a good temporal correlation of the light curves of the two coronal sources. Both sources exhibit energy dependent structure (Sui et al. 2003; Liu, W. et al. 2004). In general, for the lower source, high-energy emission comes from higher altitudes, while the opposite is true for the upper source. As time proceeds, the separation of emission between different energies becomes smaller near the impulsive phase peak and it becomes larger at other times. Imaging spectroscopy shows that the two sources have very similar spectra (a power-law during the early phase). This observation suggests that the two XR coronal sources are produced by the same population of accelerated/heated electrons moving in two opposite directions from the reconnection region, and thus consistent with the general picture outlined above.

We present the observations and data analysis in §4.2 and conclude this chapter with §4.3.

4.2 Observations and Data Analysis

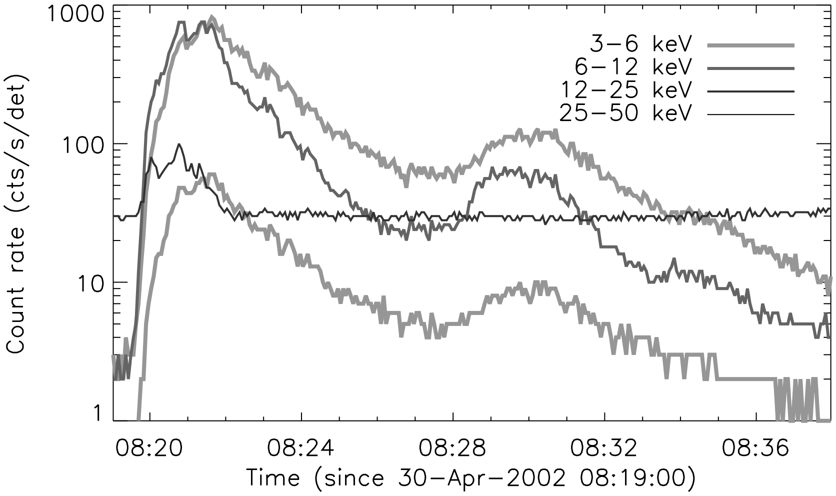

Figure 4.1: *RHESSI* light curves of the 2002 April 30 flare.

The flare under study occurred on April 30, 2002. Figure 4.1 shows the light curves in four energy bands between 3 and 50 keV. There are two pulses, with the first being much brighter and harder. There is no count rate increase above 25 keV during the second pulse.

4.2.1 Energy-dependent Source Structure During the First Pulse

Let us first check the energy-dependent source morphology around the peak time of the first pulse. Figure 4.2 shows PIXON images at different energy during 08:20:27–08:20:56 UT. At low energies, there is a single round-shaped source, which we call the lower coronal source (i.e., the usual LT source), with its centroid above the solar limb. At a slightly higher energy, 9–10 keV, a cusp shape appears in the upper portion of the source. At even higher energies (*middle*), another source, which we call the upper coronal source, can be clearly seen above the first source. At 16–19 keV, then, the two sources get closer and there seems to be an "X" shape cusp in between. As energy further increases, the opposite occurs and the upper source eventually becomes invisible at 33–37.9 keV.

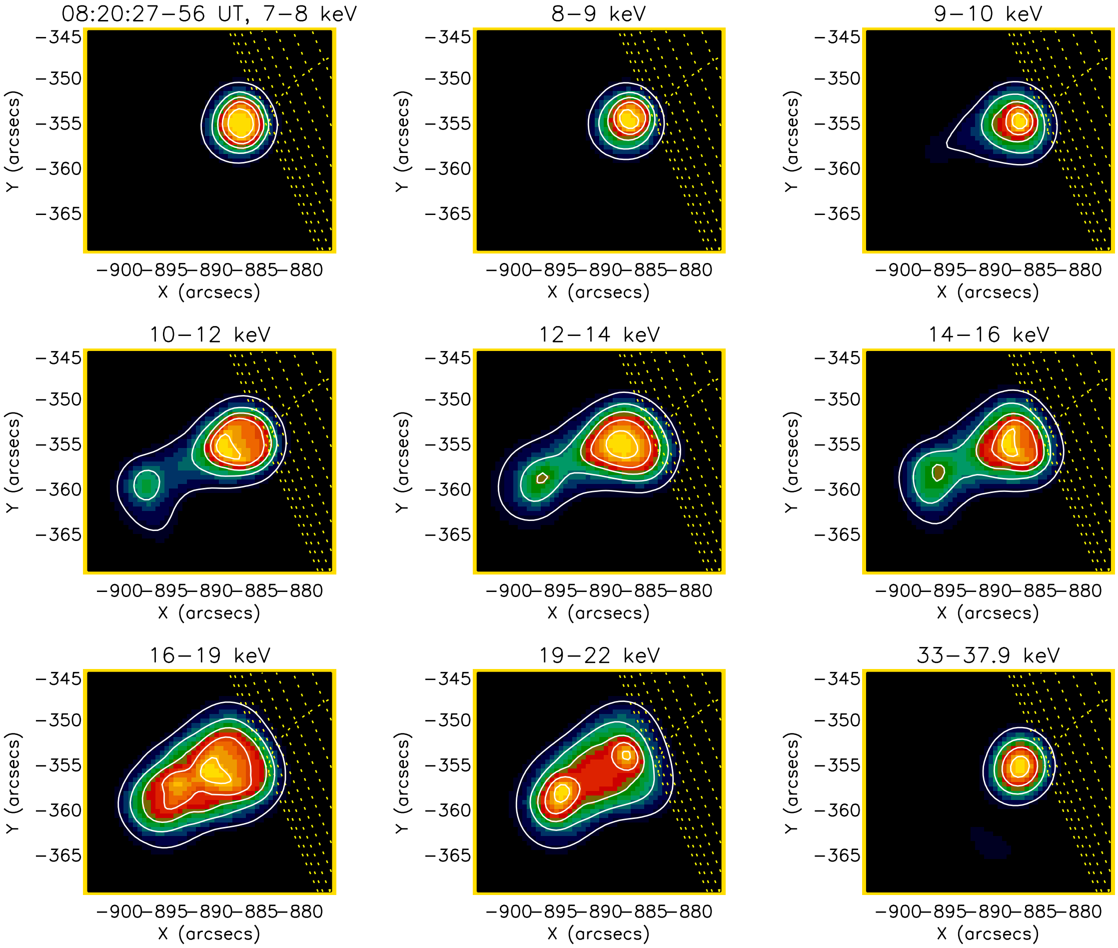

Figure 4.2: *RHESSI* PIXON images in different energy bands at 08:20:27–08:20:56 UT, around the peak time of the main (first) HXR pulse. The contour levels are 10%, 30%, 50%, 70%, and 90% of the maximum of each individual image.

One can zoom in and overplot several images together to perceive more details. As shown in Figure 4.3, the upper coronal source monotonically shifts toward lower altitudes with increasing energies. The lower coronal source, in general, behaves oppositely, with some fluctuations. At 16–19 keV (*green*), the two sources are at the closest distance with the centroids of their 93% contours separating by $\sim 4''$.

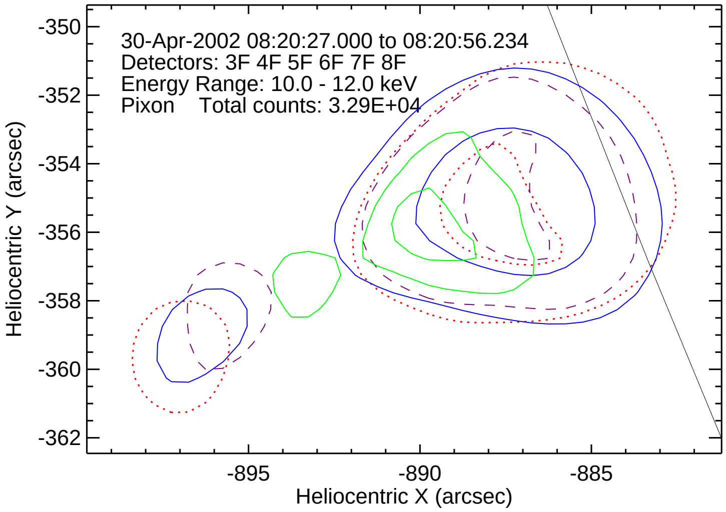

Figure 4.3: Overlay of images in four energy bands, 10–12 (*red dotted*), 12–14 (*blue solid*), 14–16 (*purple dashed*), and 16–19 keV (*green solid*), same as those shown in Figure 4.2. The contour levels are at 30% & 85%, 43% & 80%, 45% & 85%, and 82% & 93% of the maximum of individual image, for the above four bands, respectively. This plot was produced by the GUI in the *RHESSI* software package.

We can also appreciate this by plotting the height (above the limb) of the source centroid as a function of energy, with that of the upper (lower) coronal source shown in Figure 4.4*a* (4.4*b*). The time interval mentioned above (as in Figure 4.2) corresponds to the blue, diamond symbols. The energy-dependent pattern is clearly present, particularly pronounced for the upper coronal source. Below 19 keV, the centroid of the upper (lower) source shifts to lower (higher) altitudes with increasing energies. Then there is a turn-over at 19–22 keV, because the two sources are separate again (see Figure 4.2). Between 22 and 33 keV, the two sources can not be spatially resolved due to lower counts (poor statistics) and thus the centroid here shown in Figure 4.4*b*) represents that of the two

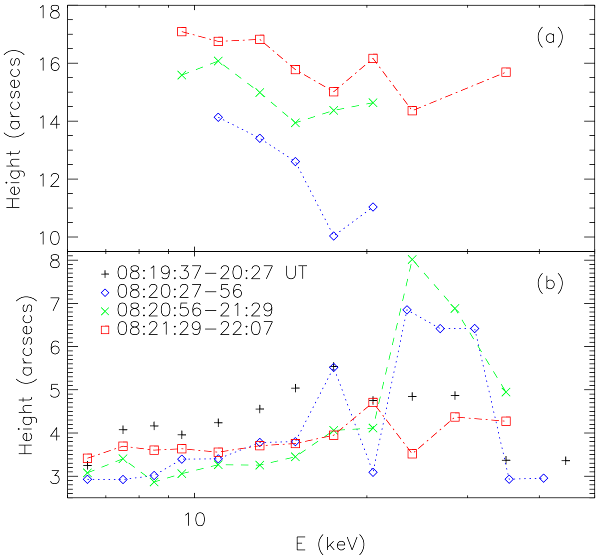

Figure 4.4: Height above the limb of the centroids for (*a*) the upper and (*b*) the lower coronal sources, plotted as a function of energy, within four time intervals during the first impulsive pulse.

sources combined. Beyond 33 keV, the upper coronal source is not detectable, and the centroid now represents the lower source alone and thus its height drops.

This energy-dependent source morphology is similar to that reported by Sui & Holman (2003) and Sui et al. (2004), which the authors interpreted as magnetic reconnection taking place between the two sources. In their interpretation, plasmas with higher temperatures are located closer to the reconnection site, which results in higher-energy emission coming from the middle while lower-energy coming from further outside. In the framework of stochastic acceleration model, a higher level of turbulence is presumably present closer to the reconnection site (the central engine of a flare); it can result in a stronger particle acceleration or plasma heating than a decreased turbulence level which is further away from the reconnection site. Our observation here seems to support that scenario. In addition, the small distance of $\sim 4''$ here identifies a region within which the reconnection site is located, and as we know of, this is among the smallest sizes of evidence of reconnection observed on the Sun.

The turn-over of the centroid heights (for both sources) at about 20 keV is presumably caused by the fact that higher-energy electrons require a higher column depth to stop them and thus they tend to produce their nonthermal bremsstrahlung at larger distances from where they are accelerated and released. The disappearance of the upper coronal source toward the high-energy end may indicate a transition from the LT-dominant thin-target emission to the leg/FP-dominant thick-target emission. Note that there does not seem to be any emission (with its centroid) from inside the limb during the whole course of the flare, suggesting that the FPs are (at least partially) occulted by the solar disk.

We have repeated the same analysis for another three times during the first HXR pulse, which are also shown in Figure 4.4. The result generally exhibits the same pattern mentioned above. Note that, in the very beginning (08:19:37–08:20:27 UT), no distinct sources are detected and only one source is visible, whose centroid is shown in Figure 4.4*b* as black plus signs. As to the temporal evolution, the upper source rises with time (from blue, to green, and then to red), while the lower source first falls and then rises. The latter could come about because we have a morphological change from a single source at early times to two distinct sources later. This phenomenological interpretation could explain the decrease of the LT height early during the flare observed in several other events (Sui & Holman 2003; Sui et al. 2004; Liu, W. et al. 2004).

4.2.2 Source Structure Evolution Throughout the Flare

We now change our perspective, using relatively wider energy bins as a tradeoff for finer time resolution (compared with the above analysis), and examine the evolution of the source structure through the full course of the flare in detail.

Figure 4.5 shows the images taken at 10–13 (*grey* background), 13–17 (*blue*) and 17–25 keV (*red*) at separate times. The morphology evolution follows the general trend mentioned above and we detail it below. Early (08:19:28-08:20:01 UT) in the flare, there is only a single source visible (with a slightly elongated shape at 17–25 keV). The elongation, in a direction about perpendicular (also see Figure 4.2) to the limb, becomes evident in all the three energy bands during the next time interval. Then two distinct coronal sources appears in a dumb-bell shape. As time proceeds, both sources move to higher altitudes and their separation increases. On the mid stage (third row in Figure 4.5) of the evolution, the upper coronal source tends to spread in the direction somewhat parallel with the limb, which may be associated with the exact morphology of the reconnecting magnetic field. Then at 08:26:59-08:27:32 UT (in the valley of the light curves, see Figure 4.1), only a single source is visible near the middle of the two sources at high energies (13–17 and

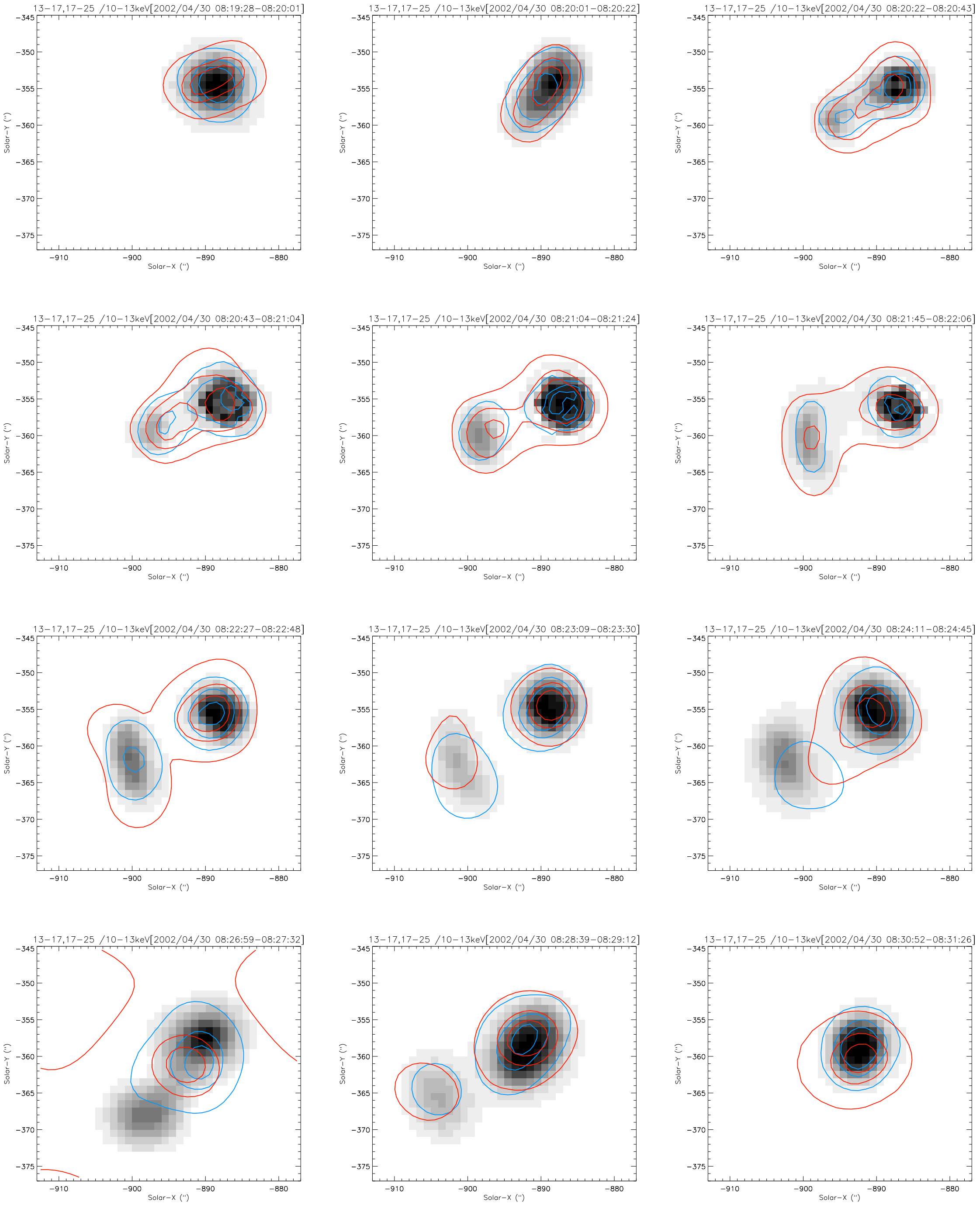

Figure 4.5: PIXON images of different energies at selected times (as noted in the title). In each panel, the grey-scale background is at 10–13 keV, while the blue and red contours are at 13–17 and 17–25 keV, respectively. The solar limb (not shown) is in the upper-right corner. Note that the 17–25 keV image at 08:26:59–08:27:32 UT, due to low count rates, does not converge well with sidelobes appearing in the corners.

17–25 keV). In the rising phase of the second pulse (08:28:39–08:29:12 UT), the dumb-bell morphology appears again at all the energies, while toward the declining phase, again, only one source is detected. In a word, we find that the double-source morphology is quite stable for a long duration of about 9 minutes (from 08:20 to 08:29 UT), but it also involves some dynamics which depends on the details of the particle energization process, the particle spectrum, and the ambient magnetic topology and density distribution.

We can examine the same phenomenon more quantitatively by checking the height of the source centroid as a function of time at different energies, which is shown in Figures 4.6*a* and 4.6*b* for the upper and lower coronal sources, respectively. We find that, again, higher-energy emission comes from lower altitudes for the upper coronal source and the lower coronal source has an opposite trend, with only a few exceptions, particularly during the declining phase of each HXR pulse, to this general rule. The initial increase of the height of the lower coronal source results from the elongation (see the second panel in Figure 4.5) of the whole source, and the following decrease of the height is a consequence of the transition from a single-source to a double-source structure. As time proceeds, the two source generally move together to high altitudes, with the upper one moving faster (note slightly different vertical scales in Figures 4.6*a* and 4.6*b*) and thus their separation becomes larger.

We also note that the separation between different energies of the upper coronal source decreases with time during the rising and plateau portion of the first pulse (08:20–08:22 UT), and the separation increases again afterwards. Similar feature is present in the lower coronal source, which show a larger separation during the rising and declining phases than the peak time of both pulses. This is consistent with that during the rising phase of the second pulse (near 10:00 UT) in the 2003 November 03 X3.9 flare (see Figure 3.3*b*). This may indicate the spatial gradient of turbulence strength or particle acceleration rate is larger (thus smaller spatial separation) around the peak the impulsive phase, associated with a stronger turbulence level at this time.

4.2.3 Temporal and Spectral Correlation of the Two Coronal Sources

We now examine the relationship of the light curves and spectra between the two coronal sources. Figures 4.6*c*—4.6*e* show their light curves at 10–13, 13–17, and 17–25 keV, respectively. As can be seen, the two curves basically follow the same trend of temporal variation in all three energy bands shown here, meaning they are actually correlated, except that

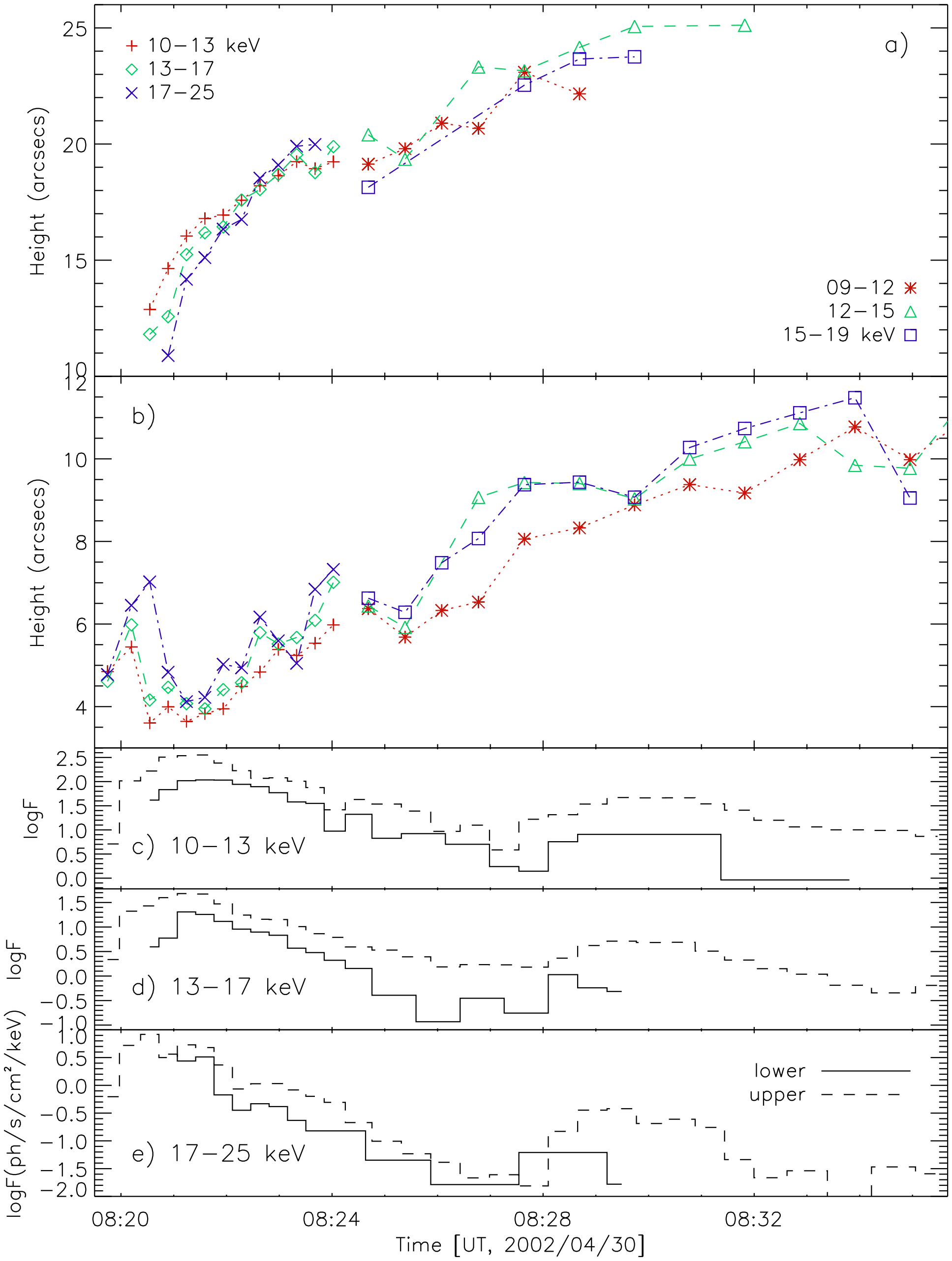

Figure 4.6: Height (above the limb) of the centroids at different energies for (*a*) the upper and (*b*) the lower coronal sources. Before 08:24 UT, we use wide energy bins, 10–13, 13–17, and 17–25 keV, with short time intervals to assure sufficient time resolution during the first pulse; after that, we used slightly narrower energy bins, 9–12, 12–15, and 15–19 keV, with longer time intervals. (*c*), (*d*), and (*e*) light curves of the upper (*solid*) and lower (*dashed*) coronal sources, in the energy bands of 10–13, 13–17, and 17–25 keV, respectively.

the upper coronal source appears later and disappears earlier due to its faintness.

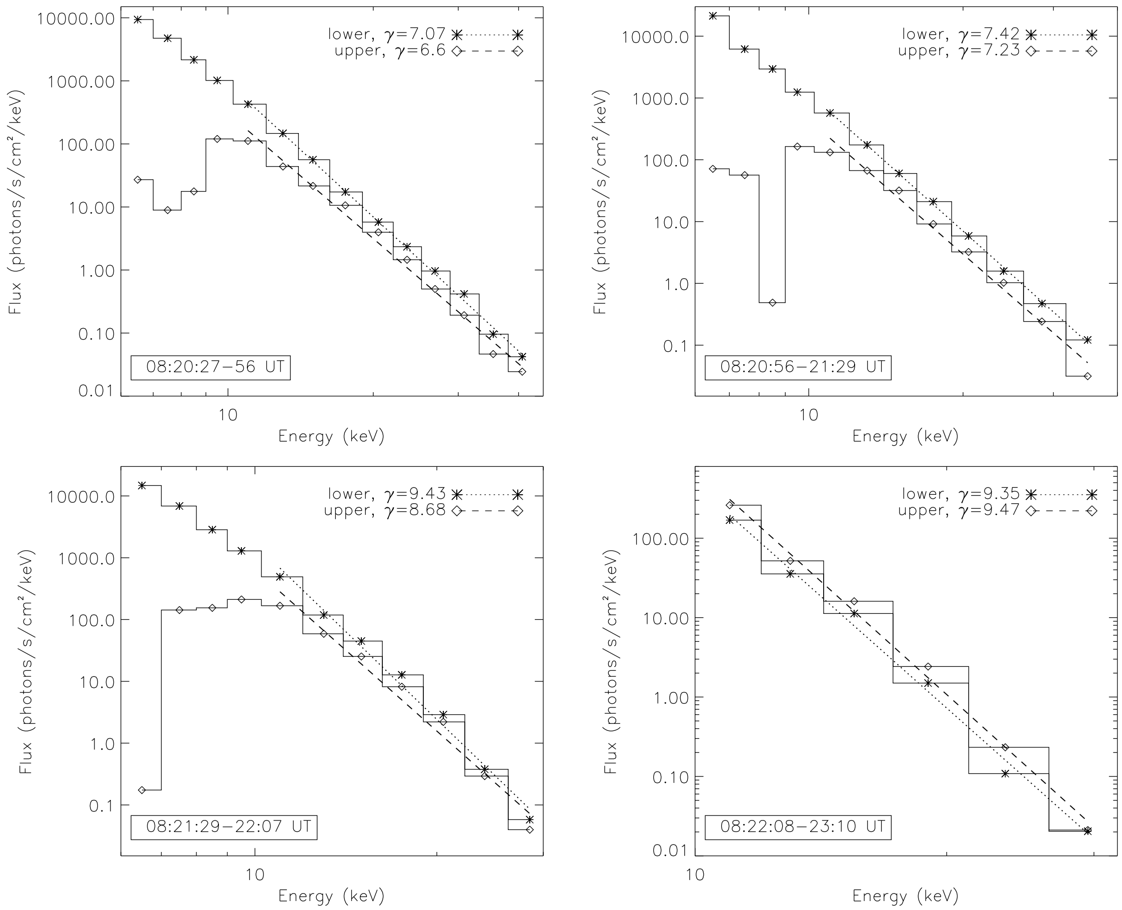

Figure 4.7: Imaging spectroscopy of the two coronal sources at four separate times. The power-law fit is shown as the dotted (dashed) line for the lower (upper) source.

We also obtained the spectra (i.e., imaging spectroscopy) of the two sources from images (as those used in § 4.2.1) taken at different energies, which are shown in Figure 4.7. Around the peak time of the first pulse, for example, each of the two spectra (*top left*) can be fitted with a power law above $\sim 10\,\mathrm{keV}$, with a spectral index of 7.07 ± 0.11 and 6.60 ± 0.24, respectively. Note that, at low energies, the upper coronal source is dominated by the lower one, exceeding the current dynamic range of about 10 of *RHESSI* and thus its spectrum here is not accurate. At other times (Figure 4.7), a similar fit can be performed, and the spectrum index increases with time. The indexes are summarized in Table 4.1. We note in passing that Jiang et al. (2006) found that after 08:22 UT, a thermal spectrum fits the data better than a power law for the spatially integrated spectrum. Therefore, the spectrum here with an index greater than ∼ 8 is most probably a thermal rather than a power-law spectrum. However, we show the indexes here to demonstrate the similarity of the two spectra, without invoking a detailed discussion of the nature of the spectrum itself. In addition, due to the limited number of data points and thus poor statistics available here, a robust fit of the imaging spectrum is rather difficult. (In a sense, the indexes here work as a hardness ratio between high and low energies.)

Table 4.1: Power-law indexes of imaging spectroscopic fits of the two coronal sources during different time intervals.

Sources	08:19:37 –20:27 UT	08:20:27 –56	08:20:56 –21:29	08:21:29 –22:07	08:22:08 –23:10	08:23:10 –24:13	08:24:13 –25:15
Lower	5.27 ± 0.12	7.07 ± 0.11	7.42 ± 0.08	9.43 ± 0.44	9.35 ± 0.38	9.72 ± 0.39	9.15 ± 0.19
Upper	—	6.60 ± 0.24	7.22 ± 0.34	8.68 ± 0.61	9.47 ± 0.34	9.82 ± 0.61	9.46 ± 0.39

On the basis of the temporal correlation of the light curves and the close spectrum shapes (indexes) of the two coronal sources, it is suggested that they are produced by the same population of electrons that are accelerated during the reconnection process and move in presumably opposite (upward and downward) directions. Such a correlation provides more direct evidence to the interpretation outlined earlier.

4.3 Summary and Discussion

We have performed imaging and spectral analysis of a flare that occurred on April 30, 2002, which confirms early works and provides stronger evidence of magnetic reconnection taking place between the coronal sources observed in X-rays. Our main findings are as follows.

1. There are two coronal sources, closely spaced, during the impulsive and gradual phases of the flare. They co-exist for about 9 minutes, longer than that reported by Sui & Holman (2003) and Sui et al. (2004).

2. The two sources both exhibit energy-dependent morphology. That is, higher-energy emission comes from higher altitudes for the lower source, while the opposite is true for the upper source. When the two sources get closer with increasing energies, an "X" shape of emission appears and a small distance of about $4''$ between the emission peaks is identified. This suggests that reconnection occurs within this small region.

3. As time proceeds, the two source generally move together to high altitudes, with the upper one moving faster and thus their separation becomes larger.

4. For each source, the separation of emission between different energies becomes smaller near the peak time of each pulse and it becomes larger at other times, consistent with our earlier finding (Chapter 3). This, in the framework of the stochastic acceleration model, suggests that a stronger turbulence level (thus a larger acceleration or heating rate and a higher HXR flux) is associated with a larger spatial gradient (i.e., smaller spacing) of turbulence or hardness of the electron spectrum.

5. The light curves of the two sources are temporally correlated. Their spectra obtained from imaging spectroscopy are very similar. This suggests that the same (or very similar) population of electrons, presumably accelerated or heated in the same acceleration region, is responsible for producing the two XR sources.

All the above findings fit in the picture of magnetic reconnection taking place between the two sources. This is another, yet stronger, case of a double-coronal-source morphology, in addition to the very few other events reported by Sui & Holman (2003), Sui et al. (2004), Veronig et al. (2005), and Gan & Li (2006). Note that Sui & Holman (2003) interpreted the increase of separation between the two sources as formation and growth of a large scale current sheet. This is understandable in terms of the morphological change from an X-type neutral point to a double-Y shaped structure. Such a change is basically an ideal MHD process. However, we should also note that magnetic reconnection in a flare involves release and dissipation of magnetic energy, a non-ideal MHD procedure, which eventually dissipates and destructs a current sheet. A more comprehensive imaging spectroscopic study or a brighter flare is needed in the future to shed light on the details of the physical processes involved. We also look forward to future efforts to carry out theoretical modeling of such observations.

Chapter 5

Asymmetric Conjugate HXR Footpoints: the 2003/10/29 X10 Flare

5.1 Introduction

As stated in Chapter 1, HXR observations provide most useful information on the accelerated particles and their acceleration agent. Magnetic field measurements of the flaring region can give incisive clues to magnetic reconnection development. Combining this two types of observations can help uncover the details of energizing process in flares.

The 2003 October 29 X10 flare is an excellent event with both types of observation available. It was well observed by *RHESSI*, *SOHO*/MDI, and several ground-based observatories. It occurred near the disk center, where line-of-sight magnetic field measurements have minimum projection effects. Its long duration ($\sim$ 20 minutes) of emission from HXR FPs provides an excellent opportunity to track the evolution of FP position and the associated magnetic field. There is a rich database of multiwavelength observations for this flare and a wide range of literature covering different aspects, making it one of the best studied events (e.g., Xu et al., 2004, 2006; Yang et al., 2004; Krucker et al., 2005).

We have carried out analysis of the 2003 October 29 X10 flare, focusing on the footpoint (FP) HXR emission and the associated magnetic field. We find that the mean HXR flux of the two FPs exponentially correlates with the mean magnetic field. The two conjugate

FPs showing asymmetric characteristics, with the stronger FP associated with the weaker B field, which is consistent with the magnetic mirroring effect. During the evolution, however, the HXR flux ratio of the two FPs cannot be quantitatively explained solely by this effect.

We present such a study in this chapter, with observations and data analysis described in next section, followed by a summary of the main findings and discussions. We look forward to theoretical investigations of these observations in the framework of stochastic acceleration and particle transport model in a future work.

5.2 Observations and Data Analysis

5.2.1 Overview of Multiwavelength Observations

The event under study was a X10 class, white-light, two-ribbon flare. It occurred in AR 10486 on October 29, 2003, during the unprecedented Halloween storms (e.g., Liu, W. et al. 2004; Krucker et al. 2005). Yang et al. (2004), using photospheric local-correlation tracking, reported strong shear flows present near the magnetic neutral lines of this active region prior to the flare onset. This is consistent with the unusually large amount of free energy of $(5.7 \pm 1.9) \times 10^{33}$ ergs stored in this AR found by Metcalf et al. (2005), who used Mees vector magnetogram data and virial theorem to reconstruct the force-free coronal magnetic field. Liu & Hayashi (2006) investigated the large scale coronal magnetic filed of AR 10486 and its associated high productivity of CMEs, using potential field extrapolations. Xu et al. (2004, 2006) presented their high-resolution near-infrared (continuum at $1.56\,\mu$m) observation of this event, which marked the first reported white-light flare observed at the opacity minimum. Liu et al. (2006) reported the large scale activities associated with this flare, using multiwavelength observations (including H_α — Moreton waves, HXR, radio, etc). They identified remote brightenings more than 2×10^5 km away from the main flare site and reported a SOHO/LASCO CME associated with this flare with a speed of $\sim 2000\,\mathrm{km\,s^{-1}}$. These works provide a rich multiwavelength perspective for this well studied event.

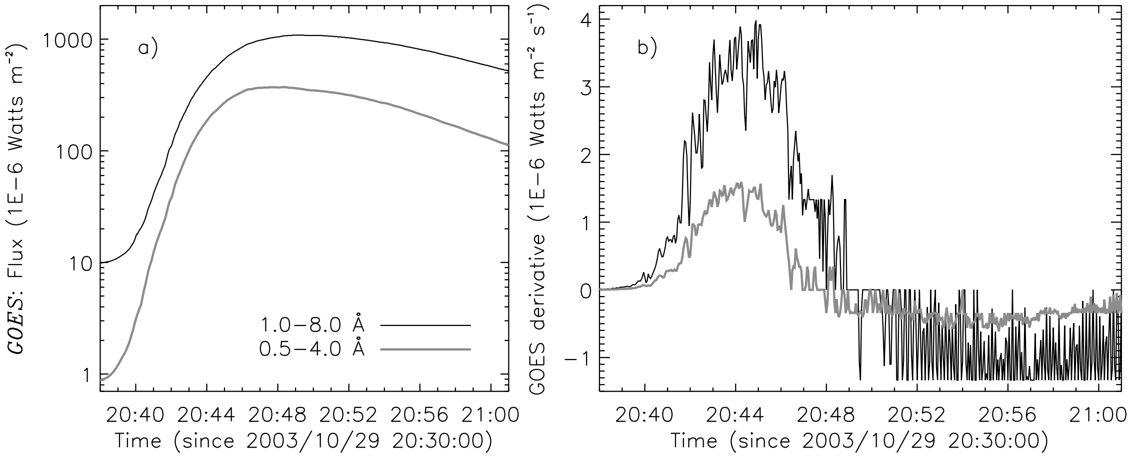

Figure 5.1: *GOES*-10 1–8 Å and 0.5–4 Å channel fluxes (*a*) and their time derivatives (*b*).

5.2.2 General *RHESSI* Observation and Footpoint Motions

RHESSI had a very good general coverage of this event. Unfortunately, *RHESSI* light curves, particularly at high energies, were heavily contaminated by particle events (from Earth's radiation belts) during the course of the flare. Here we show the *GOES* fluxes and their time derivatives[1] to represent the overall XR light curves (Figure 5.1).

The **flare morphology** and its evolution are shown in Figure 5.2, with *RHESSI* contours at 15–21 and 50–100 keV overplotted on *TRACE* 195 Å images which were recorded at a nearby time. The *TRACE* images reveal an arcade of loops and the arcade runs from the north-east to the south-west. Early during the flare, several FPs (*blue*, 50–100 keV) disperse along the arcade, which were identified to be co-spatial as ribbons seen in near-infrared (Xu et al. 2004) and *TRACE* 1600 Å wavelengths. The 15–21 keV emission appears elongated (and sheared) along the arcade as well and seems to come from between the adjacent FPs, presumably from the corresponding LT sources. Toward the south-west, part of the 15–21 keV emission seems to overlap with the FP emission or between the nearby FPs, suggesting multiple loops involved. As time proceeds, the FP structure becomes simpler and only two distinct, conjugate FPs are present. The two FPs move away from each other. The LT sources, on the other hand, behave in the opposite way, in which several LT sources (*red*) appear on the arcade, between the two FPs.

Let us examine the motions of the FPs in detail. Figure 5.3 shows the centroids of the

---

[1] The *GOES* time derivatives could be used as a protocol of HXR light curves, assuming the Neupert effect is at work here. See Chapters 6 and 8 for more discussion of this effect.

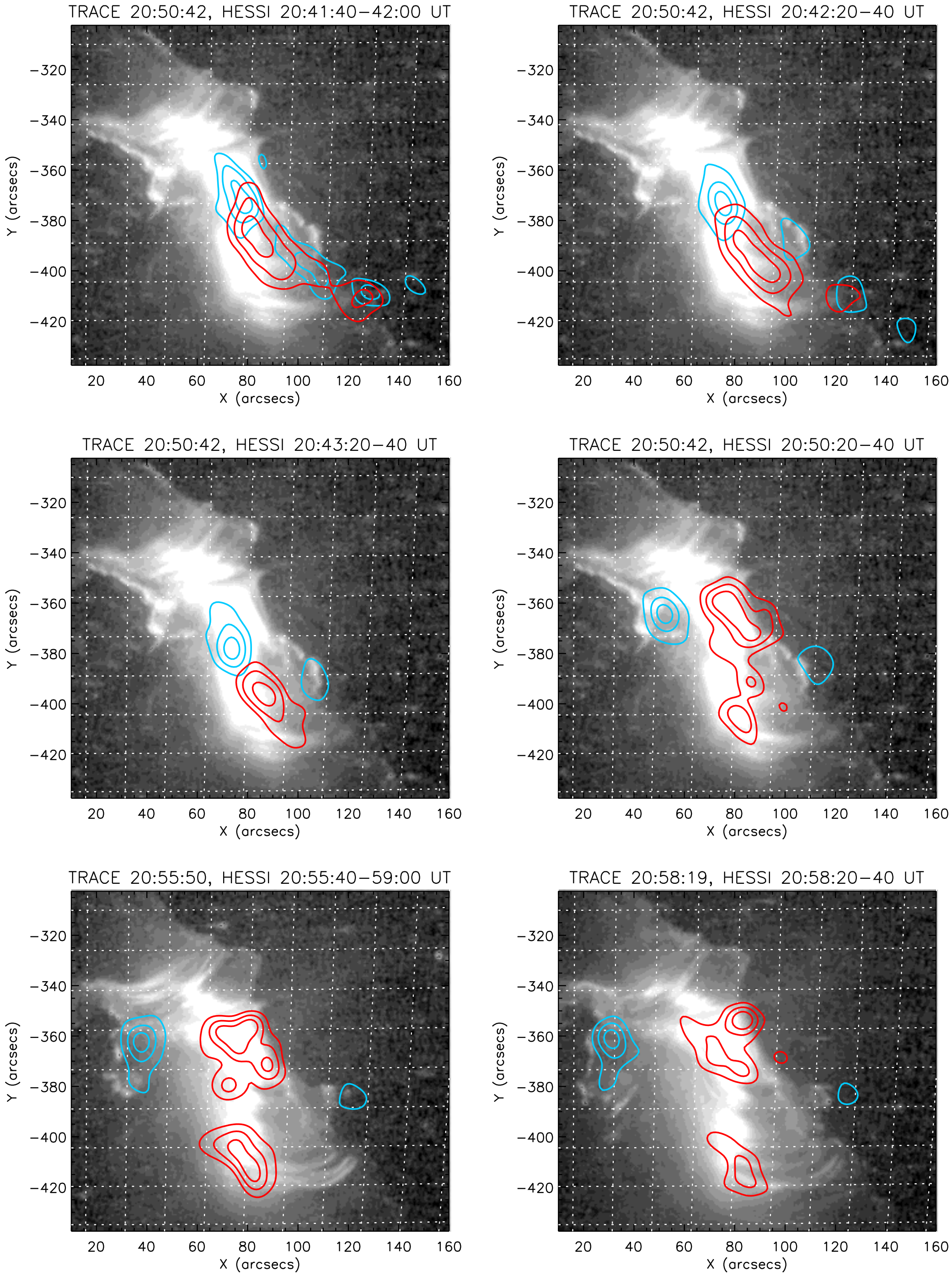

Figure 5.2: *TRACE* 195 Å images with *RHESSI* 15-21 (*red*, mainly LT) and 50-100 keV (*blue*, mainly FPs) images overplotted at selected times. The contour levels are selected between the 20% and 80% levels of the maximum of each individual image. The heliographic longitudes and latitudes are marked by white dotted lines (1° spacing). The same *TRACE* image is repeated in the upper four panels because 195 Å images are not always available.

two FPs at different times (from blue to red), with the pre-flare *SOHO*/MDI magnetogram as the background. As can be seen, the two FPs are located on the two sides of a magnetic neutral line, with one FP being to the east in a negative (*dark*) magnetic field and the other to the west in a positive (*bright*) magnetic field.

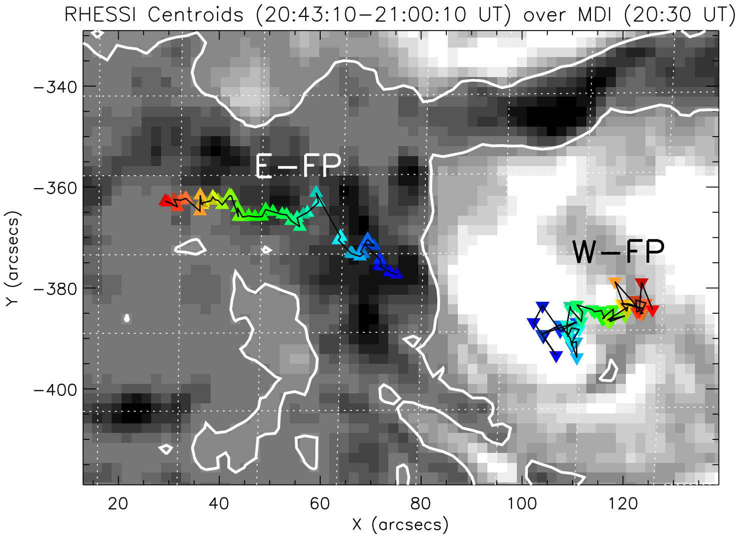

Figure 5.3: *RHESSI* FP centroids overplotted on a background *SOHO*/MDI magnetogram. The centroids were obtained from images in the 60-100 keV band, reconstructed at a 20 s interval from 20:43:10 (*blue*) to 21:00:10 UT (*red*). The pre-flare (08:30 UT) magnetogram has the neutral lines marked in white. The dark (bright) grey scale indicates a negative (positive) magnetic field that points away (toward) the observer.

As time goes on, the two FPs generally move away from each other and from the neutral line, and the **shearing** between the line connecting the FPs and the neutral line decreases. This can be seen clearly from Figure 5.4, which shows the displacement of on FP relative to the other in the direction perpendicular (*top*) and parallel(*middle*) to the neutral line, as a function of time. We find that the perpendicular displacement almost monotonically (and linearly) increases with time, covering a range of nearly $70''$ during the interval of about 17 minutes. In contrast, the parallel distance varies less than $\sim 10''$, roughly on a constant level. From these two distances, we calculated the angle between the two FPs and the neutral line, which is plotted in the bottom panel of Figure 5.4. We find that this inclination angle increases by about 15° and approaches 90° (potential field) in the end. This indicates newly reconnected magnetic field lines are less and less sheared during the course of the flare, similar to that found by Masuda et al. (2001) and Asai et al. (2003). Note that the HXR flux (see Figure 5.5) generally decreases during this time interval, which is roughly anti-correlated with the inclination angle. This result is consistent with the concept that highly sheared magnetic fields are highly non-potential and thus contains more free energy, which is capable of producing stronger particle acceleration and more HXRs. The reader is also reminded that an opposite process took place prior to the flare — that is — strong shearing flows (Yang et al. 2004) were observed near the neutral line, as mentioned earlier. This process increased the shearing of the magnetic field lines and built up magnetic stress and free energy in the system during the pre-flare phase. The flare, on the other hand, in a sense, relaxed the stress and untwisted the shearing, while the previously stored free energy was being released at the same time. The resulting magnetic field was closer to a potential field than the pre-flare one.

5.2.3 Conjugate Footpoints: HXR Fluxes and Magnetic Fields

Krucker et al. (2005) summarized the *RHESSI* observation of this flare. They studied the motion of *one* (the stronger eastern) FP and found a rough temporal correlation between the HXR flux and reconnection rate, characterized by the product $B \times v$ or $B^2 \times v$, the latter of which is proportional the Poynting flux (Isobe et al., 2002; Asai et al., 2003) into the reconnection region. The authors also calculated the electron energy deposition rate (by a rough fitting to the HXR spectrum with an index of $\gamma = 2.5$) and found it roughly correlating with the magnetic energy annihilation rate, $B^2 \times v$. We have carried out similar analysis for both FPs and found the FP velocities had irregular variations and large uncertainties, but, to the zeroth order, were roughly constant (see the rough linear time history of the perpendicular distance in Figure 5.4, *top*). Thus we will not discuss FP velocities in detail here, but will focus on the HXR fluxes, the magnetic fields, and their relationship of the two conjugate FPs.

Figure 5.5*a* shows the history of the 60–100 keV HXR fluxes of the two FPs. The error bars of the flux were obtained from the RMS of the residual maps of the cleaned images. Note that the counts produced by the radiation belt particle events are removed in the *RHESSI* image reconstruction procedure, because the corresponding count rate is not modulated by the spacecraft spin and thus not imaged (Hurford et al. 2002). The

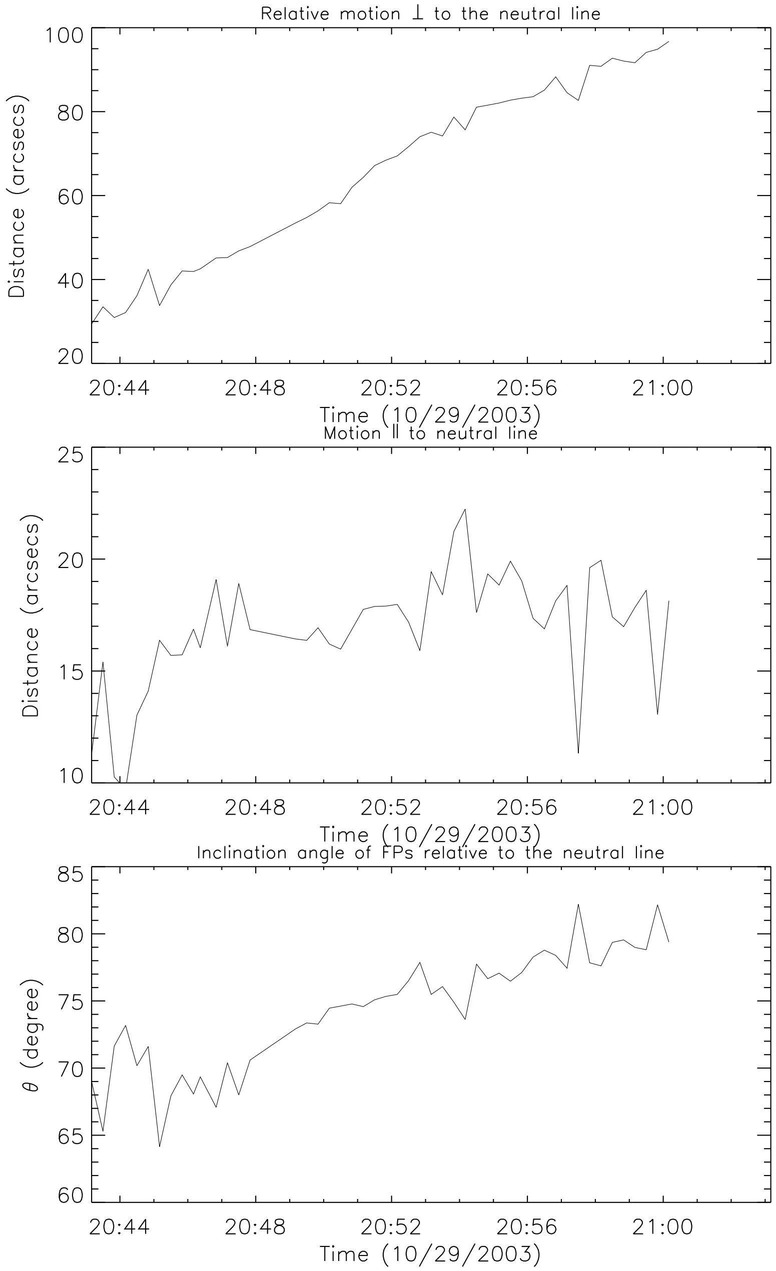

Figure 5.4: *Top and middle*: The relative displacement of the two FPs in the direction perpendicular and parallel to the neutral line, respectively. *bottom*: the inclination angle of the line connecting the FPs relative to the neutral line.

light curves here obtained from the images are therefore free from particle events noise. We find that the two fluxes follow each other and generally decrease with time with some fluctuations, particularly early in the flare. They correlate very well, which can also be seen from Figure 5.6*a* where one flux is plotted vs. the other. The Pearson's linear and Spearman's rank correlation coefficients are 0.955 ± 0.135 and 0.974, respectively, indicating a high correlation. We fitted the logarithms of the data with a straight line (*dashed*). Such a strong linear correlation is expected, because it is believed that the two FPs are produced by the same population of electrons that leave the LT acceleration region in opposite directions and reach the two ends of the same magnetic loop.

Figure 5.5*b* shows the history of the magnetic fields of the two FPs obtained from the *SOHO*/MDI magnetogram (see Figure 5.3). To account for the solar differential rotation, for each FP position, we rotated it backward to the time of the magnetogram (08:30 UT) and read the magnetic field value from the MDI pixel where the new FP position is registered in. We find that, again, the overall trend of the magnetic field is decreasing with time, particularly for the W-FP (*diamond*). Note that we have larger (than the HXR fluxes) fluctuations here, which partly come from registering the FP to an MDI pixel which has a size of about $2''$. The magnetic field measurement has a nominal noise of 20 G (Scherrer et al., 1995), which is less than 10% for most of the magnetic field values here. However, the main source of uncertainty could be the co-alignment[2] of *RHESSI* and *SOHO* images, for which we, unfortunately, do not have a good estimate, and thus the error bars are not shown for magnetic field values here. The two magnetic field strengths seem to be correlated, to some extent, but this is not so obvious. We plot one field vs the other in Figure 5.6*b*, which yields a Pearson's linear and Spearman's rank correlation coefficients of 0.524 ± 0.135 and 0.537, much smaller than that of the HXR fluxes.

If one plots the HXR flux vs. the magnetic field, both averaged between the two FPs, one obtains Figure 5.6*c*. We find a moderate linear correlation (Pearson's $r = 0.762 \pm 0.135$) between the two quantities, with a straight-line fit shown as the dashed line. Note the flux here is in logarithmic scale. This means that the average HXR flux *exponentially* correlates with the average magnetic field. Assuming the speeds of the FPs remain roughly constant (despites its large uncertainties as mentioned above), this translates into that the HXR production rate correlates with the magnetic field annihilation rate. We also note that such a correlation intuitively fits in the picture of magnetic shearing described earlier.

---

[2] Krucker et al. (2005) suggested that the co-alignment is good within $2''$ for this flare.

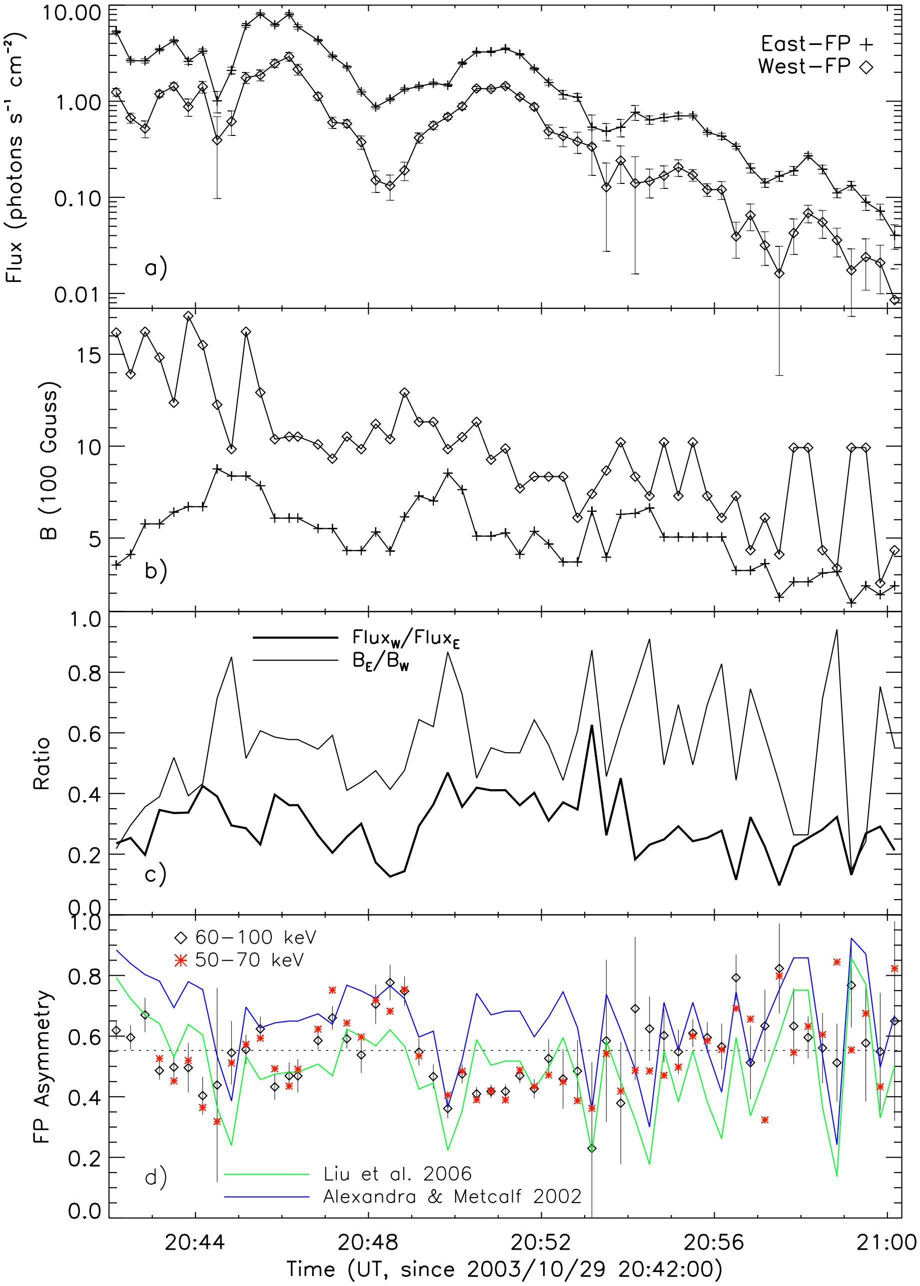

Figure 5.5: History of the HXR fluxes of the two FPs and their associated magnetic fields. (*a*) Light curves at 60–100 keV of the eastern (*plus, higher*) and western (*diamond, lower*) FPs. (*b*) Magnetic fields (differential rotation corrected) registered by SOHO/MDI at the then current positions of the eastern (*plus, lower*) and western (*diamond, higher*) FPs. (*c*) The ratios of the HXR fluxes (western-to-eastern) and magnetic fields (eastern-to-western) of the two FPs. (*d*) Asymmetry A of the FP fluxes in two energy bands, 60–100 (diamond) and 50–70 keV (asterisk). The blue and green lines are predicted asymmetry based on a simple loss-cone argument.

Early in the flare, the FPs are connected by *highly* sheared magnetic field lines, which have *larger* magnetic strength; as a results, *more* magnetic energy is available and *larger* energy release rate gives rise to *stronger* particle acceleration and *stronger* HXRs at the FPs. As time proceeds, the FPs come from less sheared field lines, which are of smaller magnetic strength; consequently, a smaller acceleration rate results from less magnetic energy density and produces less high-energy electrons and HXRs.

The **exponential** nature of the dependence of the HXR flux on the magnetic field indicates that particle acceleration is very sensitive to magnetic field (particularly at higher B values) and there are nonlinear processes involved in the energy release process. In the stochastic acceleration model (Petrosian & Liu, S. 2004), the *plasma parameter* α is proportional to B, it determines the wave dispersion relation, and thus heavily affects the acceleration rate nonlinearly. It is therefore understandable that the HXR flux exponentially depends on the magnetic field of the FPs. We should, however, note that the FP magnetic field strength discussed here is not that in the reconnection region, which is high in the corona and is thus difficult to measure (Lin et al. 1998). It is not unreasonable, on the other hand, to assume the coronal field strength is more or less proportional to the value at the FP magnetically connected to the reconnection region.

5.3 Footpoint Asymmetry & Magnetic Mirroring

5.3.1 Observational Motivation

The two conjugate FPs exhibit asymmetric characteristics, as already noted by Xu et al. (2004), Liu, W. et al. (2004b), Liu, C. et al. (2006), and Krucker et al. (2005). From Figures 5.5*a* and 5.5*b* we clearly see that the *brighter* eastern FP (E-FP) is located in a *weaker*, negative (*dark*, Figure 5.3) magnetic field, while The *dimmer* western FP (W-FP) comes from a *stronger*, positive (*bright*) field.

As to the evolution of the FP position, the E-FP moves at an average velocity of $37.7\,\mathrm{km\,s^{-1}}$ (projected in the direction perpendicular to the neutral line), which is about two times *faster* (see Figure 5.3) than that of the W-FP ($17.8\,\mathrm{km\,s^{-1}}$). This makes the product vB about balanced between the two FPs, meaning that about the same amount of magnetic flux is annihilated from each side (cf., Fletcher & Hudson 2001 reported unbalanced fluxes though for the 2000 July 14 flare).

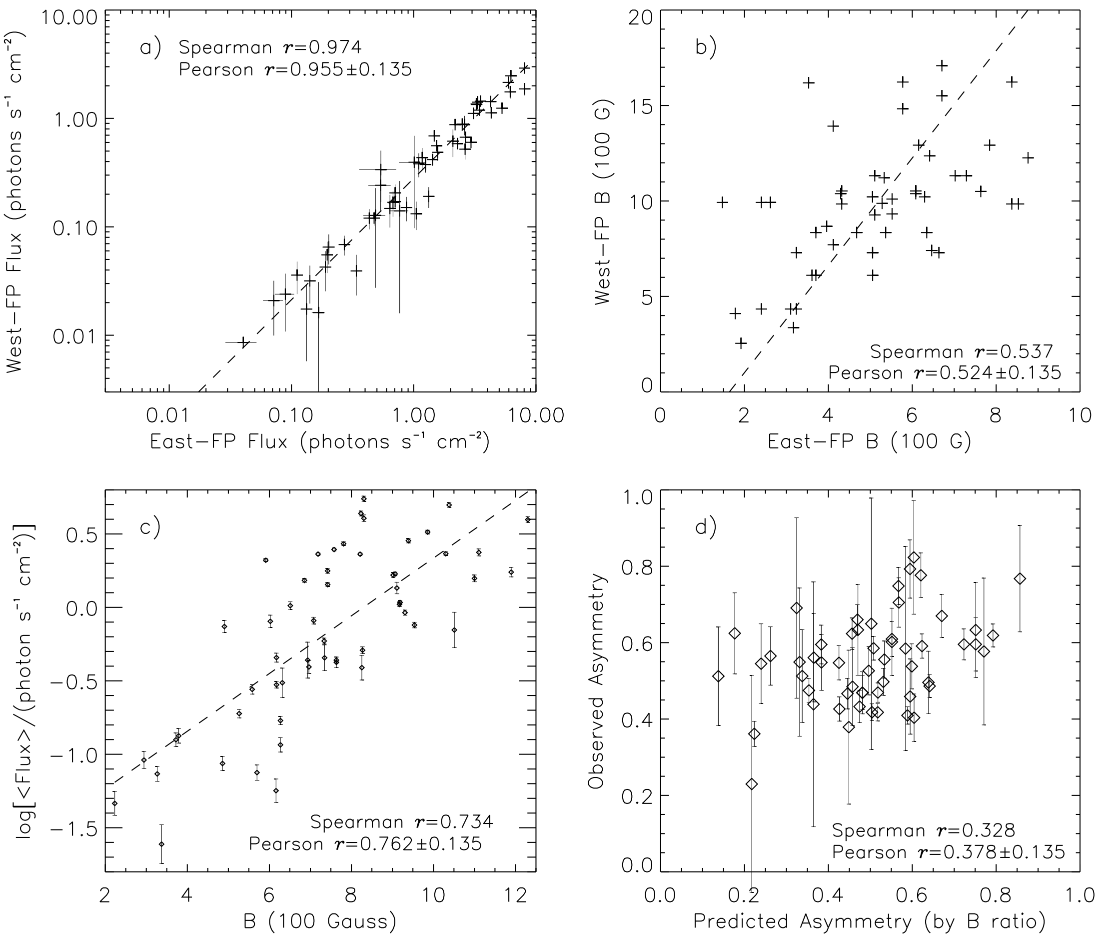

Figure 5.6: Various correlations associated with the HXR fluxes and magnetic fields of the two FPs. (*a*) HXR flux (60–100 keV, Fig. 5.5*a*) of the western FP vs. that of the eastern FP, which yields a strong linear correlation. The dashed line is the straight-line fit to the logarithmic values of the data. (*b*) Same as (*a*) but for the magnetic fields (see Fig. 5.5*b*). (*c*) HXR flux (logarithmic) vs. magnetic field, both averaged between the two FPs. A linear fit to the data is shown as the dashed line, which indicates an exponential dependence of the FP flux on its magnetic field. (*d*) Observed FP asymmetry (Fig. 5.5*d*, see text) of the 60–100 keV band, plotted against asymmetry predicted from the magnetic field asymmetry based on a loss-cone scenario.

5.3.2 Literature Review

In the literature, the association of the stronger HXR FP with the weaker B field is ascribed to the **magnetic mirroring** effect. A stronger FP magnetic field is associated with a larger field convergence rate, which results in more electrons being mirrored back to the corona before they reach the dense chromosphere and produce HXRs there. The opposite is true for a weaker FP magnetic field. If such a scenario operates, an anti-correlation between the flux ratio and the magnetic field ratio is expected and was reported in some flares (e.g., Li et al., 1997; Qiu et al., 2001) Goff et al. (2004), however, from a study of 32 *Yohkoh* flares found a mixture of anti-correlation and no correlation, but the authors did not carry out a time or energy dependent analysis because of *Yohkoh*'s limited time and energy resolution.

It is convenient to define the normalized asymmetry, following Alexander & Metcalf (2002),

$$A \equiv \frac{I_1 - I_2}{I_1 + I_2} = \frac{1 - R}{1 + R}, \tag{5.1}$$

where $R = I_2/I_1$ is the ratio of the HXR fluxes, I_2 and I_1, of the two conjugate FPs. By this definition, A ranges from -1 to 1, with $|A| = 1$ being perfect asymmetry and $A = 0$ being exact symmetry.

For some flares, the asymmetry exhibits **energy dependence**, which is not expected from the magnetic mirroring effect if the pitch angle distribution is the same at all energies. This is because mirroring is, to the first order, independent of particle energy. Alexander & Metcalf (2002) found in the 2002 March 17 flare higher asymmetry in the intermediate energy range and lower asymmetry at both low and high energies. McClements & Alexander (2005) by running their Fokker-Planck transport code, attributed this to an asymmetric, energy-dependent injection process at the LT. They argued that there were more electrons injected to one leg of the loop than to the other. This interpretation may have its theoretical difficulties.

Some flares also have their FP *aymmetry changed with time.* In the 2002 March 17 flare, (Alexander & Metcalf 2002) as time proceeds, the asymmetry even switches its sign, i.e., the previous dimmer FP turns brighter than the other. Siarkowski & Falewicz (2004) also found time dependent variations and quasi-periodic flip/switch of the asymmetry in a *Yohkoh* event (the X5.3 flare of August 25, 2001).

5.3.3 Analysis

The long duration of the HXR FPs in this flare and *RHESSI* 's excellent time and energy resolution allowed us to study the FP asymmetry and as well as its time and energy dependence in unprecedented detail, which is an advantage over previous works.

We have calculated the western-to-eastern FP HXR flux ratio ($R = I_2/I_1$, where I_1 and I_2 are the HXR fluxes of the E-FP and W-FP, respectively, and $I_1 > I_2$ here) and the magnetic field ratio ($R_B = B_1/B_2$, $B_1 < B_2$), which are plotted in Figure 5.5*c*. As can be seen, there seems to be some timing correlation between these two ratios, particular early during the flare (say, before 20:54 UT). We also plot one ratio (R_F) against the other (R_B) (not shown). We find a very weak correlation, with a Spearman's rank correlation coefficient of 0.328 and a Pearson's linear coefficient of 0.381 ± 0.135.

The resulting asymmetry (by equation 5.1) in the 60–100 keV band is plotted in Figure 5.5*d* together with error bars. For comparison, we also show the asymmetry in the 50–70 keV band as red asterisks, which is slightly different from the 60–100 keV one but they basically follow the same trend of variation.

We would like to see how well the mirroring effect operates in this flare, disregarding all the collisional transport effects. The loss cone angle is given as

$$\theta_i = \arcsin \sqrt{B_0/B_i}\,, \tag{5.2}$$

where B_0 is the magnetic field at the injection site where particles escape the acceleration region in the corona, and B_i is the magnetic field at the ith ($i = 1, 2$) FP in the chromosphere. Because the coronal magnetic field generally can not be directly measured, in this simple back-of-envelop calculation, we assume $B_0 = \min\{B_1, B_2\} = B_1$, i.e., no convergence on the side of the smaller FP field. If we also assume an isotropic pitch angle distribution of the electrons upon injection from the acceleration region, the fractional flux of the electrons whose pitch angle is located inside the loss cone (thus these electrons will directly precipitate to the chromosphere) can be evaluated by integrating over the solid angle (Alexander & Metcalf 2002):

$$F_i = \frac{1}{4\pi}\int d\Omega = \frac{1}{4\pi}\int_0^{2\pi} d\phi \int_0^{\theta_i} \sin\theta d\theta = \frac{1-\mu_i}{2}\,, \tag{5.3}$$

where $\mu_i = \cos\theta_i$, and $i = 1, 2$. Such a fraction should be independent of electron energy by our assumption and is proportional to the HXR flux I_i at the corresponding FP. Then it follows that

$$A_L = \frac{F_1 - F_2}{F_1 + F_2} = \frac{\mu_2 - \mu_1}{2 - (\mu_2 + \mu_1)}\,, \tag{5.4}$$

where the subscript L denotes loss-cone based calculation, to distinguish this from the observed asymmetry by equation (5.1).

Note Alexander & Metcalf (2002) assumed that an electron reflected by mirroring on the side (B_2) of strong magnetic convergence would pass through the LT region transparently and can precipitate to the other FP (B_1) of weak convergence if its pitch angle meets the condition, $\theta_2 < \theta < \theta_1$ (or $\mu_1 < \mu < \mu_2$), and makes it enter the loss cone there. In the stochastic acceleration model, the LT region has strong turbulence present which can scatter electrons that are reflected back by mirroring and thus change their pitch angle. Thus we believe that the contribution of the electrons that are reflected and then precipitate at the other end of the loop should not be considered. Rather, an equal, isotropic injection to both halves of the loop is a good approximation. This makes our equation (5.4) differ from Eq. (6) of Alexander & Metcalf (2002).

The predicted asymmetry A_L by equation (5.4) is shown as the green line in Figure 5.5*d*. For comparison purposes, we also show that calculated by Eq. (6) of Alexander & Metcalf (2002) in blue color. As we can see, the predicted asymmetry (*green*) shows a rough correlation with the observed one, particularly in the trend of variations at early times. Late into the flare (after about 20:54 UT), the correlation pattern is smeared, partly due to the large variations of the magnetic field. We also plot the observed asymmetry as a function of the predicted one in Figure 5.6*d*. Again, some weak correlation can be seen, as also indicated by the relatively smaller correlation coefficients, Spearman's rank correlation $r = 0.328$ and Pearson's linear coefficient of 0.378 ± 0.135. It is interesting to note that the Spearman's rank coefficient here is identical to that between the flux ratio R and the magnetic field ratio R_B, because the rank correlation is preserved during the nonlinear transformation of the functional forms (from R to A, and from R_B to A_L).

Aside from the temporal evolution, we also checked the energy dependence of FP asymmetry. Figure 5.7 shows the asymmetry A as a function of photon energy, obtained from images taken at the peak time (20:51:20–20:51:48 UT) of one HXR pulse. As is obvious, the asymmetry stays about constant (around the mean value of 0.538, shown as the dashed line). The uncertainty becomes large at high energies because of low count statistics and thus poor image quality. Note that, unfortunately, due to strong pileup effects, the spectrum below about 50 keV is not trustworthy, and we have to restrict ourselves to higher energies for this analysis. Similar analysis has been done for several other times and we found similar energy-independent results. In this sense, such asymmetry is consistent with the pure (no collision) magnetic mirroring effect.

We have also accumulated a sample of several flares that show distinct conjugate FPs with good image quality. Our initial analysis of these flares indicates there is no universal energy-dependent pattern of HXR flux asymmetry, as can be seen from Figure 5.7, where various patterns are present. The large uncertainties given by the current imaging spectroscopic capability of *RHESSI* software makes the answer even more obscure. The particular interpretation of the energy-dependent asymmetry by McClements & Alexander (2005) seems to be *ad hoc* for such an individual event.

5.3.4 Discussion

From the above analysis, we can conclude that, to the first order, the asymmetry observed here is consistent with the magnetic mirroring effect. That is, the stronger HXR FP is associated with the weaker magnetic field. However, we find that the predicted asymmetry (based on a pure loss-cone argument) can not fully explain the observation (see, e.g., Figure 5.6*d*), which could result from several reasons. The first is the uncertainties in the observations, particularly of the magnetic field, as noted earlier. The second reason is that our model could be too simple to describe the physics sufficiently accurately (but it does catch some observed features). For example, the assumption that the coronal magnetic field at the injection site is equal to that of the weaker FP may not be valid, and this can introduce some uncertainty when evaluating the predicted asymmetry. Aside from these uncertainties, we would like to point out several other possibilities, which are related to possible intrinsic asymmetry in the particle acceleration and transport process.

One possibility of deviation from the loss-cone argument is **intrinsic anisotropy** of the particle distribution escaping from the acceleration region. This can originate from the acceleration process. Particularly, in the framework of the stochastic acceleration model, scattering of particles (by turbulence) is energy-dependent. In the HXR producing energy range, 10 to several hundred keV, the scattering timescale for electrons decreases with energy (see Petrosian & Liu, S. 2004, Fig. 11), which means higher-energy electrons are

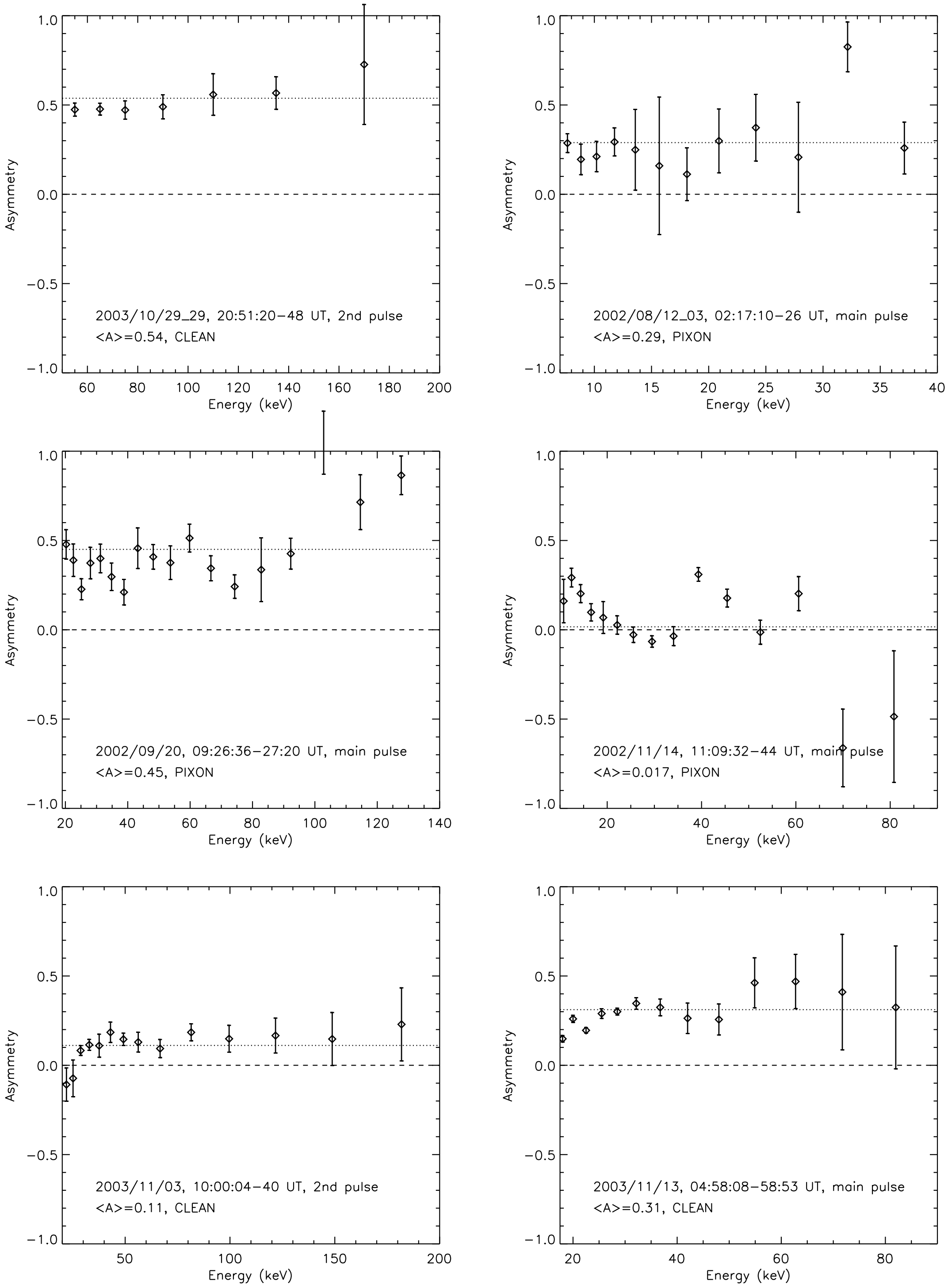

Figure 5.7: Energy dependent FP flux asymmetry for the 2003/10/29 X10 flare (*top left*) and other events. The dotted line marks the mean value and the dashed line marks zero (perfect symmetry).

closer to isotropic distribution because of strong scattering. This could result in energy-dependent FP flux asymmetry observed in HXRs.

Other factors, such as **transport effects**, can produce further asymmetry. The first transport effect is the **energy dependence** of Coulomb collisions. Low-energy particles are more subject to Coulomb energy loss ($\dot{E}_{\rm Coul} \propto 1/\beta$) and pitch angle scattering ($D_{\mu\mu,{\rm Coul}} \propto 1/\gamma^2\beta^3$), and thus they tend to have an isotropic distribution and lose their memory of the initial pitch angle distribution with which they escape the acceleration region. The opposite is true for high-energy particles and they tend to preserve their initial pitch angle distribution and isotropy if any in the acceleration region. Consequently, we would expect at low photon energies, the FP asymmetry is closer (than at high energies) to the loss-cone prediction based on the isotropic assumption and magnetic mirroring.

Another transport effect is the **density dependence** of Coulomb collisions, which affects the FP asymmetry in two ways, since the Coulomb pitch angle diffusion coefficient and Coulomb energy loss rate are both proportional to the ambient density n_e. (1) If, for some reason, the densities in the two legs of the loop are different, Coulomb collisions would affect the two sides differently, and produce different pitch angle distribution, even if the particles are injected isotropically from the acceleration region. (2) The other way density asymmetry operates is related to Coulomb loss, bremsstrahlung radiation, and the way we calculate the FP photon flux. For one half of the loop with a *higher* density, there are *more* electrons stopped in the leg and thus there are *less* electrons reaching the transition region. In addition, the bremsstrahlung radiation intensity is proportional to the local density as well as the electron flux. Thus both effects combine and produce more photons in the leg and less photons beneath the transition region for the higher-density half of the loop, compared with the other half with a lower density.

The second effect above can also be understood in terms of the column depth. Because given an electron spectrum, the resulting photon emission $I(N)$ as a function of column depth N is determined. Its spatial distribution $I(s)$, i.e., as a function of distance s, then solely depends on the density distribution $n(s)$ via $I(s) = I(N)dN/ds = I(N)n(s)$. For the higher-density half of the loop, the column depth at the transition region, $N_{\rm tr} = \int_0^{s_{\rm tr}} n(s)ds$, is larger, and thus the cumulative emission above the transition region $\int_0^{N_{\rm tr}} I(N)dN$ is larger too. Therefore, the remaining emission below the transition region, $\int_{N_{\rm tr}}^{\infty} I(N)dN = \int_0^{\infty} I(N)dN - \int_0^{N_{\rm tr}} I(N)dN$ (which we take as the FP flux), is smaller than the lower-density half of the loop.

We have done a back-of-envelop test of the density effects using the empirical expression of Leach & Petrosian (1983, Eq. 11; also see equation 6.5 in Chapter 6). For an injected power-law (index δ) electron spectrum, the resulting thick-target photon emission intensity at energy k (in units of rest electron energy $m_e c^2 = 511$ keV, m_e being the electron mass) can be written as

$$I(\tau) = \left(\frac{\delta}{2} - 1\right)\left(\frac{k+1}{k^2}\right)\left(1 + \tau \frac{k+1}{k^2}\right)^{-\delta/2} , \tag{5.5}$$

where τ is the column depth, in units of $1/[4\pi r_0^2 \ln\Lambda] = 5 \times 10^{22}\ \mathrm{cm}^{-2}$, for $r_0 = e^2/m_e c^2 = 2.8 \times 10^{-13}$ cm being the classical electron radius and $\ln\Lambda = 20$ being the Coulomb logarithm. Note that this emission profile is normalized as

$$\int_0^\infty I(\tau, k) d\tau = 1\,.$$

Integrating equation (5.5) yields the cumulative photon emission from the injection site ($\tau = 0$) to the transition region ($\tau = \tau_{\rm tr}$),

$$F(\tau_{\rm tr}) = \int_0^{\tau_{\rm tr}} I(\tau) d\tau = 1 - \left(1 + \tau_{\rm tr} \frac{k+1}{k^2}\right)^{1-\delta/2} , \tag{5.6}$$

whose complement gives the emission cumulated below the transition region,

$$\widetilde{F}(\tau_{\rm tr}) = \int_{\tau_{\rm tr}}^\infty I(\tau) d\tau = 1 - F(\tau_{\rm tr}) = \left(1 + \tau_{\rm tr} \frac{k+1}{k^2}\right)^{1-\delta/2} . \tag{5.7}$$

In this simple test, we assume a symmetric loop geometry with a length of 2.284×10^9 cm and a uniform density for *each half* of the loop. We fix the density of one half at $n_0 = 5 \times 10^9\ \mathrm{cm}^{-3}$ and vary the other half's density for several values of n with $n/n_0 = 2, 4, 8, 16$, which corresponds to different values of the column depth at the transition region $\tau_{\rm tr}(n)/\tau_{\rm tr}(n_0) = 2, 4, 8, 16$. We then, for each density value, calculate the photon intensity ratio of the two FPs,

$$R = \frac{\widetilde{F}[\tau_{\rm tr}(n)]}{\widetilde{F}[\tau_{\rm tr}(n_0)]} = \left[1 + \tau_{\rm tr}(n) \frac{k+1}{k^2}\right]^{1-\delta/2} \left[1 + \tau_{\rm tr}(n_0) \frac{k+1}{k^2}\right]^{-(1-\delta/2)} , \tag{5.8}$$

and plot it as a function of photon energy. We have repeated this test for two spectrum indexes, $\delta = 4$ and 6, which is shown in Figure 5.8. Clearly, such density asymmetry can indeed produce significant asymmetry in photon fluxes, particularly at low energies or for a soft electron spectrum. For example, with $\delta = 6$, a factor of 4 difference in the density can make the FP flux at 30 keV on the denser side of the loop be only $\sim 70\%$ of that on the other side.

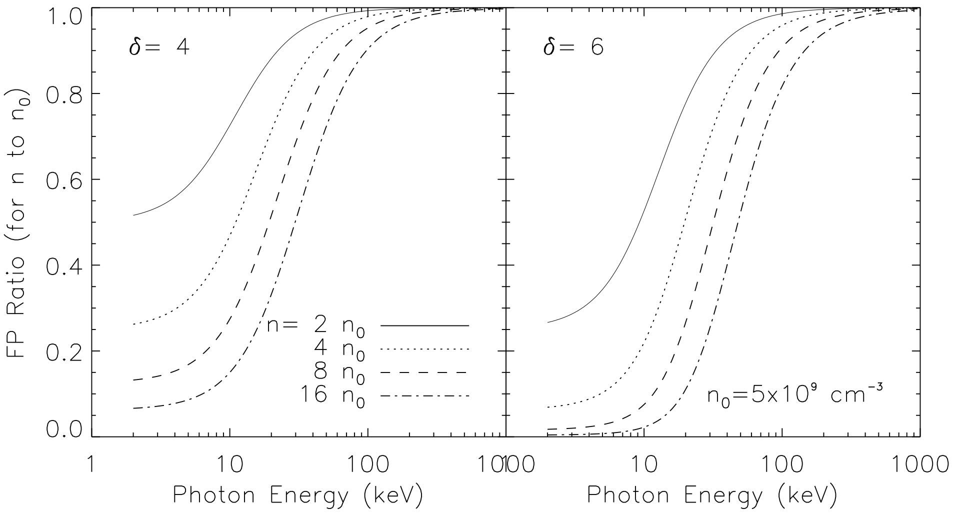

Figure 5.8: FP photon flux ratio as a function of energy for different ratios of the densities in two halves of the loop. The two panels are the same except different electron spectrum index values, 4 (*left*) and 6 (*right*).

In reality, the above mentioned asymmetry in the loop density could come about for several possible reasons. (1) The first is that reconnection (by its name) essentially takes place between magnetic field lines that are previously not connected and the densities associated with the different bundles of field lines are not necessarily the same. It takes a while (on the order of the sound travel time) for the newly reconnected loop to reach a quasi-equilibrium in density within its two halves, but the observed HXRs could be produced before such an equilibrium is reached. (2) Another possible reason is that we believe there exists an region of strong plasma turbulence, i.e., the acceleration region, near the LT, which may sits between the two halves of the loop and may interfere (or prevent) the density equilibration process. In particular, if the initial temperatures are quite different in the two halves, the presence of turbulence in the LT region can suppress thermal conduction significantly and delay thermal (and density) equilibrium. Note that this does not necessarily mean pressure is not in equilibrium either, because a high density can compensate a low temperature to produce a moderate pressure.

5.4 Summary

We have presented HXR data analysis of an X10 flare observed with *RHESSI* on October 29, 2003. Occurring on the solar disk, this flare has two well-defined conjugate FPs showing asymmetric characteristics. One FP is about 3 times brighter in HXR flux than the other, and its line-of-sight magnetic field is about 2 times weaker, which is consistent with the magnetic mirroring effect. As time proceeds, the two FPs move away from the magnetic neutral line, with the brighter one moving faster, and the magnetic field decreases. We find that the logarithm of the mean HXR flux of the two FPs correlates with the mean magnetic field, while the speeds of the FPs remains roughly constant. This means that the HXR production rate correlates with the magnetic field annihilation rate. During this evolution, however, the HXR flux ratio of the two FPs cannot be explained solely by the mirroring effect. At the same time, the inclination angle between the neutral line and the line connecting the two PFs increases and approaches 90°, indicating the newly reconnected magnetic field lines (at higher altitudes) are less sheared.

This observation is consistent with the classic magnetic reconnection model for solar flares in general, but it also requires more thorough theoretical investigations to shed light on the details of the dependence of energy release on the magnetic inhomogeneity as well as the relationship of asymmetric HXR emission and the particle acceleration and transport processes. We hope to address the theoretical treatment of the asymmetric HXR emission in the framework of stochastic acceleration model in the future.

We have also carried out a survey for flares that occur on the solar disk and thus have good magnetic field measurements and these events will be studied in the future to get a statistical picture of the FP HXR flux asymmetry and its associated magnetic field.

Chapter 6

RHESSI Observation of Chromospheric Evaporation: the 2003 November 13 M1.7 Flare[1]

6.1 Introduction

Chromospheric evaporation was first suggested by Neupert (1968) to explain the origin of the hot, dense, soft X-ray–emitting plasma confined in the coronal loops during solar flares. The basic scenario is as follows. Magnetic reconnection heats the plasma and accelerates particles high in the corona. The released energy is transported downward along the newly reconnected closed flaring loop by nonthermal particles and/or thermal conduction, heating the chromospheric material rapidly (at a rate faster than the radiative and conductive cooling rates) up to a temperature of $\sim 10^7$ K. The resulting overpressure drives a mass flow upward along the loop at a speed of a few hundred km s^{-1}, which fills the flaring loop with a hot plasma, giving rise to the gradual evolution of soft X-ray (SXR) emission. This process should also result in a derivative of the SXR light curve in its rising portion that closely matches the hard X-ray (HXR) light curve, which is called the Neupert effect and is observed in some (but not all) flares (Neupert, 1968; Hudson, 1991; Dennis & Zarro, 1993; Dennis et al., 2003; Veronig et al., 2005).

Hydrodynamic (HD) simulations of chromospheric evaporation have been carried out

---

[1] Most of the material in this chapter was published in Liu, W., Liu, Jiang, & Petrosian (2006).

with an assumed energy transport mechanism (e.g., electron "beam" or conductive heating, Fisher et al., 1985c; Mariska et al., 1989; Gan et al., 1995; Yokoyama & Shibata, 2001; Allred et al., 2005) leading to various predictions on the UV-SXR spectral lines produced by the evaporated plasma, as well as the density and temperature profiles along the flaring loop. Most of the observational tests of these predictions rely on the blueshifted components of SXR emission lines produced by the upflowing plasma, first reported by Doschek et al. (1980) and Feldman et al. (1980), who used spectra obtained from the *P78-1* spacecraft. Similar observations were subsequently obtained from X-ray spectrometers on the *Solar Maximum Mission* (*SMM*; Antonucci et al., 1982, 1984), the *Hinotori* spacecraft (Watanabe, 1990), the *Yohkoh* spacecraft (Wuelser et al., 1994), and the *Solar and Heliospheric Observatory* (*SOHO*; Brosius, 2003; Brosius & Phillips, 2004). Wuelser et al. (1994), on the other hand, observed co-spatial SXR blueshifts (upflows) and H_α redshifts (downflows), as expected from HD simulations (Fisher et al., 1985a). A summary of relevant observations from *SMM* can be found in Antonucci et al. (1999).

All the aforementioned observations, however, were indirect evidence in the sense that the evaporation process was not imaged directly. On the basis of HD simulations, Peres & Reale (1993) derived the expected X-ray brightness profile across the evaporation front and suggested that the *Yohkoh* Soft X-Ray Telescope (SXT) or X-ray imagers with equivalent or better spatial and temporal resolution should be able to detect the front. Indeed, Silva et al. (1997) found that the HXR and SXR sources of the 1994 June 30 flare moved toward the loop top (LT) during the impulsive phase. Since the flare was located near the center of the solar disk, they identified such motions as the horizontal counterpart of the line-of-sight motion revealed by the blueshifted emission lines observed simultaneously by the *Yohkoh* Bragg Crystal Spectrometer (BCS).

RHESSI, with its superior spatial, temporal, and spectral resolution (Lin et al., 2002), provides us with opportunities to study the chromospheric evaporation process in unprecedented detail. We report in this chapter our analyses of the spatial and spectral evolution of a simple flare on 2003 November 13 with excellent *RHESSI* coverage. Because the flare occurred near the solar limb, it presented minimum projection effects and a well-defined loop geometry that allows direct imaging of the HXR brightness profile along the loop. The observations and data analyses are presented in §6.2, followed by a derivation of the evolution of the density profile along the flaring loop in §6.3. We summarize the major findings of this chapter and draw conclusions in §6.4.

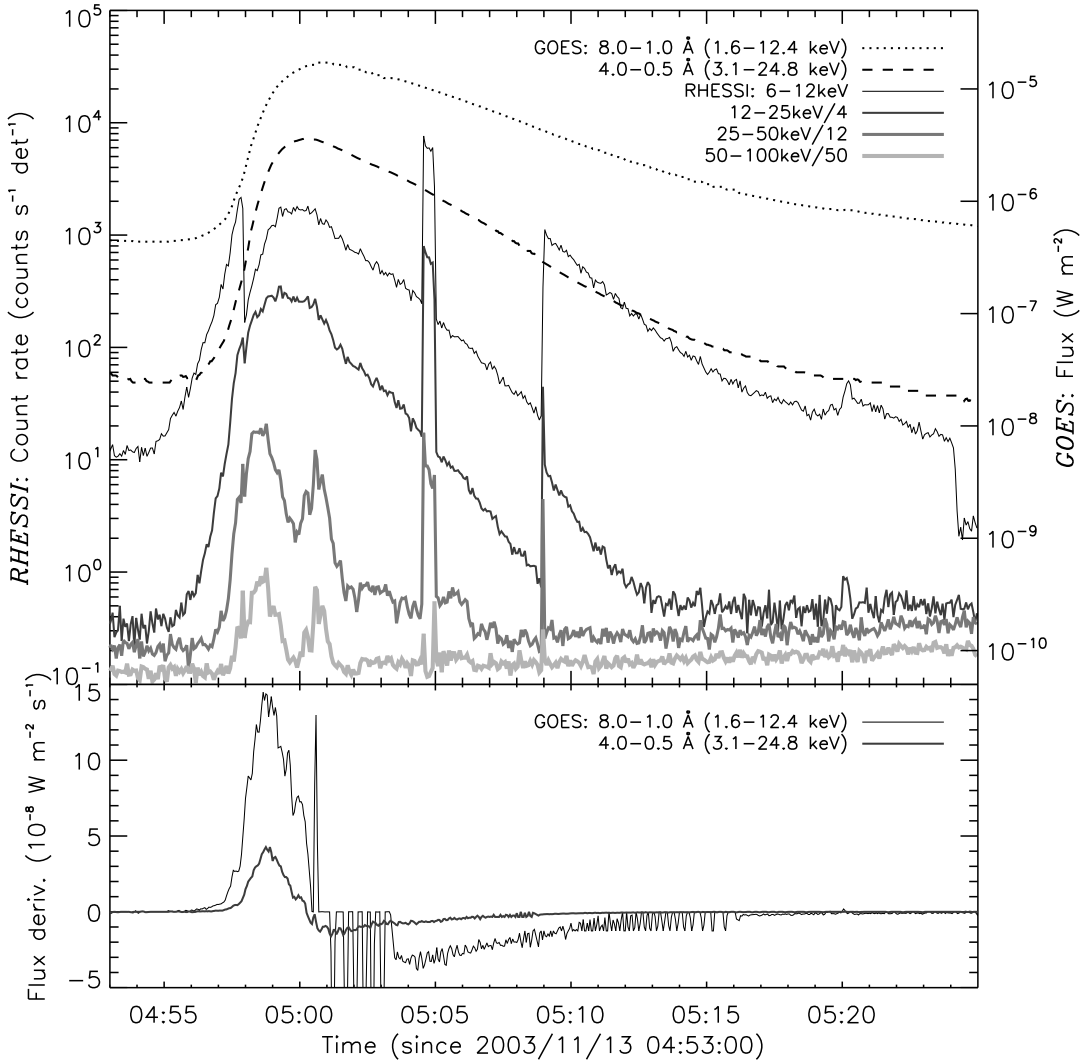

Figure 6.1: *Top*: *RHESSI* and *GOES-10* light curves. The *RHESSI* count rates are averaged over every 4 s, with scaling factors of 1, 1/4, 1/12, and 1/50 for the energy bands 6-12, 12-25, 25-50, and 50-100 keV, respectively. The sharp steps in the *RHESSI* light curves are due to attenuator state changes, and the sudden drop of the 6-12 keV count rate near 05:24 UT results from the spacecraft eclipse. The *GOES* fluxes in the bandpass of 8-1 Å (1.6-12.4 keV) and 4.0-0.5 Å (3.1-24.8 keV) are in a cadence of 3 s. *Bottom*: Time derivative of the *GOES* fluxes. Note that the periodic spikes of the low-energy channel after 05:00:24 UT are calibration artifacts (from Liu, W. et al. 2006).

6.2 Observations and Data Analyses

The flare under study is a *Geostationary Operational Environmental Satellite* (*GOES*) M1.7-class flare that occurred on 2003 November 13 in AR 0501 after it appeared on the east limb. This event followed a period of extremely high solar activities in late October and early November when a series of X-class flares, including the record-setting X28 flare of 2003 November 4, took place (Xu et al., 2004; Liu, W. et al., 2004a; Metcalf et al., 2005; Veronig et al., 2006). *RHESSI* had excellent coverage of this flare. Figure 6.1 shows the *RHESSI* and *GOES-10* light curves. The *GOES* 8-1 Å (1.6-12.4 keV) and 4.0-0.5 Å (3.1-24.8 keV) fluxes rise gradually and peak at 05:00:51 and 05:00:15 UT, respectively. The *RHESSI* high-energy ($>$ 25 keV) count rates, on the other hand, exhibit two pulses peaking at 04:58:46 and 05:00:34 UT, the first one of which is stronger. The steps in the *RHESSI* light curves are due to the attenuator (shutter) movements (Lin et al., 2002). Before 04:57:57 UT and after 05:08:59 UT, there were no attenuators in, and between the two times the thin attenuator was in, except for a short period near 05:05 UT when the attenuator briefly moved out.

Figure 6.2 shows the evolution of the flare at different energies, which may be divided into three phases. (1) Before 04:57:57 UT is the rising phase, when the emission mainly comes from a flaring loop to the south. (2) Between 04:57:57 and 05:08:59 UT is the impulsive phase, during which another loop to the north dominates the emission. This loop appears to share its southern footpoint (FP) with the loop to the south, which is barely visible because of its faintness as compared with the northern loop and *RHESSI*'s limited dynamic range of $\sim$10. (3) After 05:08:59 UT is the decay phase, when the shutters are out and two off-limb sources (identified as the LTs of the two loops) dominate. The relatively higher altitudes compared with earlier LT positions are consequences of the preceding magnetic reconnection, as seen in several other *RHESSI* flares (Liu, W. et al., 2004a; Sui et al., 2004). Clearly the southern loop, which extends to a relatively higher altitude, evolves more slowly and is less energetic than the northern one. We focus on the evolution of the northern loop during the first HXR pulse (04:58-05:00 UT) in this chapter.

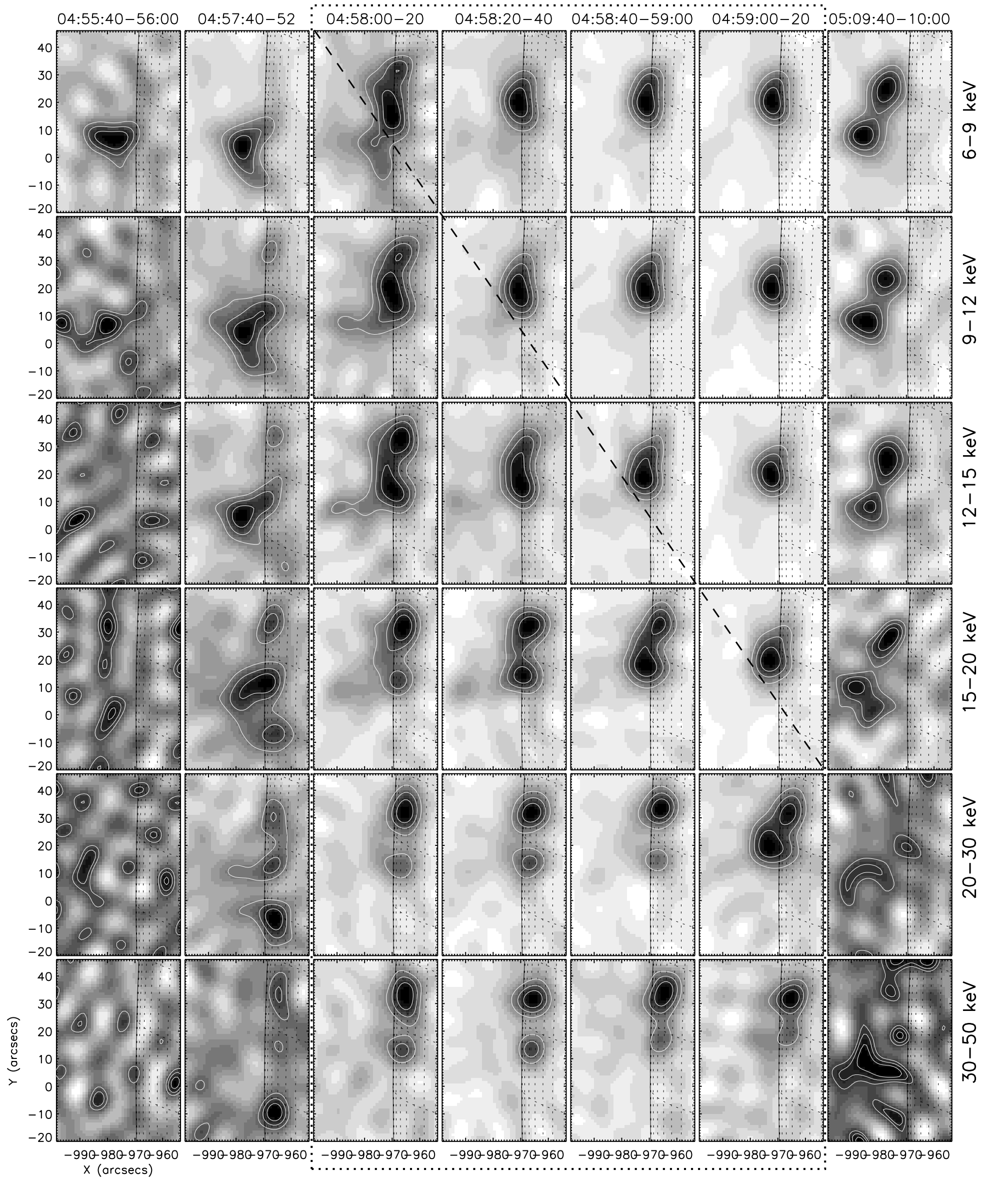

Figure 6.2: Mosaic of CLEAN images at different energies (*rows*) and times (*columns*). Contour levels are set at 40%, 60%, and 80% of the maximum brightness of each image. The front segments of detectors 3-6 and 8 were used for reconstructing these images and the others presented in this chapter, yielding a spatial resolution of $\sim 7''$. We selected the integration intervals to avoid the times when the attenuator state changed. The large dotted box encloses the images during the first pulse of the impulsive phase, and within this time interval the dashed diagonal line separates the frames showing double sources or an extended source from those with a compact single LT source (from Liu, W. et al. 2006).

6.2.1 Pileup Effects

It is necessary to check if pulse pileup[2] is important in this flare before we can make a more quantitative interpretation of the data. The reason is that although we have applied the first-order pileup correction (Smith et al., 2002) in our spectral analysis, such a correction is challenging for images and is not available at present. There are several ways to do the check, of which the detector live time is the first and simplest indicator. We first accumulated spatially integrated spectra for every 1 s time bin during the interval of 04:58:01-04:59:49 UT,[3] using the front segments of all nine detectors except detectors 2 and 7, which have degraded energy resolution (Smith et al., 2002). We then obtained the live time (between data gaps) from the spectrum object data and averaged it over the seven detectors being used. The resulting live time generally decreases with time, ranging from 96% to 89%, with a small modulation produced by the spacecraft spin. In this M1.7 flare, such a live time is comparably high (cf. the live time of $\sim 55\%$ during the 2002 July 23 X4.8 flare and of $\sim 94\%$ during the 2002 February 20 C7.5 flare) and indicates minor pileup severity.

Another approach involves inspecting the change of the spectrum due to pileup. We accumulated spectra over each spacecraft spin period (~ 4 s, with the same set of detectors mentioned above) and used the pileup correction to obtain the relative fraction of the pileup counts among the total counts as a function of energy (Smith et al., 2002). We find that the pileup counts amount to less than $\sim 10\%$ of the total counts at all energies until 04:59:01 UT, when the live time drops to 91%. After that, the relative importance of the pileup counts continues to increase, but remains below $\sim 20\%$ of the total counts before 04:59:17 UT. Toward the end of the first HXR pulse (04:59:45-04:59:49 UT, live time of $\sim 90\%$), the ratio of pileup counts to total counts exceeds 10% in the entire 20-40 keV range and humps up to 43% near 28 keV. We integrate both the pileup counts and total counts over the 20-40 keV band and plot their ratio versus time as a general indicator of pileup severity (see Figure 6.3). Clearly this ratio is $\lesssim 15\%$ during the first two-thirds of the interval shown and does not reach the moderate $\sim 25\%$ level until the very end.

We therefore conclude that pileup effects are generally not very significant for this flare, especially during the first minute of the impulsive phase, because the count rate is

---

[2] Two photons close in time are detected as one photon and have their energies added. Pileup of three or more photons is possible, but at a much lower probability (Smith et al., 2002).

[3] This time interval is also used in studying the evolution of the source morphology in §6.2.2 (see text about Figure 6.6), which covers the bulk of the first HXR pulse.

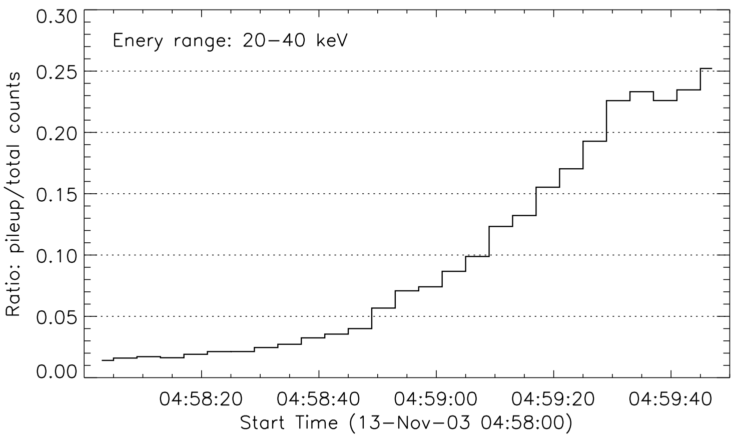

Figure 6.3: Ratio of pileup counts to total counts, both integrated over the 20-40 keV range in time bins of one spacecraft spin (from Liu, W. et al. 2006).

not too high and the thin shutter is in at times of interest, which further attenuates the count rate. It should be noted that the two piled-up photons (that result in a single photon seen in the image) most probably originate from the same location on the Sun, and pileup of photons across different sources is relatively unimportant (G. Hurford 2006, private communication). Therefore, the source geometry would not be significantly affected by pileup, except that there could be a “ghost” of a low-energy source appearing in a high-energy image for very large (e.g. X-class) flares. However, the spectra of individual sources derived from images are distorted, which is relatively more significant at the LT than at the FPs. This is because ample low-energy photons are more abundant than high-energy photons, and have the highest probability to produce pileup, and generally most of the low-energy photons are emitted by the LT source.

6.2.2 Source Structure and Evolution

We now examine the images in greater detail. The top left panel of Figure 6.4 shows *RHESSI* CLEAN (Hurford et al., 2002) images of the northern loop at 9-12, 12-18, and 28-43 keV for 04:58:22-04:58:26 UT. (Although the 4 s integration time is rather short, the image quality is reliable, with a well-defined source structure.) At 9-12 keV the LT dominates and the emission extends towards the two FPs, which dominate the emission at 28-43 keV and above, with the northern FP (N-FP) much brighter than the southern one

(S-FP). One of the most interesting features of the source structure is that emission from the legs of the loop dominates at the intermediate energy (12-18 keV). Similar structures are also observed for several other time intervals during the first HXR pulse (see discussions below). We find that emission from the legs is a transient phenomenon at intermediate energies, because when we integrate over a long period and/or a broad energy band, the LT and/or FP sources become dominant. To our knowledge, no images like this have been reported before. We attribute this in part to the relatively short integration time and to *RHESSI*'s high energy resolution.

For comparison with observations at other wavelengths, the same images at 9-12 and 28-43 keV (*solid contours*) are shown with the *SoHO* EUV Imaging Telescope (EIT), the Michelson Doppler Imager (MDI) magnetogram, and the MDI white-light maps in the other panels of Figure 6.4, where the dashed contours depict the southern loop at 6-9 keV for 04:57:40-04:57:52 UT. The EIT image at 04:59:01 UT (*top right*) shows emission at 195 Å that is co-spatial with the SXR emission from the northern loop. The brightest 195 Å emission, an indicator of the highest differential emission measure (and thus the highest density) at $\sim 1.3 \times 10^6$ K, appears to be close to the N-FP, which is also the strongest FP in HXRs.[4] The bottom left panel of Figure 6.4 displays the X-ray emission along with the post-flare (05:57 UT) MDI magnetogram. This clearly shows that the northern loop straddles a polarity reversal, with the brighter N-FP associated with a stronger magnetic field.[5] The southern loop (*dashed contours*) is associated with an even weaker magnetic field. Here we show the MDI magnetogram recorded 1 hr after the flare's impulsive phase, because during a flare there are many uncertainties in the magnetic field measurement. The bottom right panel of Figure 6.4 shows the MDI continuum map at 12:47 UT (about 8 hr after the flare), suggesting that the flare occurred above the lower sunspot region (*dark area*). Note that during this interval the sunspot has moved westward about 4° in heliographic longitude. We do not plot the MDI white-light map at the time of the flare because then the sunspot was nearly on the limb and was barely visible.

---

[4] EIT 195 Å passband images have a relatively narrow temperature response range, with a characteristic temperature of 1.3×10^6 K (see Dere et al., 2000, Fig. 12), and emission intensity would be lower for both higher and lower temperatures.

[5] Note that since this flare occurred near the solar limb, the line-of-sight magnetogram measures mainly the horizontal (parallel to the solar surface) component of the magnetic field. The vertical component is more relevant here because flaring loops are usually perpendicular to the surface. However, it would be reasonable to assume that the vertical component scales with the horizontal one, and the polarity reversal line in the latitudinal direction is essentially not subject to the line-of-sight projection effect, as seems very likely here.

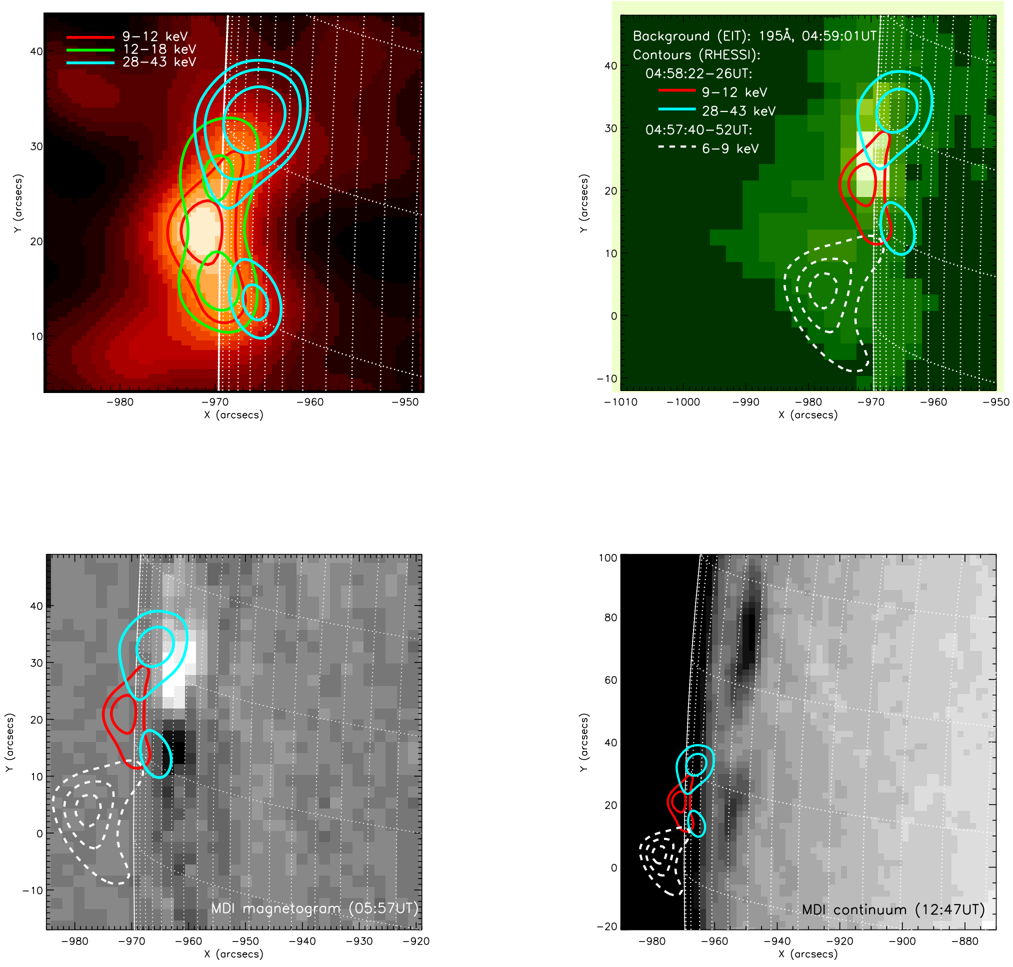

Figure 6.4: *Top left*: *RHESSI* images for 04:58:22-04:58:26 UT during the first HXR pulse. The background is the image at 9-12 keV. The contour levels are at 75 and 90% for 9-12 keV, 70% and 90% for 12-18 keV, and 50%, 60%, and 80% for 28-43 keV. *Top right*: EIT 195 Å image at 04:59:01 UT, showing co-spatial EUV emission in the northern HXR loop. The solid contours are the same as in the top left panel at 9-12 and 28-43 keV, except that the contour levels are 50% and 80% for the latter. A 6-9 keV *RHESSI* image (same as the second panel in the first row of Figure 6.2) for 04:57:40-04:57:52 UT is plotted as dashed contours (at 50%, 70%, 90% levels) that depict the southern loop. The same set of contours is plotted in the two bottom panels as well. *Bottom left*: MDI magnetogram at 05:57 UT. The line-of-sight magnetic field in the map ranges from -351 G (*black*; away from the observer) to 455 G (*white*), with the FPs near the strong magnetic field regions. *Bottom right*: MDI continuum map at 12:47 UT, showing the sunspots. The heliographic grid spacing is 2° (from Liu, W. et al. 2006).

Next we consider the evolution of the northern loop. We note that, as shown in the four columns for 04:58:00-04:59:20 UT (boxed by the dotted line) in Figure 6.2, the FPs initially appear at all energies but later on dominate only in the high-energy bands, while the LT is first evident at low energies and becomes more and more prominent at relatively higher energies, as indicated by the dashed diagonal line. The emission from the LT also extends towards the legs at intermediate energies, and in a given energy band the emission concentrates more and more at the LT with time. These are expected to be common features of flares with a single loop because of chromospheric evaporation, which can increase the plasma density in the loop, making the LT dominant at progressively higher energies. However, because the 20 s integration time is relatively long, these images do not uncover the details of the evaporation process. To remedy this, we have carried out three different but complementary analyses of the images with higher time or energy resolution.

Temporal Morphological Evolution at Different Energies

To study the source morphology change over short time intervals, we model the loop geometry and study the evolution of the HXR brightness profile along the loop. We first made CLEAN images in two energy bands of 6-9[6] and 50-100 keV over the time interval of 04:58:12-04:58:53 UT which covers the plateau portion of the first HXR pulse. From these two images we obtained the centroids (indicated by the white crosses in Figure 6.5*a*) of the sources identified as the LT (6-9 keV) and the two FPs (50-100 keV), respectively. Assuming a semi-circular loop that connects the three centroids, we located the center of the circle, which is marked by the plus sign in Figure 6.5*a*. The grey scale in Figure 6.5*a* was obtained by superposition[7] of 30 images (six 8 s intervals from 04:58:08 to 04:58:56

---

[6] Since the thin attenuator was in at that time, counts below 10 keV are likely dominated by photons whose real energy is about 10 keV higher than the detected energy. This is due to strong absorption of lower energy ($<$ 10 keV) photons by the attenuator and escape of the germanium K-shell fluorescence photons that are produced by photoelectric absorption of higher energy (10-20 keV) photons in the germanium detector (see Smith et al., 2002, §5.2). However, for the flare under study, the 6-9 keV image most likely reveals the real LT morphology, because there are ample thermal photons at lower energies originating from the LT source and photons at slightly higher energies seem to come from the same location.

[7] Because we are interested in determining the average loop geometry during the first pulse when the low-energy X-ray flux has changed dramatically, using this approach to map the loop will ensure a relatively uniform brightness profile along the whole loop by assigning equal weights to images at different energies. On the other hand, if one simply integrates over the entire time range of 04:58:08-04:58:56 UT and the energy band of 9-50 keV, the source morphology will be dominated by the LT source that emits most of the photons at a later time and at relatively lower energies, which may not properly depict the loop

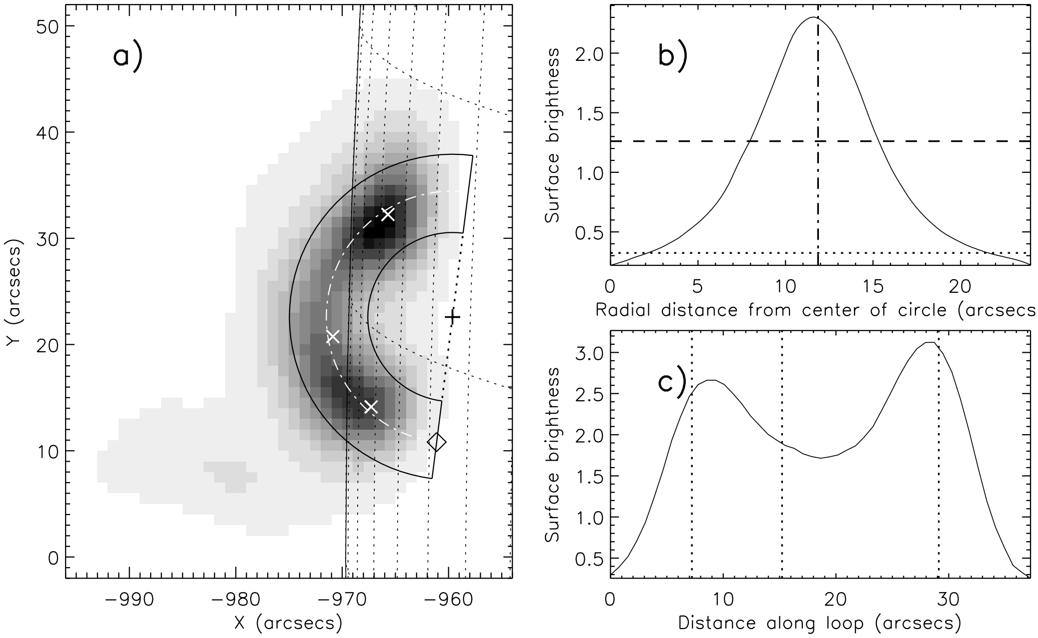

Figure 6.5: (*a*) Synthesized image obtained by superimposing 30 8 s images between 04:58:08 and 04:58:56 UT for five energy bands: 9-12, 12-15, 15-20, 20-30, and 30-50 keV. The three crosses mark the LT and two FPs identified as the emission centroids of the corresponding sources in the 04:58:12-04:58:53 UT images at 6-9 and 50-100 keV, respectively. The solid lines represent the semi-circular model loop with the center of the circles marked by the plus sign. The white dot-dashed line indicates the central arc (see below) of this loop, and the diamond indicates the start point of the distance in (*c*). (*b*) Radial brightness profile averaged along the loop, obtained from the image shown in (*a*). The distance is measured from the center of the circles. The horizontal dashed line marks the 50% level of the maximum, and the crossings of this line with the profile define the radii of the two solid semi-circles in (*a*). The 5% level is represented by the horizontal dotted line. The vertical dot-dashed line denotes the radial position of the central arc of the loop. (*c*) Same as (*b*), but for the surface brightness along the loop's central arc, averaged perpendicular to the loop. The three vertical dotted lines mark the corresponding positions of the crosses in (*a*) [from Liu, W. et al. 2006].

UT in five energy bands: 9-12, 12-15, 15-20, 20-30, and 30-50 keV) reconstructed with the PIXON algorithm (Metcalf et al., 1996; Hurford et al., 2002). Figures 6.5*b* and 6.5*c*, respectively, show the intensity profiles perpendicular to and along the loop (averaged over the respective orthogonal directions). The inner and outer circles (at $r = 8''.0$ and $15''.3$) in Figure 6.5*a* show the positions of the 50% values of the maximum intensity in Figure 6.5*b*. However, to infer the intensity profile along the loop, we use radially integrated flux down to the 5% level. This enables us to include as much source flux as possible (with little contamination from the southern loop). We define the mean of the radii at the 5% level as the radius of the central arc of the loop (indicated by the white dot-dashed line in Figure 6.5*a*).

With the above procedure, one can study the evolution of the brightness profile along the loop at different energies. Figure 6.6 shows the results obtained from PIXON images with an integration time of one spacecraft spin period (~4 s) from 04:58:01 to 04:59:49 UT for three energy bands (20-30, 15-20, and 12-15 keV). Using a simple algorithm, we determine the local maxima whose slopes on both sides exceed some threshold value and mark them with filled circles. We compare each profile with its counterpart obtained from the CLEAN image (with the same imaging parameters) and use the rms of their difference to estimate the uncertainty as indicated by the error bar near the right-hand end of the corresponding profile. For each panel, the rms difference of all the profiles, as a measure of the overall uncertainty, is shown by the error bar in the upper right corner. This uncertainty is about 10% for the three energy bands; as expected, it increases slightly at higher energies, which have lower counts.

Figure 6.6*a* displays the profile at 20-30 keV, which, as expected (see Figure 6.2), shows emission from the two FPs with fairly constant positions until the very last stage, when the LT emission becomes dominant.[8] At this stage, the S-FP becomes undetectable and the N-FP has moved very close to the LT. At lower energies (15-20 keV; Figure 6.6*b*) the maxima tend to drift toward the LT gradually and eventually merge into a single LT source. At even lower energies (12-15 keV; Figure 6.6*c*) this trend becomes even more pronounced and the drift starts earlier, except that here the shift is not monotonic and there seems to be a lot of fluctuation. We also repeated the same analysis at a higher cadence (every 1 s,

---

geometry during the HXR pulse.

[8] As noted earlier, pulse pileup in the 20-40 keV range becomes relatively important at this very late stage, which means that a fraction of the 20-30 keV photons seen in the image are actually piled-up photons at lower energies.

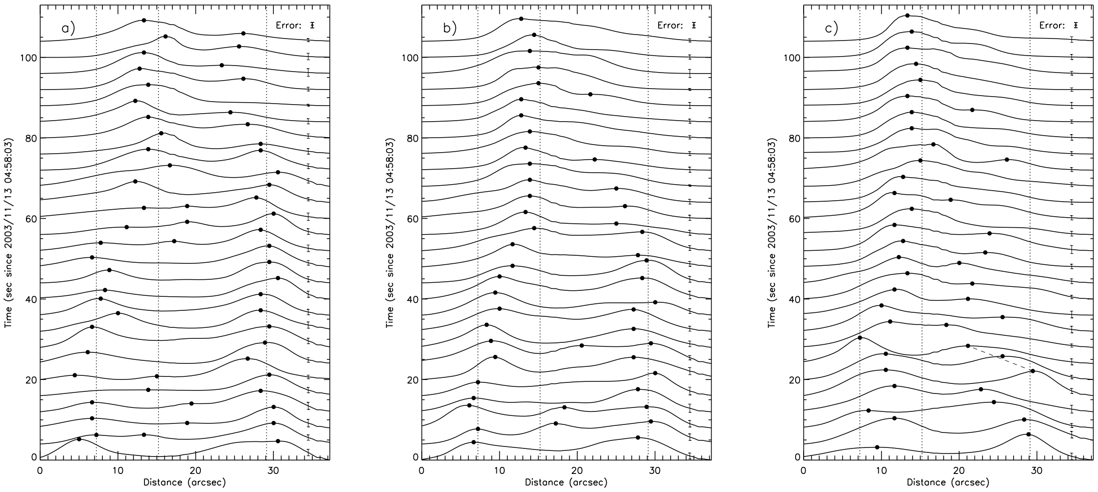

Figure 6.6: (*a*) Evolution of the 20-30 keV brightness profile along the loop in a cadence of 4 s starting at 04:58:03 UT. Each profile is normalized to its own maximum and has an integration time of 1 spacecraft spin period (~4 s) whose central time is used to label the vertical axis. The filled circles mark the local maxima, and the three vertical lines are the same as those in Figure 6.5*c*. The error bar on each curve indicates an estimated uncertainty of the profile, and the stand-alone error bar in the upper right corner represents the overall uncertainty (13%) of all the profiles. (*b*, *c*) Same as (*a*) but for 15-20 and 12-15 keV, with an overall uncertainty of 12% and 10%, respectively. With the dashed straight line in (*c*), we estimate the speed of the emission maximum at ~10^3 km s^{-1}. Note the slightly different scales among the three panels for the profiles and their error bars (from Liu, W. et al. 2006).

~ 4 s integration interval) with both the PIXON and CLEAN algorithms. The evolution of the resulting profiles (although oversampled and thus not independent for neighboring profiles) appears to be in line with that shown here at a 4 s cadence obtained with PIXON. The general trends of these results indicate that high-energy HXR-producing electrons lose their energy and emit bremsstrahlung photons higher and higher up in the loop as the flare progresses. This can come about simply by a gradual increase of the density in the loop, presumably due to evaporation of chromospheric plasma. From the general drift of the maxima we obtain a timescale ($\sim$tens of seconds) and a velocity of a few hundred km s^{-1}, consistent with the sound speed or the speed of slow magnetosonic waves. As stated above, at low energies we see some deviations from the general trend, some of which do not appear to be random fluctuations. If so, and if we take one of the evident shorter timescale trends, that shown by the dashed line in Figure 6.6*c*, we obtain a large velocity[9] of $756\,\mathrm{km\,s^{-1}}$ that is comparable to the Alfvén or fast magnetosonic wave speed. This may indicate that another outcome of energy deposition by nonthermal particles is the excitation of such modes, which then propagate from the FPs to the LT and might be responsible for the circularly polarized zebra pattern observed in the radio band (Chernov et al., 2005). This, however, is highly speculative, because the spatial resolution ($\sim 7''$) is not sufficiently high for us to trust the shorter timescale variation. The longer timescale general trend, however, is a fairly robust result.

Energy-dependent Structure at Separate Times

Instead of examining the source structure with high time resolution, we can investigate it with higher energy resolution at longer integration intervals as a tradeoff for good count statistics and image quality. To this end, we have made PIXON images during three consecutive 24 s intervals starting from 04:58:00 in 20 energy bins within the 6-100 keV range. Figure 6.7 shows a sample of these images at 04:58:24-04:58:48 UT.

Figures 6.8*a*-6.8*c* show the X-ray emission profile along the loop at different energies for the three intervals.[10] As in Figures 6.6*a*-6.6*c*, the high-energy emission is dominated by the FPs, but there is a decrease of the separation of the FPs with decreasing energies

---

[9] Among the highest observed upflow velocities in chromospheric evaporation are those of about 10^3 km s^{-1} (Antonucci et al., 1990) and 800 km s^{-1} (Doschek et al., 1994), obtained from blueshifted Fe XXV spectra.

[10] Note that pileup effects, as discussed earlier, are insignificant during this period of time (see Figure 6.3).

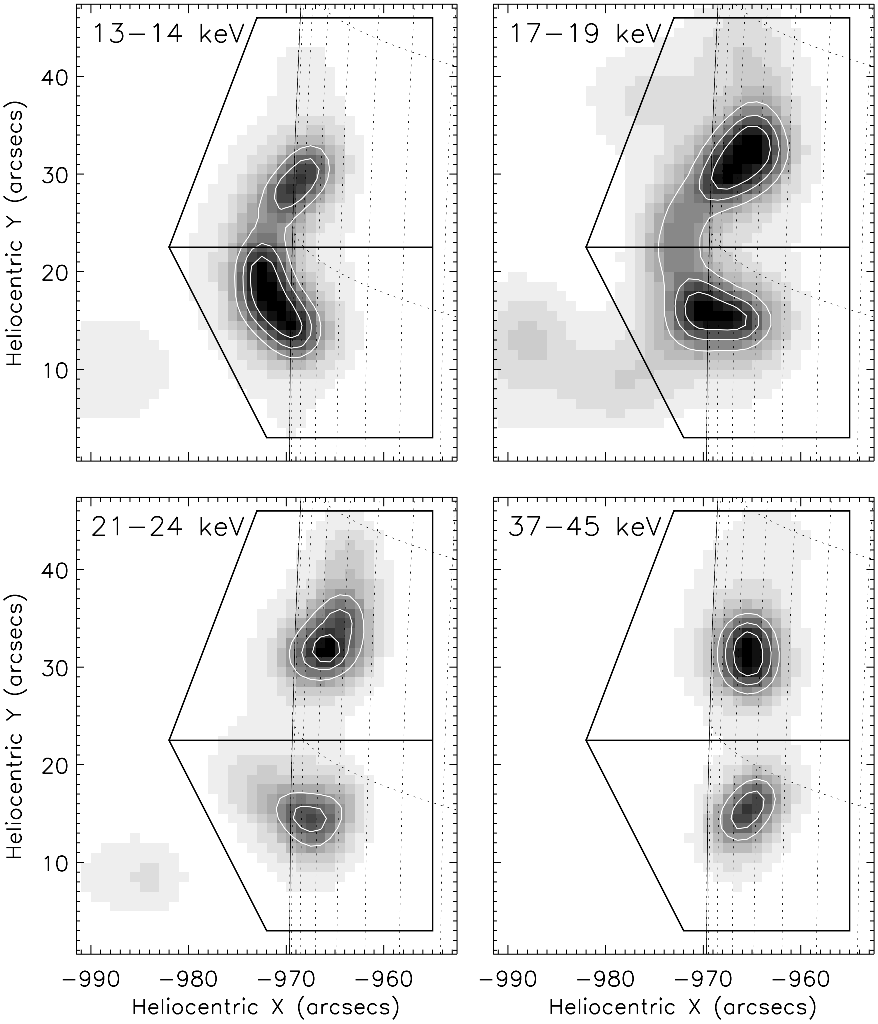

Figure 6.7: PIXON images at 04:58:24-04:58:48 UT in different energy bands. The overlaid boxes were used to divide the loop into halves to calculate the corresponding centroids (from Liu, W. et al. 2006).

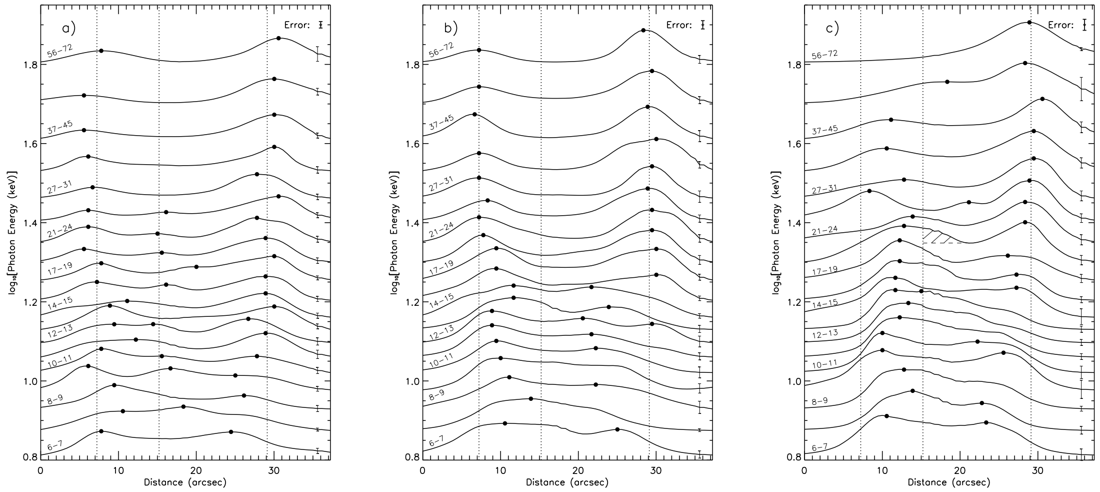

Figure 6.8: (*a*) Brightness profiles (obtained in the same way as in Figure 6.6) at different energies for the time interval of 04:58:00-04:58:24 UT. The vertical axis indicates the average photon energy (in logarithmic scale) of the energy band for the profile. Representative energy bands (in units of keV) are labeled above the corresponding profiles. The vertical dotted lines are the same as in Figures 6.5 and 6.6. (*b*, *c*) Same as (*a*) but for 04:58:24-04:58:48 and 04:58:48-04:59:12 UT, respectively. The error bars show the uncertainties of the corresponding profiles. The overall uncertainties, as indicated by the stand-alone error bar in the upper right corner of each panel (note different scales, similar to Figure 6.6), are 14%, 13%, and 14%, respectively. The hatched region in (*c*) represents the LT emission (19-21 keV) removed for the derivation of the density distribution in Figure 6.15 (see text) [from Liu, W. et al. 2006].

and with time. Again, at later stages the LT dominates and the profile becomes a single hump. The general trend again suggests an increase of the gas density in the loop. At lower energies (< 15 keV), the profile is more complicated, presumably due to many physical processes (in addition to chromospheric evaporation), such as thermal conduction and transport of high-energy particles, thermal and nonthermal bremsstrahlung, wave excitation and propagation, wave-particle coupling, and even particle acceleration, which may be involved. We believe that a unified treatment of acceleration and HD processes with physical conditions close to the flare is required for interpretation of these results to uncover the details.

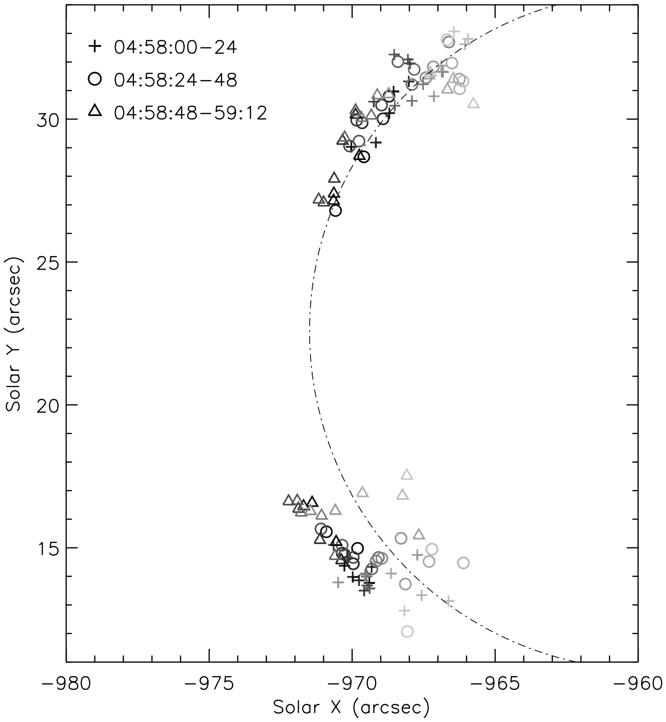

Figure 6.9: Centroids of the northern and southern halves of the loop at different energies for the three 24 s time intervals (same as those in Figures 6.8*a*-6.8*c*). Energy increases from dark to light grey symbols. The dot-dashed line marks the central arc of the model loop (same as in Figure 6.5*a*) [from Liu, W. et al. 2006].

To quantify this aspect of the source structure evolution, we divided the loop into two halves, as shown by the boxes in Figure 6.7, and calculated their emission centroids. The resulting centroids at the three times, together with the central arc of the model loop, are plotted in Figure 6.9. As can be seen, for each time interval the centroids are distributed along the loop, with those at higher energies being further away from the LT, and the entire pattern shifts toward the LT with time. Figure 6.10 shows the centroid positions of the northern half of the loop (where the source motions are more evident) along and perpendicular to the loop during the three intervals. This again shows that the higher energy emission is farther away from the LT and that the centroids shifted towards the LT with time, but similarly there are some complicated patterns at low and intermediate energies. All these are consistent with the general picture proposed above for the chromospheric evaporation process.

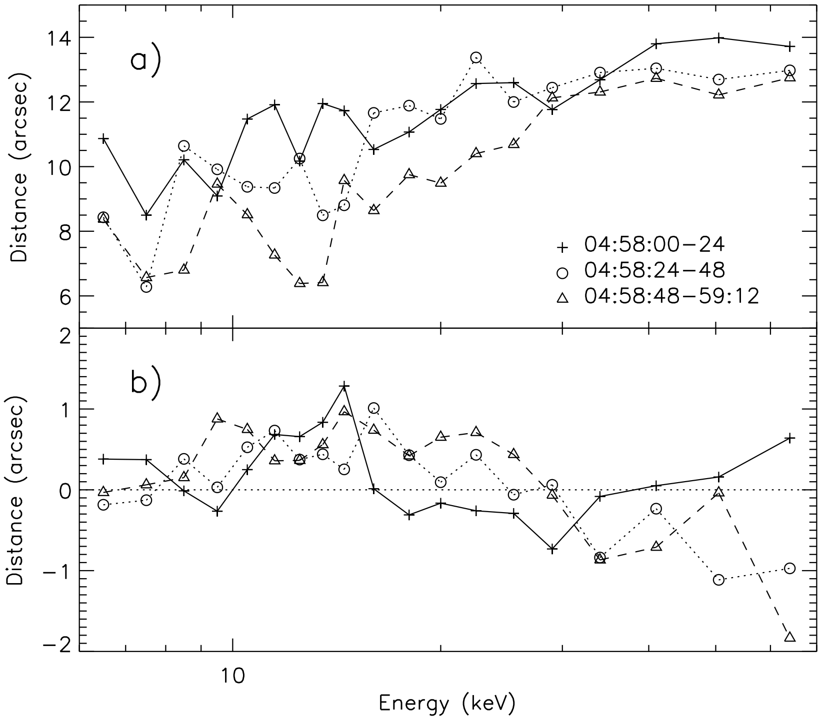

Figure 6.10: Positions of the northern centroids projected along (*a*) and perpendicular to (*b*; note the different scales) the central arc (the line in Figure 6.9) of the loop. The distance in (*a*) is calculated from the average LT position, as shown in Figure 6.5*a* (from Liu, W. et al. 2006).

Evolution of Overall Source Compactness

To further quantify the source motions, we obtained the brightness-weighted standard deviation or the second moment of the profiles. In general, the moment measures the compactness of the overall emission but does not yield the sizes of individual sources whose measurement is still challenging for *RHESSI* (Schmahl & Hurford, 2002). Hence, our attention should be paid to the general trend of the moment rather than to its absolute values, which may be subject to large uncertainties and thus may be less meaningful. The moments of the profiles resulting from CLEAN images (in three energy bands over 8 s intervals) are plotted in Figure 6.11*b*. There is a general decrease of the moment, with the decline starting earlier at lower energies. Such a decrease is expected if the two FPs move closer to each other. However, caution is required here because a decrease of this quantity could also come about by other causes, say, by an increasing dominance of the brightest source. We therefore checked the original images and the corresponding profiles when interpreting our results. To estimate the uncertainty of the moment, for each energy band we repeated the calculation with different integration time (6.11*c*). The resulting moments remain essentially unchanged, and, as expected, the fluctuations of the moment decrease with increasing integration time. We also plot in 6.11*c* the moment (*solid curve*) obtained from PIXON images with an integration time interval of two spin periods (~ 8 s), which basically agrees with its CLEAN counterpart in the general trend. The gradual[11] decrease of the moment is consistent with the motion of the centroids of sources up the legs of the loop, which can take place by a continuous increase of the gas density in the loop due to evaporation.

6.2.3 Spectral Analysis

Spectral analysis can be used to study the evaporation process as well. With an isothermal plus power-law model, we fitted the spatially integrated *RHESSI* spectra down to 6 keV (Smith et al., 2002) for every 8 s interval during the impulsive phase. The emission measure (EM) and temperature of the isothermal component (*asterisks*) are plotted in Figures 6.11*d* and 6.11*e*, respectively. The EM rises almost monotonically with time from 0.6 to 14.2 $\times 10^{49}$ cm^{-3}. This translates into an increase of the plasma density [$n = (\mathrm{EM}/V)^{1/2}$] by a factor of $\sim$5 if we assume a constant volume V. The temperature remains almost

---

[11] On the other hand, the jumps (if real) of the moment may suggest a transient phenomenon.

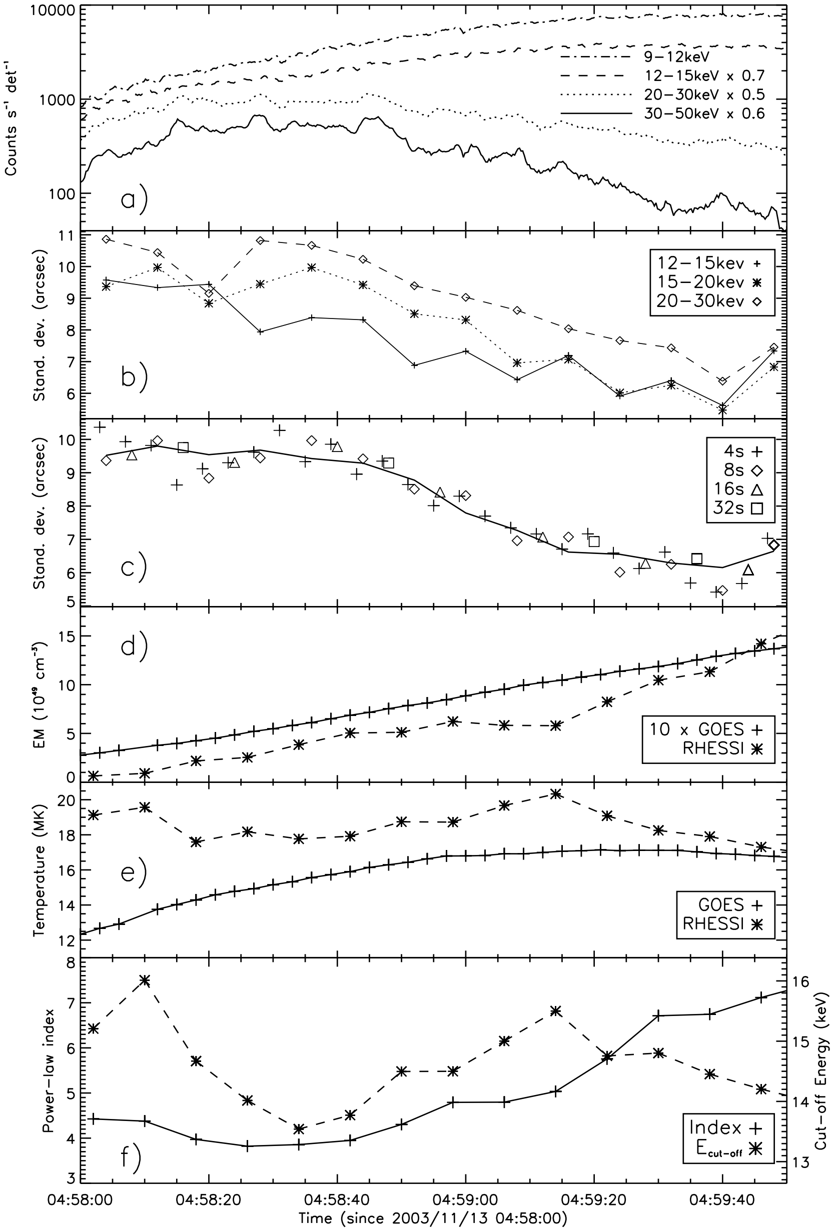

Figure 6.11: (*a*) *RHESSI* light curves (demodulated to remove artificial periodicity caused by the spacecraft spin). (*b*) Evolution of the standard deviation of the brightness profiles along the loop in three different energy bands obtained from CLEAN images. (*c*) Same as (*b*) but in the 15-20 keV band and with different integration time intervals indicated in the legend. The solid curve denotes the result from the PIXON images with an $\sim$ 8 s integration time interval. (*d*, *e*) Evolution of the emission measure (in units of 10^{49} cm^{-3}) and temperature (in units of MK), respectively, of the thermal component of the spatially integrated *RHESSI* spectrum obtained from fits to a thermal plus power-law model and from thermal fits to the *GOES* spectrum. The *GOES* emission measure is scaled by a factor of 10. (*f*) Evolution of the power-law index and the low-energy cutoff of the *RHESSI* power-law component (from Liu, W. et al. 2006).

constant with a trend of slight decrease with time. The EM and temperature derived from the *GOES* data (*plus signs*) are also shown for comparison. In general, the *GOES* results are smoother and the temperature increases monotonically but remains below that of the *RHESSI* data, consistent with previous results (Holman et al., 2003). This is expected because *RHESSI* is more sensitive to higher temperatures than *GOES*. However, surprisingly, the *GOES* emission measure is also lower than that of *RHESSI*, as opposed to what is the case more generally (see Holman et al., 2003). It is not clear whether or not this is due to a problem related to the *RHESSI* calibration at low energies. Nevertheless, the continuous increase of the EM at comparable rates does suggest a gradual increase of the plasma density.

The best-fit parameters of the power-law component with a low-energy cutoff are plotted in Figure 6.11*f*. The power-law index γ (*plus signs*) is anti-correlated with the high-energy light curves (see Figure 6.11*a*) and shows a soft-hard-soft behavior. It starts at 4.43 at 04:58:02 UT, drops to 3.82 at the impulsive peak (04:58:26 UT), and rises to 7.12 at 04:59:46 UT. The high indexes (> 5) may be an indicator of high-temperature thermal rather than nonthermal emission. Thus, in what follows we limit our analysis to times up to 04:59:20 UT. The low-energy cutoff (*asterisks*) of the power law is about 15 keV and is near the intersection of the isothermal (exponential) and power-law components.

6.2.4 The Neupert Effect

The Neupert effect is commonly quoted as a manifestation of chromospheric evaporation (Dennis & Zarro, 1993), and a simple energy argument (e.g. Li et al. 1993) is often used to account for the relationship between SXR and HXR fluxes (F_{SXR} and F_{HXR}). In the thick-target flare model, the nonthermal F_{HXR} represents the *instantaneous* energy deposition rate ($\dot{\mathcal{E}}_e$) by the electron beam precipitating to the chromosphere, but the thermal F_{SXR} is proportional to the *cumulative* energy deposited; that is, the time integral of $\dot{\mathcal{E}}_e$. It naturally follows that the temporal derivative of the SXR flux, $\dot{F}_{SXR}$, should be related to F_{HXR}.

The simplest test of the Neupert effect is usually carried out by plotting $\dot{F}_{SXR}$ and F_{HXR} in some energy band. There are many reasons why a simple linear relationship would not be the case here. The first and most important is that $\dot{\mathcal{E}}_e$ is related to F_{HXR} through the bremsstrahlung yield function Y ($F_{HXR} = \dot{\mathcal{E}}_e Y$), which is not a constant and depends on the spectrum of the electrons or HXRs (see, e.g., Petrosian 1973). Here the most crucial factor is the low-energy cutoff (E_1) of the nonthermal electrons, but the spectral index also plays some role. The total yield of all the bremsstrahlung photons produced by a power-law spectrum of electrons with energies above E_1 (in units of 511 keV) is

$$Y_{total} = \frac{16}{3}\left(\frac{\alpha}{4\pi \ln \Lambda}\right) E_1 \left(\frac{\delta - 2}{\delta - 3}\right), \tag{6.1}$$

and the yield of the photons whose energies are greater than E_1 is

$$Y_{E_1} = \frac{16}{3}\left(\frac{\alpha}{4\pi \ln \Lambda}\right) E_1 \left(\frac{2}{\delta - 1}\right)^2 \left(\frac{1}{\delta - 3}\right), \tag{6.2}$$

where $\alpha = 1/137$, $\ln \Lambda = 20$ is the Coulomb logarithm, and δ is the spectral index of the power-law electron flux. We plot in Figure 6.12 Y_{E_1} as a function of δ for $E_1 = 20$ keV. As shown in Figure 6.11*f*, both the low-energy cutoff and the spectral index of the nonthermal emission vary during the pulse, indicating variations in the electron spectrum and thus breaking the linearity of the SXR-HXR relationship. Other factors that can also produce further deviations are energy deposition by protons (and other ions), by conduction, and

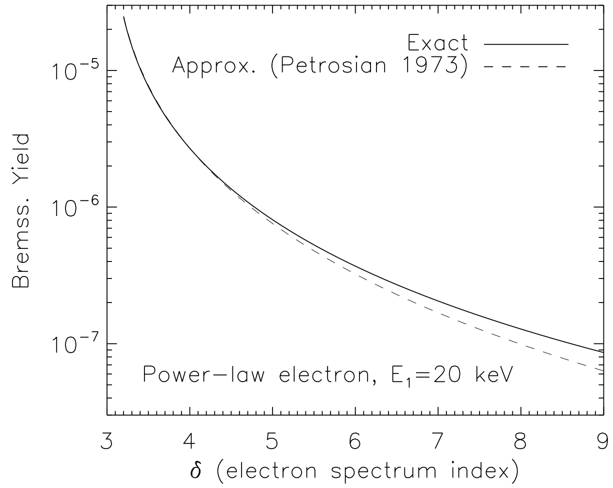

Figure 6.12: Bremsstrahlung yield in the thick-target model for a power-law electron spectrum with a low-energy cutoff of $E_1 = 20$ keV. The dashed line corresponds to the approximate result from Eq. (6.2) here or Eq. (30) in Petrosian (1973). The solid line comes from more accurate results from numerical integration of Eq. (29) in Petrosian (1973).

possible ways of dissipation of energy other than simply heating and evaporating the chromospheric plasma by nonthermal electrons. A detailed treatment of the problem requires solutions of the combined transport and HD equations, which is beyond the scope of this chapter. Veronig et al. (2005), who included some of these effects in an approximate way, found that the expected relationship was mostly not present in several *RHESSI* flares. Finally, one must include the fact that the chromospheric response of SXR emission will be delayed by tens of seconds, depending on the sound travel time (and its variation) and other factors.

The flare under study has shown no indication of gamma-ray line emission, which means that the contribution of protons most probably is small. In the currently most favorable model, in which the electrons are accelerated stochastically by turbulence (see, e.g., Petrosian & Liu, S., 2004) the turbulence can suppress heat conduction during the impulsive phase and possibly also during the decay phase (Jiang et al., 2006). Because there do not appear to be large changes in the shape of the loop during the impulsive phase, other energy dissipation processes, such as cooling by expansion, may also be negligible. Assuming these to be the case, we have performed the Neupert effect test in two ways, the first of which is the common practice of examining the relation between $\dot{F}_{SXR}$ and F_{HXR}. We then examine the relation between $\dot{\mathcal{E}}_e$ and $\dot{F}_{SXR}$ by taking into account the variation of the bremsstrahlung yield.

Correlation of $\dot{F}_{SXR}$ and F_{HXR}

The temporal derivatives of the fluxes of the two *GOES* channels are shown in the bottom panel of Figure 6.1. As is evident, during the rising portion of the *GOES* fluxes the derivatives of both channels indeed match the first pulse of the *RHESSI* HXR light curves ($>$ 25 keV), but not during the second weaker pulse (where the 1-8 Å derivative shows some instrumental artifacts). This may be due to the fact that the Neupert effect of the second pulse is overwhelmed by the cooling of the hot plasma produced during the first stronger pulse. Nevertheless, the SXR light curves (of both *GOES* and *RHESSI*) exhibit a slightly slower decay rate than that expected from the first pulse alone. This most likely is the signature of the energy input by the second pulse, which slows down the decay of the first pulse.

We note in passing that the SXR light curves start rising several minutes prior to the onset of the HXR impulsive phase. This is an indication of preheating of the plasma before production of a significant number of suprathermal electrons. The 6-12 keV curve rises faster than the *GOES* curves at lower photon energies, which is consistent with the picture that the primary energy release by reconnection occurs high in the corona, where the relatively hotter plasma is heated before significant acceleration of electrons (as suggested in Petrosian & Liu, S., 2004), and before transport of energy (by accelerated electrons or conduction) down the flare loop to lower atmospheres where cooler plasmas are heated subsequently and produce the *GOES* flux. On the other hand, the increase of the SXR flux at the beginning is dominated by the southern loop, which shows little evidence of chromospheric evaporation. The phenomenon therefore may be a unique feature of this flare.

To quantify the SXR-HXR relationship, we cross-correlated the *RHESSI* 30-50 keV photon energy flux (F_{30-50}; Figure 6.13*a*) and the derivative of the *GOES* low-energy channel flux ($\dot{F}_{SXR}$; Figure 6.13*c*) in the SXR rising phase (04:58:00-04:59:51 UT). The resulting Spearman rank correlation coefficient (see Figure 6.13*f*), an indicator of an either linear or nonlinear correlation, shows a single hump with a maximum value of 0.91 (corresponding to a significance of $\sim 10^{-13}$) at a time lag of 12 s. This suggests a delay of $\dot{F}_{SXR}$ relative to F_{30-50}, which is expected given the finite hydrodynamic response time (on the order of the sound travel time of $\sim$20 s for a loop size of $\sim 10^9$ cm and $T \sim 10^7$ K) required for redistribution of the deposited energy. Such a delay is evident in the numerical simulations of Li et al. (1993), who also found that the density enhancement contributes more to the total SXR emissivity than the temperature increase for longer duration (≥ 30 s) HXR bursts during the decay phase. In Figure 6.13*d*, we plot the two quantities with the *GOES* derivative shifted backward by 12 s to compensate the lag of their correlation. A linear regression (*dotted line*) gives $F_{30-50} = (1.95 \pm 0.15)\dot{F}_{SXR} - (3.68 \pm 0.48)$ with an adjusted coefficient of determination (the so-called R-squared) of $R^2_{adj} = 0.81$, which is close to 1, suggesting a good linear correlation.

Correlation of $\dot{F}_{SXR}$ and $\dot{\mathcal{E}}_e$

We also carried out the same analysis for the electron energy power $\dot{\mathcal{E}}_e$, assuming a thick-target model of power-law electrons with a low-energy cutoff of $E_1 = 25$ keV. We first obtained the energy flux of all the photons with energies greater than E_1, F_{E_1}, from the

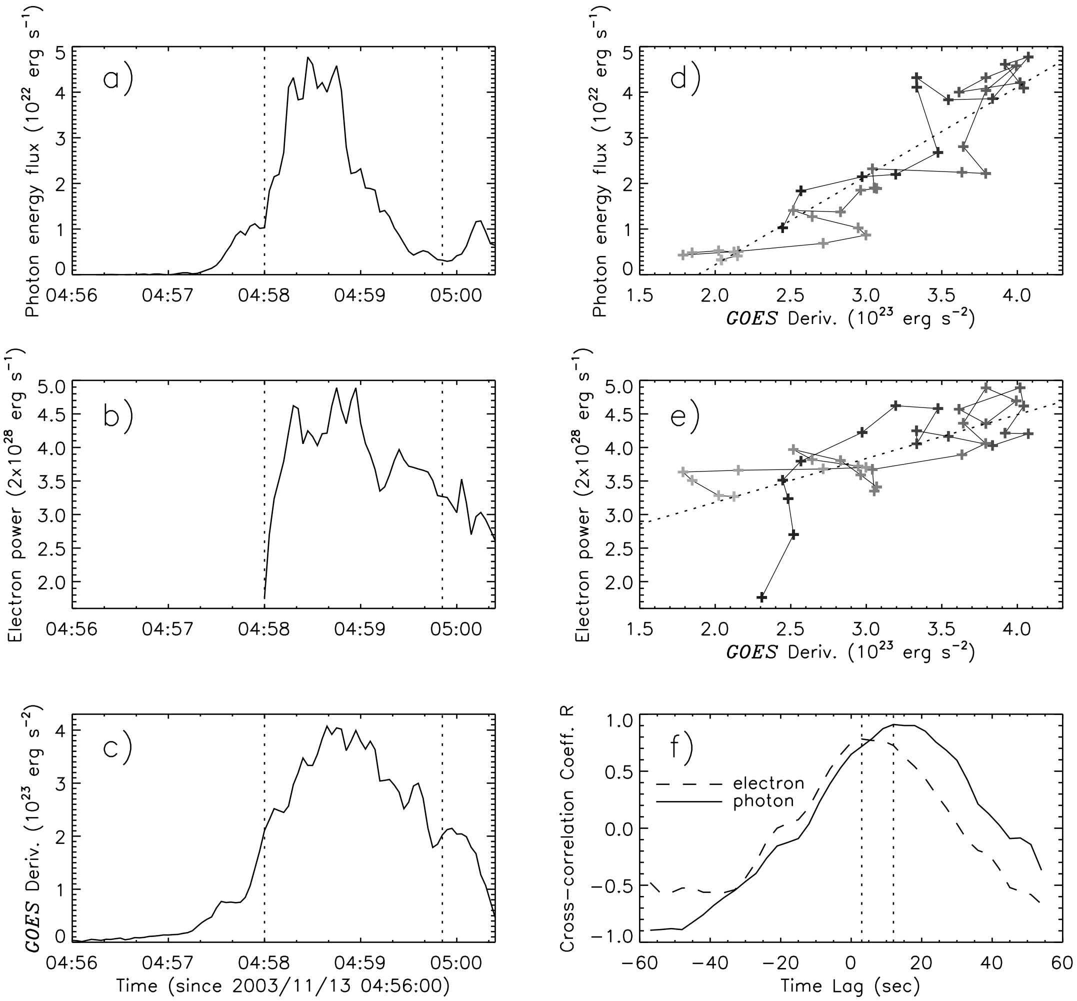

Figure 6.13: (*a*) Photon energy flux at 30-50 keV (F_{30-50}) at the Sun inferred from the *RHESSI* observation at 1 AU, assuming isotropic emission. The two vertical dotted lines outline the time interval (04:58:00-04:59:51 UT) used for the cross-correlation analysis (see below). (*b*) Power ($\dot{\mathcal{E}}_e$) of the power-law electrons with a low-energy cutoff of 25 keV inferred from the photon energy flux assuming a thick-target model. (*c*) Same as (*a*) but for the derivative ($\dot{F}_{SXR}$) of the *GOES* low-energy channel (1-8 Å) flux. (*d*) HXR energy flux F_{30-50} vs. SXR derivative $\dot{F}_{SXR}$ (shifted back in time by 12 s to account for its delay, as revealed by the cross-correlation analysis; see *f*) within the interval of 04:58:00-04:59:51 UT. The grey scale of the plus signs (connected by the solid lines) from dark to light indicates the time sequence. The dotted line is the best linear fit to the data. (*e*) Same as (*d*) but for $\dot{\mathcal{E}}_e$ and $\dot{F}_{SXR}$, which is shifted back by 3 s in time. (*f*) Spearman rank correlation coefficient R of the photon energy flux (electron power) and $\dot{F}_{SXR}$ plotted as a function of time lag of the latter relative to the former. The dotted lines mark the peak values of $R = 0.91$ and 0.78 at a lag of 12 and 3 s, respectively (from Liu, W. et al. 2006).

30-50 keV photon energy flux F_{30-50}:

$$F_{E_1} = \int_{E_1}^{\infty} J(E)EdE = F_{30-50}\frac{E_1^{-\gamma+2}}{30^{-\gamma+2} - 50^{-\gamma+2}}, \tag{6.3}$$

where $J(E) \propto E^{-\gamma}$ is the photon flux distribution at the Sun (in units of photons keV^{-1} s^{-1}), which is obtained from spectrum fitting (see §6.2.3) and is assumed to extend to infinity in energy space. We then calculated the power of the electrons by

$$\dot{\mathcal{E}}_e = F_{E_1}/Y_{E_1}, \tag{6.4}$$

where the bremsstrahlung yield Y_{E_1} is given by equation (6.2).[12] The resulting value of $\dot{\mathcal{E}}_e$ is plotted versus time and versus the *GOES* derivative in Figures 6.13*b* and 6.13*e*, respectively. The dotted line in Figure 6.13*e* shows a linear fit ($R^2_{adj} = 0.49$) to the data: $\dot{\mathcal{E}}_e = (0.65 \pm 0.11)\dot{F}_{SXR} + (1.88 \pm 0.34)$. The corresponding Spearman rank correlation coefficient has a peak value of 0.78 (significance of $\sim 10^{-8}$) at a time lag of 3 s (Figure 6.13*f*). As evident, $\dot{\mathcal{E}}_e$ yields no better correlation with $\dot{F}_{SXR}$ than F_{30-50} does, which is similar to the conclusion reached by Veronig et al. (2005). During the HXR decay phase (after 04:59:20 UT), the spectrum becomes softer ($\gamma > 5$) and $\dot{\mathcal{E}}_e$ decreases much slower than F_{30-50}, since the bremsstrahlung yield (equation [6.2]) decreases with the spectral index. As noted above, for these high spectral indexes, the emission might be thermal rather than nonthermal. The inferred electron power is thus highly uncertain for these times.

As stated earlier, the total energy of the nonthermal electrons is very sensitive to the low-energy cutoff E_1, which is generally not well determined (cf. Sui et al., 2005). We thus set E_1 as a free parameter and repeat the above calculation for different values of E_1 (ranging from 15 to 28 keV). We find that, as expected, the temporal $\dot{\mathcal{E}}_e$-$\dot{F}_{SXR}$ relationship highly depends on the value of E_1. For a small value of E_1 ($\lesssim$ 20 keV), $\dot{\mathcal{E}}_e$ keeps rising until ~04:59:50 UT (near the bottom of the F_{30-50} light curve), which makes the $\dot{\mathcal{E}}_e$-$\dot{F}_{SXR}$ correlation completely disappear. On the other hand, for a large value of E_1 ($>$ 20 keV), the correlation is generally good during the impulsive pulse (through 04:59:10 UT), and the larger the value of E_1, the better the correlation. This is because the conversion factor

---

[12] We used more accurate results from numerical integration of equation (29) in Petrosian (1973), rather than the approximate equation ([eq. 6.2]) here. However, one can still use equation (6.2) with a simple correction factor of $0.0728(\delta - 4) + 1$ in the range $4 \leq \delta \leq 9$ to achieve an accuracy of $\lesssim 1\%$.

$E_1^{-\gamma+2}/(30^{-\gamma+2}-50^{-\gamma+2})$ in equation (6.3) is an increasing (decreasing) function of the photon spectral index γ if value of E_1 is sufficiently small (large). For a small value of E_1, for example, the photon energy flux F_{E_1} may have a somewhat large value in the valley of the F_{30-50} light curve when γ is high. In addition, during this time interval the bremsstrahlung yield Y_{E_1} becomes small, since δ is large (see equation [6.2]), and consequently this may result in a very large value of $\dot{\mathcal{E}}_e$ by equation (6.4).

As to the magnitude of the energy flux of nonthermal electrons, Fisher et al. (1985c) in their HD simulations found that the dynamics of the flare loop plasma is very sensitive to its value. For a low-energy flux ($\leq 10^{10}$ ergs cm^{-2} s^{-1}), the upflow velocity of the evaporating plasma is approximately tens of km s^{-1}; for a high-energy flux ($\geq 3 \times 10^{10}$ ergs cm^{-2} s^{-1}), a maximum upflow velocity of approximately hundreds of km s^{-1} can be produced. For the flare under study, we estimate the area of the cross-section of the loop to be $A_{loop} \lesssim 1.6 \times 10^{18}$ cm^2, where the upper limit corresponds to the loop width determined by the 5% level in Figure 6.5*b*. We read the maximum electron power of $\dot{\mathcal{E}}_{e,max} = 9.8 \times 10^{28}$ ergs s^{-1} from Figure 6.13*b*, which is then divided by $2A_{loop}$ (assuming a filling factor of unity) to yield the corresponding electron energy flux: $f_{e,max} \gtrsim 3.1 \times 10^{10}$ ergs cm^{-2} s^{-1}. The source velocity estimated in §6.2.2 on the order of a few hundred km s^{-1} is consistent with that predicted by Fisher et al. (1985c). For comparison, we note that Milligan et al. (2006) also obtained an energy flux of $\geq 4 \times 10^{10}$ ergs cm^{-2} s^{-1} from *RHESSI* data for an M2.2 flare during which an upflow velocity of ~230 km s^{-1} was inferred from simultaneous co-spatial *SOHO* Coronal Diagnostic Spectrometer (CDS) Doppler observations.

In summary, the *GOES* SXR flux derivative $\dot{F}_{SXR}$ exhibits a Neupert-type linear correlation with the *RHESSI* HXR flux F_{30-50} during the first HXR pulse. However, unexpectedly, the correlation between the electron power $\dot{\mathcal{E}}_e$ and $\dot{F}_{SXR}$ is not well established on the basis of the simple analysis presented here, which suggests that a full HD treatment is needed to investigate the chromospheric evaporation phenomenon (see discussions in §6.4).

6.3 Loop Density Derivation

For the 1994 June 20 disk flare, Silva et al. (1997) interpreted the moving SXR sources as thermal emission from the hot ($\sim 30-50$ MK) plasma evaporated from the chromosphere on the basis of the good agreement of the emission measure of the blueshifted component and that of the SXR from the FPs. For the limb flare under study here, Doppler shift measurements are not available. Meanwhile, a purely thermal scenario would have difficulties in explaining the systematic shift of the centroids towards the FPs with increasing energies up to ~70 keV, as shown in Figure 6.10. A nonthermal scenario appears more appropriate. That is, the apparent HXR FP structure and motions can result from a decrease in the stopping distance of the nonthermal electrons with decreasing energy and/or increasing ambient plasma density caused by the chromospheric evaporation (as noted earlier in §6.2.2). One can therefore derive the density distribution along the loop from the corresponding X-ray emission distributions (e.g., Figure 6.8) without any preassumed density model (cf. Aschwanden et al., 2002). This approach is described as follows.

For a power-law X-ray spectrum produced by an injected power-law electron spectrum, Leach (1984) obtained a simple empirical relation (also see Petrosian & Donaghy, 1999, §2) for the X-ray intensity $I(\tau, k)$ per unit photon energy k (in units of 511 keV) and column depth τ [in units of $1/[4\pi r_0^2 \ln\Lambda] = 5 \times 10^{22}$ cm^{-2} for $r_0 = 2.8 \times 10^{-13}$ cm and $\ln\Lambda = 20$]:

$$I(\tau, k) = A\left(\frac{\delta}{2} - 1\right)\left(\frac{k+1}{k^{2+\gamma}}\right)\left(1 + \tau\frac{k+1}{k^2}\right)^{-\delta/2}, \qquad (6.5)$$

where γ and δ (which is equal to $\gamma + 0.7$) are the photon and electron spectral indexes, respectively, A is a constant normalization factor, and $d\tau = nds$, where s is the distance measured from the injection site. This equation quantifies the dependence of the emission profile (or source morphology) on the electron spectral index and column depth. In general, when δ decreases (spectrum hardening), the intensity at a given photon energy rises (drops) at large (small) values of τ and thus the emission centroid shifts to larger values of τ. This is expected because for a harder spectrum, there are relatively more high-energy electrons that can penetrate to larger column depths and produce relatively more bremsstrahlung photons there. The opposite will happen when the spectrum becomes softer. During the impulsive peak, which shows a soft-hard-soft behavior (see §6.2.3), one would expect that the emission centroids would shift first away from and then back toward the LT (if the density in the loop stays constant). If we know the spectral index, the emission profile can therefore yield critical information about the density variation in both space and time.

To compare the above empirical relation with observations, we first integrate $I(\tau, k)$

over an energy range $[k_1, k_2]$,

$$J(\tau; k_1, k_2) = \int_{k_1}^{k_2} A\left(\frac{\delta}{2} - 1\right)\left(\frac{k+1}{k^{2+\gamma}}\right)\left(1 + \tau\frac{k+1}{k^2}\right)^{-\delta/2} dk, \tag{6.6}$$

and then integrate $J(\tau; k_1, k_2)$ over τ to obtain the cumulative emission,

$$F(\tau; k_1, k_2) = \int_0^{\tau} J(\tau; k_1, k_2) d\tau = \frac{1-\gamma}{k_2^{1-\gamma} - k_1^{1-\gamma}} \int_{k_1}^{k_2} \left[1 - \left(1 + \tau\frac{k+1}{k^2}\right)^{1-\delta/2}\right] k^{-\gamma} dk, \tag{6.7}$$

where we have chosen

$$A = \left(\int_{k_1}^{k_2} k^{-\gamma} dk\right)^{-1} = \frac{1-\gamma}{k_2^{1-\gamma} - k_1^{1-\gamma}}, \tag{6.8}$$

so that $F(\tau = \infty; k_1, k_2) = 1$. Comparison of $F(\tau; k_1, k_2)$ with the observed emission profiles gives the column depth $\tau(s)$, whose derivative with respect to s then gives the density profile along the loop.

Specifically for this flare, we assume that the nonthermal electrons are injected at the LT indicated by the middle vertical dotted line in Figure 6.8 and denote the profile to the right-hand side of this line (i.e., along the northern half of the loop) as $J_{obs}(s; k_1, k_2)$, where $[k_1, k_2]$ is the energy band of the profile. The observed cumulative emission is then given by

$$F_{obs}(s; k_1, k_2) = \frac{\int_0^s J_{obs}(s; k_1, k_2) ds}{\int_0^{s_{max}} J_{obs}(s; k_1, k_2) ds}, \tag{6.9}$$

where s_{max} (corresponding to $\tau = \infty$) is the maximum distance considered and $F_{obs}(s; k_1, k_2)$ has been properly normalized. Then $\tau = \tau(s; k_1, k_2)$ can be obtained by inverting

$$F(\tau; k_1, k_2) = F_{obs}(s; k_1, k_2), \tag{6.10}$$

where the integration over k in equation (6.7) can be calculated numerically.

It should noted, however, that not all the profiles in Figure 6.8 are suitable for this calculation, because low-energy emission is dominated by a thermal component, especially in the LT region and at later times. We thus restrict ourselves to the energy ranges of 12-72, 13-72, and 17-72 keV, respectively, for the three 24 s intervals. The lower bound is the energy above which the power-law component dominates over the thermal component, determined from fits to the spatially integrated spectrum for each interval, as shown in Figure 6.14. Within these energy ranges, separate leg or FP sources rather than a single LT source can be identified in the corresponding image, which is morphologically consistent with the nonthermal nature of emission assumed here. To further minimize the contamination of the thermal emission in our analysis, we have excluded the LT portion of the emission profile in excess of the lowest local minimum (if it exists) between the LT and leg (or FP) sources. An example of this exclusion is illustrated by the hatched region in Figure 6.8*c* for the 19-21 keV profile. This was done by simply replacing the profile values between the LT and the local minimum positions with the value at the minimum.

We calculated $\tau(s; k_1, k_2)$ for every emission profile within the energy ranges mentioned above for the three intervals in Figure 6.8, with photon indexes of $\gamma = 4.46$, 3.97, and 4.23, respectively. From the geometric mean of the column depths obtained at different energies, $\bar{\tau}$, we derived the density profile $n(s) = \mathrm{d}\bar{\tau}(s)/\mathrm{d}s$ for each time interval. The results are shown in Figure 6.15, where we bear in mind that attention should be paid to

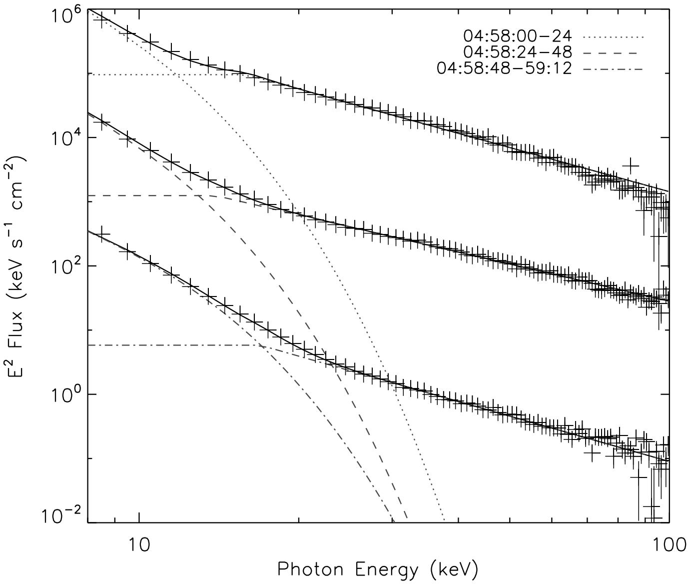

Figure 6.14: Spatially integrated spectra (νF_ν) for the three 24 s time intervals, as indicated in the legend. From the top to the bottom, the second and third spectra are shifted downward by 2 and 4 decades, respectively. The broken lines indicate the thermal and power-law components of the fits to the data, and the solid lines are the sum of the two components. The thermal and power-law components intersect at about 12, 13, and 17 keV, respectively for the three intervals, above which the power-law component dominates (from Liu, W. et al. 2006).

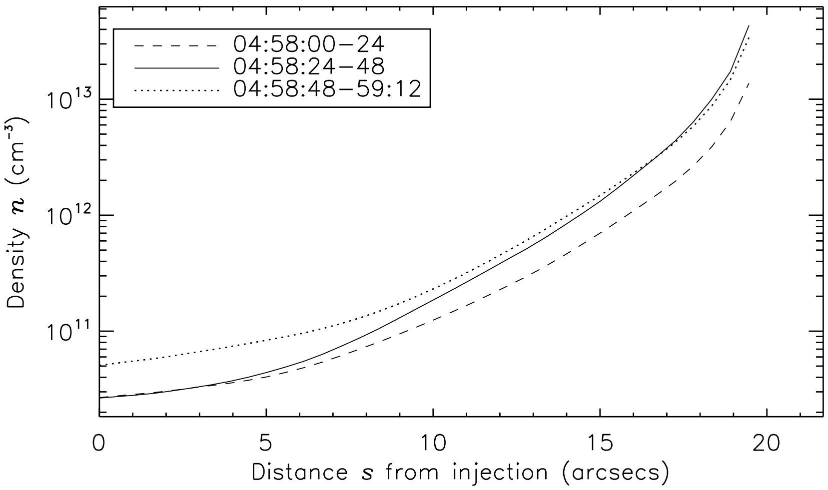

Figure 6.15: Averaged density profiles along the loop inferred from the HXR brightness profiles during the three time intervals (from Liu, W. et al. 2006).

the overall trend rather than the details of the density profile and its variation, because the profile here only spans about 3 times the resolution ($\sim 7''$) and thus is smoothed, making neighboring points not independent. As can be seen, between the first and second intervals, the density increases dramatically in the lower part of the loop, while the density near the LT remains essentially unchanged. The density enhancement then shifts to the LT from the second to the third interval. This indicates a mass flow from the chromosphere to the LT. The density in the whole loop is about doubled over the three intervals, which is roughly consistent with the density change inferred from the emission measure[13] (see Figure 6.11*d*). These results are again compatible with the chromospheric evaporation picture discussed in §6.2.2.

6.4 Summary and Discussion

We have presented in this chapter a study of *RHESSI* images and spectra of the 2003 November 13 M1.7 flare. *RHESSI*'s superior capabilities reveal great details of the HXR source morphology at different energies and its evolution during the impulsive phase. The

---

[13] From 04:58:12 through 04:59:00 UT, the *RHESSI* (*GOES*) emission measure rises by a factor of 5.3 (2.3), which translates to an increase of the density by a factor of 2.3 (1.5), assuming a constant volume.

main findings are as follows.

1. The energy-dependent source morphology in general shows a gradual shift of emission from the LT to the FPs with increasing energies. Over some short integration intervals, emission from the loop legs may dominate at intermediate energies.
2. The emission centroids move toward the LT along the loop during the rising and plateau portions of the impulsive phase. This motion starts at low energies and proceeds to high energies. We estimate the mean velocity of the motion to be hundreds of km s^{-1}, which agrees with the prediction of the hydrodynamic simulations by Fisher et al. (1985c). There are also shorter time scale variations that imply much higher velocities ($\sim 10^3$ km s^{-1}) but we are not certain if they are real because of instrumental limitations.
3. Fits to the spatially integrated *RHESSI* spectra with a thermal plus power-law model reveal a continuous increase of the emission measure (EM) while the temperature does not change significantly. The *GOES* data show a similar trend of the EM but a gradual increase of the temperature.
4. The time derivative of the *GOES* SXR flux is correlated with the *RHESSI* HXR flux, with a peak correlation coefficient of 0.91 at a delay of 12 s, in agreement with the general trend expected from the Neupert effect. However, the correlation between the electron power and the *GOES* derivative is no better than the SXR-HXR correlation.
5. From the observed brightness profiles, we derive the spatial and temporal variation of the plasma density in the loop, assuming a nonthermal thick-target bremsstrahlung model. We find a continuous increase of the density, starting at the FPs and legs and then reaching to the LT. All these results fit into a picture of continuous chromospheric evaporation caused by the deposition of energy of electrons accelerated during the impulsive phase.

Several of the new features of this event (such as the leg emission at intermediate energies) may be common to many solar flares. Expanding the sample of flares of this kind will be very helpful in understanding the underlying physical processes. The new findings reside near the limit of *RHESSI*'s current temporal, spatial, and spectral resolution. As advanced imaging spectroscopy capabilities are being developed and spatial resolution is being improved in the *RHESSI* software (Hurford et al., 2002), it will be critical to obtain the spatially resolved photon spectrum along the loop. This will yield incisive clues to the nature of the moving X-ray sources and relevant energy transport mechanisms and will be useful to check the reality of the short-timescale variations.

There are several important questions that need to be further addressed in future observational and theoretical investigations: (1) What is the nature of the moving X-ray sources? Could they be characterized as thermal emission from the evaporated hot plasma or as nonthermal emission from the precipitating electrons, or a mixture of both? Could they be related to magnetohydrodynamic (MHD) waves or evaporation fronts? (2) What are the roles of different heating agents of the chromosphere; that is, electron beams, thermal conduction, and/or direct heating by turbulence or plasma waves during the impulsive phase?

We have pointed out some of the many physical processes that come into play in answering such questions. Here we describe possible directions for future theoretical studies. We have shown that a more physical test of the Neupert effect between the electron power and the SXR flux derivative does not reveal a better correlation than the usual HXR versus SXR derivative correlation. Although the observed source velocity agrees with those of HD simulations, there are some features that current simulations have not addressed. To answer these questions requires an updated numerical calculation in which one combines the model of particle acceleration and transport with the HD simulation of the atmospheric response to energy deposition to form a unified picture of solar flares. For example, one can use the output electron spectrum from the stochastic particle acceleration model (Hamilton & Petrosian, 1992; Miller et al., 1997; Park et al., 1997; Petrosian & Liu, S., 2004) as the input to the transport and HD codes rather than simply assuming a power-law electron spectrum, as in previous HD simulations. Such a study can shed light on the relative importance of particle beams and thermal conduction in evaporating chromospheric plasma and the roles that MHD waves may play in heating the flaring plasma; in particular, addressing our tentative observation of the fast source motion, which suggests possible presence of MHD waves in the flare loop. A better understanding of their propagation, damping, and excitation mechanisms is necessary for uncovering the energy release process during flares. In the following two chapters, we will present our combined Fokker-Planck and HD simulations along this line of research.

Chapter 7

Modeling Impulsive Phase Solar Flares: a Combined Hydrodynamic and Fokker-Planck Approach

7.1 Introduction

Particle acceleration & transport and the dynamical response of the atmosphere are two of various important processes of energization and dynamics involved in solar flares. As mentioned earlier in Chapter 1, these two processes are in fact coupled and must be studied together in a self-consistent way. Due to the forbidding complexity of the subject, however, people tend to decouple the processes and study one at a time while assuming some simple forms for the others. The past efforts, according to their focus, can be divided into two categories: particle acceleration and/or transport and atmospheric response.

For the former, one of the main streams of study solves the Fokker-Planck equation and and keeps tracking of particle distribution function (while there have been researchers who took the approach of Monte Carlo simulation). For example, by assuming a static atmosphere model, particle transport (including Coulomb collision and magnetic mirroring) was studied by Leach & Petrosian (1981) and was extended to the relativistic regime (including synchrotron loss and pitch angle scattering) by McTiernan & Petrosian (1990).

Other similar studies were performed by MacKinnon & Craig (1991); McClements (1992); Syniavskii & Zharkova (1994); Zharkova et al. (1995). Particle acceleration by turbulence, for instance, was investigated by Hamilton & Petrosian (1992); Miller et al. (1996); Park et al. (1997); Petrosian & Liu, S. (2004) in more recent years.

For the atmospheric response, although the solar atmosphere is magnetized and thus a full magnetohydrodynamic (MHD) description is desired, a majority of efforts were put into numerical hydrodynamic (HD) simulations assuming a fixed magnetic configuration. Because in a low β (magnetic field dominated) environment as in the solar corona, the plasma cannot move across the magnetic field line readily, it is reasonable to assume the material flow follows the magnetic field, which justifies 1D (distance along the magnetic field line) HD models. These models usually assume a simple spectrum of the accelerated particles which are injected at the apex of the loop and the energy deposited by the particles at different distances along the loop is calculated in a simplified way. This energy deposition, which drives fluid dynamics, is the input to the HD code. Such studies include Nagai & Emslie (1984); Fisher et al. (1985c,b,a); Mariska et al. (1989); Gan & Fang (1990) and recent works by Abbett & Hawley (1999); Allred et al. (2005).

From a theoretical point of view, a combined treatment of particle acceleration & transport and the atmospheric response has become progressively desired and doable, based on advances in both directions over two decades and particularly in recent years. Miller has made progress (Miller & Mariska, 2005) in coupling his stochastic particle acceleration code (Miller et al., 1996) with the Naval Research Laboratory (NRL) Solar Flux Tube Model hydrodynamic code (Mariska, Li, & Emslie 1989, hereafter MEL89). Winter & Martens (2006) combine their Monte Carlo simulation of test particle dynamics and a similar HD code. They inject a power-law electron beam at the apex of the loop and tracked the particle transport and the atmospheric response processes.

From an observational point of view, new observations, particularly X-ray images and spectra obtained by the recent *RHESSI* satellite and the previous *Yohkoh* satellite, have posed new challenges and questions to theories. For example, we (Liu, W. et al. 2006) reported an event of chromospheric evaporation imaged by *RHESSI* for the first time. As shown in Chapter 6, during this event, HXR sources at intermediate energies (12-15 keV) were observed to appear at the leg of the flaring loop, in contrast to the commonly observed LT and FP sources at low and high energies, respectively. Such sources shifted from the FPs to the LT as time progressed, and exhibited very high speed ($\sim 10^3$ km s^{-1}) during several short time intervals. Surprisingly, our Neupert (1968) effect test revealed that the electron energy power, a more physically relevant quantity, did not yield a better correlation with the *GOES* SXR flux derivative than the more conventional HXR flux. To fully understand these observations and address the apparent discrepancies, again, requires a coupled treatment of the particle acceleration and transport and the atmospheric response processes.

An accurate treatment of this problem requires a detailed evaluation of the heating rate by nonthermal electrons, which is a key input to flare HD simulations. Previous works in this regard suffer from two major shortcomings. (1) The first is that the calculation of the energy deposition is based on approximate analytical solutions (e.g., Brown, 1973; Emslie, 1978). This can be remedied by a combined particle and HD simulation, with the inclusion of a full Fokker-Planck treatment of the electron transport. (2) The other drawback is the simple, non-realistic, form of the injected electron spectrum used, which was usually assumed to be some form of power-law distribution that makes the analytical solution tractable. Fisher et al. (1985c), for example, assumed a power-law spectrum with an index of $\delta = 4$ and a sharp cutoff at energy $E_1 = 20\,\mathrm{keV}$ (i.e., no electrons present below E_1). MEL89 introduced a "soft" cutoff, below which the spectrum is a power-law with a positive index of $\delta = 2$. Recently, Allred et al. (2005)[1]. used the "more realistic" broken power-law electron spectrum derived from *RHESSI* HXR observations (Holman et al. 2003). As we will show later, the heating rate is sensitive to the electron spectrum and thus use of inaccurate spectrum would make the HD result deviate from reality significantly. On the basis of the SA model, Petrosian & Liu, S. (2004) have provided a more realistic electron spectrum that has a continuous form from the background thermal distribution at low energies to nonthermal distribution at high energies. We use such an spectrum in the work described below. We will see that the low energy electrons actually play an important role in heating (via collision and conduction) and in affecting the subsequent hydrodynamical process.

In this chapter, we present a review of the Fokker-Planck modeling and show it can be combined with a HD simulation of the atmospheric response during the impulsive phase (§7.2). The former component uses the unified code of particle acceleration, transport, and bremsstrahlung raditaion (Petrosian et al., 2001). The latter uses the NRL Solar Flux

---

[1] They also improved the heating rate calculation by adopting the technique of Hawley & Fisher (1994) to include the variation of hydrogen ionization state and by calculating radiative transfer and XEUV heating.

Tube Model code (MEL89). We obtained the spatial distribution and temporal evolution of the resulting HXRs and SXRs, and check them against available *RHESSI* observations (e.g., Liu, W. et al. 2006; Sui et al. 2006). Result from some model calculations are presented in and §7.3. We summarize the major findings of this chapter and draw conclusions in §7.4.

7.2 Simulation Models

7.2.1 Stochastic Acceleration Model

Here we briefly summarize the acceleration model used in this study, which was adopted from Petrosian & Liu, S. (2004, hereafter PL04). We focus on acceleration by waves that propagate parallel to the background magnetic field.

The Fokker-Planck Equation

Let us rewrite the Fokker-Planck (F-P) equation that governs electron acceleration (equation 1.1)

$$\frac{\partial f_{\rm ac}}{\partial t} = \frac{\partial}{\partial E}\left[D(E)\frac{\partial f_{\rm ac}}{\partial E}\right] + \frac{\partial}{\partial E}\{[A(E) - \dot{E}_L]f_{\rm ac}\} - \frac{f_{\rm ac}}{T_{\rm esc}(E)} + Q(E)\,. \tag{7.1}$$

where $f_{\rm ac} \equiv f_{\rm ac}(t, E)$ is the electron distribution function (in units of electrons $\rm cm^{-3}\,keV^{-1}$, integrated over all pitch angles; the subscript "ac" denotes acceleration region, cf. the $f(E, s, \mu)$ in the transport code), $E = \gamma - 1$ (γ being the Lorentz factor) is the electron kinetic energy in units of $m_e c^2$ (m_e is the electron mass), $D(E)$ and $A(E)$ are the energy diffusion and systematic acceleration coefficients, $T_{\rm esc}$ is the particle escape time, $Q(E)$ is the total injection flux of particles into the acceleration region that acts as source term in the equation.

$$\dot{E}_L = \dot{E}_{\rm Coul} + \dot{E}_{\rm synch} \tag{7.2}$$

is the absolute value of the net systematic energy loss rate, which is a combination of Coulomb loss (assuming a cold background plasma)

$$\dot{E}_{\rm Coul} = 4\pi r_0^2 \ln\Lambda c n_e/\beta\,, \tag{7.3}$$

and synchrotron loss

$$\dot{E}_{\rm synch} = 4r_0^2 B^2 \beta^2 \gamma^2 / 9 m_e c \,, \tag{7.4}$$

where $\beta = v/c$, n_e is the electron number density, $r_0 = e^2/m_e c^2 = 2.8 \times 10^{-13}$ cm is classical electron radius, $\ln \Lambda = 20$ (good for coronal conditions, Leach 1984) is the Coulomb logarithm, and B is the background magnetic field. Note equation (7.4) is valid only for isotropic pitch angle distribution, which is assumed to be the case in the acceleration region because of strong scattering of particles by turbulence.

In order to solve the F-P equation and keep tracking the evolution of the distribution function $f_{\rm ac}(t, E)$, one needs to know all the terms in the equation. Since the form of the energy loss rates are well known and the injection flux $Q(E)$ (say, thermal or Maxwellian distribution) is to be assumed by specific models, the central task left is to determine the diffusion coefficient $D(E)$, the direct acceleration rate $A(E)$, and the escape time $T_{\rm esc}$, which we describe as follows.

Dispersion Relation and Resonance Condition

In general, plasma waves can be described by their dispersion relations, and when particles are accelerated by turbulence, the wave-particle interaction is determined by the resonance condition.

We assume a fully ionized H and ^{4}He plasma with the relative abundance of electron/proton/α-particle = 1/0.84/0.08. The **dispersion relation** for parallel propogating waves in such a plasma is:

$$\frac{k^2}{\omega^2} = 1 - \frac{\alpha^2}{\omega} \left[\frac{1}{\omega - 1} + \frac{(1 - 2Y_{\rm He})\delta}{\omega + \delta} + \frac{Y_{\rm He}\delta}{\omega + \delta/2} \right] , \tag{7.5}$$

where ω *is the wave frequency in units of the nonrelativistic electron gyrofrequency* $\Omega_e = (eB_0)/(m_e c)$ (e is the electron charge and B_0 the large-scale magnetic field), k *is the wavenumber in units of* Ω_e/c, $Y_{\rm He} = 0.08$ is the ^{4}He abundance, the *plasma parameter* α and the electron-to-proton mass ratio δ are given by

$$\alpha = \omega_{pe}/\Omega_e = 3.2 (n_e / 10^{10} {\rm cm}^{-3})^{1/2} (B_0 / 100\,{\rm G})^{-1} \quad \text{and} \quad \delta = m_e/m_p \,, \tag{7.6}$$

where $\omega_{pi} = (4\pi n_e e^2/m_e)^{1/2}$ is the electron plasma frequency and m_p is the proton mass. From this dispersion relation, we have five distinct wave modes (branches): electromagnetic wave branch (EM), electron-cyclotron branch (EC), modified proton-cyclotron branch (PC'), ^{4}He-cyclotron branch (HeC), and a second electromagnetic wave branch (EM') (see PL04, Fig. 11, for details).

Via the **resonance wave-particle interaction**, energy can be transfered from particles to waves and vice versa (Dung & Petrosian, 1994). For a particle with a velocity βc and a pitch angle cosine μ the resonance condition can be written as

$$\omega - k_{||}\beta\mu = \frac{n\omega_i}{\gamma}, \tag{7.7}$$

where n is the harmonic number of the gyrofrequency (not particle number density), $k_{||}$ is the parallel component of the wave vector, $\omega_i = q_i m_e / e m_i$ is the particle gyrofrequency in units of Ω_e. In our case of electron acceleration by parallel waves, $k_{||} = k$, $n = -1$, $\omega_e = -1$ (while $\omega_p = m_e/m_p = \delta$ for protons), and the resonance condition reduces to

$$\omega - k\beta\mu = \frac{1}{\gamma}. \tag{7.8}$$

It appears as a straight line in the k–ω plot, with the $v = \beta\mu$ being the slope and $1/\gamma$ being the intercept. For an electron with a given velocity and pitch angle, in order to determine how it is accelerated by waves, one must first need to determine with which wave branch(es) (see PL04, Fig. 11) and at what frequency (or wave number) this straight line intersect. That is, one needs to find the roots k_j and their corresponding ω_j ($j = 1, ..., N$) of the combined nonlinear equations (7.5) and (7.8), which is done numerically in the SA code. Because of the complexity of the dispersion relation and the large dynamic range of the wavenumber, it is not a trivial task to accurately find the roots. For different particles, say, electrons and protons, their roots are located on different branches, and thus they are accelerated at different rates (see PL04, e.g., Fig. 12 for a comparison).

Turbulence Spectrum and Fokker-Planck Coefficients

To determine how much energy a particle can gain from its interaction with waves, one also needs to know the **energy spectrum of the turbulence**. Following PL04, we assume a turbulence spectrum of a broken power-law with three indexes q, $q_{\rm l}$ and $q_{\rm h}$ and two critical wavenumbers $k_{\rm min}$ and $k_{\rm max}$,

$$\mathcal{E}(k) = (q-1)\mathcal{E}_0/k_{\rm min}\begin{cases} (k/k_{\rm min})^{q_{\rm l}}, & \text{for } k < k_{\rm min};\\ (k/k_{\rm min})^{-q}, & \text{for } k_{\rm min} < k < k_{\rm max};\\ (k_{\rm max}/k_{\rm min})^{-q}(k/k_{\rm max})^{-q_{\rm h}}, & \text{for } k > k_{\rm max}, \end{cases} \tag{7.9}$$

where we choose $q_{\rm l} = 2(> 0)$, $q = 1.7$ is the Kolmogorov value, and $q_{\rm h} = 4$ is a typical index for waves subject to strong damping (Vestuto et al., 2003). The cutoff at high wavenumber $k_{\rm max}$ is assumed to be caused by, say, thermal damping. Following Liu, S. et al. (2006), we define

$$\bar{\mathcal{E}}_0 \equiv (q-1)\mathcal{E}_0 k_{\rm min}^{q-1} \tag{7.10}$$

and a characteristic interaction rate τ_p (or its inverse, the characteristic timescale, PL04) that is an indicator of the turbulence intensity

$$\tau_p^{-1} = \frac{\pi}{2}\Omega_{\rm e}\left(\frac{\mathcal{E}_0}{B_0^2/8\pi}\right)(q-1)k_{\rm min}^{q-1} = \frac{\pi}{2}\Omega_{\rm e}\left(\frac{\bar{\mathcal{E}}_0}{B_0^2/8\pi}\right). \tag{7.11}$$

Once the resonance interactions are found and the turbulence spectrum is given, one can proceed to evaluate the **Fokker-Planck coefficients**:

$$D_{ab} = \frac{(\mu^{-2}-1)}{\tau_p\gamma^2}\sum_{j=1}^{N}\chi(k_j)\begin{cases} \mu\mu(1-x_j)^2, & \text{for } ab = \mu\mu;\\ \mu p x_j(1-x_j), & \text{for } ab = \mu p \,\text{or}\, p\mu;\\ p^2 x_j^2, & \text{for } ab = pp, \end{cases} \tag{7.12}$$

where

$$\chi(k_j) = \frac{\mathcal{E}(k_j)/\bar{\mathcal{E}}_0}{|\beta\mu - \beta_g(k_j)|} \qquad \text{and} \qquad x_j = \mu\omega_j/\beta k_j\,, \tag{7.13}$$

p is the particle momentum, $\beta_g = d\omega/dk$ is the wave group velocity, and the summation over j is for all the possible resonance interactions (the roots found above). Note the F-P coefficients are symmetric, $D_{p\mu} = D_{\mu p}$.

F-P Equation Coefficients and Timescales

Finally, we are ready to derive the coefficients in the Fokker-Planck equation. Let us first define two ratios of the F-P coefficients:

$$R_1(\mu,p) = \frac{D_{pp}}{p^2 D_{\mu\mu}}\,, \quad R_2(\mu,p) = \frac{D_{p\mu}}{p D_{\mu\mu}}\,. \tag{7.14}$$

We also define the pitch angle averaged acceleration and scattering times (PL04, cf., Liu, S., Petrosian, & Mason 2006):

$$\begin{aligned}
\tau_{\rm ac} &= \frac{p^2}{\bar{D}_{pp}} = \frac{2p^2}{\int_{-1}^{1} d\mu (D_{pp} - D_{p\mu}^2/D_{\mu\mu})} = \frac{2}{\int_{-1}^{1} d\mu D_{\mu\mu}(R_1 - R_2^2)}\,, && (7.15)\\
\tau_{\rm sc} &= \frac{1}{2}\int_{-1}^{1} d\mu \frac{(1-\mu^2)^2}{D_{\mu\mu}} \ll L/v\,, \quad \bar{D}_{pp} \equiv \frac{1}{2}\int_{-1}^{1} d\mu (D_{pp} - D_{p\mu}^2/D_{\mu\mu})\,, && (7.16)
\end{aligned}$$

where the factor $2 = \int_{-1}^{1} d\mu$ and L is the size of the acceleration region. Note that we assume isotropic pitch angle distribution here and the R_2^2 term in equation 7.15 should be dropped if isotropy is not satisfied (e.g., Liu, S., Petrosian, & Mason 2006). Accordingly, the diffusion coefficient[2] (Petrosian, 2001) and the direct acceleration rate[3] can be written as

$$\begin{aligned}
D(E) &= \beta^2 \bar{D}_{pp} = \frac{\beta^2}{2}\int_{-1}^{1} d\mu (D_{pp} - D_{p\mu}^2/D_{\mu\mu}) && (7.17)\\
&= \frac{\beta^2 p^2}{\tau_{\rm ac}} = \frac{\beta^2 p^2}{2}\int_{-1}^{1} d\mu D_{\mu\mu}(R_1 - R_2^2)\,, && (7.18)\\
A(E) &= \frac{1}{\beta\gamma^2}\frac{d\beta\gamma^2 D(E)}{dE} - \frac{d}{dE}D(E) = \frac{D(E)}{E}\frac{2-\gamma^{-2}}{1+\gamma^{-1}}\,. && (7.19)
\end{aligned}$$

We also obtain the escape time that combines nonrelativistic and extreme relativistic cases

$$T_{\rm esc} = \frac{L}{\sqrt{2}v}\left(1 + \frac{\sqrt{2}L}{v\tau_{\rm sc}}\right)\,, \qquad (7.20)$$

and define the direct acceleration time, $\tau_a = E/A(E)$.

Now that all the coefficients, including $D(E)$, $A(E)$, and $T_{\rm esc}$ in the F-P equation have been evaluated, the equation can be solved numerically by the Chang-Cooper method (Park & Petrosian, 1996). In this particular study, we assume a steady state solution (the acceleration code is capable of solving the time-dependent F-P equation though), because the transport code is of steady state and we need a self-consistent treatment throughout. Once the electron spectrum, $f_{\rm ac}(E)$, in the acceleration region is obtained, we evaluate

---

[2] There is a typo in Eq. (12) of PL04, where E^2 should be replaced with $\beta^2 p^2$, but the calculation there was actually correct.

[3] Subtracting the $dD(E)/dE$ term results from the different ways of writing the F-P equation, see equation 7.1 here and Eq. (10) of PL04.

the *escaping electron flux*

$$F_{\mathrm{esc}}(E) = \frac{f_{\mathrm{ac}}(E)}{T_{\mathrm{esc}}(E)} L\,, \tag{7.21}$$

which is then passed to the transport code as an injection. We can define the ratio between the escape flux and the LT flux ($v f_{\mathrm{ac}}$):

$$R_{\mathrm{esc}} = \frac{F_{\mathrm{esc}}}{v f_{\mathrm{ac}}} = \frac{L}{v T_{\mathrm{esc}}} = \sqrt{2}\left(1 + \frac{\sqrt{2}L}{v\tau_{\mathrm{sc}}}\right)^{-1}\,. \tag{7.22}$$

The equivalent *thick-target electron flux* (Petrosian & Donaghy 1999; PL04) is calculated by:

$$F_{\mathrm{thick}}(E) = \frac{\beta c}{\dot{E}_L} \int_E^{\infty} \frac{f_{\mathrm{ac}}(E')}{T_{\mathrm{esc}}(E')} dE'. \tag{7.23}$$

7.2.2 Particle Transport and Radiation Model

The next step is to run the **transport code** that follows the electron distribution as the electrons stream down the newly reconnected magnetic field line and travel through different layers of the atmosphere. In order to run the transport code, we need the knowledge of two things. The first is the energy and pitch angle distribution of the injected particles, which is given above as the escaping electron flux (assumed isotropic in the forward direction) by the acceleration code. The second is the background density and abundance distribution along the loop. Here we assume a fully ionized, pure hydrogen plasma,[4] whose distribution is taken from the result of the HD code (see below).

The transport code solves the fully relativistic, steady-state, F-P equation (see McTiernan & Petrosian, 1990, Eq. 1), which includes Coulomb energy loss (no energy diffusion)[5] and pitch angle diffusion, synchrotron energy loss and pitch angle diffusion, as well as magnetic field convergence. Following McTiernan (1989), we neglect the reverse current (Syniavskii & Zharkova, 1994; Zharkova et al., 1995), which is a good approximation if the electron flux is sufficiently small; we hope to include this effect in the future to achieve

---

[4] Although this assumption is not self-consistent with the abundance assumed in the acceleration code, it simplifies the calculation of the Coulomb logarithm (assume $\ln \Lambda = 20$) which is needed for evaluating the Coulomb loss. This assumption will only affect the normalization in the resulting electron flux as well as the photon emission very slightly. Again, this makes room for future improvement.

[5] We again assume a cold background plasma here, which is a good approximation for solar flares, particularly because accelerated particles lose most of their energy in the cold chromosphere. However, in principle, particles could gain energy as well by colliding with background particles when their velocities are smaller than those of the background ones, and thus Coulomb diffusion in energy should be included in the future (see more discussion in Chapter 10).

a more self-consistent treatment. The variable[6] to be solved is the electron flux spectrum $F(E, s, \mu)$ as a function of energy E, distance s from the injection point (at the boundary of the acceleration region), and pitch angle cosine μ. It is evaluated as

$$F(E, s, \mu) = \frac{1}{A_0} \int c\beta f(E, s, \mu) dA(s) = c\beta f(E, s, \mu) \frac{A(s)}{A_0} \tag{7.24}$$

where $f(E, s, \mu)$ is the density distribution function in units of electrons $\mathrm{cm}^{-3}\,\mathrm{keV}^{-1}\mathrm{sr}^{-1}$ (cf. $f_{\mathrm{ac}}(E)$ in the acceleration code which is integrated over all pitch angles), and we integrate the differential electron flux $c\beta f(E, s, \mu)$ over the cross-sectional area $A(s)$ of the loop and then divide it by a constant equivalent area A_0. Thus $F(E, s, \mu)$ (a real physical flux) has units of electrons $\mathrm{s}^{-1}\,\mathrm{cm}^{-2}\,\mathrm{keV}^{-1}\mathrm{sr}^{-1}$ (in the code, $\mathrm{keV}^{-1}\mathrm{sr}^{-1}$ is replaced with per $m_e c^2$ per unit pitch angle cosine). The (angle integrated) injection from the acceleration code serves as the boundary condition at $s = 0$, namely,

$$F(E, s, \mu)|_{s=0} = F_{\mathrm{esc}}(E)/2\,, \tag{7.25}$$

where the factor $2 = \int_{-1}^{1} d\mu = \cos 0 - \cos \pi$ is the range of the pitch angle cosine. During the steady state calculation, we also set a symmetric boundary condition at the injection site, where particles running away from the domain is reflected back to the loop with identical energy but opposite pitch angle cosine.

Once we know the electron distribution at all the depths, we calculate the thin-target nonthermal **bremsstrahlung radiation** intensity, $I(\epsilon, s)$, as a function of photon energy ϵ and distance s. $I(\epsilon, s)$, emitted by a unit length along the loop, is integrated over the loop cross-sectional area $A(s)$ and has units of photons $\mathrm{s}^{-1}\,\mathrm{cm}^{-1}\,\mathrm{keV}^{-1}$,

$$I(\epsilon, s) = A_0 \int_{\epsilon}^{\infty} dE \left[n_p(s) \frac{d\sigma}{d\epsilon} \int_{-1}^{1} d\mu F(E, s, \mu) \right]\,, \tag{7.26}$$

where $n_p(s)$ is the proton number density[7] ($n_p = n_e$ in our case) and $d\sigma/d\epsilon$ is the angle-averaged[8] differential bremsstrahlung cross-section given by Koch & Motz (1959). The

---

[6] The code actually solves for $F(E, s, \mu)/\beta^2 = cf(E, s, \mu)A(s)/(\beta A_0) \equiv c\Phi A(s)/A_0$, where Φ is the same as that defined in (McTiernan & Petrosian, 1990).

[7] In general, n_p should include H^+ as well as protons in He^{++} and other ions.

[8] Angle-dependent radiation will be included in the future (see Chapter 10)

looptop (LT) emission is evaluated as

$$I_{\rm LT}(\epsilon) = A_0 \int_{\epsilon}^{\infty} dE \left[n_p(0) \frac{d\sigma}{d\epsilon} \right] c\beta f_{\rm ac}(E) \,, \tag{7.27}$$

where $n_p(0) = n_p(s)|_{s=0} = n_{p\,,\rm ac}$ is the proton density and $c\beta f_{\rm ac}(E)$ is the angle-integrated electron flux, both in the acceleration region. The equivalent footpoint (FP) photon spectrum is calculated by averaging the intensity below the transition region, located at distance of $s = s_{tr}$

$$I_{\rm FP}(\epsilon) = \frac{1}{s_{max} - s_{tr}} \int_{s_{tr}}^{s_{max}} I(\epsilon, s) ds \,. \tag{7.28}$$

Both $I_{\rm LT}(\epsilon)$ and $I_{\rm FP}(\epsilon)$ can be compared with HXR observations, say, obtained by the *Yohkoh* and *RHESSI* satellites. If the coronal density is negligibly tenuous and if the chromospheric density is sufficiently high, $(s_{max} - s_{tr}) I_{\rm FP}(\epsilon)$ would approach the thick-target spectrum

$$I_{\rm thick}(\epsilon) = \int_0^{\infty} I(\epsilon, N) dN \,, \tag{7.29}$$

where $dN = n_p ds$ is the column depth.

7.2.3 NRL Hydrodynamic Model

The NRL Solar Flux Tube Model (MEL89) assumes a two-fluid plasma composed of electrons and ions that can only move along the magnetic field in a flux tube, due to the line-tying condition in a low-β environment. The user-specified geometry (e.g., vertical or semi-circular) of the tube is characterized by $A(s)$, the cross-sectional area of the tube as a function of distance s, and $g(s)$, the component of the gravitational acceleration in the direction of the magnetic field. The model solves the one-dimensional equations of mass, momentum, and energy conservation,

$$\frac{\partial \rho}{\partial t} + \frac{1}{A(s)} \frac{\partial}{\partial s} [A(s) \rho v] = 0, \tag{7.30}$$

$$\frac{\partial}{\partial t}(\rho v) + \frac{1}{A(s)} \frac{\partial}{\partial s} [\rho v^2 A(s)] = \rho g - \frac{\partial P}{\partial s}, \tag{7.31}$$

$$\frac{\partial U}{\partial t} + \frac{1}{A(s)} \left\{ \frac{\partial}{\partial s} A(s) \left[(E + P) v - \kappa_e \frac{\partial T_e}{\partial s} - \kappa_i \frac{\partial T_i}{\partial s} \right] \right\} = \rho v g - L_{\rm rad} + S, \tag{7.32}$$

$$\frac{\partial}{\partial t}\left(\frac{P_e}{\gamma-1}\right)+\frac{1}{A(s)}\left[\frac{\partial}{\partial s}A(s)\left(\frac{\gamma v P_e}{\gamma-1}-\kappa_e\frac{\partial T_e}{\partial s}\right)\right]=-L_{\rm rad}+S+\gamma_{\rm eq}(T_i-T_e), \quad (7.33)$$

where ρ is the mass density, v is the fluid velocity, and $P = P_e + P_i$ is the total pressure, a combination of the electron pressure P_e and the ion pressure P_i, which are given by the equations of state

$$P_e = n_e k_{\rm B} T_e \quad \text{and} \quad P_i = n_i k_{\rm B} T_i \,, \quad (7.34)$$

where $k_{\rm B}$ is the Boltzmann constant, n_e and T_e (n_i and T_i) are the electron (ion) number density and temperature, respectively. Here, the combined kinetic and thermal energy is given by

$$U = \frac{1}{2}\rho v^2 + \frac{P}{\gamma-1}\,, \quad (7.35)$$

where $\gamma = 5/3$ is the ratio of specific heats; κ_e and κ_i are the electron and ion thermal conductivities, respectively,

$$\kappa_e = 1.1\times10^{-6}T_e^{5/2}\,, \quad \kappa_i = \kappa_e/25\,; \quad (7.36)$$

$L_{\rm rad} = n_e n_p \Phi(T_e)$ is the radiative energy loss rate (MEL89), where n_p is the hydrogen number density and $\Phi(T_e)$ is the optically-thin radiative loss function; S is the heating rate,

$$S = S_0 + S_e\,, \quad (7.37)$$

where S_0 is the background heating, set to be $8.31\times10^{-3}\,{\rm ergs\,s^{-1}\,cm^{-3}}$ (MEL89), presumably caused by coronal heating in the quiet sun active region, and S_e is heating by nonthermal electrons, which will be provided by the Fokker-Planck transport model in this study. $\gamma_{\rm eq} = 1.4\times10^{-17}n_e^2T_e^{-3/2}$ is the rate coefficient for electron-ion temperature equilibration; in this particular study, we assume $T_e = T_i$ and thus the $\gamma_{\rm eq}(T_i - T_e)$ term vanishes. We also assume that the plasma consists of fully ionized hydrogen. The electron and ion number densities, n_e and n_i, are then related to the mass density by

$$n_e = \frac{\rho Z}{\mu m_p(1+Z)} \quad \text{and} \quad n_i = n_e/Z\,, \quad (7.38)$$

where $Z = 1.0$ is the mean ionic charge and $\mu = 0.5$ (in units of proton masses m_p) is the mean mass[9] per particle.

---

[9] In the original model of MEL89, the plasma consists of fully ionized hydrogen and helium with the helium assumed to be 6.3% of the hydrogen by number density, corresponding to $Z = 1.059$ and $\mu = 0.5724$.

The hydrodynamic equations are solved by a finite difference scheme. The code uses time-step splitting, in which the hydrodynamic calculation takes place first, using the Flux Corrected Transport (FCT) method, and then the implicit part of the code takes care of thermal conduction and radiation. Note that there is no physical or artificial viscosity in this model, but the FCT achieves similar effects to stablize the calculation as artificial viscosity usually does and make conservative physical quantities actually conserved in the meantime. Because of lacking of viscosity, hydrodynamic waves, once excited, can exist for a long duration with little or no damping, as we will see in Chapter 9. A reflective (or symmetric) boundary condition is imposed at both the top (loop apex) and bottom (deep into the chromosphere) boundaries. Details of the numerical scheme and the model parameters can be found in Mariska et al. (1982) and MEL89.

7.2.4 Combining the Particle and Hydrodynamic Codes

We now describe how we combine the flare particle code and the NRL HD code. Since the two codes are independent and mature on their own rights, there is no need to rewrite a whole new code that includes functionality of both. Rather, one would like to have a wrapper that can coordinate between the two codes and have them communicate while running independently on each side. By doing so, one can keep each code essentially intact and self-contained. Fortunately this is possible because the communication between the two codes could be as simple as passing back and forth a 1D array. As we noted above, in order to determine the electron distribution at each depth, the transport code needs the background density profile that can be provided by the HD code. On the other hand, the HD code needs to know how much energy[10] is deposited by the accelerated electrons as a function of distance, which can be obtained from the particle transport calculation. Then this energy deposition rate (or electron heating rate) will work as a driver for the hydrodynamics, which will change the density distribution, which, in turn, will be fed back to the particle code. We detail below how to implement this approach.

This minor difference would only affect the mass normalization here slightly.

[10] We neglect the momentum exchange between accelerated electrons and the background particle, which is a valid approximation because of electron's small mass. See Chapter 10 for a discussion on future work.

Electron Heating Rate and Thermal Conduction

As we noted in §7.1, the **heating rate** is critical in HD simulations, but was not calculated properly in previous works. Here we improve on this by calculating the electron energy loss directly from the electron distribution obtained from the transport calculation, with two equivalent approaches.

The electron heating rate S_e (in units of $\mathrm{ergs\,s^{-1}\,cm^{-3}}$), as defined in the HD equations (see equation 7.37), is equal to the energy deposition rate in a unit volume by fast electrons. It can be evaluate from the energy loss rate $\dot{E}_{\mathrm{Coul}}$ (due to Coulomb collisions) as

$$S_e(s) = \int_{E_{\min}}^{E_{\max}} dE \int_{-1}^{1} f(E, s, \mu) \dot{E}_{\mathrm{Coul}} d\mu \,, \tag{7.39}$$

where $[E_{\min}, E_{\max}]$ is the range of the energy bins used, $\dot{E}_{\mathrm{Coul}}$ is given by equation (7.3), the electron distribution function $f(E, s, \mu)$ can be obtained from the corresponding electron flux $F(E, s, \mu)$ via equation (7.24).

Alternatively, one can calculate the (net downward) energy flux carried by the electrons

$$F_{\mathrm{erg}}(s) = \frac{A_0}{A(s)} \int_{E_{\min}}^{E_{\max}} dE \left[\int_0^1 \mu E F(E, s, \mu) d\mu - \int_{-1}^{0} \mu E F(E, s, \mu) d\mu \right] , \tag{7.40}$$

and differentiate it to obtain the net energy gain in a unit volume

$$S_e(s) = dF_{\mathrm{erg}}(s)/ds \,, \tag{7.41}$$

where $\mu E F(E, s, \mu)$ is the energy flux projected (by the factor μ) along the loop the factor $A_0/A(s)$ accounts for the variation of the cross-sectional area. This approach is, in practice, equivalent to the above one (equation 7.39), because, in the deka keV to hundreds of keV energy range, the combination of synchrotron loss and bremsstrahlung HXRs only constitutes a negligible fraction ($\lesssim 10^{-4}$) of the total energy loss due to Coulomb collisions. We took the second approach in our simulation, and let the transport code calculate the heating rate and pass it to the HD code.

As to **thermal conduction**, we use the usual Spitzer conductivity without suppression, unlike what we do for the decay phase (see Chapter 9). This is because, during the impulsive phase, in addition to direct turbulence heating (believed to be present in the turbulence or acceleration region), there is significant acceleration taking place. The energized particles can escape and carry energy away from the acceleration region, which serves as a energy “conduction” channel. In contrast, during the decay phase, acceleration already subsides, and heating and suppression of conduction due to turbulence is the main energization agent. In addition, strong turbulence during the impulsive phase might act differently from weak turbulence in the decay phase. These arguments, however, are speculative and more in-depth investigation is required in the future.

Code Communication Timescale

Ideally, the flare particle code and the hydrodynamic code should work interactively and communicate at every time step during the time advance. Unfortunately, although we have a time-dependent acceleration code, the transport code is of steady state and it would require extensive programming to upgrade it to a time-dependent version. However, fortunately, under certain assumptions, the required programming work can be significantly simplified and reasonably good accuracy can be achieved.

Our approach is to have the two codes communicate at certain intervals. Each communication consists of two parts. The first part is that the HD code passes the density profile to the flare particle code. Then the flare code runs a full *steady state* calculation from acceleration of particles, to the particle transport and bremsstrahlung radiation. Then it comes the second part of the communication, in which the flare code passes the electron heating rate (energy deposition) to the HD code. The HD code then runs its own time-dependent calculation until the next communication. Then two questions arise: (1) what is the optimum timescale for the two code to communicate; (2) what heating rate function should be provided to the HD code between adjacent communications. We address these below.

(1) The **communication timescale** should not be shorter than that on which a steady state particle transport calculation is valid. The timescale in the electron transport process can be expressed in terms of the lifetime τ_e of electrons. It is determined by the energy loss (mainly due to Coulomb collisions for nonrelativistic electrons) time in a given magnetic loop geometry and the atmospheric condition. For a low-energy electron, the Coulomb loss time is relatively short, but it would take relatively longer time for the electron to reach the dense transition region where it can lose most of its energy. The opposite is true for a high-energy electron. A combination of these factors results in the lifetime $\tau_e(E)$, which depends on the electron energy E and the atmospheric structure. For example, Petrosian

(1973, see Eq. (9) and Fig. 1 there) assumed a gravitationally stratified atmosphere with a scale height of $H = kT/mg$, and obtained $\tau_e(E)$ as a function of E for nonrelativistic electrons. $\tau_e(E)$ has a maximum (at some critical energy $E_{\rm cr}$) which is (Petrosian, 1973, Eq. 11)

$$\tau_{e,\,\max}(H, n_e) \approx 0.07\,\sec \left(\frac{H}{10^8\,\rm cm}\right) \left(\frac{n_e H}{10^{18}\,\rm cm^{-2}}\right)^{-1/4}, \tag{7.42}$$

where n_e is the electron number density at the injection site. For timescales greater than $\tau_{e,\,\max}$, it is reasonable to assume a steady state solution for the F-P transport equation. To be conservative, if we take the coronal temperature to be $T = 10^6$ K and the density at the acceleration region to be $n_e = 10^{10}\,\rm cm^{-3}$, we obtain $\tau_{e,\,\max} = 1.5$ s at $E_{\rm cr} = 65$ keV. On the other hand, if one assumes a constant coronal density of $n_e = 10^{10}\,\rm cm^{-3}$ and an exponential rise of density (with a scale height of $H = 603\,\rm km$, given $T \approx 10^4\,\rm K$ in the chromosphere) starting at the transition region, then the required time is

$$t_e = l/v + \tau_{e,\max}(H, n_e) \lesssim 0.1\,\sec \left(\frac{l}{10^9\,\rm cm}\right) \left(\frac{E}{25\,\rm keV}\right)^{-1/2} + 0.05\,\sec\,, \tag{7.43}$$

where l is the length of the coronal portion of the loop, the electron velocity v is evaluated with the non-relativistic approximation, and $\tau_{e,\max}(H, n_e) = 0.05\,\rm s$ (at $E_{\rm cr} = 6.5$ keV) is obtained from equation (7.42). For a loop of $l = 10^4\,\rm km$ and an electron of $E = 25\,\rm keV$, such a timescale is $t_e \lesssim 0.15\,\rm s$. We therefore take a conservative $\Delta t = 2\,\rm s$ as the time interval for the two codes to communicate.

(2) Since the $\Delta t = 2\,\rm s$ interval is much shorter than the HD response time[11], **between adjacent communications**, we assume that the energy deposition by nonthermal electrons as a function of column depth $S_e(N)$ (in units of $\rm ergs\,s^{-1}\,cm^2$, where $\rm cm^2$ means per unit column depth) is constant in time. This is true (i) if we neglect energy losses (synchrotron and bremsstrahlung) other than Coulomb loss, which is valid for X-ray producing electrons (energy range from tens of keV to hundreds of keV); and (ii) if the loop cross-sectional area $A(s)$ is a constant, i.e., a uniform loop. We have made the code meet these two conditions. Then the spatial distribution of the heating rate $S_e(s,t)$ varies with time only according to the redistribution of density and the variation of column depth as a function of distance,

$$S_e(s,t) = S_e(N) n_e(s,t)\,. \tag{7.44}$$

---

[11] This can be characterized by the sound travel time, which is about 60 s in a coronal loop of 10^4 km long with a temperature of $T = 10^6\,\rm K$ (sound speed $c_s = 166\,\rm km\,s^{-1}$).

This means that at each time t, for a given distance s, we first identify its corresponding column depth $N(s,t) = \int_0^s n_e(s,t)ds$, then use this $N(s,t)$ to evaluate the heating rate $S_e(N)$, and finally multiply $S_e(N)$ with the local density to convert the units from $\mathrm{ergs\,s^{-1}\,cm^2}$ to $\mathrm{ergs\,s^{-1}\,cm^{-1}}$ (because $S_e(s)ds = S_e(N)dN$ and $dN = n_e ds$).

Summary of Communication: Task Flow Chart

Figure 7.1: Task flow chart for Particle & HD code communication

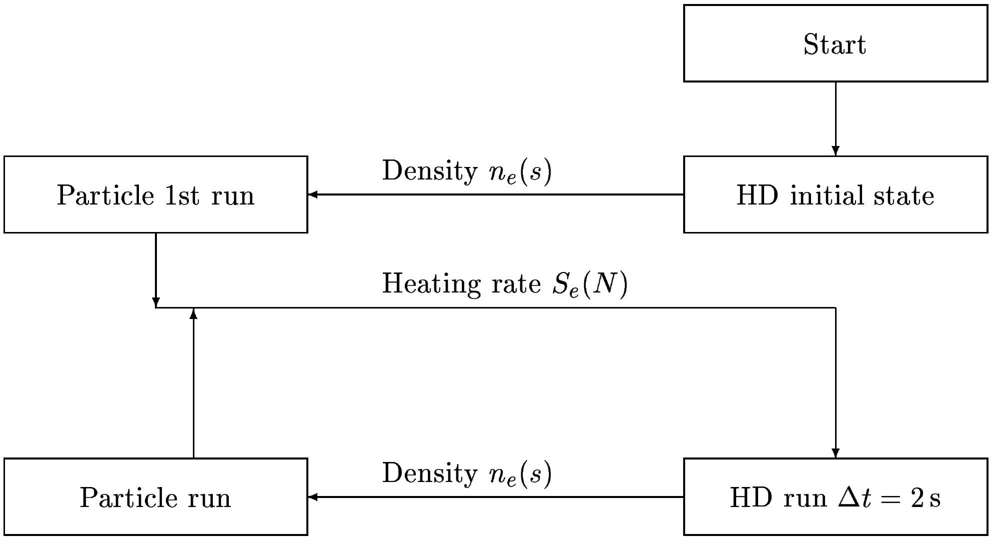

Let us now summarize the communication between the two codes with the following task flow chart. At the beginning of the simulation, the HD code passes its initial density distribution to the particle code. Based on this density profile, the particle code runs its first steady state calculation and returns the heating rate $S_e(N)$ as a function of column depth N to the HD code. Now the HD code takes this heating rate and converts it to a function of distance, $S_e(s)$, at each time step using the current density profile. While doing so, the HD code advances a time interval of $\Delta t = 2\,\mathrm{s}$, and then passes the updated density distribution back to the particle code again. This finishes a full cycle of calculation and next cycle starts over from the particle calculation again.

7.3 Simulation Result

Figure 7.2 shows the initial hydrostatic state of the plasma in one half of the loop (assumed to be symmetric), which displays the electron number density, temperature, and gas pressure vs. distance. We have a hot coronal region with $T \gtrsim 10^6\,\mathrm{K}$ and a transition region (TR) at around $s = 10\,\mathrm{Mm}$ where T quickly drops to the chromospheric value of $10^4\,\mathrm{K}$. The density, on the contrary, increases with distance from the tenuous ($< 10^{10}\,\mathrm{cm}^{-3}$) coronal portion, experiences a sharp jump at the TR, and reaches close to $10^{15}\,\mathrm{cm}^{-3}$ at the bottom ($\sim 4\,\mathrm{Mm}$ below the TR) of the simulation domain.

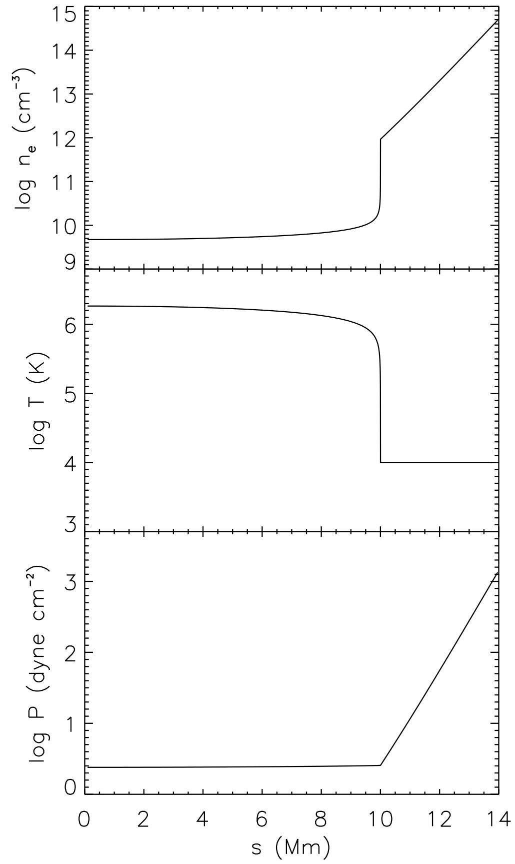

Figure 7.2: Initial state of the flare loop for the HD simulation. Distance starts from the LT where particles escape from the acceleration region.

From the same initial state, we have run five cases using different heating model parameters (which are summarized in Table 7.1). For each case, we use the identical loop geometry as MEL89 (see Chapter 9). We take a linear ramp in time for the normalization of the electron heating, with a rise of 30 s followed by a decline of another 30 s. After the first 60 s of impulsive phase calculation, we continue the simulation well into the decay phase until $t = 90\,\mathrm{s}$. We describe each of the simulation cases in the rest of this section, focusing on the evolution of the hydrodynamics and the energy and spatial distribution of the accelerated electrons and bremsstrahlung photons. We defer our investigation on the energy budget and the Neupert effect test of these case to next chapter.

7.3.1 Case R: Reference Calculation

It is instructive to run the first case with the original model of MEL89 and use it as a reference for comparing new results from our model. We use almost identical parameters as the "Reference Calculation" case in MEL89: spectrum index $\delta = 6$ and "knee" energy $E_1 = 15\,\mathrm{keV}$. The only two differences are: (1) here the "peak beam flux",[12] i.e., parameter F in Eq. (9) of MEL89, is $2.67 \times 10^{10}\,\mathrm{ergs\,cm^{-2}\,s^{-1}}$, while they used $5 \times 10^{10}\,\mathrm{ergs\,cm^{-2}\,s^{-1}}$; (2) we assume a fully ionized hydrogen plasma while they included helium which constitutes 6.3% of hydrogen number density.

The evolution of the flaring plasma is shown in Figure 7.3. We plot electron number density n_e, temperature T, gas pressure P, upward velocity v, energy deposition rate S_e, radiative loss rate L_{rad}, and heat conduction flux F_{cond} at selected times during the first 60 s of simulation. The plasma exhibits the same general evolution as that in Figure 1 of MEL89, which we briefly account as follows. As is evident, electron beam heating (S_e), which acts as the driver of the simulation, is concentrated in the upper chromosphere just below the transition region and heating in the corona is negligible early in the simulation. Heat conduction also carries energy that is deposited in the corona by nonthermal electrons down to the upper chromosphere, but this energy flux is overwhelmed by direct beam heating, particularly on the early stage of the flare. This localized beam heating, although counteracted by radiative loss that appears to be co-spatial, quickly heats chromospheric plasma, produces overpressure, and drives mass upflow. A downflow (with a velocity down to $-115\,\mathrm{km\,s^{-1}}$) in a narrow region of the chromosphere is also present to counterbalance the upward moment. Such a downflow is usually observed in blueshifted SXR or EUV

---

[12] cf., the actual energy deposition flux in Table 7.1.

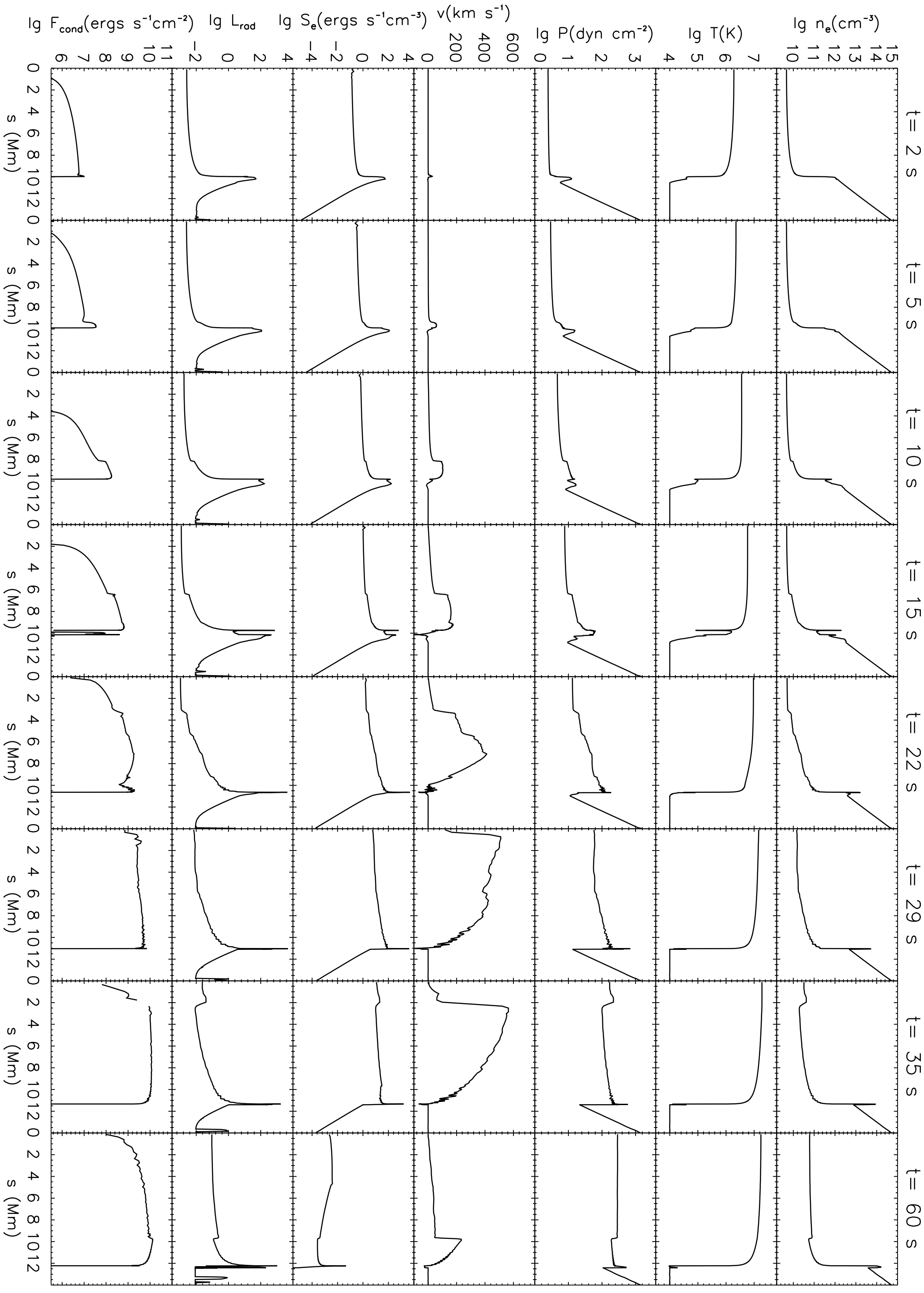

Figure 7.3: Evolution of electron density, temperature, pressure, upward velocity, energy deposition rate S_e, radiative loss rate $L_{\rm rad}$ (in same units as S_e), and heat conduction flux $F_{\rm cond}$ for Case R.

line spectrum. The downward momentum produced by electron heating could be partly responsible for photospheric seismic waves observed during major flares (Kosovichev & Zharkova, 1998; Kosovichev, 2006).

At $t = 10\,\mathrm{s}$, the upflow velocity exceeds $100\,\mathrm{km\,s^{-1}}$ and a discontinuity or an evaporation front[13] has already developed near the transition region (see the n_e panel). It travels upward and reaches the loop apex at $\sim 29\,\mathrm{s}$. It is then reflected back and material piles up there due to the reflective boundary condition imposed. This reflection can be understood as plasma flow from the other end of the loop in a symmetric loop geometry where there is no acceleration region present in the middle of the loop; or it can be assumed to be due to the encountering of the plasma with the acceleration region boundary where the upflow is stuck by strong turbulence, if we assume a geometry with an acceleration region sitting near the LT. The upflow reaches its maximum velocity of $565\,\mathrm{km\,s^{-1}}$ at $\sim 35\,\mathrm{s}$, which is delayed by 5 s from the maximum energy deposition at $t = 30\,\mathrm{s}$. The strength of evaporation subsides afterwards, but the coronal density continues to rise through the end of the simulation.

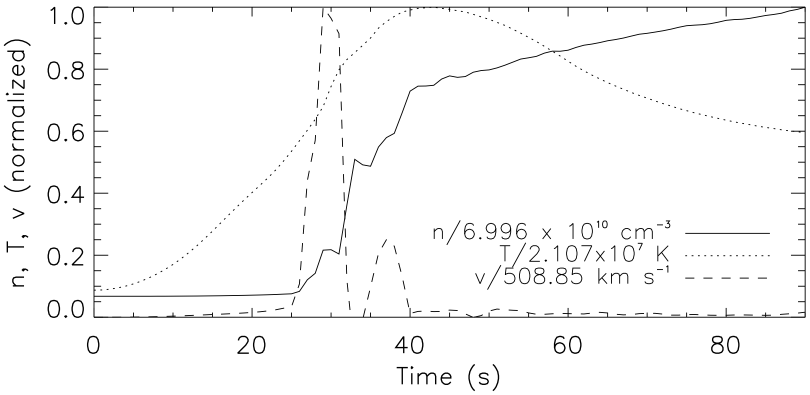

Figure 7.4: History of various quantities (electron number density, temperature, and upward velocity) at 1 Mm from the LT for Case R. Each variable is normalized to its maximum, as shown in the legend. The density curve have two sharp jumps, one followed by the other. The first jump is due to the arrival of the evaporation front from *below*, and the second one comes about because of the reflection of the front at the loop apex (coming from *above*).

---

[13] The discontinuity is not necessarily a shock if the Rankine-Hugoniot (RH) relations are not satisfied. We have not checked the RH relations since we are not concerned with such detailed gas dynamics here.

We can also inspect the plasma evolution by following the temporal variation of a physical quantity at a position fixed in space. Figure 7.4 shows the history of electron number density, temperature, and velocity at $s = 1\,\mathrm{Mm}$ (in the corona) from the loop apex. As can be seen, the density and velocity stay almost constant until $\sim 25\,\mathrm{s}$ when the evaporation front arrives and produces a sudden jump. The second jump in density results from the evaporation front reflection. In contrast, the temperature varies much smoother. It attains its maximum of $2.11 \times 10^7\,\mathrm{K}$ at $t = 44\,\mathrm{s}$ and decreases monotonically since then because conductive cooling overtakes beam heating at this position in the loop.

7.3.2 Case A: Fiducial Run with SA Model

We used the same parameters for acceleration as in PL04 (see their Fig. 12), namely $\tau_p^{-1} = 70^{-1}\,\mathrm{s}$, $n_e = 1.5 \times 10^{10}\,\mathrm{cm}^{-3}$, $B = 400\,\mathrm{G}$, $k_B T = 1.53\,\mathrm{keV}$, and the acceleration region size $L = 5 \times 10^8\,\mathrm{cm}$, and the peak rate of particle injection was selected to be $Q_0 = 5.73 \times 10^{11}\mathrm{electrons}\,\mathrm{s}^{-1}\,\mathrm{cm}^{-3}$ in order to provide a peak energy deposition flux of $2.56 \times 10^{10}\,\mathrm{ergs}\,\mathrm{s}^{-1}\,\mathrm{cm}^{-2}$ that is similar to that of Case R. We chose 200 energy bins uniformly spaced in the logarithmic space that covers the energy range of $511 \times [10^{-3}, 10^3]$ keV. There are 24 pitch angle bins set in the transport code, with uniform 12 bins symmetrically spanning each half of the $[0, \pi]$ range ($0 \leq \theta < \pi/2$ and $\pi/2 < \theta \leq \pi$; note $\theta \neq \pi/2$). We modulate the injection rate $Q(t, E)$ linearly in time, with a rise and drop time duration of 30 s, respectively.

The $E^2 F(E)$ electron flux spectrum (where $F(E) = f(E)\beta c$ is the angle-integrated electron flux) at the LT (black dashed line) is shown in Figure 7.5. It contains a quasi-thermal portion at low energies and a nonthermal tail at high energies, with a smooth transition in between (PL04). It does not invoke any artificial low energy cutoff or energy break. This particular spectrum shape is consistent with observed HXR spectra that can oftentimes be fitted with an isothermal plus power-law model. Since the acceleration parameters (e.g., τ_p^{-1}) are set constant in time, this spectrum does not change in shape, but does vary in normalization. The black dotted line indicates the electron flux escaping from the acceleration region, which is the input to the transport code and acts as a driver to the electron-beam heated HD evolution. We describe the plasma evolution below and defer a discussion of the corresponding particle transport and radiation effects afterwards.

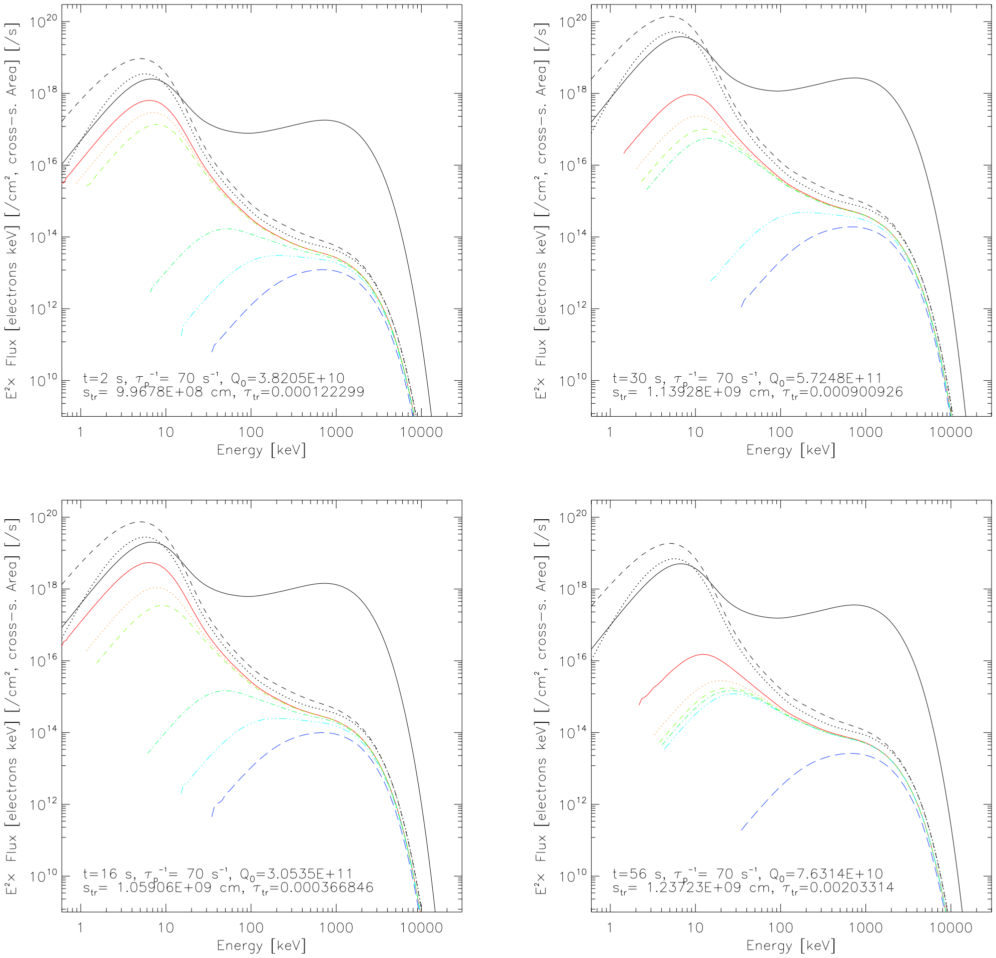

Figure 7.5: Evolution of the $E^2F(E)$ spectra for Case A, where $F(E)$ is the angle-integrated electron flux. The black dashed, dotted, and solid lines indicate the LT, escaping, and equivalent thick-target electron flux, respectively. The colored lines (from red to blue) are for the spectrum at a distance of $s = 4$, 8, 10, 11, 12, and 13 Mm from the injection site at the LT. Aside from time, other information listed includes the current values of τ_p^{-1}, the particle injection rate Q_0 (in units of electrons $\mathrm{s}^{-1}\,\mathrm{cm}^{-3}$, see text), and the distance (s_{tr}) and column depth (τ_{tr}, in units of $5 \times 10^{22}\,\mathrm{cm}^{-2}$) from the LT to the transition region.

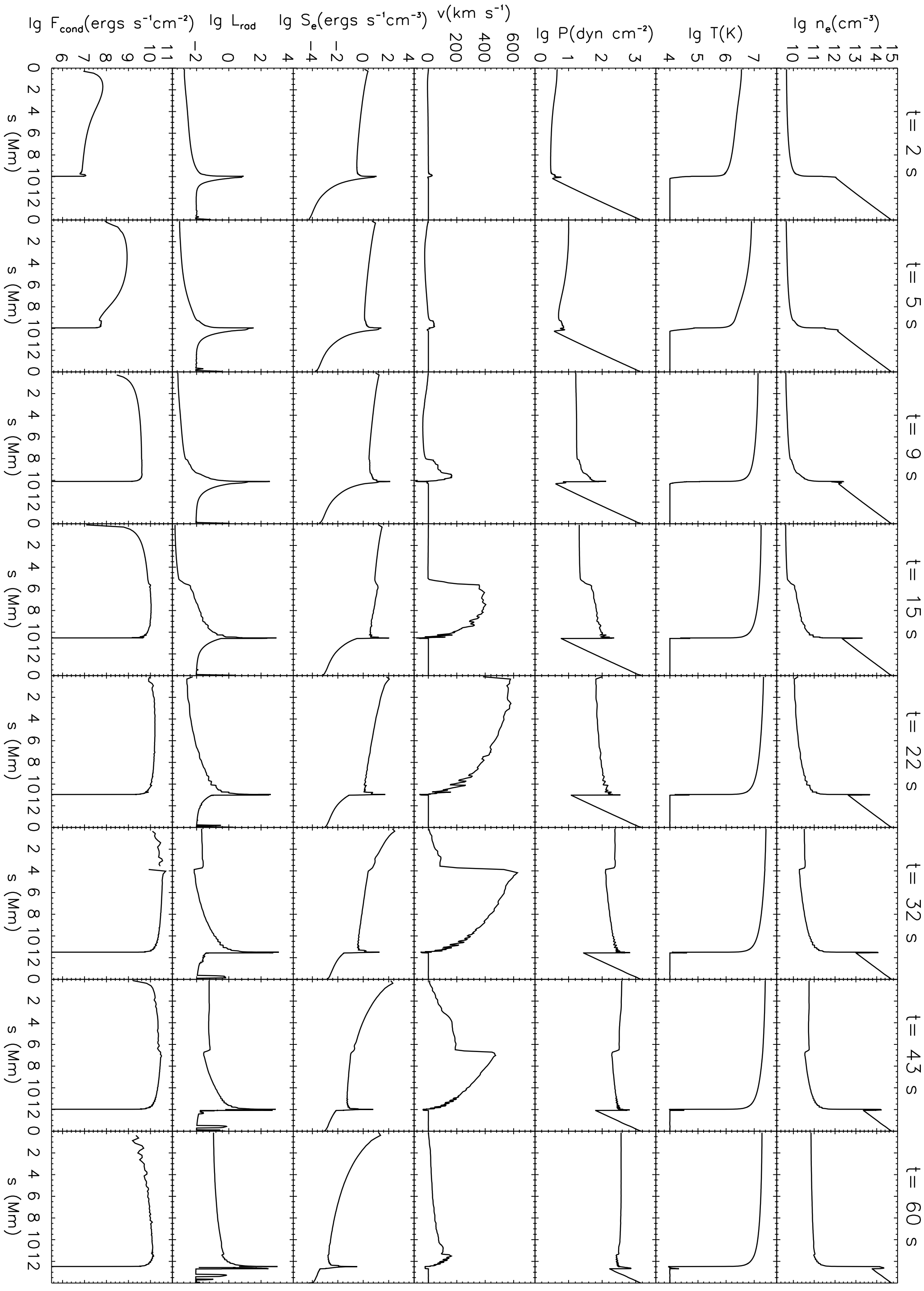

Figure 7.6: HD evolution of various quantities for Case A, similar to Fig. 7.3.

HD Evolution

Figure 7.6 shows the evolution of the plasma in the loop. As we can see, the general evolution, much faster though, is similar to that of Case R. The evaporation front reaches the loop apex at $t = 22\,\mathrm{s}$ (instead of 29 s in Case R), the maximum upflow velocity of $627\,\mathrm{km\,s^{-1}}$ is attained at $t = 22\,\mathrm{s}$ (instead of $565\,\mathrm{km\,s^{-1}}$ at $t = 22\,\mathrm{s}$ in Case R), and the maximum coronal temperature is 2.61 K (2.11 K in Case R).

These differences are a consequence of the spatial distribution of the energy deposition S_e, which first decreases (while it increases in Case R) with distance from the LT and then increases and peaks just below the transition region. In addition, the peak of the S_e curve in the chromosphere is relatively narrower than that in Case R, which means a comparably smaller fraction of energy is directly deposited in the chromosphere. This is because the electron spectrum here (Figure 7.5) has a smooth continuous distribution including the high-energy nonthermal regime and the low-energy quasi-thermal regime. There is a significant portion of the total energy content that resides in low energy electrons. These electrons give up most of their energy to the coronal portion of the loop, resulting in significant coronal heating. The coronal temperature thus increases rapidly and produces a relatively sharp temperature gradient and large heat conduction flux (see panels at $t = 2\,\mathrm{s}$ and $t = 5\,\mathrm{s}$). We note that the peak of the conduction flux, which is close to the LT at the beginning ($t = 2\,\mathrm{s}$), shifts downward and reaches the transition region at $t = 9\,\mathrm{s}$ when the upflow velocity rises sharply and exceeds $100\,\mathrm{km\,s^{-1}}$. In this sense, the evaporation is driven more by conduction than by direct heating. As evaporation develops and the coronal density increases, the coronal fraction of the energy deposition increases as well and dominates over the chromospheric portion on the late stage.

In contrast, the spectrum adopted in MEL89 is a power-law ($\delta = 6$) with a low energy cutoff at $E_1 = 15\,\mathrm{keV}$ below which the electron spectrum has a positive index of 2. This spectrum has its peak at 15 keV and electrons of this energy are stopped in the chromosphere where they lose most of their energy, where the radiative loss (which acts like a sink in the energy transfer) is most efficient. This means that a significant part of energy deposited by beaming electrons is quickly radiated away (also see Figure 8.2 and text there) in situ in the upper chromosphere and a smaller fraction of energy is available to evaporate chromospheric material than in Case A. Note that the conductively driven scenario in Case A has energy input into the transition region and produces evaporation, which occurs slightly above the radiatively-efficient layer in the upper chromosphere. This makes conductively-driven evaporation more efficient and results in higher upflow velocity and higher coronal temperature and density, as can also be seen in Figure 7.19.

Evolution of Electron Distribution

Figure 7.5 shows the evolution of **electron flux spectrum** at different locations in the loop. The black solid line represents the equivalent thick-target electron flux (see equation 7.23). As expected, it appears to be much harder than the LT flux in the 10–1000 keV range. The colored lines (from red to blue) are for spectra at $s = 4$, 8, 10, 11, 12, and 13 Mm from the LT injection site. Early into the flare ($t = 2\,\mathrm{s}$), the transition region is located at $s = 9.97\,\mathrm{Mm}$ and its column depth $\tau = 1.22 \times 10^{-4}$ (in units of $5 \times 10^{22}\,\mathrm{cm}^{-2}$). At this time, the two red lines (solid and dotted) indicates spectra in the corona, which are very similar to the escape flux because of small column depths from the injection site. The other four colored lines are spectra below the transition region, which, as expected, become harder with an increasing deficit of low energy electrons as column depth increases. This is because only high-energy electrons can penetrate deep into the chromosphere.

In this simulation case, because the LT spectrum shape does not change with time (so does the escape flux and thick-target flux), the spectrum at a particular column depth should also remain constant in shape and only vary in normalization. However, as time progresses, evaporation takes place and the height of the transition region drops, while the coronal density increases. This causes variations with time of the column depth (and the electron spectrum) at each position in space. This is just what we see here. At $t = 56\,\mathrm{s}$, for example, the transition region shifts down to $s = 12.4\,\mathrm{Mm}$ at a column depth of $\tau = 2.02 \times 10^{-3}$. In the lower-right panel of Figure 7.5, only one chromospheric spectrum is left, and the other (coronal) spectra are very alike because they are exposed in the corona and their column depths are very close.

We can also check the electron **flux distribution vs distance** at different energies, which is shown in Figure 7.7. We also display the flux in the acceleration region (LT) for comparison as the region of negative distance. In general, the electron flux decreases with distance from the injection site. The slope of these curves is steeper for low energy electrons than that for high-energy electrons because low-energy electrons lose energy faster (due to the $1/\beta$ dependence of Coulomb loss rate). The flux drops much steeper in the chromosphere (than in the corona) because of its high density and thus large column depth per unit distance. This produces a break in the curve around the transition region

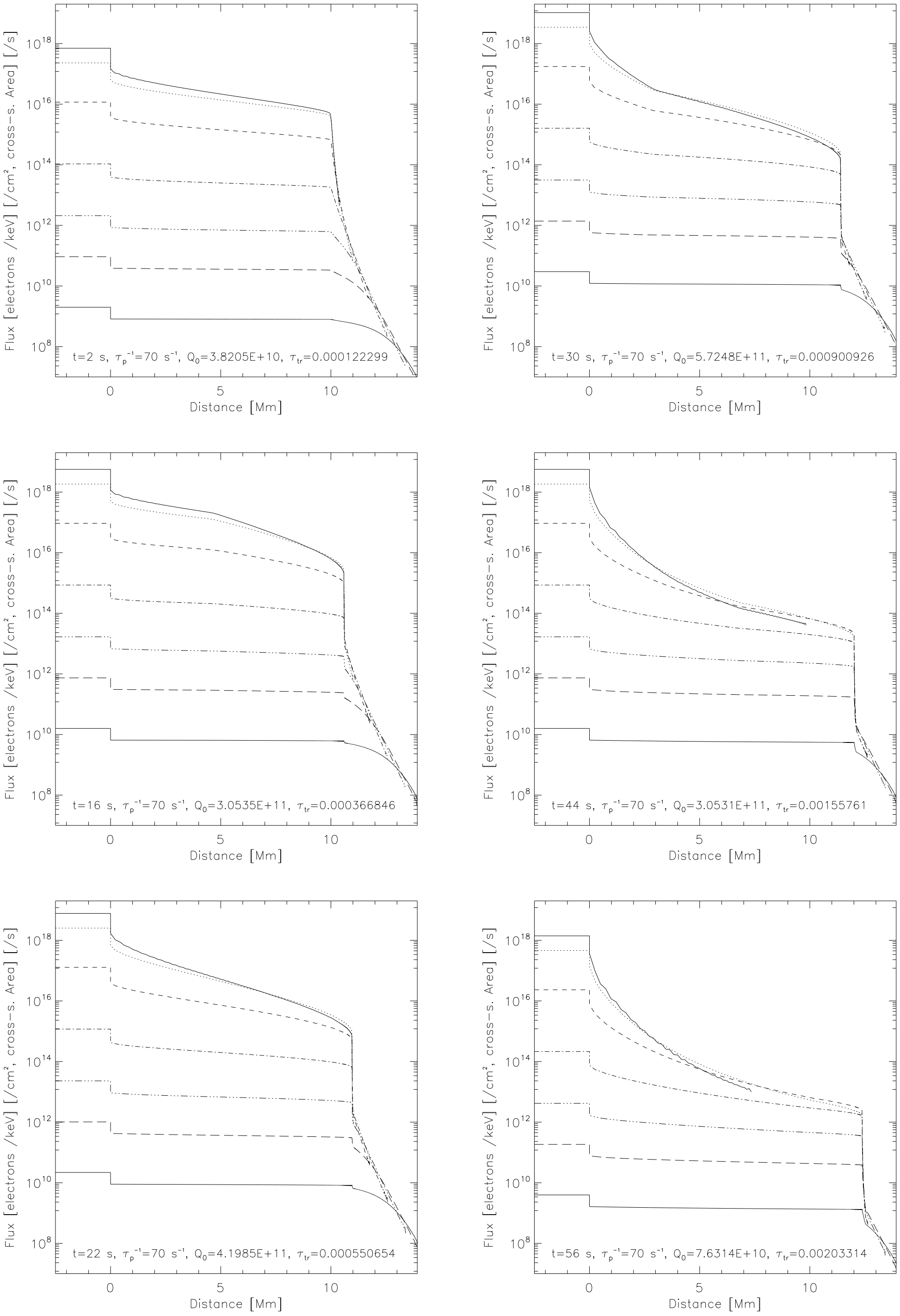

Figure 7.7: Evolution of electron flux vs depth at different energies for Case A. From top to bottom, the curves correspond to electron energies of 3.1, 6.1, 12.3, 24.5, 48.8, 97.4, and 294.1 keV, respectively. The steps in the region of negative distance denote the average electron flux ($f_{\rm ac}(E)\beta c$) in the acceleration region, one half of whose length is shown here.

and wherever a sharp density change occurs. At $t = 16\,\mathrm{s}$, for example, a break near $s = 5\,\mathrm{Mm}$ is obvious for electron energies of 3.1 and 6.1 keV. This is actually where the evaporation front is located. At $t = 22\,\mathrm{s}$, because the evaporation front already reaches the apex of the loop and the density in the whole loop has increased significantly, the electron flux distribution is much steeper than before in the whole coronal portion. Similar evaporation signatures are present throughout the duration of the flare (see the right column of Figure 7.7).

Evolution of Bremsstrahlung Radiation

Figure 7.8 shows the bremsstrahlung **photon spectra** at different depths that are produced by the accelerated electrons discussed above (see the corresponding Figure 7.5). Likewise, the LT photon spectrum (black dashed) also shows a thermal-like component in the low-energy range. It hardens in the intermediate energy range and softens again to the high-energy end. The FP spectrum (black solid) is much harder (than the LT spectrum), and in the range from tens of keV to a few hundred keV, it mimics the commonly observed power-law FP spectrum. As distance increases, the spectrum (from red to blue) becomes harder because the electron spectrum has the same trend of variation.

Note that, at $t = 2s$, the two red-colored spectra (very close to the LT spectrum in shape) are lower than the first chromospheric spectrum (green dashed) at all energies. This is because early in the course of the flare, the coronal density is low and thus the bremsstrahlung production there is at a low level too. As evaporation develops and the coronal density increases, the photon spectrum in the upper-corona portion ($s \leq 8\,\mathrm{Mm}$) of the loop becomes harder because the electron spectrum there hardens. At the same time, as more and more volume of the loop turns into the corona (since the transition region drops), some locations previously buried in the chromosphere are now exposed in the corona. These locations have lower (than before) column depth and thus softer electron spectrum, which produces softer photons spectrum as well. This can be seen from the evolution of the three green-colored spectra (at $s = 10, 11, 12\,\mathrm{Mm}$) in Figure 7.8. At $t = 56\,\mathrm{s}$, all the colored spectra (except the blue one) are from coronal locations and they appear alike in both shape and normalization simply because the density differences among these locations are now much smaller than before.

The **spatial distribution** of the photon emission at different energies (same as in Figure 7.7) is plotted in Figure 7.9. On the early stage of the flare evolution, low energy

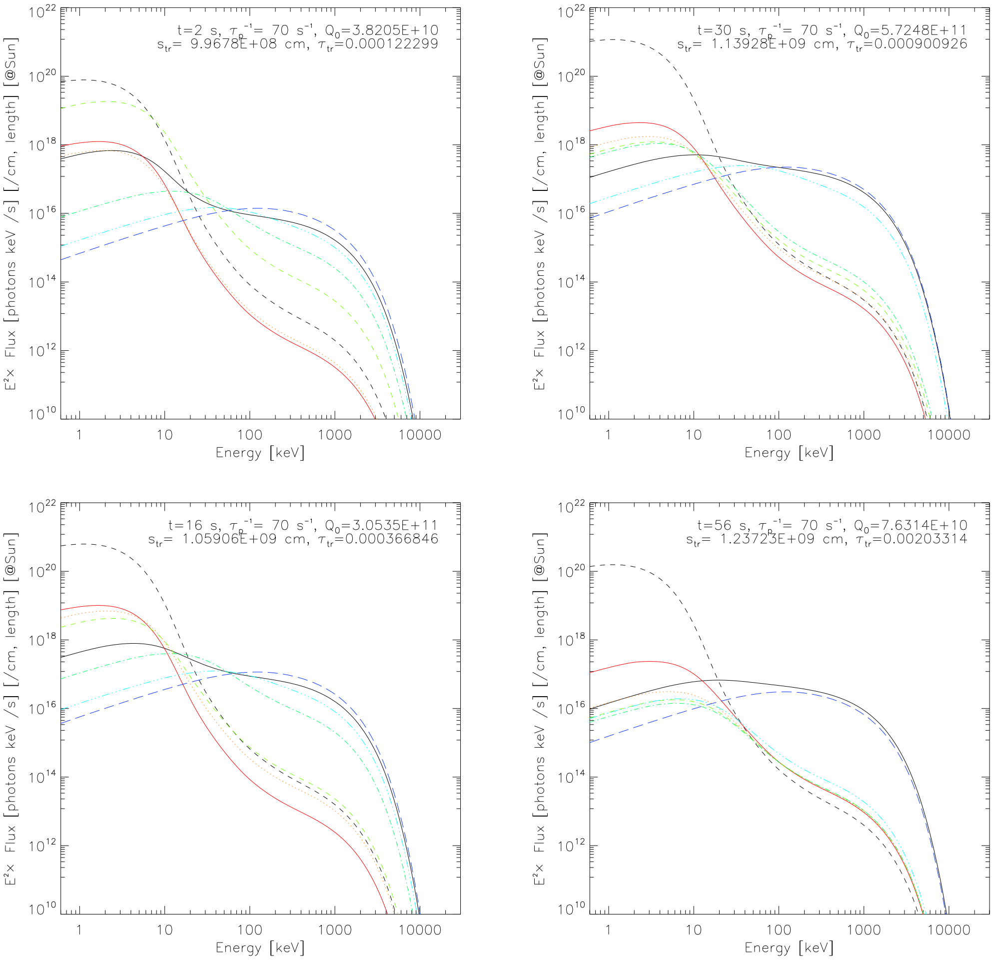

Figure 7.8: Evolution of νF_ν photon spectra at different locations for Case A. The spectrum is of photons emitted by a unit length of the loop, integrated over the loop cross-sectional area. The black dashed line indicates the LT spectrum, and the black solid line is the averaged spectrum below the transition region, which is analogous to observed FP spectra. The colored lines are for distance s = 4, 8, 10, 11, 12, and 13 Mm from the LT, same as those in Figure 7.5.

emission comes primarily from the LT, while high energy emission is concentrated below the transition region. Because the bremsstrahlung radiation is proportional to the product of the electron spectrum and the local proton density, the photon emission profile can reveal more details of the density distribution than the electron flux profile (Figure 7.7). As is evident, the emission profile follows the density features (including the evaporation front and the density spike at the transition region, see Figure 7.6) very well. As the flare develops and evaporation continues, more and more emission comes from the coronal portion of the loop. At low energies, the emission drops with distance much steeper than before in the corona due to the dramatic density increase there. At intermediate energies, we find a temporal transition from FP-dominated emission to LT-dominated emission. At very high energies, such a change is not present because even the high density corona is still more or less transparent for high energy electrons. However, the retreat of the transition region down to chromospheric heights is visible in all the emission profiles.

We should bear in mind that all the emission features described here are not necessarily observable given the current technology and spatial resolution of the active space missions. However, it worth trying to make a comparison with observations. As shown in Chapter 6, in the 2003 November 13 flare, we identified an XR emission feature that shifts from the FP toward the LT with time. In this simulation case, we also find the bremsstrahlung XR emission tracks the evaporation front. At low energies, e.g., $E = 3\,\text{keV}$, there is a local brightness enhancement at the evaporation front due to the sharp jump of density and thus increased bremsstrahlung productivity. Such a local brightness blob can exceeds the FP intensity (spatially integrated and averaged) and is comparable to the LT intensity. In principle, this blob could be imaged by *RHESSI* and could be responsible for the observed moving source. Note that at high energies, although the evaporation front is also visible in the HXR emission profile, its intensity is dwarfed by the FP emission and thus is not observable due to limited dynamic ranges of the instruments (e.g., 10 for *RHESSI*). On the other hand, thermal emission from the heated and evaporated plasma could also contribute to low energy X-rays, and such contributions could be comparable at certain energies. Of course, as photon energy increases, the thermal emission drops quickly due to its exponential decay with energy; and thus thermal contribution at high energies are negligible compared with nonthermal emission. At what photon energy thermal and nonthermal emissions are comparable? Answers to this question depends on the electron spectrum, as well as the density and temperature distribution of the thermal plasma. It

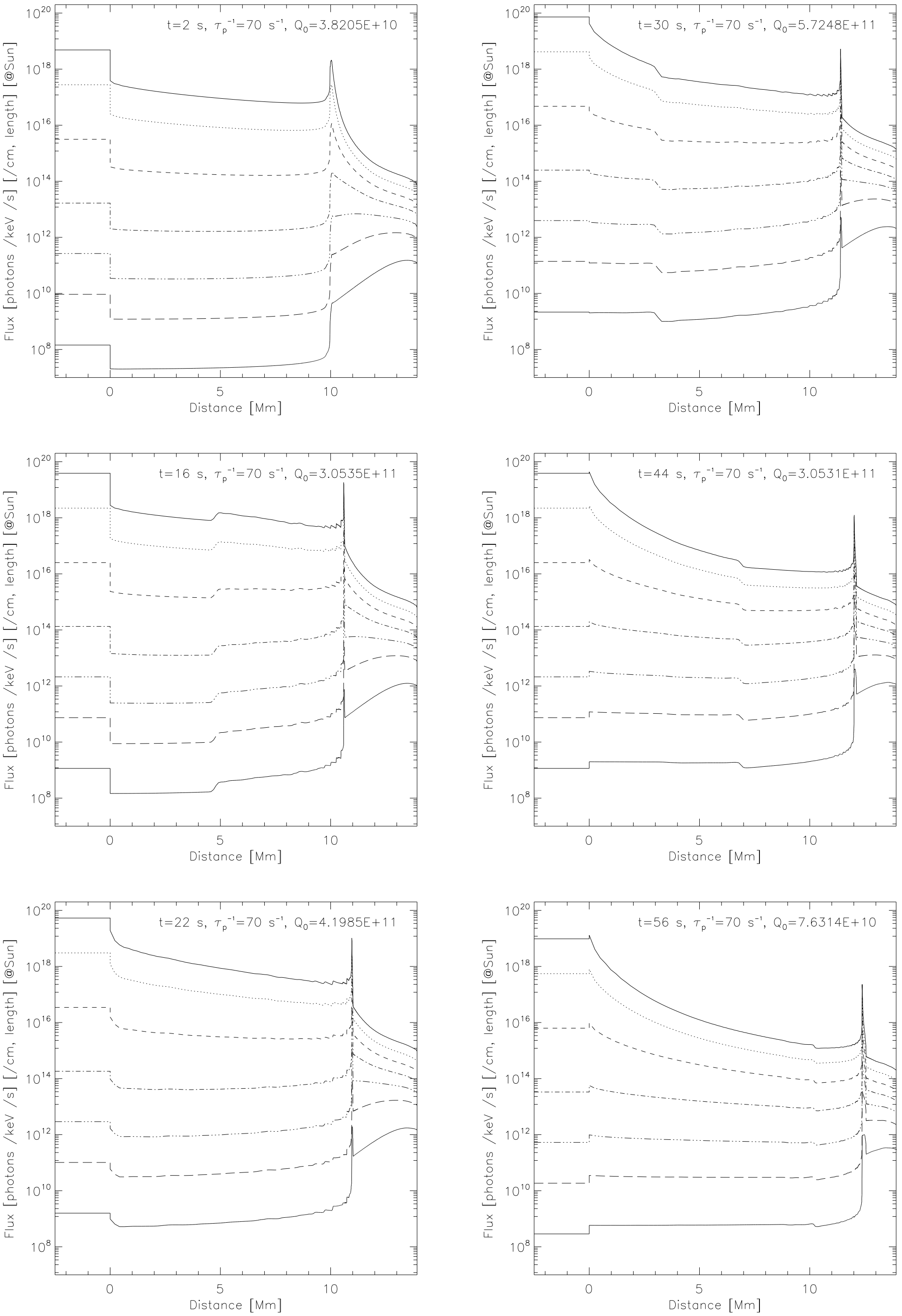

Figure 7.9: Evolution of photon emission vs depth at different photon energies of Case A. As in Figure 7.7, the energies are 3.1, 6.1, 12.3, 24.5, 48.8, 97.4, and 294.1 keV.

would be interesting to check the relative importance of thermal vs nonthermal emission and their spatial distribution, with different model parameters. Unfortunately, such a study would be beyond the scope of the current investigation.

7.3.3 Case B: Variable Electron Spectrum

This is the second simulation case using the combine particle and HD code. In addition to the time modulation of the spectrum normalization, we vary the acceleration rate τ_p^{-1} linearly with time, in the same triangular pattern. This means that the electron spectrum experiences a *soft-hard-soft* variation, as is commonly observed in solar flares (Grigis & Benz, 2004), and can be seen here.

Figure 7.10 shows the evolution of the **electron spectra** at different depths. Clearly, at the beginning ($t = 0\,\mathrm{s}$) when there is very little acceleration ($\tau_p^{-1} = 2.33\,\mathrm{s}^{-1}$), the spectra at all the depths look similar to the injected thermal distribution (not shown) which has a sharp exponential cutoff. Note that some electron spectra at large depths are too small to appear in the plot due to the extreme softness of the spectrum and the resulting sharp decrease of electron flux with distance. As time proceeds and the acceleration rate increases, the spectrum becomes harder and harder, particularly in the energy range of $[10, 10^3]$ keV. At $t = 30\,\mathrm{s}$, the thick-target flux exhibits a hump with a positive slope. Meanwhile, the quasi-thermal component at the low-energy end is present all the time. After the peak time of 30 s, spectrum softening takes place and the spectrum shape returns to that of the quasi-thermal one in the end. The corresponding photon spectra (Figure 7.11) show the same trend of soft-hard-soft variation. Other spectrum (of both electrons and photons) variations (such as those due to chromospheric evaporation) are similar to those of Case A.

Figures 7.12 shows the evolution of the electron flux (*left*) and photon intensity (*right*) **vs. distance** at different energies, which is similar to that of Figures 7.7 and 7.9, respectively. One of the main differences is that electron spectrum here is soft on the early and late stages, and consequently the plot spans a wide range on the vertical scale.

Another spectrum feature that makes Case B different from Case A is the **escaping electron flux**. As we can see from Figures 7.10, on the early and late stages of the flare when the acceleration rate is low, the escape flux (*thick dotted*) and the LT flux (*thick dashed*) are almost identical above $\sim 10\,\mathrm{keV}$; below such an energy, their difference increases with decreasing energy. Around the acceleration rate peak time (similar in Case

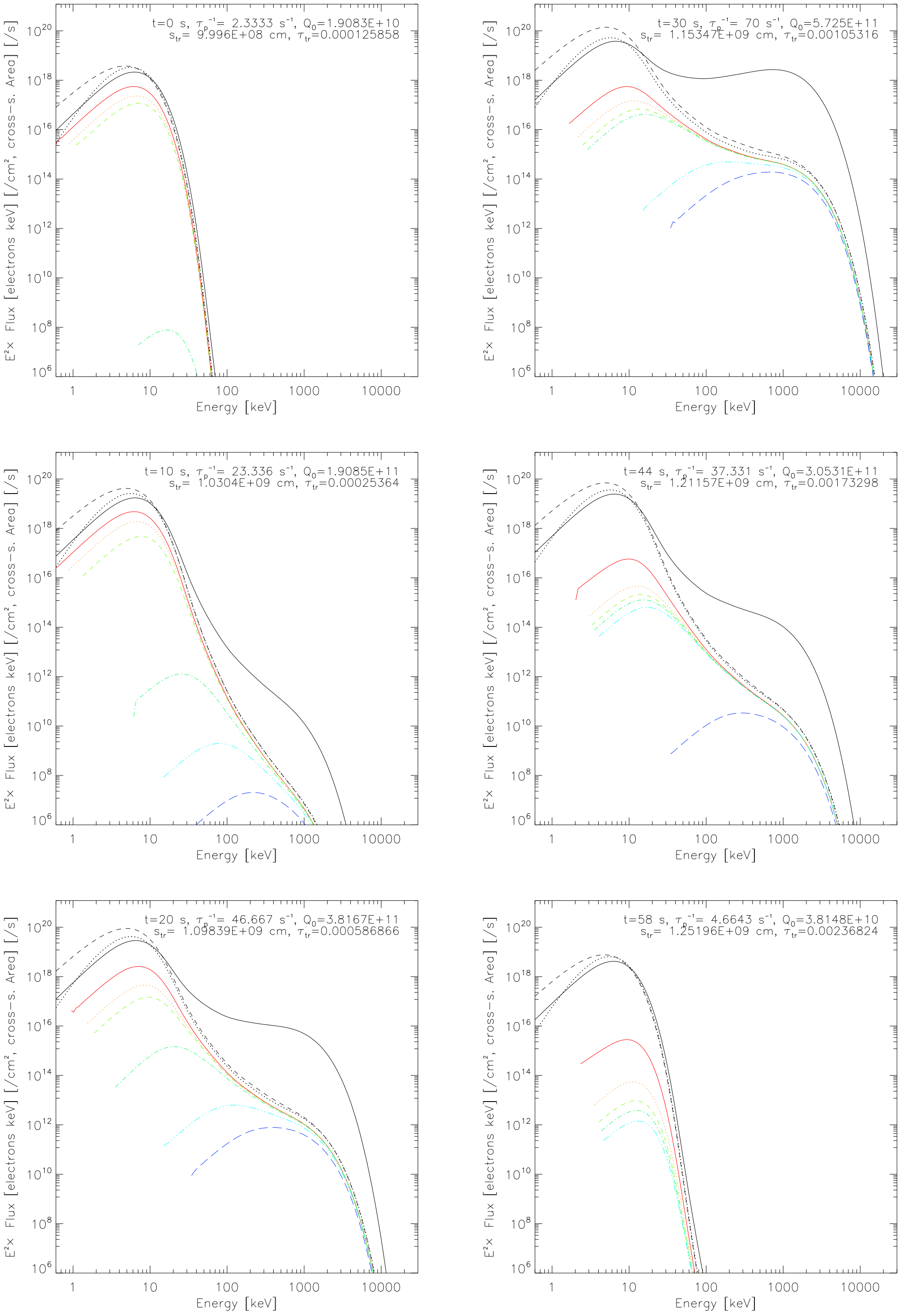

Figure 7.10: Same as Figure 7.5 (electron spectra at different depths), but for Case B. Note that at $t = 0\,\mathrm{s}$, some spectra at large depths ($s > 10\,\mathrm{Mm}$) are too small to be shown.

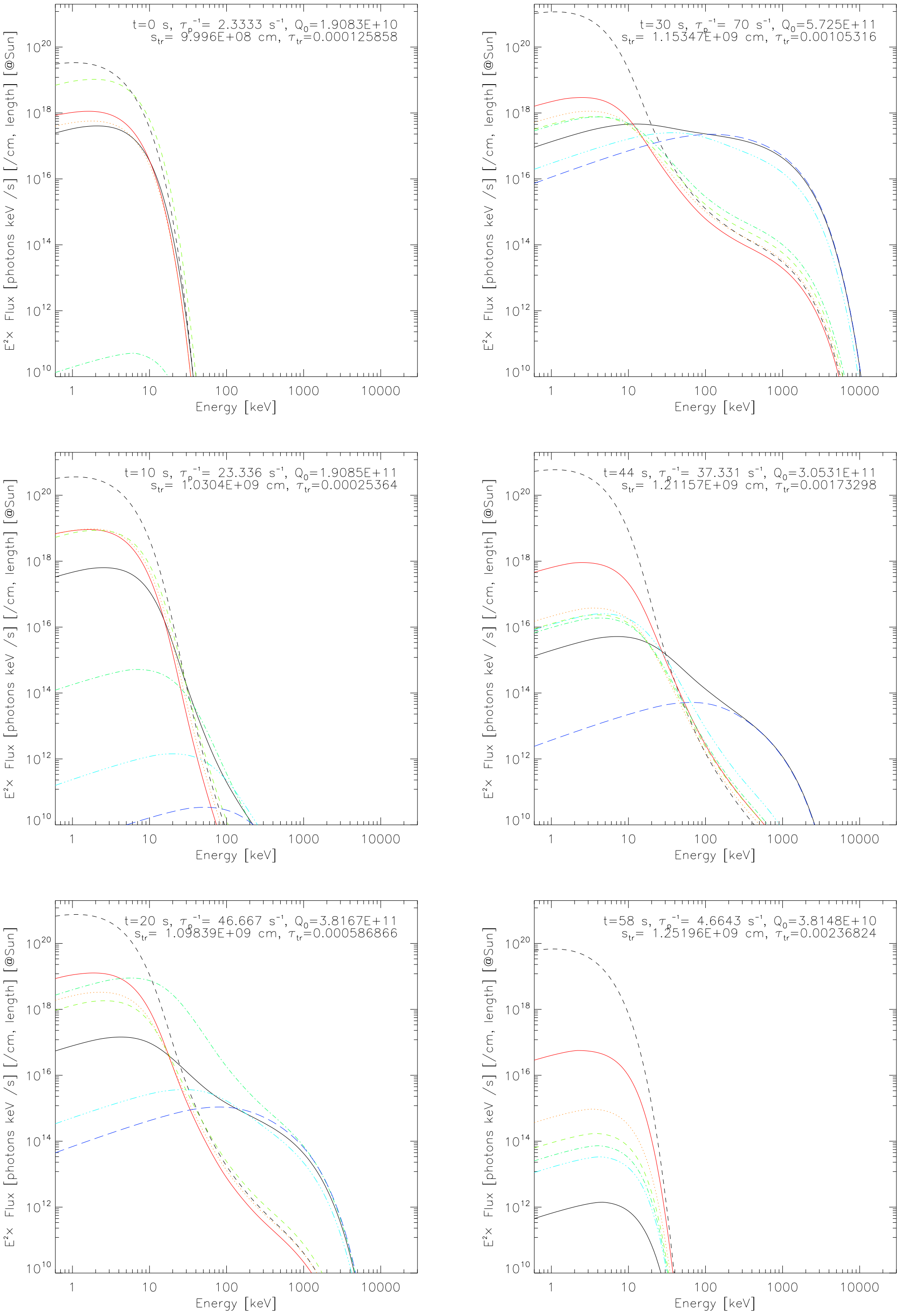

Figure 7.11: Same as Figure 7.8 (evolution of photon spectra at different depths), but for Case B.

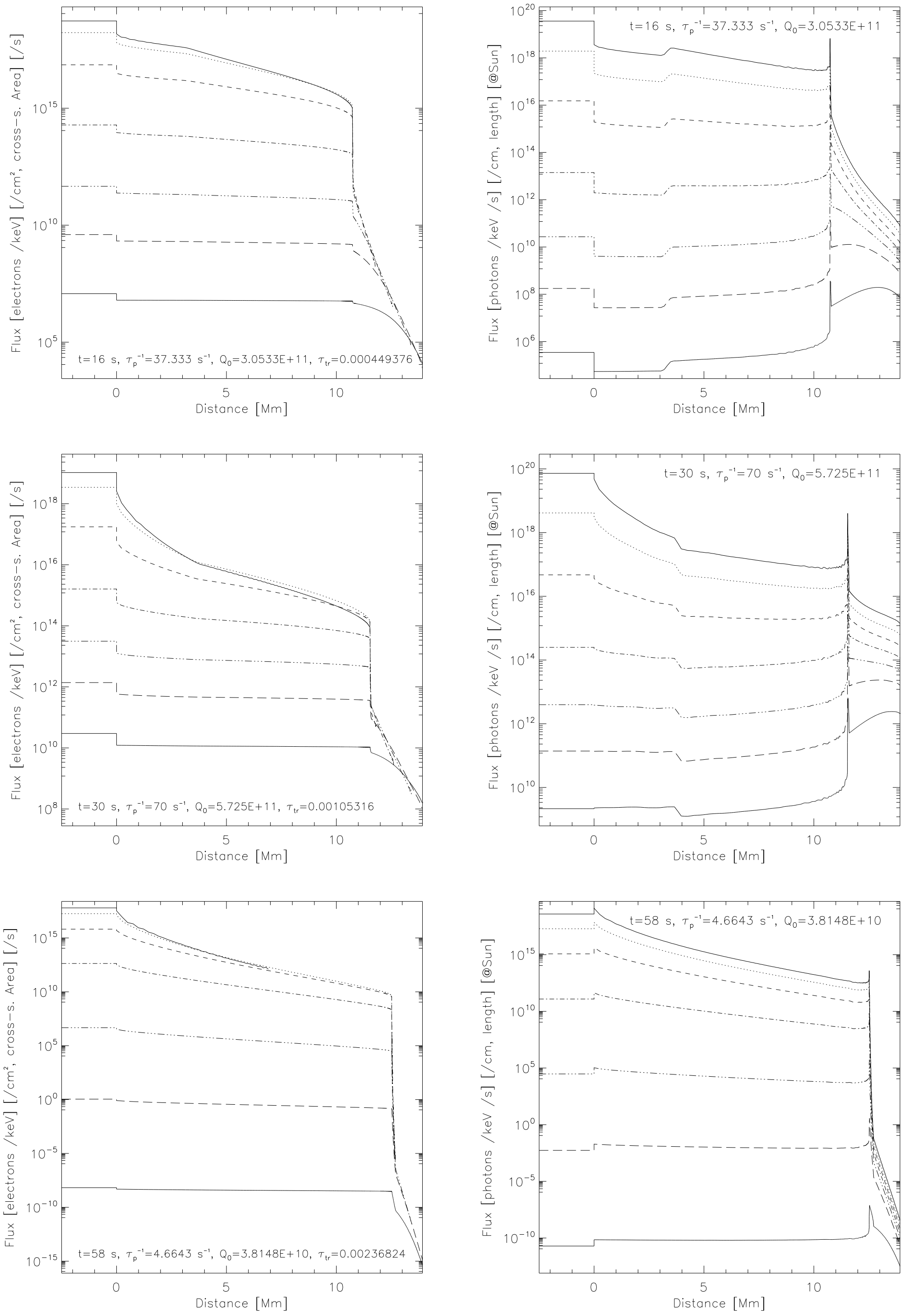

Figure 7.12: Evolution of electron (*left*) and photon (*right*) fluxes vs. distance at different energies (same as Figures 7.7 & 7.9) for Case B. Time goes from top to bottom (note different vertical scales).

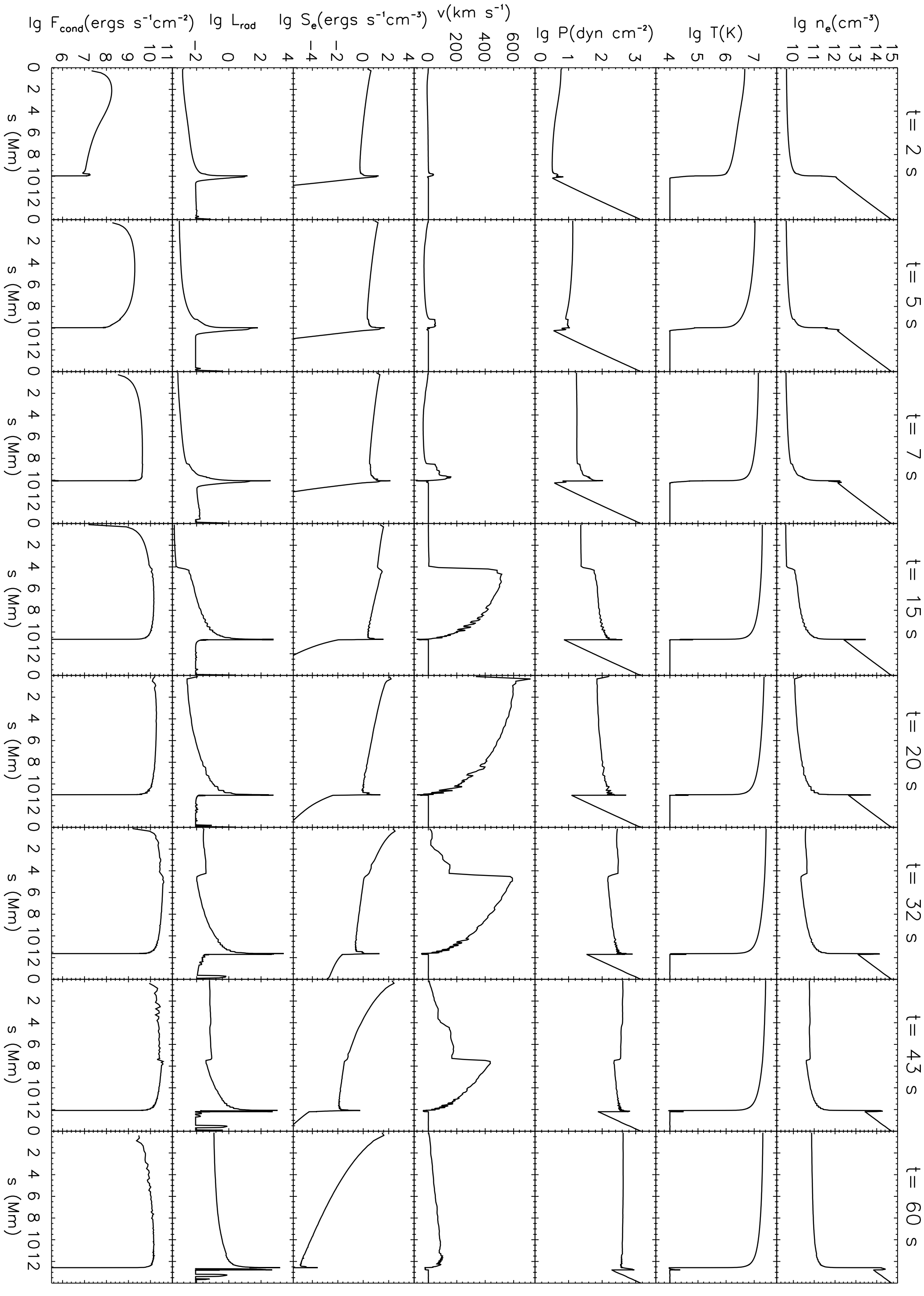

Figure 7.13: HD evolution of various quantities for Case B.

A), such an critical energy shifts to $> 10^3$ keV. This is because the escape flux is inversely proportional (equation 7.21) to the escape timescale, $T_{\rm esc}$, which depends on the scattering timescale $\tau_{\rm sc}$ through equation (7.20). From equations (7.22), (7.16), and (7.12), we see the escape-to-LT electron flux ratio $R_{\rm esc}$[14] is a decreasing function of the acceleration rate τ_p^{-1}. When τ_p^{-1} is low and the scattering timescale $\tau_{\rm sc}$ is large, at a given energy, $R_{\rm esc}$ would be relatively large. Because of this, there are relatively more electrons that escape the acceleration region and deposit their energy into the loop in Case B than in Case A, since here τ_p^{-1} has a triangular time profile with its peak value equal to that of Case A (which is constant in time there). We find the mean energy deposition flux here is $9.8 \times 10^{10}\,{\rm ergs\,s^{-1}\,cm^{-2}}$, while in Case A it is $8.3 \times 10^{10}\,{\rm ergs\,s^{-1}\,cm^{-2}}$ (also see Table 7.1). Since this case has a larger energy input rate, we would expect stronger chromospheric evaporation here, which we discuss below.

Let us now check the corresponding **HD evolution**, which is shown in Figure 7.13 At the very beginning, because very little acceleration takes place and the spectrum is very soft, the energy deposition curve drops sharply (cf., Case A) with depth into the chromosphere. As noted earlier, low energy electrons are more efficient heating the corona and we would expect that the softer spectrum, on top of the larger escaping electron flux discussed above, will generally result in stronger coronal heating. This is just the case in this run, which shows a faster evolution and more dramatic evaporation than Case A. At $t = 7\,$s (vs $9\,$s in Case A), the peak conduction has already reached the transition region and upflow velocity has become greater than $100\,{\rm km\,s^{-1}}$. At $t = 20\,$s (cf., $22\,$s in Case A) the evaporation front is reflected at the loop apex and at the same time the upflow attains its maximum velocity of $718\,{\rm km\,s^{-1}}$ (cf., $627\,{\rm km\,s^{-1}}$ at $t = 32\,$s in Case A). This case has also the highest values of maximum downflow velocity, maximum coronal temperature and density out of the five cases under study (see Table 7.1).

7.3.4 Case C: Harder Electron Spectrum

In this case, we set $\tau_p^{-1} = 100\,{\rm s^{-1}}$, which means higher rate of acceleration, and we would expect harder electron spectrum than Case A ($\tau_p^{-1} = 70\,{\rm s^{-1}}$). This is true as can be seen from the electron and photon spectra shown in Figure 7.14. Compared with Case A, the electron (*left*) flux also decreases with distance slightly slower and the photon (*right*)

---

[14] The functional (vs. E) form of $R_{\rm esc}(E)$ would depends on that of $T_{\rm esc}(E)$ or $\tau_{\rm sc}(E)$. See Figs. 11 and 12 in PL04.

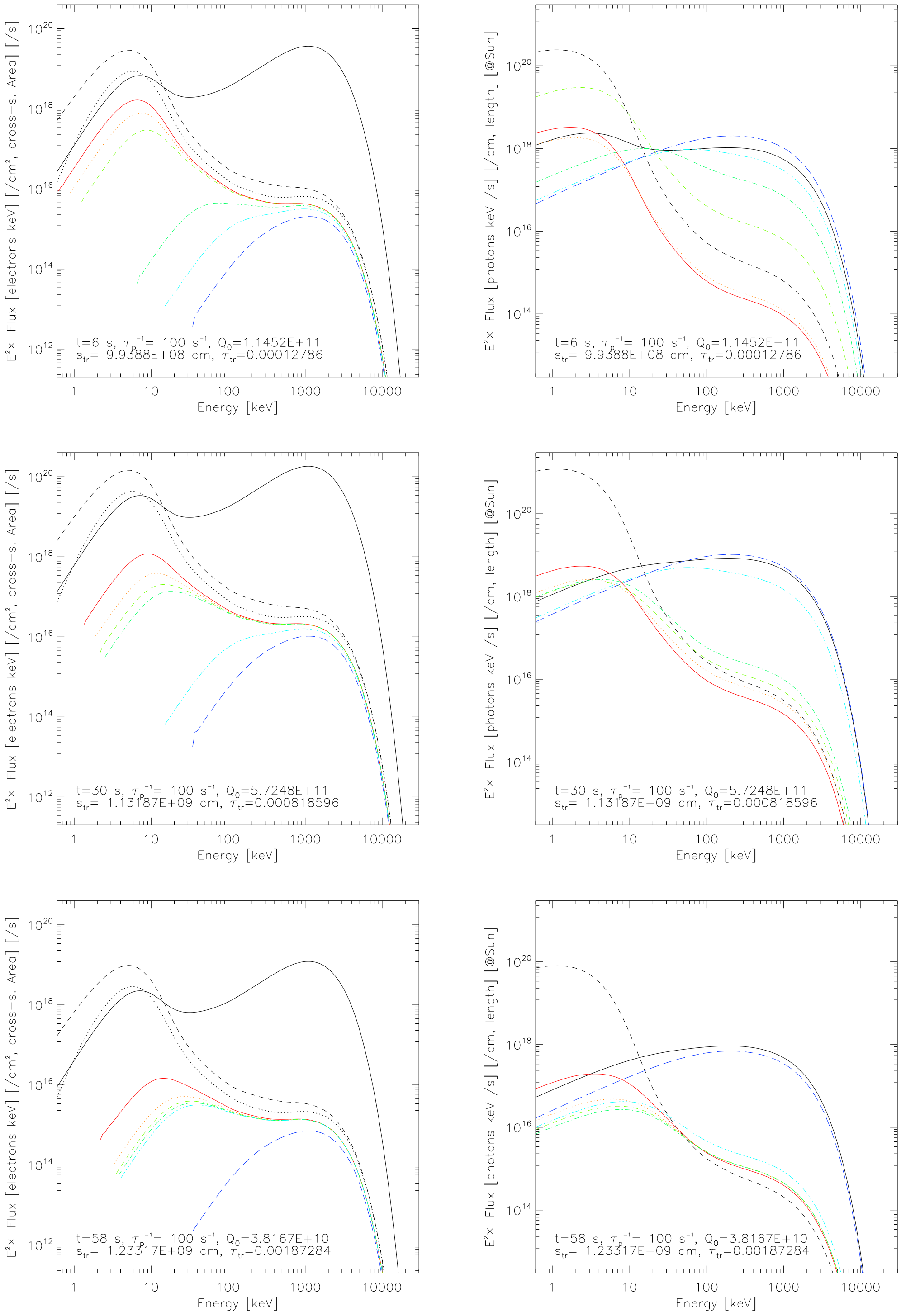

Figure 7.14: Evolution of electron (*left*) and photon (*right*) spectra at different depths for Case C. Time goes from top to bottom (similar to Figures 7.5 and 7.8).

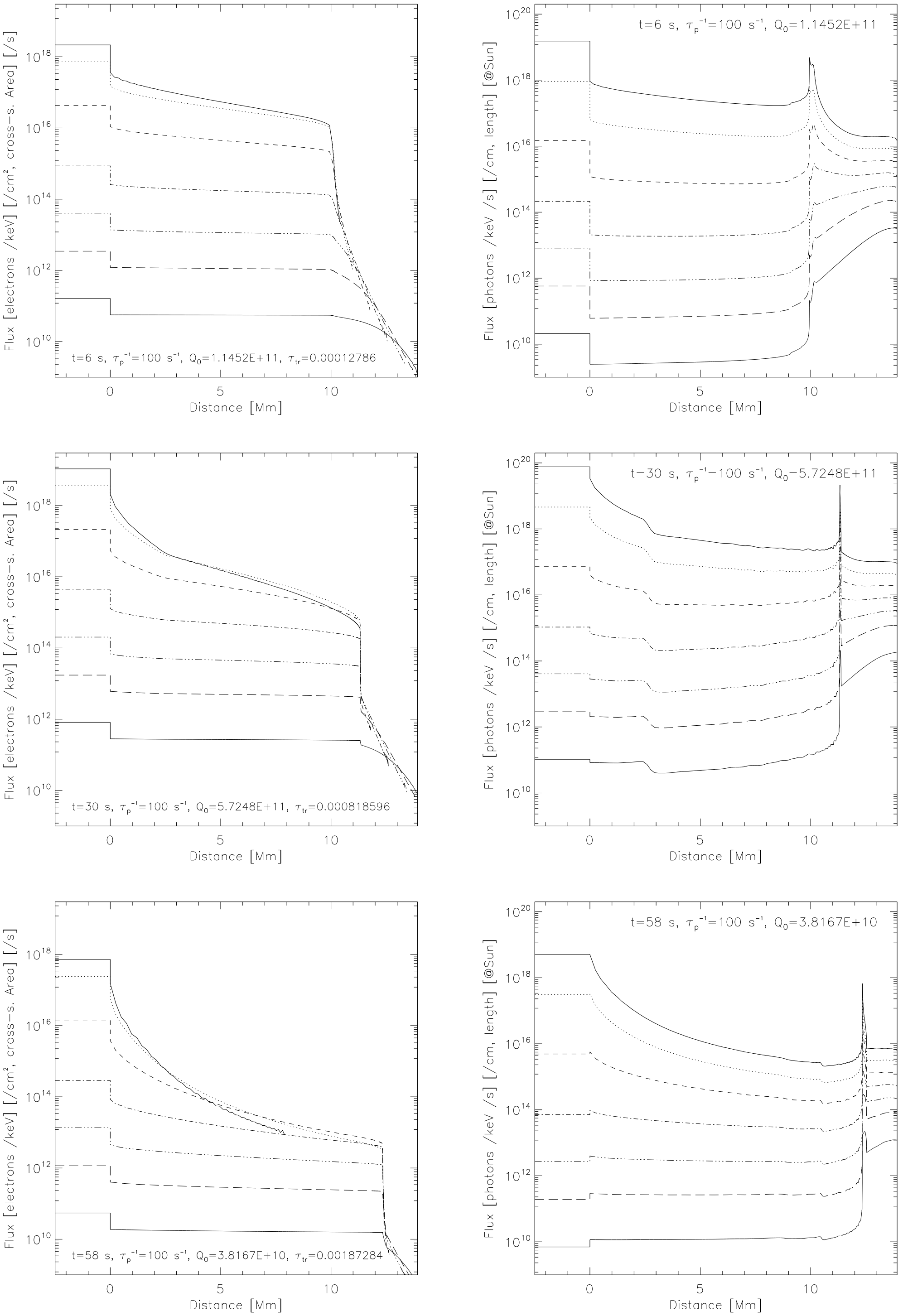

Figure 7.15: Evolution of electron (*left*) and photon (*right*) fluxes at different energies for Case C (similar to Figures 7.7 and 7.9).

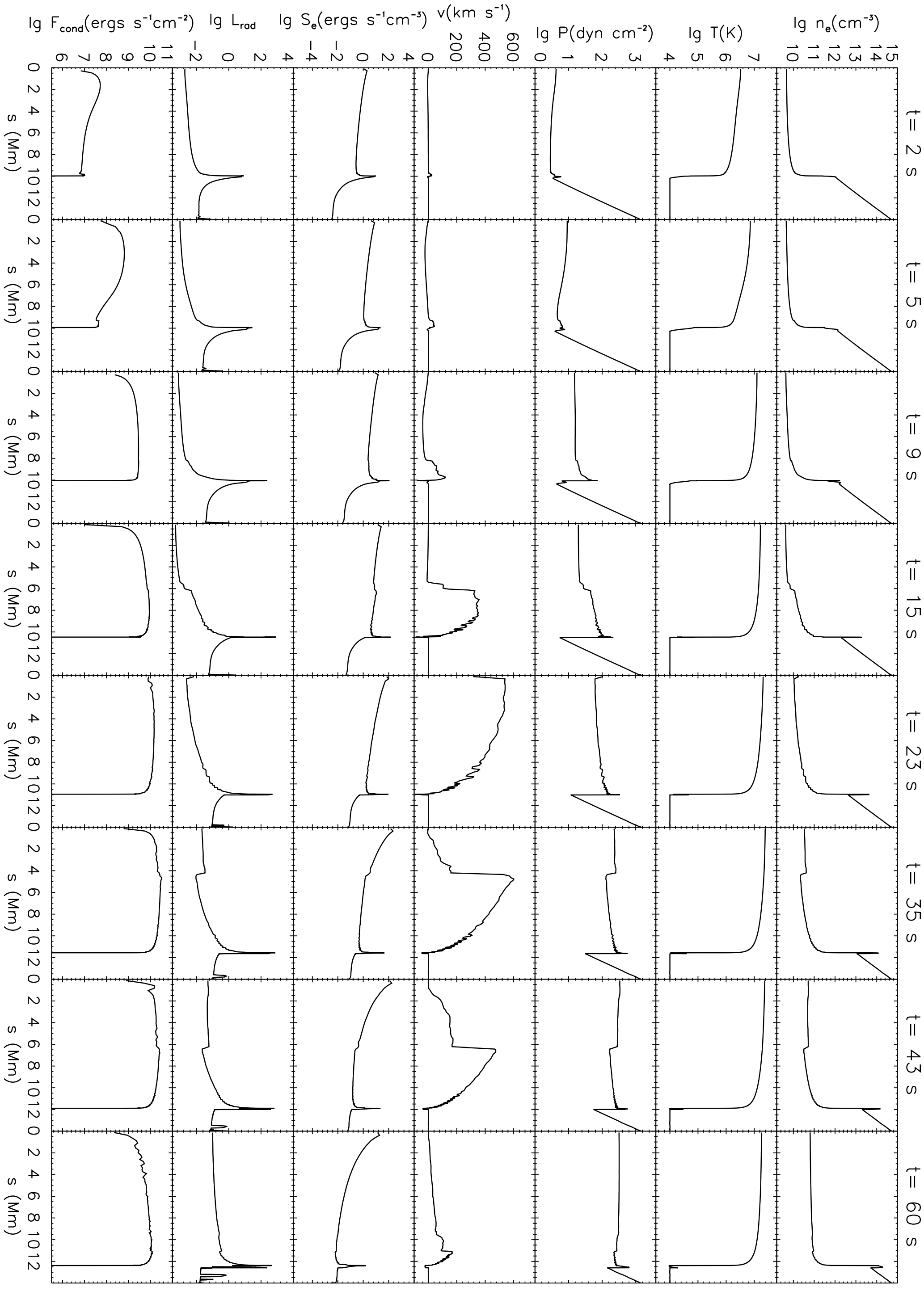

Figure 7.16: HD evolution of various quantities for Case C.

distribution shows relatively more emission coming from below the transition region than in the corona (see Figure 7.15). The normalization of HXR emission[15] is also much higher than that of Case A, again, because the harder electron spectrum here has a higher bremsstrahlung yield (see, e.g., Figure 6.12).

Another effect of the larger acceleration rate is the relatively smaller flux of escaping electrons that enters the loop. Although there are more electrons in the high-energy portion of the spectrum (thus more energy content there), most of the energy is still contained in the low-energy electrons because of the steepness of the spectrum). Therefore, the addition of energy due to more accelerated high-energy particles is relatively small, and it loses to its competing factor, i.e., the smaller escape flux, which produces a smaller overall energy flux input to the loop than Case A.

We note from Figure 7.16 that the energy deposition rate decreases slower with distance in the corona and beyond the transition region, particularly in the late phase of the flare, than that in Case A. This is due to the harder spectrum we have here, which produces slightly less coronal heating and more chromospheric heating. In addition, the relatively smaller escaping electron flux here results in less energy flux. For the same reasons discussed above, as opposed to Case B, we would also expect slightly weaker evaporation and slower evolution of the plasma, which is the case (see Table 7.1 and Figures 7.19 and 7.16). For example, the maximum coronal temperature and density are $2.48 \times 10^7\,\mathrm{K}$ and $7.84 \times 10^{10}\,\mathrm{cm}^{-3}$, respectively, which is on the order of 10% lower than those in Case A. MEL89 reached a qualitatively similar conclusion by using a harder ($\delta = 4$, vs. 6) power-law spectrum.

7.3.5 Case D: Smaller Normalization

In the last case, we used smaller normalization of $Q_0 = 5.73 \times 10^{10}\mathrm{particles\,s^{-1}\,cm^{-3}}$, which is about one order of magnitude smaller than the fiducial Case (A). This change is similar to those adopted in earlier HD simulations (see, e.g., Fisher et al., 1985c). The electron and photon spectra and spatial distribution are shown in Figure 7.18, which, as expected, all show similar shape as in Case A, but with a smaller normalization. As to the hydrodynamics, we would accordingly expect much weaker evaporation and slower and less dramatic HD evolution, as can be seen from Figure 7.17.

---

[15] The spatially integrated HXR light curve and its normalization can be seen in Figure 8.11 of next chapter too.

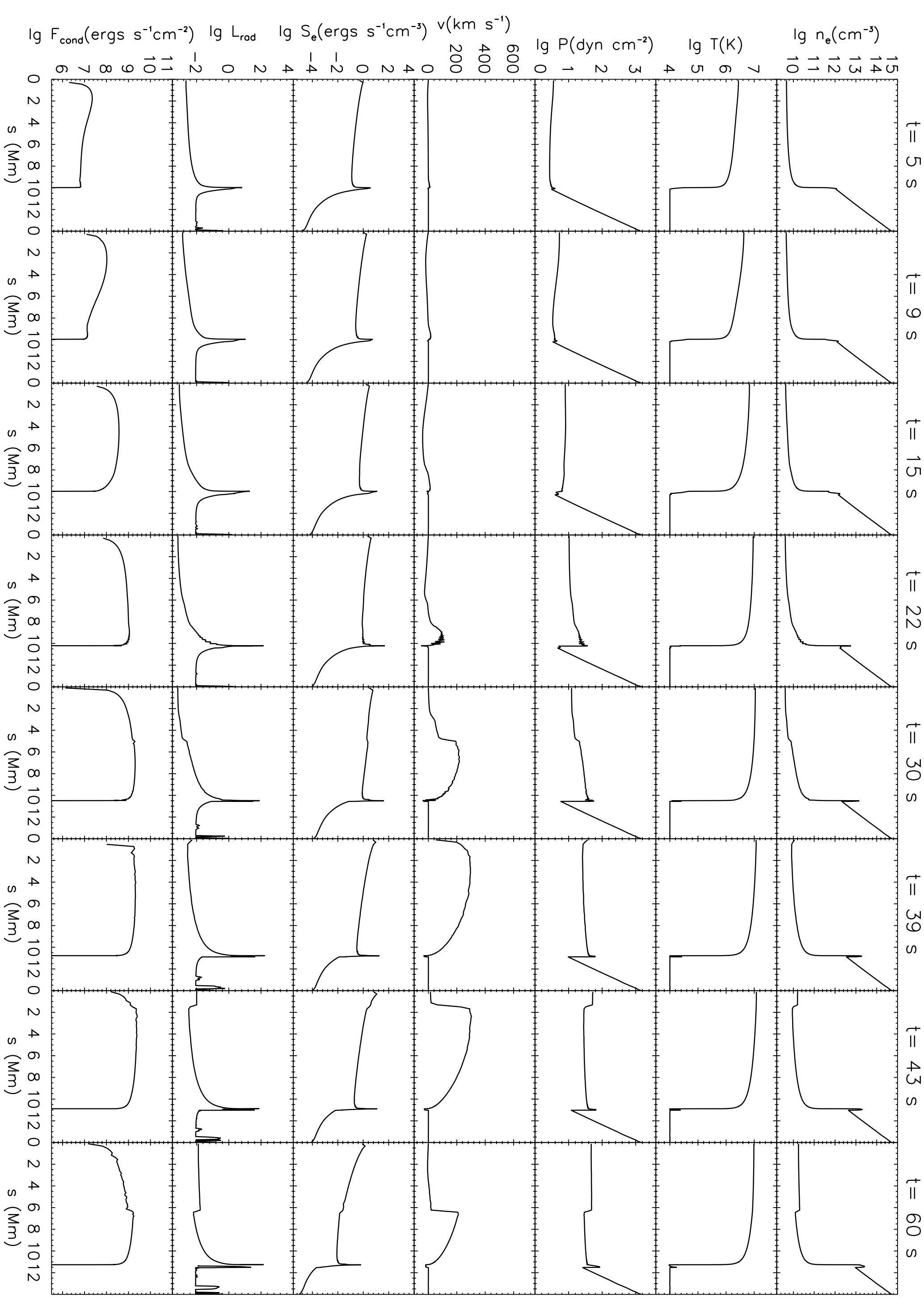

Figure 7.17: HD evolution of various quantities for Case D.

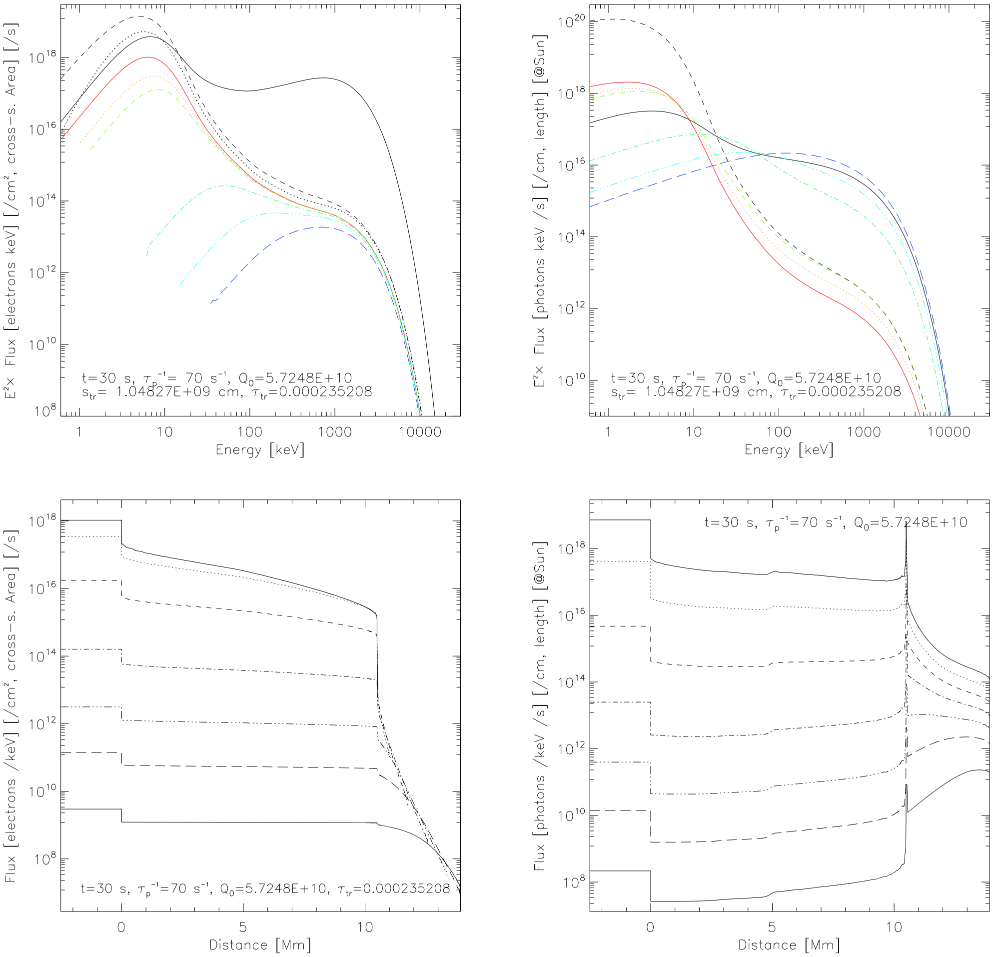

Figure 7.18: Electron & photon spectrum and flux spatial distributions for Case D at the peak injection time.

We note that, in this simulation case, we have a very low peak energy deposition flux of $2.58 \times 10^9\,\mathrm{ergs\,cm^{-2}\,s^{-1}}$, while the maximum upflow velocity is at a moderate value of $303\,\mathrm{km\,s^{-1}}$. Fisher et al. (1985c), however, reported that the evaporation velocity is sensitive to the energy flux carried by nonthermal electrons, and they found an energy flux $F < 3\times10^{10}\,\mathrm{ergs\,cm^{-2}\,s^{-1}}$ results in a gentle evaporation ($v < 100\,\mathrm{km\,s^{-1}}$). This difference is because Fisher et al. (1985c) considered a power-law electron spectrum with a sharp low energy cutoff of 20 keV (cf., 15 keV of MEL89), while our model has a continuous electron distribution extending from the thermal background at low energies to the nonthermal tail at high energies. For the same reason noted above, low energy electrons are more efficient in evaporating the chromospheric plasma via conduction. Consequently, although Case D has a low energy flux, it can produce a moderately high evaporation velocity, because a significant portion of this energy flux resides in low energy particles. In addition, Fisher et al. (1985c) used an index of $\delta = 4$ for the power-law electron spectrum, which is somewhat hard and thus less effective in evaporating chromospheric material than a softer electron population. We also note that Milligan et al. (2006), in supporting the result of Fisher et al. (1985c) from their joint EUV Doppler and HXR observations, also used a power-law electron spectrum with a cutoff energy.

7.3.6 Comparing The Cases: a Summary

Table 7.1: Summary of simulation cases.

Cases	τ_p^{-1} ($\mathrm{s^{-1}}$)	Q_0	$F_{\max}$	$\bar{F}$	$v_{\max}$ ($\mathrm{km\,s^{-1}}$)	$t_{v_{\max}}$ (s)	$v_{\min}$ ($\mathrm{km\,s^{-1}}$)	$t_{v>100}$ (s)	t_{apex} (s)	$T_{\max}$ (10^7 K)	$n_{\max}$ ($10^{10}\,\mathrm{cm^{-3}}$)
R	$\delta = 6$ $E_1 = 15\,\mathrm{keV}$	—	2.54	8.58	565	35	-115	10	29	2.11	6.96
A	70, const	57.3	2.56	8.30	627	32	-113	9	22	2.61	8.82
B	peak=70	57.3	2.54	9.80	718	20	-194	7	20	2.65	9.84
C	100, const	57.3	2.21	7.20	601	35	-153	9	23	2.48	7.84
D	70, const	5.73	0.258	0.853	303	43	-90.3	22	39	1.20	1.93

NOTE — τ_p^{-1} is set as a constant except for Case B in which τ_p^{-1} varies linearly with time and its peak value is 70; Q_0 (in $10^{10}\,\mathrm{s^{-1}\,cm^{-3}}$): peak value of injected number of electrons; $F_{\max}$ (in $10^{10}\,\mathrm{ergs\,s^{-1}\,cm^{-2}}$) and $\bar{F}$ (in $10^9\,\mathrm{ergs\,s^{-1}\,cm^{-2}}$): peak and mean energy deposition flux integrated over the whole loop; $v_{\max}$ and $t_{v_{\max}}$: maximum upflow velocity and time at which it is reached; $v_{\min}$: maximum downflow velocity, appearing in the upper chromosphere; $t_{v>100}$ and t_{apex}: time at which the upflow velocity exceeds $100\,\mathrm{km\,s^{-1}}$ (usually when the conduction front reaches the transition region) and the density jump (evaporation front) reaches the apex of the loop, respectively; $T_{\max}$ and $n_{\max}$: maximum coronal temperature and density.

We now summarize the comparison among the five cases, particularly of their HD response. The key parameters are listed in Table 7.1. The first two parameters we care about are the maximum and mean electron energy deposition fluxes ($F_{\max}$ and $\bar{F}$), because they determine, to some extent, the consequent HD evolution. As we can see, in terms of these two parameters, Cases R and A–C are very close, while Case D stands alone as a dwarf (also in terms of all the other parameters). Let us now take a close look at the group of Cases R and A–C, using Case A as the fiducial point.

Case R has a similar value of $F_{\max}$ as Case A (and even a slightly higher $\bar{F}$). However, its HD evolution is less dramatic. Its maximum upflow velocity of $v_{\max} = 565\,\mathrm{km\,s^{-1}}$ is much lower than the $627\,\mathrm{km\,s^{-1}}$ value of Case A; it takes longer (at $t = 29\,\mathrm{s}$) for the evaporation front to reach the loop apex, as opposed to the 22 s of Case A; the maximum coronal temperature of $T_{\max} = 2.11 \times 10^7\,\mathrm{K}$ and maximum coronal density of $n_{\max} = 6.96 \times 10^{10}\,\mathrm{cm^{-3}}$ are lower (by tens of percent) than those of Case A. By these criteria, Case R is also the extreme case of weak evaporation among the whole group of Cases R and A–C. Such a difference, as we elaborated earlier, mainly comes from the different electron spectrum, a power-law with a low-energy cutoff, that Case R assumes, while all the other cases take a continuous spectrum that extends to the low-energy quasi-thermal component. Another contribution to the different HD evolution is that Case R uses the approximate analytical solutions for the heating rate (e.g., Emslie, 1978), while we performed more rigorous Fokker-Planck calculation for the other cases.

Case B, in contrast, is another extreme in the group of Cases R and A–C. It has a very similar maximum energy flux, compared with Case A, but it has a mean energy flux about 18% higher (also the highest in the group), because Case B has a softer (except at the peak energy input time $t = 30\,\mathrm{s}$) electron spectrum and thus a higher escaping electron flux than Case A. Consequently, this case has the strongest evaporation, with a maximum upflow velocity of $718\,\mathrm{km\,s^{-1}}$, coronal $T_{\max} = 2.65 \times 10^7\,\mathrm{K}$ and $n_{\max} = 9.84 \times 10^{10}\,\mathrm{cm^{-3}}$, all being the highest in the group. This is also because the softer electron spectrum here has relatively more low energy electrons, who contribute more to heating the corona than heating the chromosphere. This generally results in a higher coronal temperature and more dramatic chromospheric evaporation, for the reason discussed earlier.

Case C, on the other hand, has a harder electron spectrum ($\tau_p^{-1} = 100\,\mathrm{s^{-1}}$) and somewhat smaller energy input rates ($F_{\max}$ and $\bar{F}$ are smaller than those of Case A by $\sim 13\%$). The harder electron spectrum generally results in more direct chromospheric heating than coronal heating, and it is less efficient in evaporating plasmas due to the competing radiative loss (see earlier discussions). Consequently, the resulting coronal $T_{\max} = 2.48 \times 10^7\,\mathrm{K}$ is 5% lower and $n_{\max} = 7.84 \times 10^{10}\,\mathrm{cm^{-3}}$ is 11% lower, and the maximum upflow velocity of $v_{\max} = 601\,\mathrm{km\,s^{-1}}$ is 4% smaller than that of Case A. We also note Case R has a somewhat larger downflow velocity ($v_{\min} = -153\,\mathrm{km\,s^{-1}}$) than Case A ($v_{\min} = -113\,\mathrm{km\,s^{-1}}$), which is due to more in situ direct chromospheric heating by its harder electron spectrum.

We can appreciate some of the above differences among the simulation cases from a different angle. Figure 7.19 shows the history of the electron number density n_e, temperature T, gas pressure P, and upward velocity v at $s = 1\,\mathrm{Mm}$ (in the corona) from the loop apex for all the five cases. As can be seen, Case D (*dot-dashed*) is an outlier and the curves of other cases (the group of Cases R and A–C) more or less cluster together. Among this group, Case R (*long-dashed*) is much smaller in the values and its response is significantly delayed compared with the other three. Its temperature, in particular, increases more slowly and the maximum value is much less than Cases A–C, whose differences in temperature are much smaller. This indicates much weaker coronal heating in Case R, as mentioned before.

7.4 Summary and Discussion

We have performed a combined simulation of nonthermal particles using the unified $\mathcal{F}$*lare* code (of particle acceleration, transport, and radiation) and of the hydrodynamic response of the atmosphere using the NRL HD code. We summarize our results as follows.

1. We have demonstrated that a combined simulation of particles and HD response is possible and have engineered the two codes to work together. This accomplishment marks a significant advance in computational high-energy solar physics in general and provides a powerful simulation tool to improve our understanding of solar flares in particular.

2. We have shown that using the more realistic electron spectrum from the SA model affects the spatial distribution of energy deposition and thus influences the HD evolution. The quasi-thermal component in the electron spectrum produces more coronal heating than previous models, which have a low-energy cutoff (e.g., $E_1 = 15\,\mathrm{keV}$) in the power-law distribution and thus have more direct chromospheric heating. Because of the cospatial radiative loss in the upper chromosphere, direct chromospheric heating results in a significant portion of the energy being radiated away and less

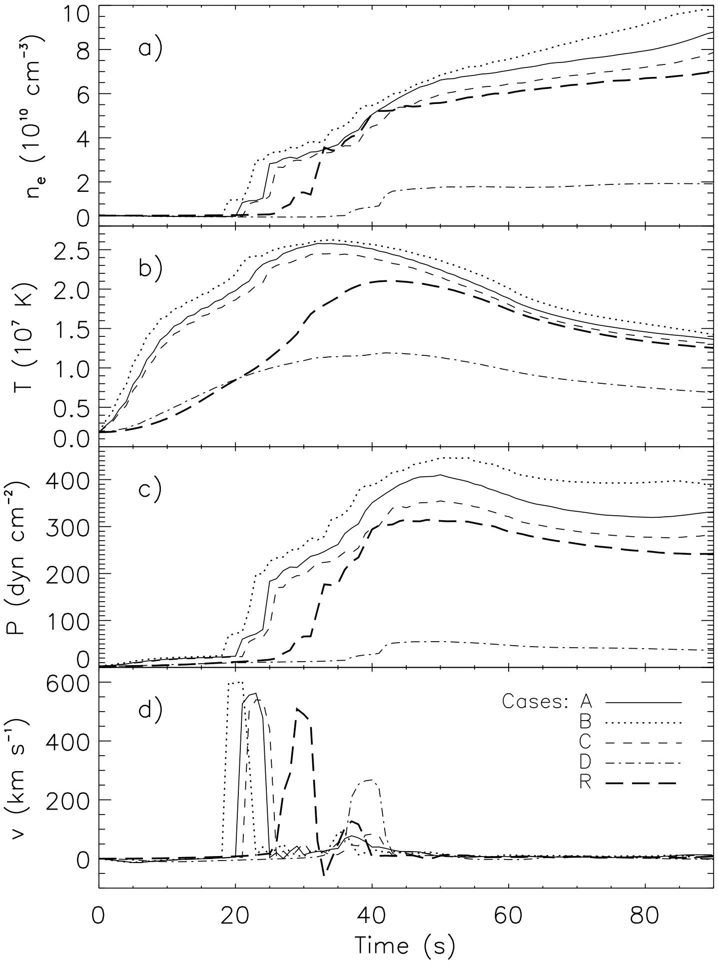

Figure 7.19: Comparison of history of various quantities (electron number density, temperature, gas pressure, and upward velocity) at 1 Mm from the LT for the five cases. Note that each of the density and pressure curve general includes two sharp jumps, which are caused by the arrival of the evaporation front, similar to that shown in Figure 7.4.

energy left available to evaporate the plasma. In this sense, our new model generally drives chromospheric evaporation more efficiently.

3. The change of the acceleration rate (τ_p^{-1}) affects the accelerated electron spectrum, as well as the escaping electron spectrum, and thus modifies the consequent HD evolution. In general, a higher acceleration rate produces a harder electron spectrum but smaller escaping electron flux, because stronger turbulence scatters particles more and traps them longer in the acceleration region. These two factors add together to produce less coronal heating (although relatively more chromospheric heating). Therefore, for the same reason mentioned above, this results in a comparably weaker chromospheric evaporation for a harder electron spectrum.

4. For the reasons noted above, the overall energy input rate is only one indicator, to some extent, of the agent for HD energetics. A smaller energy deposition flux (e.g., the $\bar{F}$ value, Case A vs. Case R) does not necessarily yield a slower HD evolution or a weaker chromospheric evaporation. Therefore, detailed energy deposition by electrons, particular its spatial distribution affects the resulting HD response.

5. Variation in the electron spectrum influences the HD response and bremsstrahlung emission in different ways. A harder electron spectrum can produce HXRs more effectively due to its higher bremsstrahlung yield, but does not necessarily produce more heating (e.g., Case C). Therefore, HXRs alone should not be used as an indicator of the electron energy input rate or subsequent plasma heating. This will be addressed in detail regarding the Neupert effect in next chapter.

This simulation experiment, has just been started for a short period of time (less than half a year). However, it opens a door to a vast area of applications to many other fields where particle acceleration and plasma flows are present, such as stellar flares and flares near the black holes and on the accretion disks. There is plenty of room for future improvement in both numerics and physics, which will be discussed in the Chapter 10.

Chapter 8

Testing the Neupert Effect With the Combined Fokker-Planck and Hydrodynamic Codes

8.1 Energy Budget and the Neupert Effect

As shown in Chapter 6 (also Liu, W. et al. 2006), a simple test of the Neupert effect does not yield a better correlation between the SXR derivative and the electron power than that between the former and the HXR flux. This is not expected to be the case, but it is not surprising either because of nonlinearity involved in the energy redistribution and radiation processes. To further understand this question, one needs to check the energy budget and calculate HXR and SXR radiation properly. Veronig et al. (2005) investigated the Neupert effect using *RHESSI* observations and reached similar conclusion as we did. However, they calculated the various energy contents in an approximate way. The combined HD and particle calculation we have done here can help shed light on this question more quantitatively.

In general, the total energy $U(t)$ in the plasma consists of thermal energy $U_{\rm th}(t)$, kinetic energy $U_k(t)$, and gravitational energy $U_g(t)$.

$$U(t) = U_{\rm th}(t) + U_k(t) + U_g(t), \tag{8.1}$$

which can be readily calculated (integrating over the loop volume) from the distribution of density ρ (or n_e and n_i), temperature T, velocity v. For example,

$$U_{\rm th} = \int \frac{P}{\gamma - 1} dV = \int 3 n_e k T dV, \tag{8.2}$$

for $\gamma = 5/3$, and $n_e = n_i$. We set the reference level (zero height) of the gravitational potential at the bottom boundary (about 4 Mm below the transition region) and this gives the the value of U_g about 1/3 of the total energy in the initial state ($t = 0$). We find in all of our simulations that the temporal variation rate of the gravitational energy only constitutes about 1% of that of the total energy and thus is unimportant in the energy budget (and not shown in our discussion below). The time derivative of these energies,

$$\dot{U}(t) = \dot{U}_{\rm th}(t) + \dot{U}_k(t) + \dot{U}_g(t), \tag{8.3}$$

gives the net energy gain of the system and should be balanced by the energy input (by electrons) rate $\dot{\mathcal{E}}_e$ and the energy loss rate L, namely,

$$\dot{U} = \dot{\mathcal{E}}_e - L\,. \tag{8.4}$$

The total energy loss rate generally has two components, radiative loss ($L_{\rm rad}$) and conductive loss ($L_{\rm cond}$) from the loop volume. In this particular study, the conduction flux vanishes at both the top and bottom boundaries, where we set the symmetric boundary condition and fix the temperature at $T = 10^4$ K, respectively, both giving rise to $\nabla T = 0$. Therefore, the only energy loss channel is through radiation (UV and optical),

$$L = L_{\rm rad} + L_{\rm cond}\,; \;\; L_{\rm cond} = 0 \implies L = L_{\rm rad}\,. \tag{8.5}$$

Thermal bremsstrahlung radiation at photon energy ϵ produced by a single temperature (i.e., Maxwellian distribution) plasma can be calculated via (Allen 2000, p 184; Emslie book p 114):

$$I_{\rm SXR} = D({\rm EM}) \frac{\exp(-\epsilon/kT)}{\epsilon\sqrt{T}} g(\epsilon/kT), \tag{8.6}$$

in which

$$D = (8/\pi m_e k)^{1/2} \kappa_{BH} Z^2 = 5.7 \times 10^{-12} Z^2 ({\rm cm}^3\,{\rm s}^{-1}\,{\rm K}^{1/2}),$$

where Z is the mean ionic charge which equals unity in our model and $\kappa_{BH} = (8\alpha/3) r_0^2 m_e c^2 =$

$7.9 \times 10^{-25}\,\mathrm{cm}^2\,\mathrm{keV}$ is the constant in the Bethe-Heithler bremsstrahlung cross-section ($\alpha = 1/137$), $\mathrm{EM} = \int n_e n_i dV = \int n_e^2 dV$ is the emission measure (assuming $n_e = n_i$), $g(\epsilon/kT) = (kT/\epsilon)^{2/5}$ is the Gaunt factor (valid for temperature range $T > 7 \times 10^5\,\mathrm{K}$, Li et al. 1993). Substituting these quantities into equation 8.6, we have

$$I_{\mathrm{SXR}} = \frac{5.7 \times 10^{-12}}{\epsilon\sqrt{T}} \exp\left(-\frac{\epsilon}{kT}\right) \left(\frac{kT}{\epsilon}\right)^{2/5} \int n_e^2 dV \quad (\mathrm{photons\,s^{-1}\,keV^{-1}}), \tag{8.7}$$

where ϵ is in keV, T in K, and n_e in cm^{-3}. In contrast to U_{th}, I_{SXR} depends on n_e and T nonlinearly. In addition, I_{SXR} is not a monotonic function of T (see Figure 8.1).

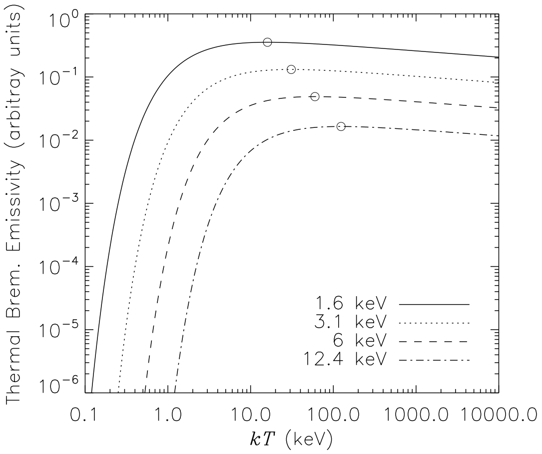

Figure 8.1: Thermal bremsstrahlung emissivity as a function of plasma temperature at different photon energies: $\epsilon = 1.6$, 3.1, 6, 12.4 keV. The open circles mark the maxima of these curves at the corresponding temperature of $T_{\mathrm{max}} = 10\epsilon/k$.

Differentiating equation (8.7) gives the temperature where the maximum of I_{SXR} is located,

$$\frac{\partial I_{\mathrm{SXR}}}{\partial T} = \frac{I_{\mathrm{SXR}}}{T}\left(\frac{\epsilon}{kT} - \frac{1}{10}\right) \Longrightarrow T_{\mathrm{max}} = 10\epsilon/k, \tag{8.8}$$

below (above) which I_{SXR} increases (decreases) monotonically with T. In other words, when a plasma is overheated and its temperature exceeds $10\epsilon/k$, its thermal radiation will decrease with increasing temperature[1]. This introduces more nonlinearity into the dependence of I_{SXR} on T. In the low temperature range, $T < T_{\mathrm{max}}$, however, a positive

---

[1] However, the total bremsstrahlung radiation increases as $\sqrt{T}$.

correlation (not necessarily linear though) between the thermal bremsstrahlung radiation $I_{\rm SXR}$ and the thermal energy $U_{\rm th}$ is expected. Or equivalently, their time derivatives, $\dot{I}_{\rm SXR}$ and $\dot{U}_{\rm th}$, would also exhibit a similar correlation.

The *GOES* low channel (1–8 Å , 1.6–12.4 keV) flux is usually used as the SXR emission in Neupert effect studies. As long as $kT < 16\,{\rm keV}$ (which is usually the case for solar flares) the condition of $kT < 10\epsilon$ is satisfied in the entire 1–8 Å channel, so that $I_{\rm SXR}$ is an increasing function of T and we expect a positive $\dot{I}_{\rm SXR}$–$\dot{U}_{\rm th}$ correlation. To check if such an correlation is present in our five simulation cases we calculate, as shown in the following subsections, the thermal bremsstrahlung emission at $\epsilon = 1.6\,{\rm keV}$ [2] and $\epsilon = 6\,{\rm keV}$, which are at the low energy end and near the middle of the 1–8 Å channel, respectively.

8.2 Case R: Reference Calculation

8.2.1 History of Energy Budget

Let us check the **energy budget history** of Case R, which is shown in Figure 8.2. The total energy, thermal energy, and kinetic energy integrated over the whole loop are plotted in panel *a*; their time derivatives together with the electron energy deposition power $\dot{\mathcal{E}}_e$ and radiative loss rate $L_{\rm rad}$ are shown in panel *b*. As is evident, early on ($t \lesssim 15\,{\rm s}$) most of the energy deposited by electrons is quickly radiated away. This is because the coronal density is low at this time and the electron energy deposition is concentrated in the upper chromosphere where radiative loss is the highest (see Figure 7.3). As a result, only a small fraction of electron energy is available to heat the plasma and produces a slow increase of the total energy (Figure 8.2*b*). However, as the flare evolves and chromospheric evaporation takes place, the coronal density increases and more electron energy is deposited above the transition region. This part of energy in turn heats and evaporates plasma more efficiently than in the upper chromosphere. Therefore, the radiative loss rate gradually drops and its competitor, electron energy deposition, takes over the control of the energy budget. This effect is present in Figure 8.2*b* as the rapid

---

[2] Note that continuum emission dominates over line emission in the *GOES* 1–8 Å channel (Culhane & Acton, 1970) and thus thermal free-free emission at a photon energy of 1.6 keV would be a good protocol for the *GOES* 1–8 Å flux. We take the low energy end (1.6 keV) because of the exponential decay (with photon energy) of thermal free-free emission. However, if one attempts to make a direct comparison with *GOES* observations, line emission must be calculated, say, using the current Chianti code, and then be added to the continuum and integrated over the entire 1–8 Å range, which is beyond the scope of this study.

rise of the total energy change rate at about $t = 20\,\mathrm{s}$.

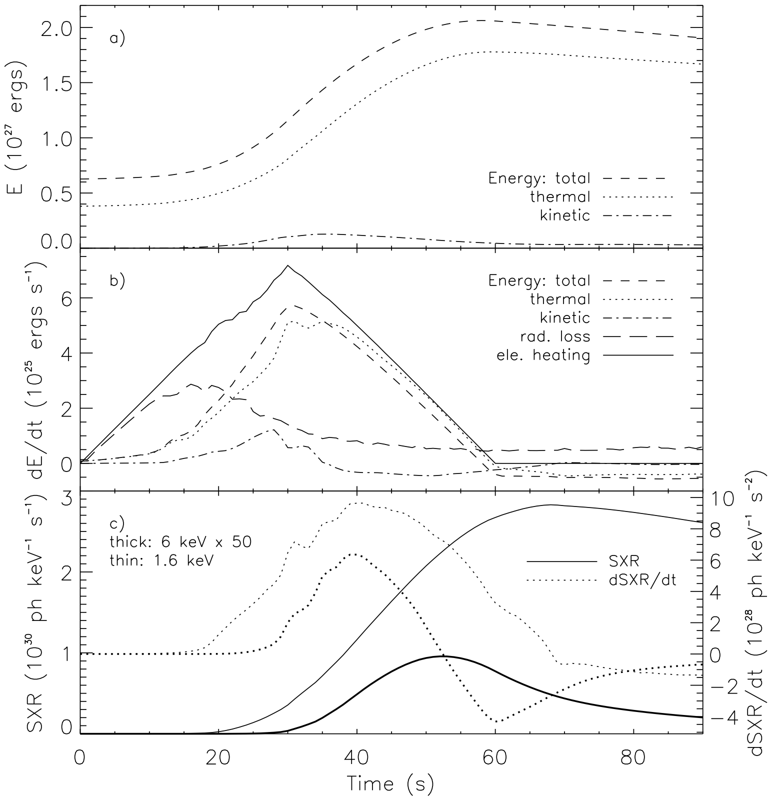

Figure 8.2: History of energy budget and X-ray emission for Case R. (*a*) Spatially integrated total energy (U), thermal energy (U_{th}), and kinetic energy (U_k) of the whole loop. (*b*) Time derivative ($\dot{U}$, $\dot{U}_{\mathrm{th}}$, and $\dot{U}_k$) of the above three energies (same line styles), together with the total electron energy deposition power ($\dot{\mathcal{E}}_e$, *solid*) and the radiative loss power (L_{rad}, *long dashed*). (*c*) SXR fluxes (I_{SXR}, *solid*) at photon energy of 1.6 (*thin*) and 6 keV (*thick*) and their time derivatives ($\dot{I}_{\mathrm{SXR}}$, *dotted*). The 6 keV light curve is rescaled up by a factor of 50.

The energy partition between the thermal and kinetic energy also evolves with time. Early in the flare, because evaporation is still in its infancy, the kinetic energy of the system is very small, and the total energy change is dominated by the variation of the thermal energy (Figures 8.2*a* and 8.2*b*). For example, at $t = 10\,\mathrm{s}$, the kinetic energy is only 8.35×10^{23} ergs changing at a rate of $1.91 \times 10^{23}\,\mathrm{ergs\,s^{-1}}$, compared with the values of the thermal energy: $U_{\mathrm{th}} = 3.99 \times 10^{26}$ ergs and $\dot{U}_{\mathrm{th}} = 3.50 \times 10^{24}\,\mathrm{ergs\,s^{-1}}$. As evaporation grows, the kinetic energy rises gradually, which makes the thermal energy deviates from the total energy curve at about $t = 15\,\mathrm{s}$. The kinetic energy change rate reaches its maximum at $t = 28\,\mathrm{s}$ just before the evaporation front arrives at the loop apex. Afterwards, $\dot{U}_k$ decreases quickly because of the reflection of the evaporation front and part of the kinetic energy is converted into the thermal energy due to local gas compression at the apex, which leads to the rapid rise of the $\dot{U}_{\rm th}$ curve (Figure 8.2*b*), although there is no sudden change in the electron energy deposition at this time. This means that, on top of the electron beam heating, gas dynamics can also change energy partition and thus can modulate the thermal energy which would be manifested in the change of the SXR flux (see below). (This effect would produce further deviation from the Neupert effect.)

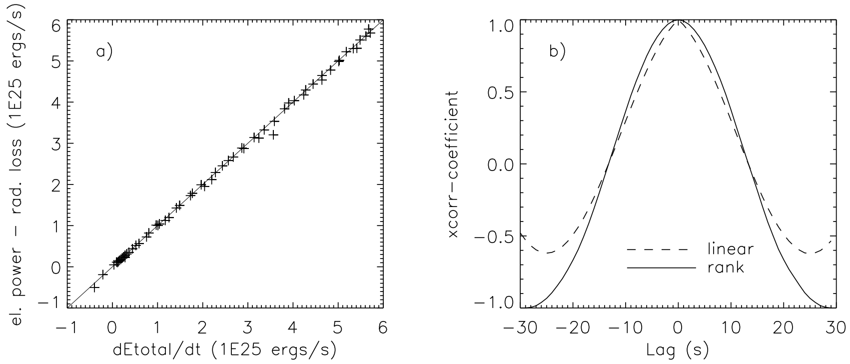

Figure 8.3: Consistency test of equation (8.4) for Case R. (*a*) The electron energy deposition power minus the radiative loss ($\dot{\mathcal{E}}_e - L_{rad}$) vs. the total energy change rate ($\dot{U}$). The diagonal line corresponds to a perfect agreement. (*b*) Pearson linear (dashed) and Spearman rank (solid) cross-correlation coefficients of the two quantities shown in (*a*), plotted as a function of the time lag. The two coefficients have their maxima of 0.99950 and 0.99956, respectively, at the zero lag.

It is necessary to see if **energy gain and loss** is actually balanced as a consistency check of the code. In Figure 8.3*a* we plot the net energy input ($\dot{\mathcal{E}}_e - L_{\rm rad}$) vs. the total energy change rate ($\dot{U}$). Clearly, the two quantities are almost in perfect agreement. We also cross-correlate the two and the Pearson linear (*dashed*) and Spearman rank[3] (*solid*) cross-correlation coefficients (Figure 8.3*b*) have a peak value of 0.99950 and 0.99956, respectively, indicating a very high correlation. Therefore we are assured that energy is conserved and equation (8.4) is indeed satisfied in our simulations. We note that this correlation is actually the "real" Neupert effect on the basis of an exact energy budget argument and we will use it as a reference point in this study.

---

[3] The Spearman rank correlation coefficient is an indicator of an either linear or nonlinear correlation.

8.2.2 Neupert Effect Test

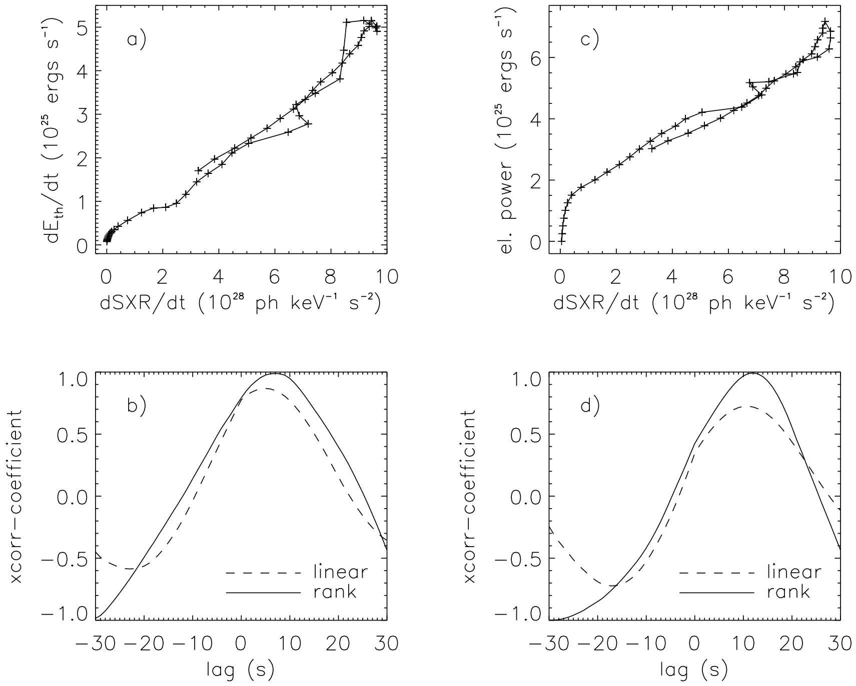

Figure 8.4: Neupert effect test for Case R. (*a*) Thermal energy change rate $\dot{U}_{\rm th}$ vs. SXR derivative $\dot{I}_{\rm SXR}$ (at photon energy of $\epsilon = 1.6\,{\rm keV}$) during the first 60 s of the flare. The solid line that connects the symbols indicates the time evolution, starting near the lower-left corner at $t = 0\,{\rm s}$. $\dot{I}_{\rm SXR}$ has been shifted back in time by 7 s to compensate its delay, as indicated by the cross-correlation analysis (see below and text). (*b*) Pearson linear (dashed) and Spearman rank (solid) cross-correlation coefficients of the two quantities shown in (*a*), plotted as a function of the time lag (> 0 means delay) of $\dot{I}_{\rm SXR}$ relative to $\dot{U}_{\rm th}$. The rank correlation coefficient reaches its maximum value of 0.989 at a lag of 7 s. (*c*) and (*d*) same as (*a*) and (*b*), respectively, but for the correlation between $\dot{\mathcal{E}}_e$ (electron energy deposition power) and $\dot{I}_{\rm SXR}$ (shifted back by 12 s).

Let us now check if the Neupert effect is present. We plot in Figure 8.2*c* the spatially integrated thermal SXR photon flux $I_{\rm SXR}$ (*solid*, photons ${\rm keV}^{-1}\,{\rm s}^{-1}$, at the Sun) at two energies, 1.6 keV (*thin*) and 6 keV (*thin*, scaled by a factor of 50). We find the lower energy SXR light curve rises earlier and faster, and decays later and slower, than the higher energy one. The shape of the 1.6 keV curve resembles that of the thermal energy (8.2*a*) because of their close relationship due to their dependence on n_e and T as noted above. It also mimics commonly observed *GOES* light curves (see, e.g., Figure 6.1 in Chapter 6). The 6 keV light curve, however, appears comparably short in duration. This is because the 6 keV thermal emission is more sensitive to higher temperature plasmas (peak temperature response at 60 keV) and the temperature dependence of the thermal bremsstrahlung emissivity is very sharp in its rise portion (see Figure 8.1). Therefore, early in the flare, when high temperature emission measure is small, there is very little 6 keV thermal emission; similarly in the decay phase, the 6 keV emission decreases quickly when the plasma cools off.

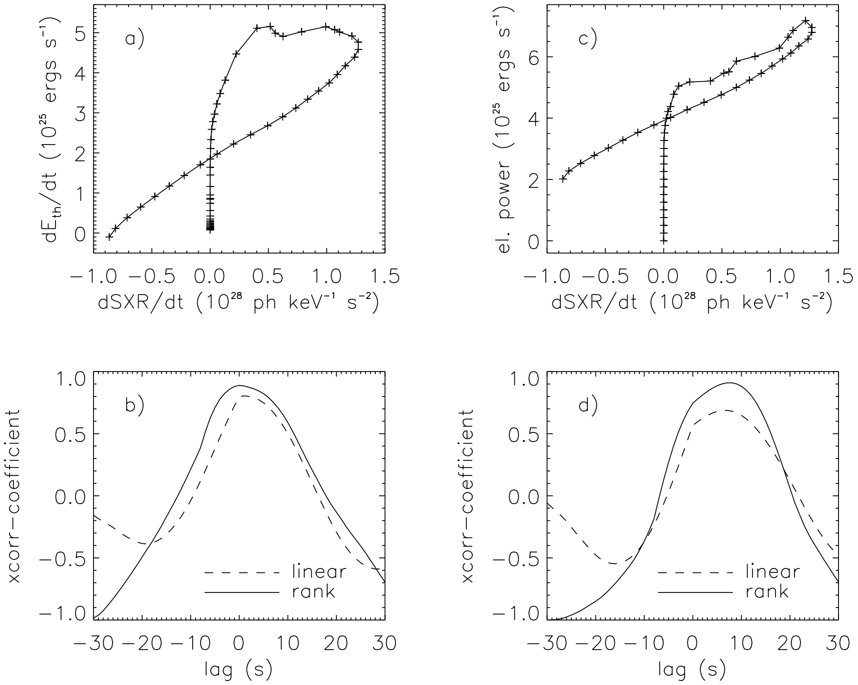

Figure 8.5: Same as Figure 8.4 (Case R), but for photon energy $\epsilon = 6\,\text{keV}$. $\dot{I}_{\text{SXR}}$ in (c) is shifted back by 8 s to compensate its delay.

To get more detailed timing information, we took the time derivatives of the two SXR fluxes, following the common practice for Neupert effect studies. The result is shown as the dotted lines (*thin*: 1.6 keV, *thick*: 6 keV) in Figure 8.2*c*. By visual comparison with the electron energy deposition power ($\dot{\mathcal{E}}_e$) and the thermal energy change rate ($\dot{U}_{\text{th}}$) in Figure 8.2*b*, we find that these curves resemble each other in a way or another. They all roughly show a triangular shape. Particularly, the $\dot{I}_{\text{SXR}}$ curves even follow $\dot{U}_{\text{th}}$ in some detail. For example, $\dot{I}_{\text{SXR}}$ at both energies exhibits a rapid rise at about $t = 29\,\text{s}$ when an abrupt increase in $\dot{U}_{\text{th}}$ occurs (due to gas dynamics, see above). However, such a detailed change is not present in the $\dot{\mathcal{E}}_e$ curve, which is equivalent to the HXR flux here[4]. Therefore, if one attempts to look for the Neupert effect by comparing the SXR derivative and the HXR flux (as people usually do), such a subtle correlation could be missing in HXRs. In this sense, a more physical Neupert effect would be the relationship between the thermal energy change rate and the SXR derivative.

We have carried out statistical analysis and checked the correlations between these various variables more quantitatively. We first cross-correlated the SXR derivative $\dot{I}_{\rm SXR}$ at 1.6 keV with the thermal energy change rate $\dot{U}_{\rm th}$ and with the electron energy deposition power $\dot{\mathcal{E}}_e$, the correlation coefficients of which are shown in Figures 8.4*b* and 8.4*d*, respectively. For $\dot{I}_{\rm SXR}$ and $\dot{U}_{\rm th}$, the linear correlation coefficient has a peak value of 0.868 at a lag of 5 s, and the rank correlation peaks (max = 0.989) at a lag of 7 s, both indicating a significant correlation and a delay of $\dot{I}_{\rm SXR}$ relative to $\dot{U}_{\rm th}$. Such a delay is also visible in Figures 8.3*b* and 8.3*c*, say, by comparing the rise portion and the peak position of the corresponding curves. Since their physical relationship is nonlinear *per se* as discussed above, we believe the rank correlation can describe the connection between $\dot{I}_{\rm SXR}$ and $\dot{U}_{\rm th}$ more generally than the linear correlation, although the two correlations give us different perspectives when looking at the same phenomenon. We thus use the delay indicated by the rank correlation to shift $\dot{I}_{\rm SXR}$ back in time and plot $\dot{U}_{\rm th}$ vs. $\dot{I}_{\rm SXR}$ in Figure 8.4*a*. We find these two quantities indeed have a strong correlation since their data points in the scatter plot very much distribute along a straight line. In contrast, for $\dot{I}_{\rm SXR}$ and $\dot{\mathcal{E}}_e$, the linear (rank) correlation coefficients reaches its maximum of 0.724 (0.993) at a lag of 11 s (12 s). This indicates a weaker linear correlation (although a slightly stronger rank correlation), compared with the correlation for $\dot{I}_{\rm SXR}$ and $\dot{U}_{\rm th}$. It also reveals a longer delay, which could be ascribed to the fact that the rise portion of $\dot{U}_{\rm th}$ itself actually delays relative to the energy deposition rate, $\dot{\mathcal{E}}_e$, (Figure 8.3*b*) because of the strong radiative loss at early times as noted before.

We also repeated the above analysis for SXR emission at photon energy of 6 keV for comparison. The result is shown in Figure 8.5. In general, we find a weaker correlation and a shorter delay (see Table 8.1). The shorter delay (despites its actual delay in the rise portion) is due to the rapid decrease of the 6 keV light curve during its decay, which

---

[4] For Case R only, the HXR flux could not be readily calculated without running the transport and radiation code for the assumed power-law electron spectrum. Here, we use $\dot{\mathcal{E}}_e$ as a protocol for the HXR flux since they are proportional to each other (because the electron spectrum remains constant in time and the bremsstrahlung yield is thus a constant as well).

mimics the same trend in the $\dot{\mathcal{E}}_e$ and $\dot{U}_{\rm th}$ curves (Figure 8.2). However, it is noted that the 1.6 and 6 keV derivatives both peak at about the same time, $t = 40\,$s. As we will show below, this is a particular feature of this Case. It is interesting to see that the curves in Figures 8.5*a* and 8.5*c* both show a crossed loop-like shape, reminiscence of that in Figure 6.13*e*.

8.3 Cases A-D: Combined HD & Particle Calculation

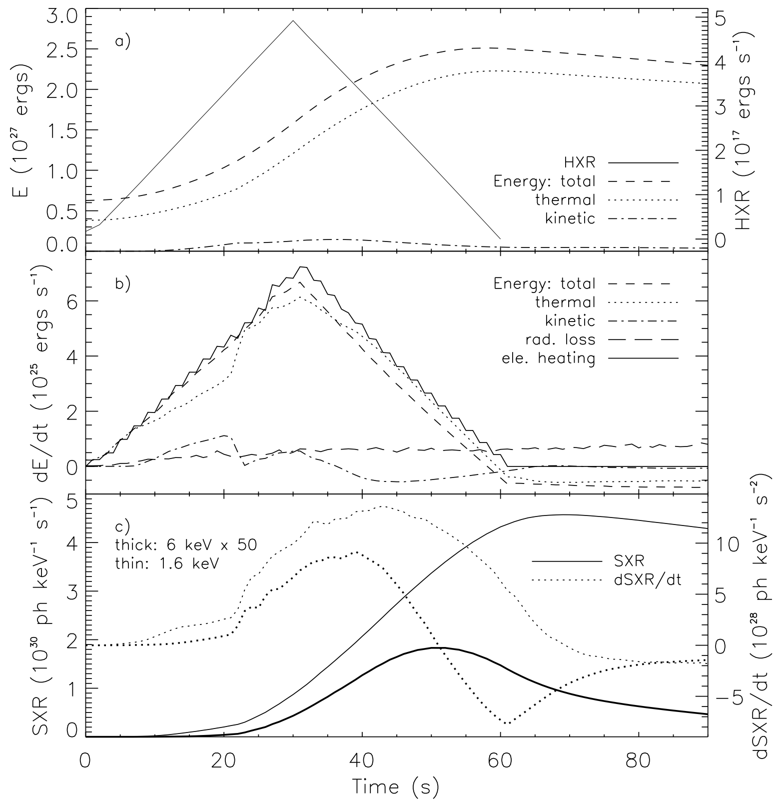

Figure 8.6: Same as Figure 8.2, but for Case A. We also plot in (*a*) the HXR emission power of all photons whose energy is greater than 20 keV.

For comparison, we did the same analysis as above for the other four cases, which we describe as follows. The only new quantity is the HXR ($E > 20\,$keV) flux calculated from our radiation code, which we will use here in place of the electron energy deposition power for cross-correlating with the SXR derivative.

8.3.1 Case A: Fiducial Run with SA Model

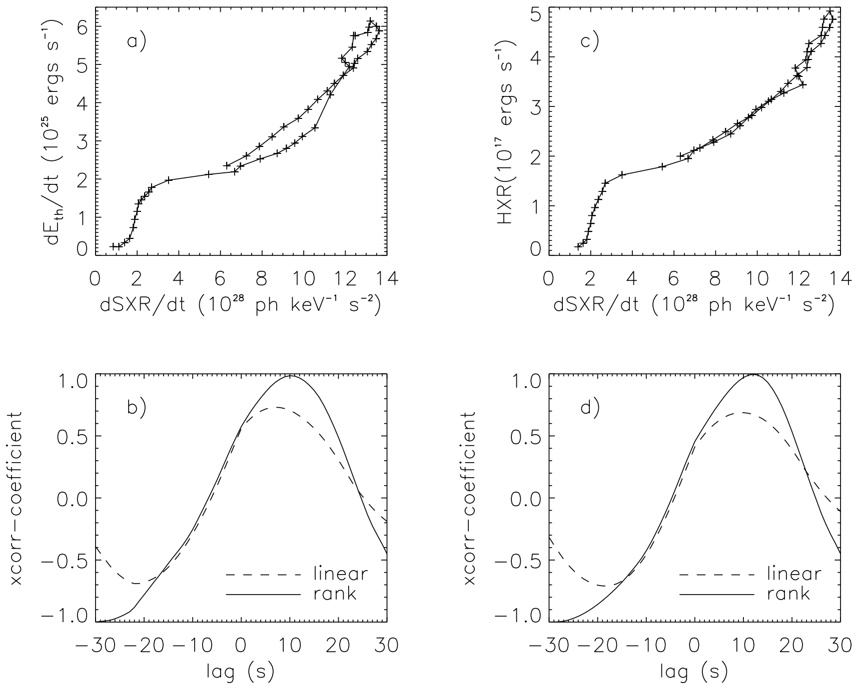

Figure 8.7: Same as Figure 8.4 but for Case A and the HXR (> 20 keV) emission power ($I_{\rm HXR}$) (rather than the electron energy deposition power). SXR derivatives in (*a*) and (*c*) are shifted back in time by 10 and 12 s, respectively, according to their delays indicated by the peak of the Pearson rank correlation coefficient shown in (*b*) and (*d*).

For Case A, the energy budget history is shown in Figure 8.6. We find that the overall evolution of the energies is similar to that of Case R (Figure 8.6). However, we do see three major differences, the first of which is relatively small importance of the radiative loss here, particularly during the rise phase of the flare. This is because, as we discussed earlier, the electron spectrum contains a quasi-thermal component at low energies and this produces relatively more energy deposition in the corona than in the upper chromosphere where radiative loss is most efficient. As a result, less energy is available for radiative loss and more energy is left to evaporate the chromospheric plasma. The second difference is that the 6 keV light curve starts its rise earlier than in Case R, because the preferential coronal heating here (vs. more chromospheric heating in Case R) produces relatively higher emission measure at high temperatures from which the

6 keV emission is more productive. The 6 keV light curve also peaks earlier than the 1.6 keV one by about 5 s, as opposed to their concurrence in Case R. For the same reason, we have stronger chromospheric evaporation, and thus higher coronal temperature and density here, resulting in a higher SXR flux with a maximum of 4.57 (vs. 2.83 in Case R) $\times 10^{30}$photons keV^{-1} s^{-1} at 1.6 keV. The third major difference is that Case A has a faster evolution and the evaporation front reaches the loop apex earlier at $t = 22$ s (vs 29 s in Case R). The associated compressional heating produces a sudden jump at this time in the thermal energy change rate, as well as in the two SXR derivative curves.

We also cross-correlated the SXR derivative with the thermal energy change rate $\dot{U}_{\rm th}$ and the HXR energy flux $I_{\rm HXR}$. The resulting correlation coefficients for the 1.6 keV photon energy are shown in Figure 8.7 We find a weaker linear correlation[5] for both $\dot{U}_{\rm th}$ and $I_{\rm HXR}$ with $\dot{I}_{\rm SXR}$, compared with that in Case R (Figure 8.4), and the peak linear correlation coefficients are 0.731 and 0.687, respectively. The Pearson rank correlation, however, are

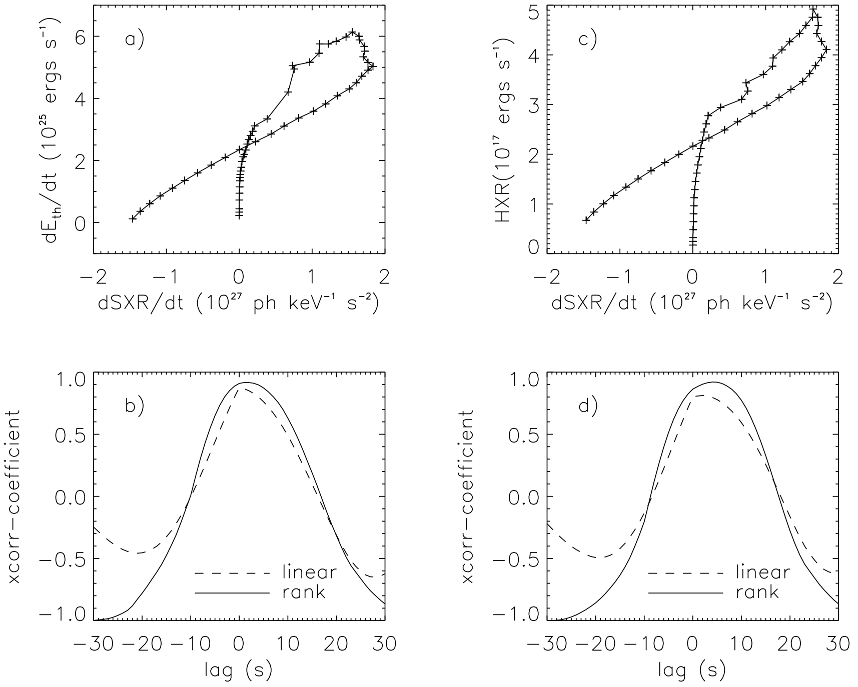

Figure 8.8: Same as Figure 8.7 for Case A but at a photon energy of 6 keV.

---

[5] This may have to do with stronger evaporation and more dramatic evolution in this Case, and thus more nonlinear phenomena are invoked.

very close to that of Case R, and the correlation coefficient for I_{HXR} is even higher (see Figure 8.7*c* and Table 8.1). This is not surprising, since a linear correlation between these quantities are actually not expected, as we discussed earlier, and their nonlinear correlation seems more likely. In contrast, the correlations for 6 keV photon energy (Figure 8.8, cf. Figure 8.5) are somewhat better than those of Case R (see Table 8.1). This might be due to the stronger coronal heating here that favors higher photon energy thermal emission. The shorter (than that in Case R) delay of the 6 keV derivative relative to the HXR flux, which was mentioned above, is also evident from the lag corresponding to the peak (linear or rank) correlation coefficient.

8.3.2 Case B: Variable Electron Spectrum

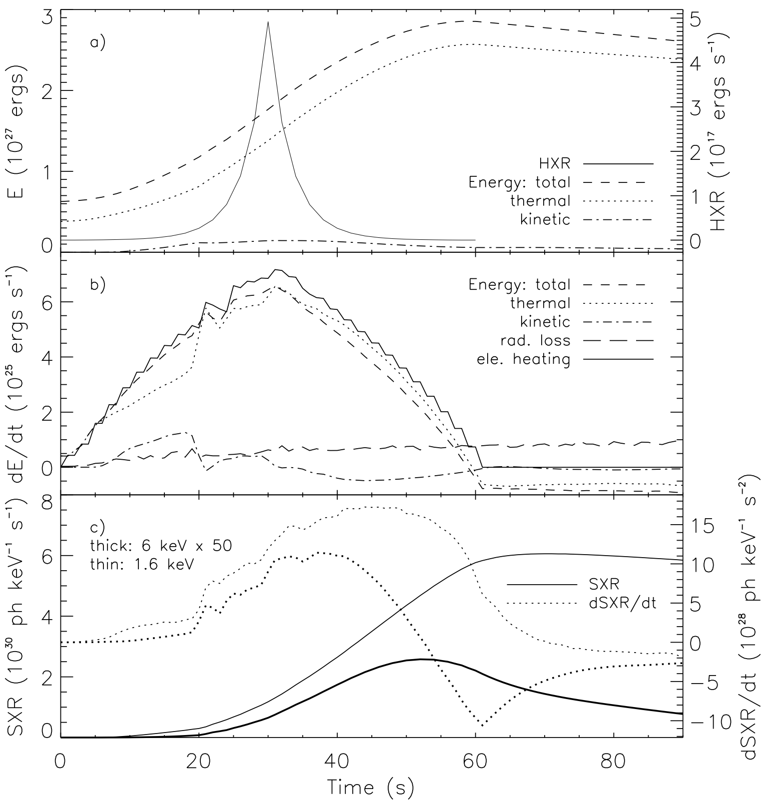

Figure 8.9: Same as Figure 8.6, but for Case B.

Case B has a particular electron spectrum that experiences a soft-hard-soft variation.

The energy budget history is shown in Figure 8.9. Compared with Case A, one of the main differences is the shape of the energy deposition rate, which appears to be warped and slightly higher than the linear one in Case A. This results in somewhat higher heating rate and faster evaporation (see Table 7.1). Another difference is the shape of the HXR light curve which differs quite a bit from the triangular one in Case A. This is because the soft-hard-soft variation of the electron spectrum, which modulates the bremsstrahlung yield and thus HXR flux on top of the triangular normalization variation. We also show the cross-correlation result for the 1.6 keV SXR in Figure 8.10. As can be seen, the linear correlation is somewhat weaker than that of Case A, especially for the HXR flux (see Figure 8.10*c*; note logarithm scale). However, the rank correlation coefficients are similar to that of Case A.

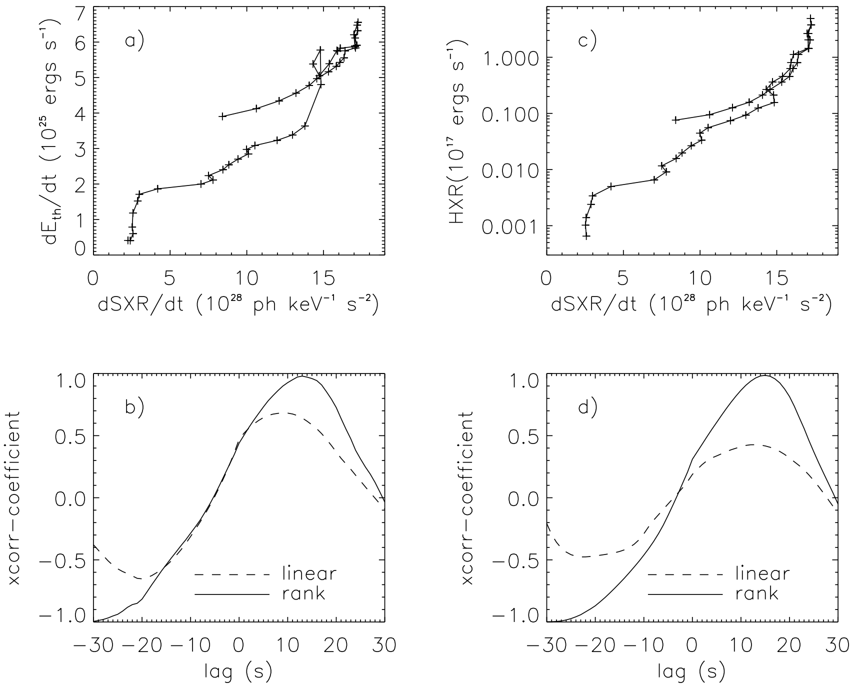

Figure 8.10: Same as Figure 8.7 but for Case B (at 1.6 keV). SXR derivatives in (*a*) and (*c*) are shifted back by 13 and 15 s, respectively, to account for their delays indicated in (*b*) and (*d*).

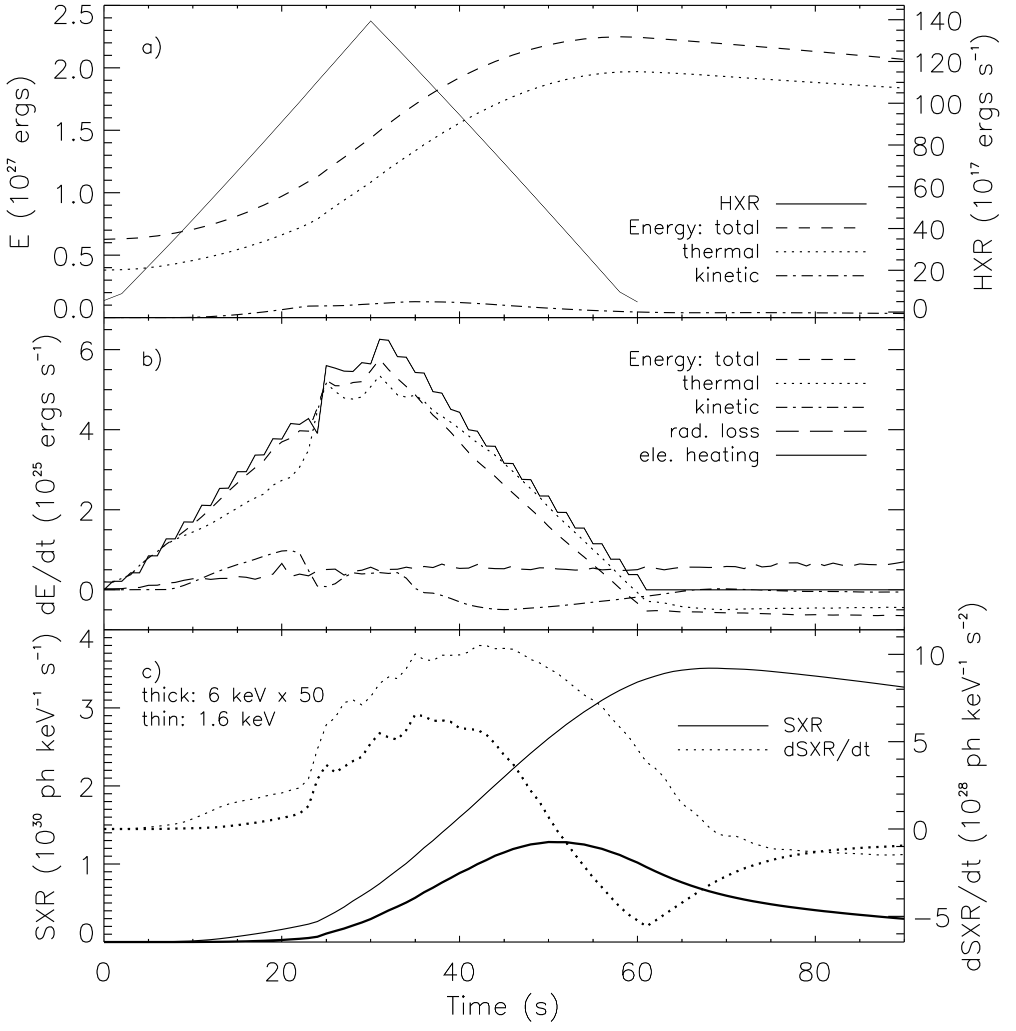

Figure 8.11: Same as Figure 8.6, but for Case C.

8.3.3 Case C: Harder Electron Spectrum

Case C has a harder electron spectrum compared with Case A because of its relatively shorter acceleration timescale ($\tau_p = 100\,\mathrm{s}^{-1}$ vs. $70\,\mathrm{s}^{-1}$). The history of the energy budget (Figure 8.11) and the cross-correlations (Figure 8.12) are similar to those of Case A, although its electron spectrum is much harder than that in Case A. The main difference is in the normalization of the HXR flux (see Figure 8.11*a*) which is about 28 times higher than that of Case A, simply because of harder electron spectrum results in a higher bremsstrahlung yield (see Figure 6.12) and thus higher HXR emission.

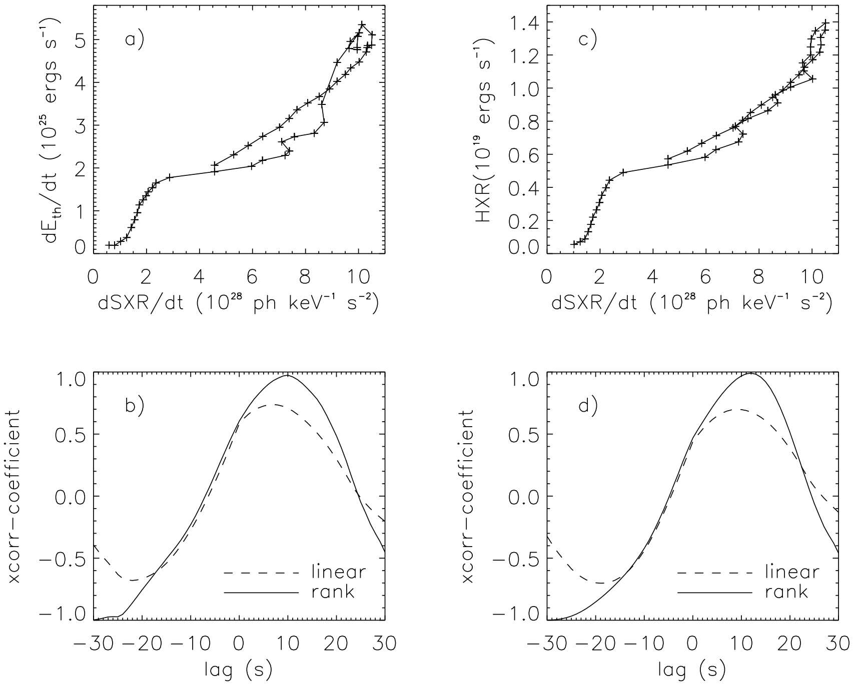

Figure 8.12: Same as Figure 8.7 but for Case C (at 1.6 keV). SXR derivatives in (*a*) and (*c*) are shifted back by 10 and 12 s, respectively, to make up for their delays.

8.3.4 Case D: Smaller Normalization

Case D has an energy input rate 10 times smaller than that of Case A and thus the flare is weaker by an order of magnitude, as can be seen from the various quantities shown in Figure 8.13. The overall energy evolution appears similar to Cases A-C, except that the

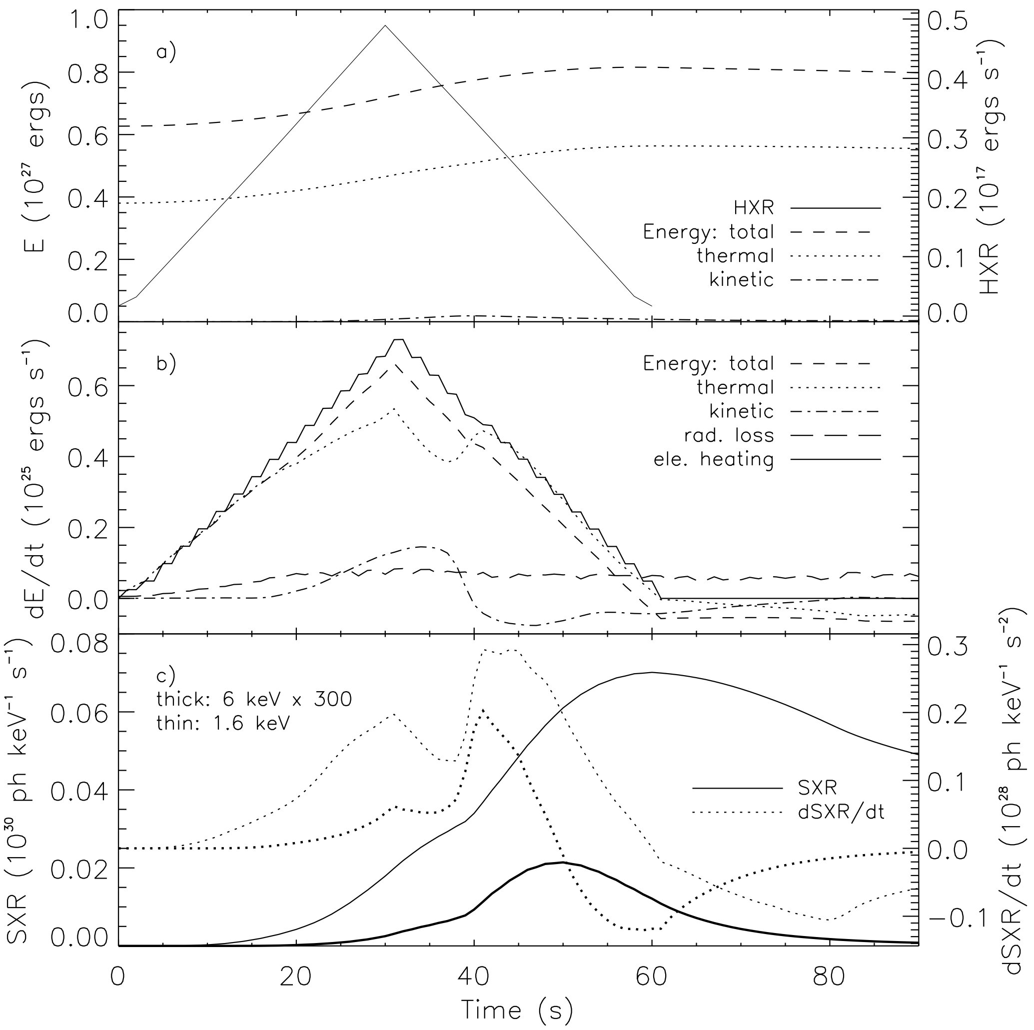

Figure 8.13: Same as Figure 8.6, but for Case D. Note that the 6 keV SXR light curve in (*c*) is rescaled by a factor of 300 (cf. 50 in the other four cases) due to the softness of the thermal spectrum in this case of weak evaporation.

evaporation front arrives at the loop apex late ($t = 39\,\mathrm{s}$, well into the decline phase). At this time, the kinetic energy change rate ($\dot{U}_k$) shows the largest continuous drop (with a range of $\Delta\dot{U}_k/\dot{U}_{\max} = 0.33$, normalized by the peak energy input rate $\dot{U}_{\max}$, cf., e.g., 0.16 for Case A) among all the five cases, partly because this drop coincides with the decrease of the energy input rate and that of the other cases takes place during the rise phase. In exchange of the decrease in $\dot{U}_k$, the thermal energy change rate still attains a net gain, despite the decrease of the total energy change rate. This rise produces a dramatic increase in SXR flux derivatives at both the 1.6 and 6 keV, which even dwarfs the first peak produced at the time of the maximum total energy input rate. The relative height of the two peaks on the $\dot{U}_{\rm th}$ curve (Figure 8.13), however, does the opposite, although the timing of the two peaks agrees that of the SXR derivative pulses. We attribute this, again, to the nonlinearity of the contribution of density and temperature to thermal bremsstrahlung emission, and particularly to the sensitive dependence on temperature, i.e., the sharp rise at low temperatures below the maximum of the emissivity curve (see Figure 8.1). The

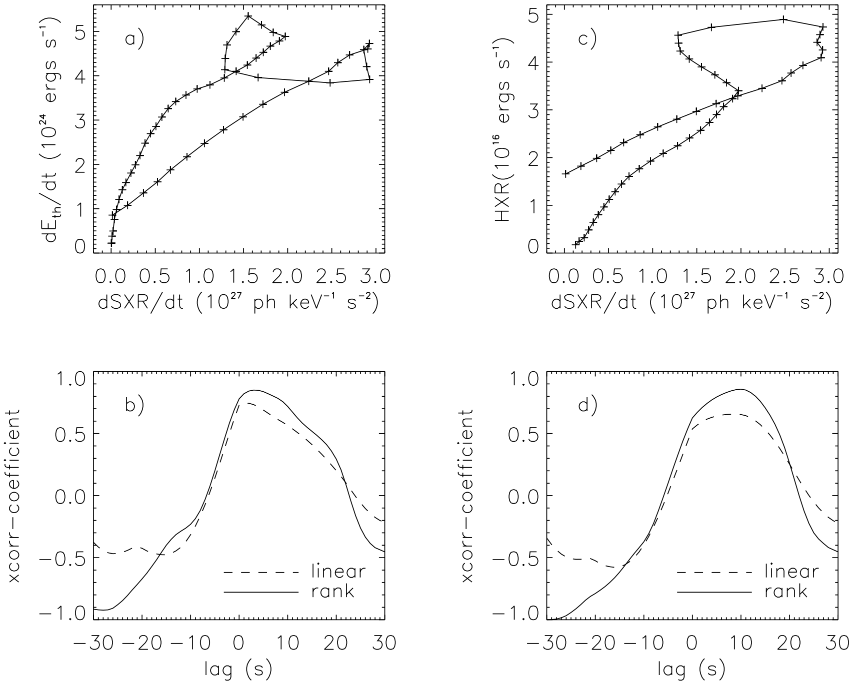

Figure 8.14: Same as Figure 8.7 but for Case D (at 1.6 keV). SXR derivatives in (*a*) and (*c*) are shifted back by 3 and 10 s, respectively.

cross-correlation result is shown in Figure 8.14. Clearly, we find a correlation much weaker the other cases for both the thermal energy change rate and the HXR flux, which can also be seen from the coefficients tallied in Table 8.1.

8.4 Summary and Discussion

We have performed a test of the Neupert effect for five simulation cases described in Chapter 7, using our SA model and the NRL HD flux tube model. We followed the temporal evolution of various energies (thermal, kinetic, and total), the electron energy deposition power, and the radiative loss, together with thermal and nonthermal bremsstrahlung radiation, spatially integrated over the whole flare volume. We then checked the temporal and statistical correlation between the SXR derivative ($\dot{I}_{\rm SXR}$) and the HXR flux ($I_{\rm HXR}$), and between $\dot{I}_{\rm SXR}$ and the thermal energy change rate ($\dot{U}_{\rm th}$). The statistical correlation analysis for all the five cases is summarized in table 8.1 and we itemize our results as follows.

Table 8.1: Neupert effect test of simulation cases ($\epsilon = 1.6$, 6 keV).

ϵ	Case	Pearson Linear Correlation				Spearman Rank Correlation			
(keV)		$\dot{U}_{\rm th}$: coef,	lag (s);	$I_{\rm HXR}$: coef,	lag	$\dot{U}_{\rm th}$: coef,	lag;	$I_{\rm HXR}$: coef,	lag
1.6	R	0.868	5	0.724	11	0.989	7	0.993	12
	A	0.731	7	0.687	10	0.985	10	0.996	12
	B	0.683	9	0.427	13	0.980	13	0.985	15
	C	0.738	7	0.699	9	0.975	10	0.991	12
	D	0.744	2	0.656	9	0.850	3	0.857	10
6	R	0.804	1	0.688	7	0.889	0	0.909	8
	A	0.876	0	0.812	2	0.916	1	0.920	4
	B	0.890	0	0.624	7	0.923	2	0.933	5
	C	0.875	0	0.815	2	0.907	1	0.910	3
	D	0.696	0	0.589	3	0.854	0	0.833	5

NOTE — For case R, the electron energy deposition rate is used as a protocol for the HXR flux (not available) to calculate the correlation with the SXR derivative.

1. We find that a correlation exists between $\dot{I}_{\rm SXR}$ and $\dot{U}_{\rm th}$, as well as between $\dot{I}_{\rm SXR}$ and $I_{\rm HXR}$. The latter correlation is in agreement with the empirical Neupert effect observed in some (but not all) flares.

2. The resulting Spearman rank (linear or nonlinear) correlation coefficients are generally greater than the Pearson (linear) correlation coefficients. When the linear correlation breaks down, the nonlinear correlation still holds (see, e.g., Case B).

This is expected since the correlation is essentially nonlinear due to the nonlinearity involved in the radiation (thermal and nonthermal bremsstrahlung) processes.

3. $I_{\rm HXR}$ and $\dot{U}_{\rm th}$ both yield comparable nonlinear correlations with $\dot{I}_{\rm SXR}$, while $\dot{U}_{\rm th}$ is relatively better correlated with $\dot{I}_{\rm SXR}$ linearly.

4. For the rank correlation, the 6 keV SXR has a smaller coefficient in each case than the 1.6 keV one. For the linear correlation, on the other hand, three (Cases A, B, & C) out of the five cases have a stronger correlation in the 1.6 keV category.

5. For the five cases, the cross-correlation analysis indicates that the 1.6 keV SXR derivative is delayed relative to the thermal energy change and the HXR flux. The delay from $I_{\rm HXR}$ is longer than that from $\dot{U}_{\rm th}$ by several seconds, this is because $\dot{U}_{\rm th}$ itself actually lags from $I_{\rm HXR}$ due to the interplay of the energy input and radiative loss, as well as the variation of energy (between thermal and kinetic) partition.

6. The 6 keV SXR exhibits a similar pattern as the 1.6 keV one, but it yields a relatively shorter delay in each category. This is because the 6 keV thermal emission is sensitive to higher temperature plasmas and thus it decays faster as the loop cools, while the 1.6 keV emission lasts longer and then decays more slowly after the impulsive phase.

7. In terms of timing of more subtle features (e.g., spikes in the curves), $\dot{U}_{\rm th}$ generally matches $\dot{I}_{\rm SXR}$, while $I_{\rm HXR}$ does not.

8. In a smaller flare (Case D), all the correlations are much weaker compared with the other flares. This is because a relatively larger fraction of the total energy variation comes from the kinetic energy in this case.

From these findings, we can conclude that, in terms of timing (concurrence and shorter delay) and both linear and nonlinear correlations, the SXR flux is better correlated with the thermal energy than with the commonly used HXR flux. Many processes, such as gas dynamics, can change the thermal energy in various ways, and signatures of such changes can appear in the SXR radiation, but not in HXRs. This is because thermal SXRs are more directly related to the thermal energy as they are both a function of plasma temperature and density. However, it should be noted that their correlation is not necessarily linear. The reason is that the thermal energy is linearly proportional to n_e and T, while the thermal bremsstrahlung emissivity is a nonlinear function of n_e and T (see equation 8.7).

There seems to be a bias for the Neupert effect in the solar physics community that a simple energy argument supports the empirical Neupert effect and a common practice of studying this is to plot the time history of the HXR flux together with the SXR derivative. We point out that a simple linear correlation between $\dot{I}_{\mathrm{SXR}}$ and I_{HXR} is not expected, even for purely nonthermal electron heated flare models. As we already noted in Chapter 6, there are several reasons why linearity could break down here. (1) $\dot{I}_{\mathrm{SXR}}$ is not proportional to the electron energy input power, but rather closely related (not proportional either) to the thermal energy change rate $\dot{U}_{\mathrm{th}}$. (2) The HXR flux is proportional to the electron energy deposition power with a factor of the bremsstrahlung yield, which is not a constant in time but varies with the electron spectrum in a nonlinear way. The energy deposition power also depends on the electron spectrum, but in a different way. (3) The total energy gain is a result of electron energy input power minus radiative loss rate and most of the radiative loss resides in UV and optical (not SXR) wavelengths. (4) The total energy gain is redistributed (partitioned) to different energy forms, i.e., thermal, kinetic, and gravitational energies. Clearly, through this long chain of energy transform, a linear correlation between the SXR derivative and the HXR flux is not expected to be the case. The existence of the Neupert effect in a particular flare supports the purely electron-heating model, but not vice versa. Further deviation from such a correlation will occur when other processes, such as direct heating by turbulence (rather than electrons) is present.

Chapter 9

Hydrodynamic Simulations of the Decay Phase: Testing Suppression of Conduction

9.1 Introduction

Suppression of thermal conduction by turbulence plays important roles in many astrophysical and space plasma environments. Chandran & Cowley (1998), for example, found entangled magnetic fields in a turbulent intracluster plasma can reduce the Spitzer (1962) conductivity by a factor of 10^2–10^3.

For solar flares, Jiang et al. (2006) reported spatial confinement and lower than expected energy decay rate of the X-ray loop-top (LT) source during the flare decay phase observed by *RHESSI* . This observation was interpreted as suppressed thermal conduction and/or simultaneous heating, which were assumed to be produced by turbulence or plasma waves at the LT. The same turbulence, with different strength and other properties, could aslo be responsible for acceleration of particles during the impulsive phase.

Jiang et al. (2006) assumed that the plasma in the flaring loop is in a hydrostatic state, which works well as a zeroth order approximation and made their semi-analytical work tractable. Antiochos & Sturrock (1978), however, from their simplified analytical derivation, found the bulk flow of the plasma could suppress thermal conduction as well, but they did not include radiative loss in their model. Plasma flows (or convection), in general, can carry energy from one place to another, in a way that works in parallel with thermal conduction.

It is thus necessary to improve on previous works by Jiang et al. (2006) and Antiochos & Sturrock (1978) by including the hydrodynamic response of the plasma, its feedback to the conduction, and a full calculation of radiative loss. This will help shed light on energy transport and the evolution of the flaring plasma. We will also extend the domain considered in Jiang et al. (2006) to beneath the transition region, such that we can include all the energy flow channels, i.e., radiative loss in the chromosphere and possible conduction flux through there. Such a work is reported in this chapter. The numerical model and simulation result are presented in §9.2 and §9.3, respectively. We summarize the main findings in §9.4.

9.2 Simulation Model of Suppression of Conduction and Plasma Heating

We use the NRL flux-tube model by Mariska et al. (1989), as described in Chapter 7. The only difference here is that we used the abundance in the original code, i.e., helium being 6.3% of the hydrogen number density, rather than a simply pure hydrogen plasma. Accordingly, the mean ionic charge is taken as $Z = 1.059$ and the mean mass per particle is $\mu = 0.5724$ in units of proton masses m_p. We have adopted the suppression of conduction and additional heating due to turbulence from Jiang et al. (2006), with necessary modifications due to the absence of the isobaric condition, which we describe as follows.

The electron, ion (as in Chapter 7), and combined Spitzer conductivities are

$$\begin{aligned} \kappa_e &= 1.1 \times 10^{-6} T_e^{5/2}, \qquad \kappa_i = \kappa_e/25, & (9.1) \\ \kappa &= \kappa_e + \kappa_i = \kappa_S T^{5/2} \text{ (where } \kappa_S = 1.14 \times 10^{-6}\, \mathrm{ergs\, cm^{-1}\, s^{-1}\, K^{-7/2}}), & (9.2) \end{aligned}$$

in which we assume $T_e = T_i = T$. The corresponding conductive heat flux is

$$\mathcal{F}_{\mathrm{Spit}} = \kappa \nabla T = \kappa_S T^{5/2} \nabla T \,. \tag{9.3}$$

Following Jiang et al. (2006), in presence of suppression of thermal conduction, the conductive flux should be modified as (Spicer, 1979):

$$\mathcal{F}_{\text{cond}} = \frac{1}{1+\tau_{\text{sc}}^{-1}/\tau_{\text{Coul}}^{-1}}\mathcal{F}_{\text{Spit}} = \left(\frac{\kappa_S T^{5/2}}{1+\tau_{\text{sc}}^{-1}/\tau_{\text{Coul}}^{-1}}\right)\nabla T \ , \tag{9.4}$$

where

$$\tau_{\text{Coul}}^{-1} \simeq 150 \left(\frac{T}{10^7\,\text{K}}\right)^{-3/2} \left(\frac{n_e}{10^{11}\,\text{cm}^{-3}}\right) \quad \text{s}^{-1} \tag{9.5}$$

is the mean Coulomb collision rate of the thermal electrons carrying the heat flux, and the mean wave scattering rate is assumed to be a guassian (width w) function of distance ($l = s_{\text{max}} - s$) from the loop apex,

$$\tau_{\text{sc}}^{-1} = 150\mathcal{S}_0 \exp[-(l/w)^2] \quad \text{s}^{-1} \, , \tag{9.6}$$

such that the ratio of the wave scattering to Coulomb collision rate is

$$\tau_{\text{sc}}^{-1}/\tau_{\text{Coul}}^{-1} = \mathcal{S}(s) \left(\frac{T}{10^7\,\text{K}}\right)^{3/2} \left(\frac{n}{10^{11}\,\text{cm}^{-3}}\right)^{-1} \, , \tag{9.7}$$

where $\mathcal{S}(l) = \mathcal{S}_0 \exp[-(l/w)^2]$ and the dimensionless $\mathcal{S}_0$ represents the strength of suppression (and of turbulence). Note that here we dropped the isobaric assumption taken by Jiang et al. (2006), which is not necessarily satisfied in a dynamic flare loop. Consequently equation 9.7 here is slightly different from that given by Jiang et al.

For a given turbulence condition, the inverse of the corresponding particle acceleration (or heating) timescale is (Jiang et al. 2006)

$$\tau_{\text{ac}}^{-1} \simeq \xi (v_{\text{A}}/v_{\text{th}})^2 \tau_{\text{sc}}^{-1} = \xi \left(\frac{B^2 m_e}{12\pi k_B \rho T}\right) \tau_{\text{sc}}^{-1} \, , \tag{9.8}$$

where $v_{\text{A}} = B/(4\pi\rho)^{1/2}$ is the Alfvén velocity (B the magnetic field), $v_{\text{th}} = (3k_{\text{B}}T/m_e)^{1/2}$ is the thermal velocity of the electrons (m_e the electron mass), and the coefficient ξ depends on the wave spectrum and wave-particle coupling (Schlickeiser, 1989). Accordingly, the energy change (heating) rate can be written as

$$\dot{\mathcal{E}}_h = U_{\text{th}}\tau_{\text{ac}}^{-1} = U_{\text{th}}\xi \left(\frac{B^2 m_e}{12\pi k_B \rho T}\right) \tau_{\text{sc}}^{-1} \tag{9.9}$$

$$= \frac{25}{2\pi}\left(\frac{m_e}{\mu m_p}\right)\frac{\mathcal{S}_l}{\gamma - 1} \exp[-(l/w)^2](\xi B^2) \, , \tag{9.10}$$

where we have substituted equations (9.6) and (9.8), and used $U_{\mathrm{th}} = P/(\gamma - 1)$ for the thermal energy density, and $P = P_e + P_i = (n_e + n_i)k_B T = \rho k_B T/\mu m_p$ for the pressure. We use this $\dot{\mathcal{E}}_h$ for the heating rate S_e in equation (7.37) in the HD calculation and use ξB^2 as a parameter to adjust the relative importance of heating (vs. suppression of conduction, see discussions in §3 of Jiang et al. 2006).

9.3 Numerical Results

We have performed a simulation of four cases with model parameters summarized in Table 9.1. For each case, we used the data saved at $t = 64\,\mathrm{s}$ from a previous impulsive phase simulation as the initial state, from which we continue the calculation. A uniform background heating of $8.31 \times 10^{-3}\,\mathrm{ergs\,s^{-1}\,cm^{-3}}$ (same as that used in Chapter 7, which translates to a total energy input rate of $2.35 \times 10^{22}\,\mathrm{ergs\,s^{-1}}$)[1] was applied. On top of that, for Cases B and C, we alternatively applied additional heating ($\dot{\mathcal{E}}_h$, or S_e) and suppression of conduction, respectively; for Case D, we used both additional heating and suppression, while we used none of them for Case A.

Table 9.1: Summary of simulation cases.

Cases	model	ξB^2	$\mathcal{S}_0$	mean energy decay ($10^{24}\,\mathrm{ergs\,s^{-1}}$)	n_e ($10^{10}\,\mathrm{cm^{-3}}$)	T ($10^6\,\mathrm{K}$)
A	none	–	–	8.07	6.16	1.48
B	heating only	10	20	6.66	7.78	6.54
C	suppression	0	20	7.24	4.68	7.20
D	heating & suppression	10	20	6.01	4.11	15.9

Note — The mean energy decay rate is calculated for the time interval of $[0, 500\,\mathrm{s}]$. n_e and T are the values at the loop apex at $t = 500$ s.

9.3.1 Case A: No Heating or Suppression of Conduction

Figure 9.1 shows the evolution of various HD variable as a function of distance along the loop (from the bottom, cf., Figure 7.3). The system starts with a hot, relatively dense corona, heated by electrons during the preceding impulsive phase. We find the density and temperature in the coronal portion of the loop decreases with time. This occurs because of cooling in the form that heat conduction (*bottom*, not suppressed here) carries energy to the transition region and the upper chromosphere where radiative loss function (second

---

[1] As we will see later, this amount of energy input is negligible compared with the other energy contents.

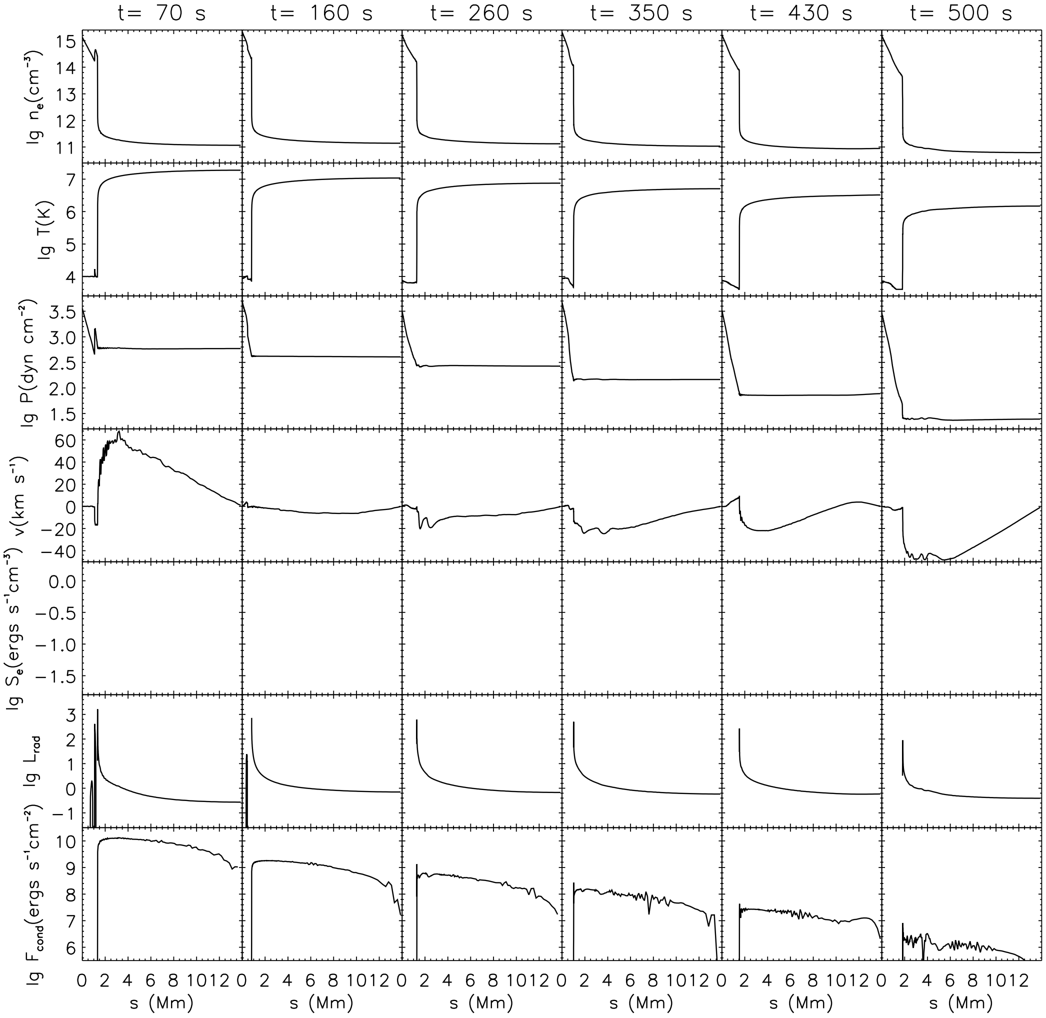

Figure 9.1: HD evolution of various quantities for Case A: electron number density, temperature, gas pressure, upward velocity, heating rate S_e, radiative loss rate $L_{\rm rad}$ (in same units as S_e), and heat conduction flux $F_{\rm cond}$, as a function of distance from the bottom (FP) of the loop. Note that $S_e = 0$ in this Case and the corresponding panels are left blank intentionally for a better comparison with the other cases.

to the *bottom*) peaks, and then energy is radiated away there. Note that direct radiative loss in the upper corona is negligibly small compared with conductive cooling (also see, e.g., Jiang et al. 2006). As a result of cooling and reduced pressure gradient (not sufficient to support material against gravity) in the corona, the plasma simply condenses and falls back to the chromosphere. This can be seen from the velocity curve, which shows generally increasing negative (downward) values. We also note that early in the decay phase (e.g., $t = 70\,\mathrm{s}$), however, chromospheric evaporation (upflow) still takes place because of residual conductive heating from the hot corona.

The evolution of the energy contents, which are spatially integrated over the loop volume, is shown in Figure 9.2 (*top*). The total energy monotonically decrease with time. The thermal energy (*dotted*) follows the same trend and clearly dominates over the gravitational (*dot-dashed*) and kinetic (*dashed*) energy, which stay at about the same level. The *bottom* panel shows the time derivatives of these energy contents, together with the radiative loss rate. We find the absolute value of the total energy change rate decreases with time, which is correlated with the radiative loss (this simply means energy conservation, see §8.2.1).

We note that there are some fluctuations in the gravitational and kinetic (smaller *absolute* amplitudes) energy, which are more pronounced in the *bottom* panel of Figure 9.2. The absolute value of the thermal energy change rate (< 0) also show, on top of its general decreasing trend, some modulations that seem to be anti-correlated with those of the gravitational and kinetic energy. We interpret this as conversion of energy among different forms in the plasma (also see Chapter 8).

To see this point clearly and identify the source of the fluctuations, we plot the same energy budget history for the corona (*left*) and for the chromosphere (*right*) separately in Figure 9.3 in which we used the position where $T = 1 \times 10^7\,\mathrm{K}$ as the boundary between the two regions. For the corona portion (Figure 9.3), the thermal energy and the total energy curves almost overlap each other, and they simply show a featureless monotonic decay; so does the gravitational energy. Only the kinetic energy exhibits some fluctuations, but without a simple pattern. For the chromosphere (Figure 9.3, *right*, note logarithmic scale), in contrast, the total energy initially decrease slightly and then stays almost constant and the fraction of the thermal energy is smaller than that in the corona. The fluctuations and the anti-correlation of the gravitational and thermal energy are evident. This results from the **chromospheric oscillation** (Mariska et al., 1982), which can be seen from the

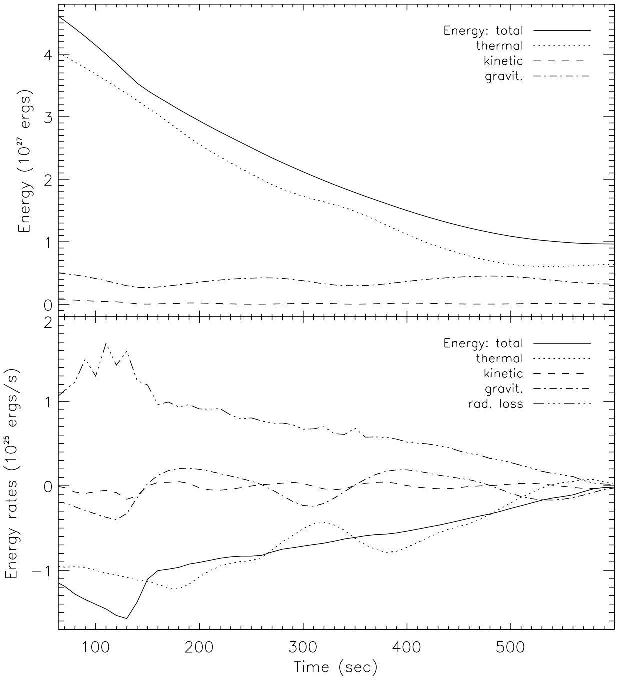

Figure 9.2: Energy evolution for Case A. *top*: Total, thermal, kinetic, and gravitational energy, integrated over the volume of the loop, as a function of time. *bottom*: Time derivative of the above energy contents, together with the radiative loss rate.

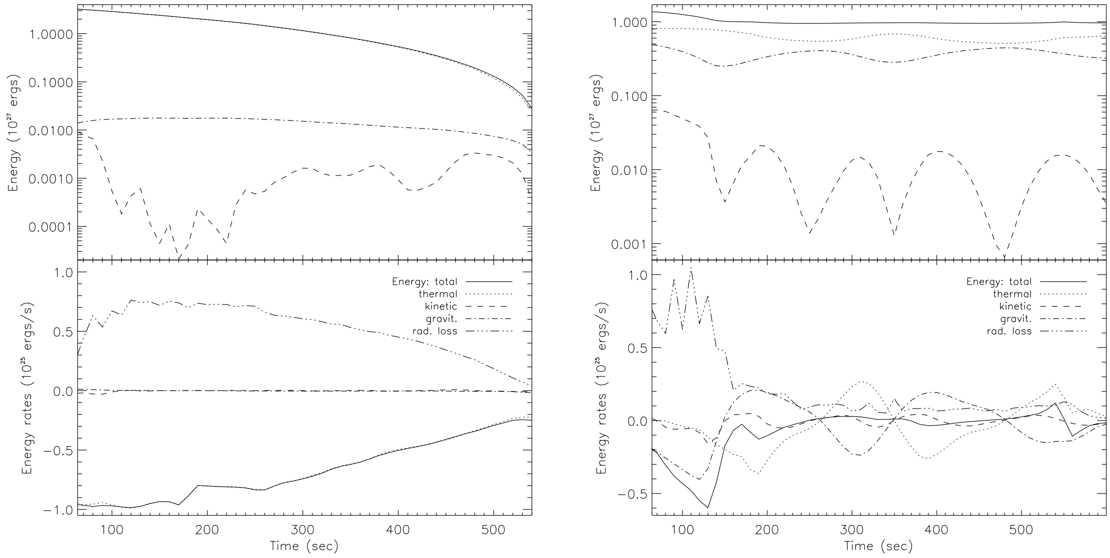

Figure 9.3: Same as Figure 9.2, but for the corona (*left*) and chromosphere (*right*) only.

top panel of Figure 9.1, where the height of the transition region rises and drops back and forth. (This can be more clearly seen in a movie, not shown). The alternative rarefication and compression of the chromospheric material performs energy conversion between the two forms: thermal and gravitational energy. We note that the kinetic energy (Figure 9.3, *upper right*) shows larger *relative* amplitudes and, particularly, about twice as higher frequency as the gravitational energy. The kinetic energy reaches its minimum when the gravitational energy reaches its maximum or minimum. This is because the chromosphere oscillates like a loaded[2] spring in the vertical direction and each cycle in the gravitational energy variation includes *two* cycles of acceleration and deceleration, resulting two cycles in the kinetic energy curve.

9.3.2 Case B: Heating Only

In this Case, we applied additional heating in the corona. The spatial distribution of the heating is of a gaussian shape which peaks at the loop apex (see Figure 9.4, row 5). The evolution of the HD variable is shown in Figure 9.4, which is very similar to Figure 9.1 for Case A, except that here the coronal density, temperature, and pressure decay slightly more slowly due to heating. Note that the temperature still distributes more or less uniformly in the corona despite more heating at the LT. The downflow (due to condensation) velocity is lower than that in Case A too. The conduction flux stays higher because of higher temperature here. The history of the energy budget (not shown) is also very similar to that of Case A (Figure 9.2).

9.3.3 Case C: Suppression of Conduction Only

Here instead of applying additional heating, we suppress the conduction with a gaussian profile. Compared with Case A, the heat conduction flux (Figure 9.5) varies more dramatically from the LT to the FP. At $t = 70\,\mathrm{s}$, for example, F_{cond} increases by nearly three orders of magnitude from the loop apex to near the transition region, as opposed to the variation of about one order of magnitude in Case A. As a result, the temperature slope in the corona is larger here (because the there is more suppression in the LT than near the FP). The overall temperature decay, as expected, is delayed, compared with Case A. The

---

[2] Most of the loading is provided by cooling and condensation in the overlying layers in this simulation (Mariska et al., 1982), simply because material falls back from the corona and thus pushes chromosphere downward.

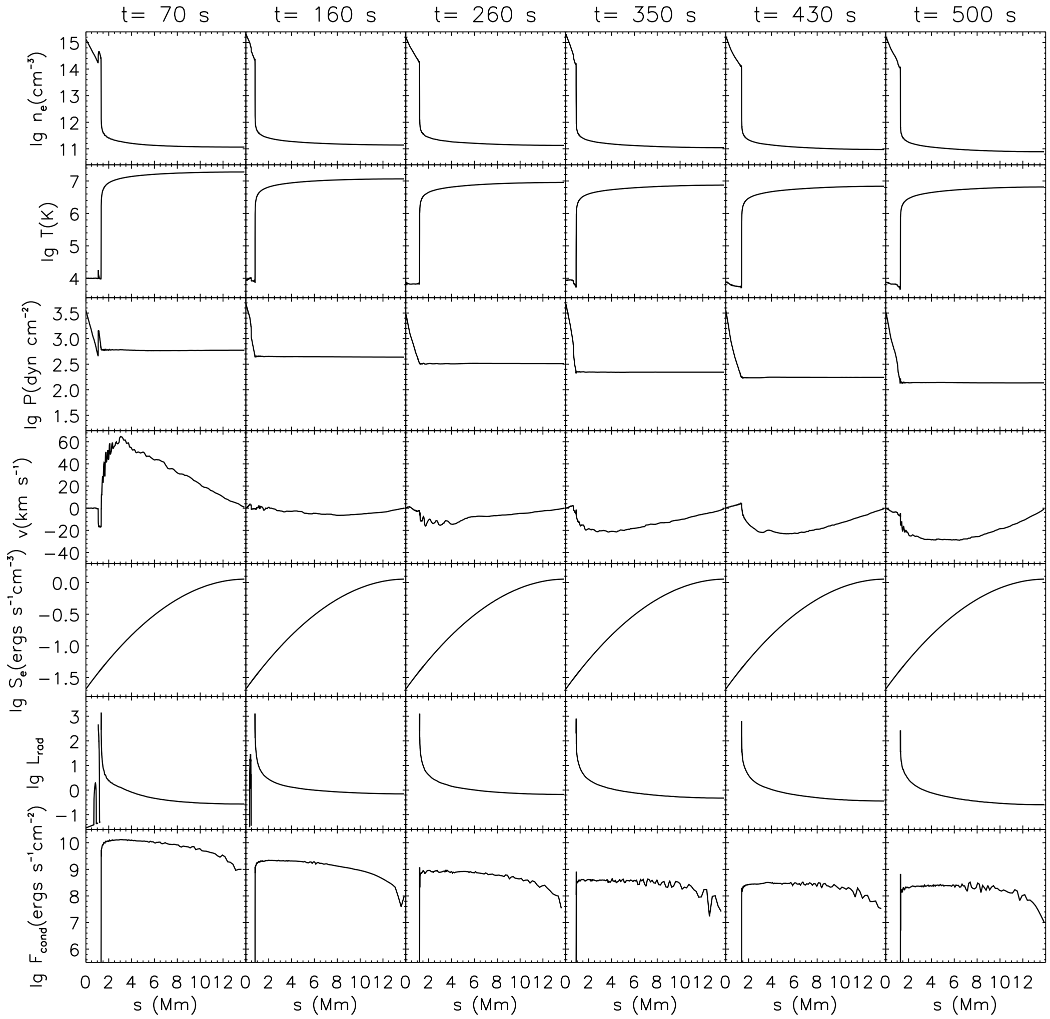

Figure 9.4: Same as Figure 9.1, but for Case B.

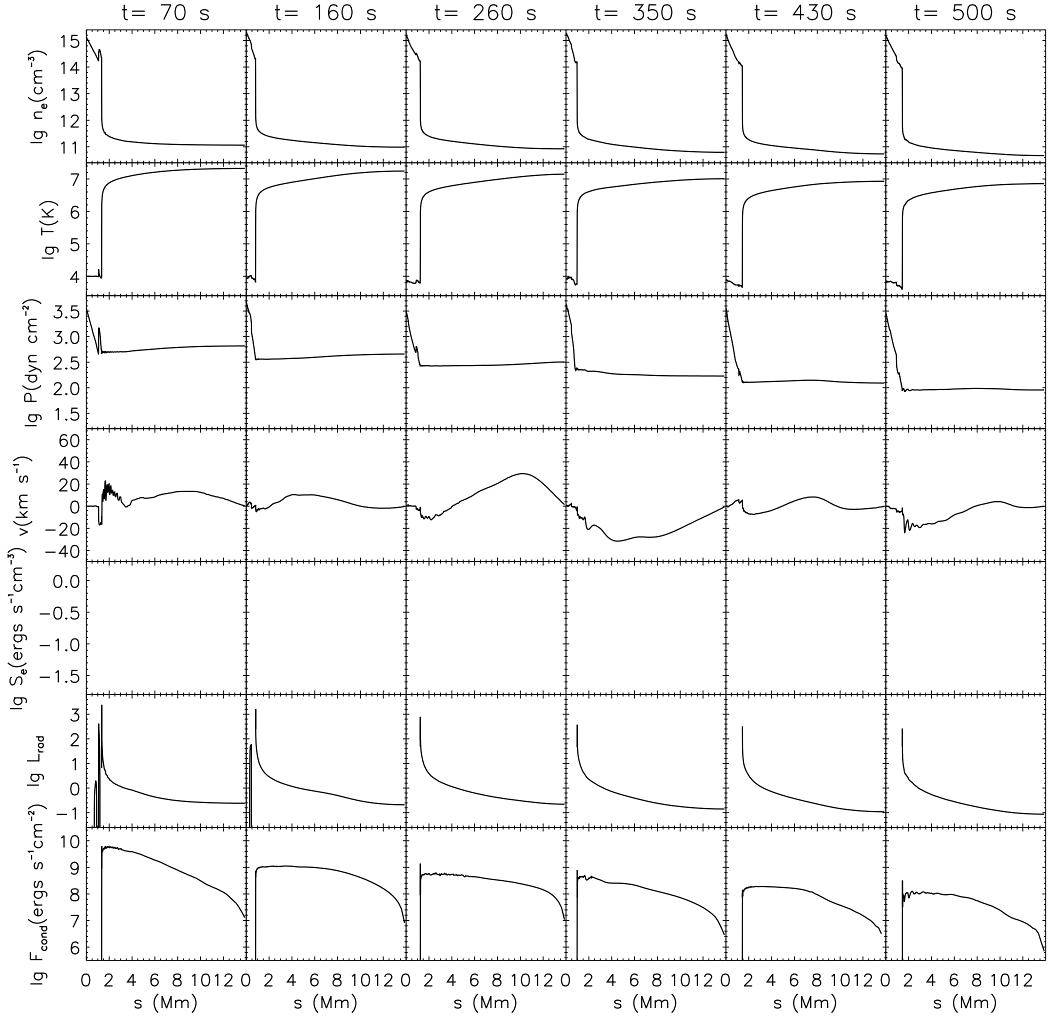

Figure 9.5: Same as Figure 9.1, but for Case C.

energy budget is very similar to that of Case D (see below, Figure 9.7) and thus is not not shown here. A new feature caused by suppression of conduction here is the traveling waves (see the velocity in Figure 9.5) in the corona, for which we defer our discussion to next section.

9.3.4 Case D: Heating and Suppression of Conduction

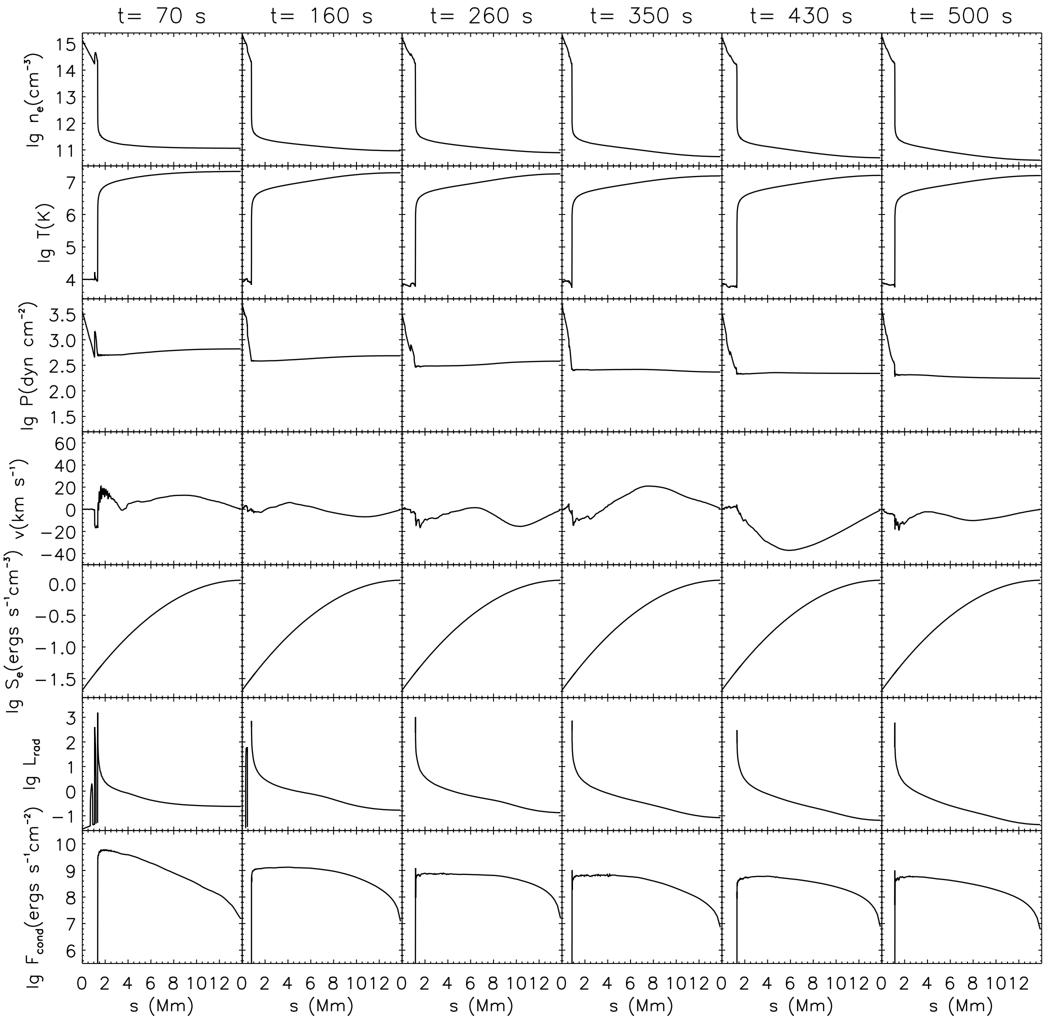

Figure 9.6: Same as Figure 9.1, but for Case D.

Now we combine heating and suppression of conduction used above together in Case D. As can be seen in Figure 9.6, the overall evolution is similar to that of Case C, except even more delayed decay here. The energy history is plotted in Figure 9.7 (*left*). The constant heating rate is shown as the *long dashed* line, which in addition to the suppression of conduction, counteracts the energy decay.

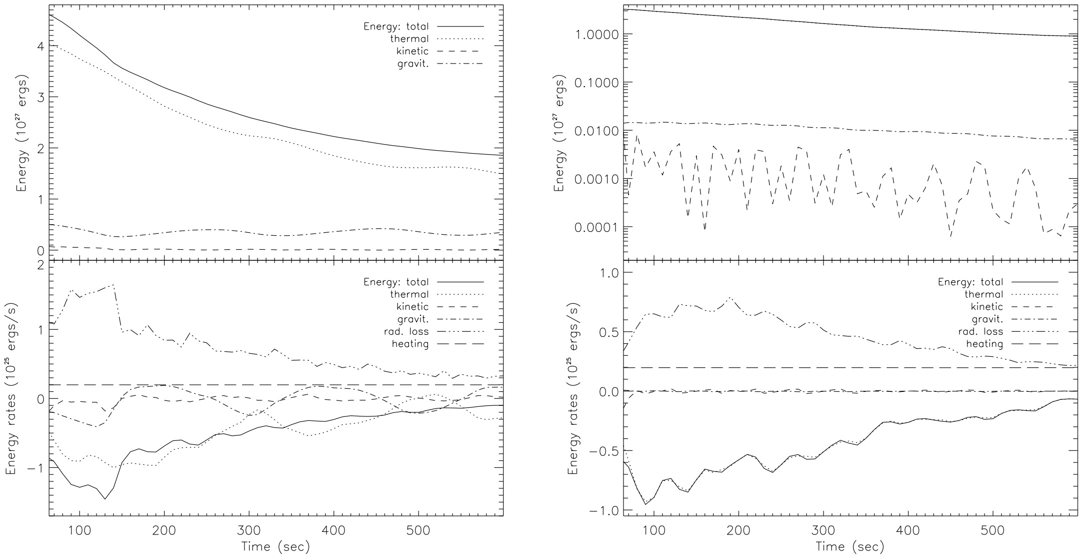

Figure 9.7: Same as Figure 9.3, but for the whole loop (*left*) and the corona portion (*right*) of Case D, with the additional quantity, heating rate, plotted as the *long-dashed* line in the bottom panels.

Another difference here, compared with Figure 9.2 for Case A, is the short-period fluctuations in the thermal energy change rate (*dotted*, *bottom* panel). Such fluctuations are superimposed on the existing long-period ($\sim$ 200 s) fluctuations caused by the chromospheric oscillation. Again, we plot the energy contents in the corona and the chromosphere separately, and we find the chromosphere (not shown) has a similar energy evolution as in Case A. However, the corona behaves quite differently, as can be seen in Figure 9.7 (*right*). The above mentioned short-period fluctuations are present in the velocity (*dashed*, *top right*), the thermal (and total) energy change rate, as well as the radiative loss (*bottom right*). These fluctuations are caused by the traveling waves, which results in alternative compression (heating) and rarefication (cooling) of the plasma. Such waves can also be seen in the velocity curves in Figure 9.6. The same effects are present in Case C, but not in Case B. We suggest the imposed suppression of conduction is responsible for the growth of such waves,[3] for which the strong disturbance to the fluid during the turbulent impulsive phase could be the seeds.

We also note that the lifetime of the traveling waves here may be exaggerated, because there is no viscosity included in this model. Such an approximation is good for the impulsive phase since the contribution of viscosity to the momentum and energy equations are overwhelmed by the other more dramatic agents (e.g., electron heating). However, during the slow (on timescales of 10 times longer than that of the impulsive phase) evolution of the decay phase, viscosity may play a role, particularly in damping the waves.

9.3.5 Comparing Cases A-D

We now compare the four simulation cases more directly. Figure 9.8 shows the normalized temperature (*top*) and thermal bremsstrahlung emission (*bottom*, at 6 keV) profiles, together with the density squared n_e (*middle*) at selected times for all the cases. In general, the curves of Cases A and B form one group (called Group 1), and those of Cases C and D form another (Group 2), exhibiting the expected shapes due to different conduction suppression and/or heating imposed.

Case B has a temperature profile very close to that of Case A, despite its localized heating near the LT. This is because heat conduction (without suppression) is so efficient (Jiang et al. 2006) that the energy addition by localized heating is quickly conducted away from the LT and this makes the coronal temperature close to a uniform distribution. Cases C and D have a more confined high temperature region near the LT, due to their suppressed conduction. They also have a lower coronal density because their higher coronal temperature requires less material to produce sufficient pressure.

The thermal emission profiles, in general, follow the shape of the corresponding temperature profiles. Cases C and D have narrower emission profiles, same as their temperature profiles, particularly early during the decay phase. This is consistent with that found by Jiang et al. (2006). At some other times (e.g., $t = 360$ s), this pattern does not always hold. This is because thermal emission (equation 8.7) is an increasing function of both T (nonlinear) and n_e^2 (or emission measure, linear). In our simulation, T increases with distance (from FP to LT), while n_e^2 behaves oppositely. The interplay of these two quantities determines the resulting thermal emission profile. It is thus not surprising that the

---

[3] Note there are similar coronal waves in Cases A and B, but they are of much smaller amplitudes and do not produce noticeable effects as in Cases C and D.

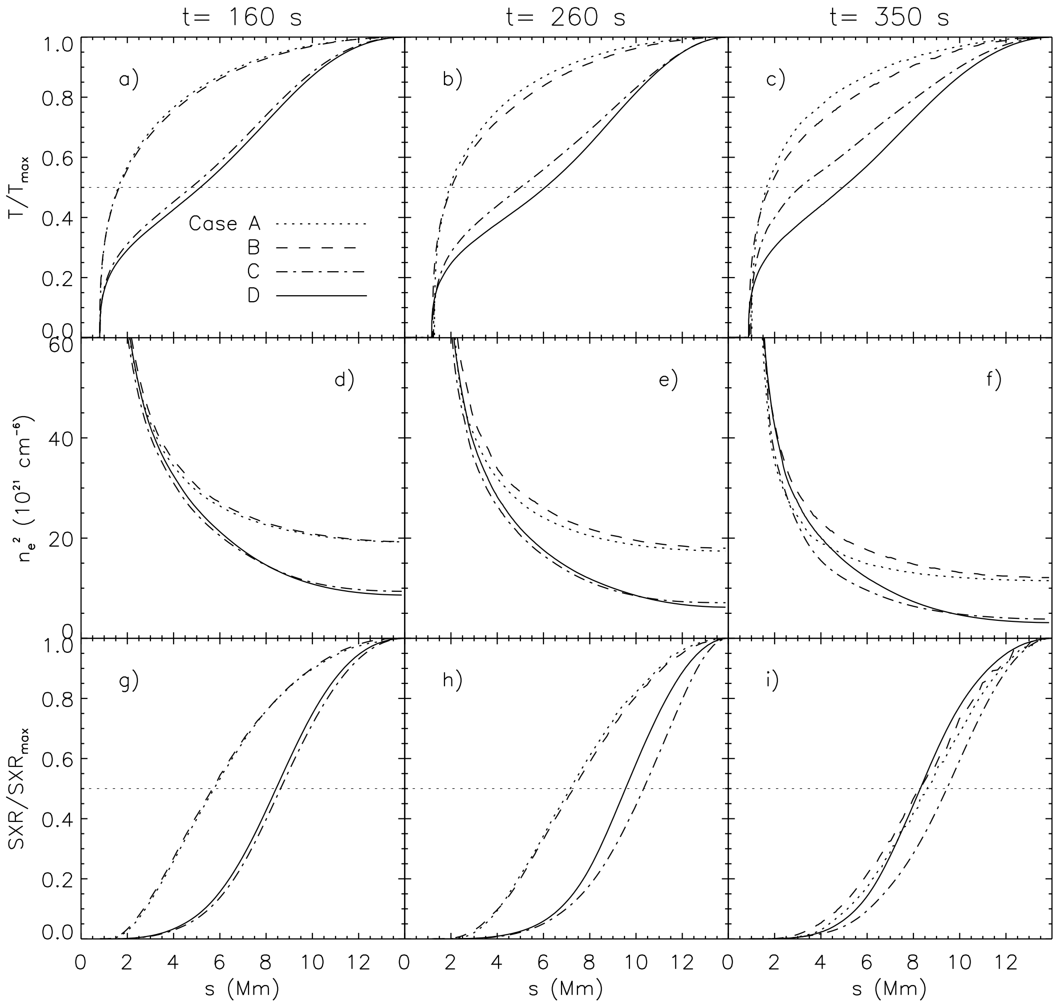

Figure 9.8: Comparison of temperature, density squared n_e^2, and thermal bremsstrahlung emission (at 6 keV) profiles among Cases A-D at selected times. Each of the temperature and emission profiles are normalized to its individual maximum. Each column is of the same time. The *dotted* horizontal line marks the 50% leavel.

emission profile does not necessarily follow the shape of the corresponding temperature curve exactly. Sometimes, a hump[4] (not shown) in the thermal emission can be produced and it shifts back and forth along the loop, which is due to the enhanced local density and temperature by traveling waves (see discussions above). These new features were not present in the hydrostatic solutions of Jiang et al. (2006).

Figures 9.9a and 9.9b show the history of density squared n_e^2 and temperature, respectively, at the loop apex. Again, we see that Group 1 (Cases A and B) has similar values of n_e^2, and so do Group 2 (Cases C and D) whose values are less than that of Case A by up to a factor of four. Group 1 have an increasing density at early times before its decreasing phase, while the density of Group 2 has a generally decreasing trend. This happens because in Group 1 chromospheric evaporation continues to bring material to the corona early into the decay phase, as can be seen in the large upward velocity values in Figures 9.1 and 9.4. Group 2, on the other hand, has a higher coronal temperature due to suppression and thus a higher LT pressure (see Figures 9.5 and 9.6) that produces a downward pressure gradient force to counteracts the evaporation upflow. This results in lower upflow velocities and decreasing (and lower) LT densities in Group 2.

As to the temperature, from Case A to D, we generally have increasing values at a given time, except on the very late stage when the curves of Cases B and C cross each other. This is expected because we have increasing suppression and/or heating applied. For example, Case D combines these effects of Cases B and C together, so it has the highest LT temperature. After $t \sim 500$ s, its LT temperature even slightly increases. This comes about because of the decreasing LT density and constant continuous heating and suppression of conduction.

Figures 9.9c and 9.9d show the spatially integrated total energy and thermal XR emission flux. They also exhibit similar patterns as the LT temperature. As is evident, the n_e^2, T, and XR emission curves of Group 2 all show similar fluctuations, which are caused by the traveling waves mentioned above.

We note that the average energy decay rate (Figure 9.9c) of Case D (with combined suppression and heating) is about 3/4 of that of Case A. Such a difference is much less than that of Jiang et al. (2006, see Fig. 13 there), with otherwise comparable parameters. This is because they assumed hydrostatic solutions and the calculation was restricted to

---

[4] The bright feature in X-rays moving along the loop is similar to the *TRACE* observation of the bright EUV blob that travels back and forth from one end of the loop to the other (Ryutova & Shine, 2006).

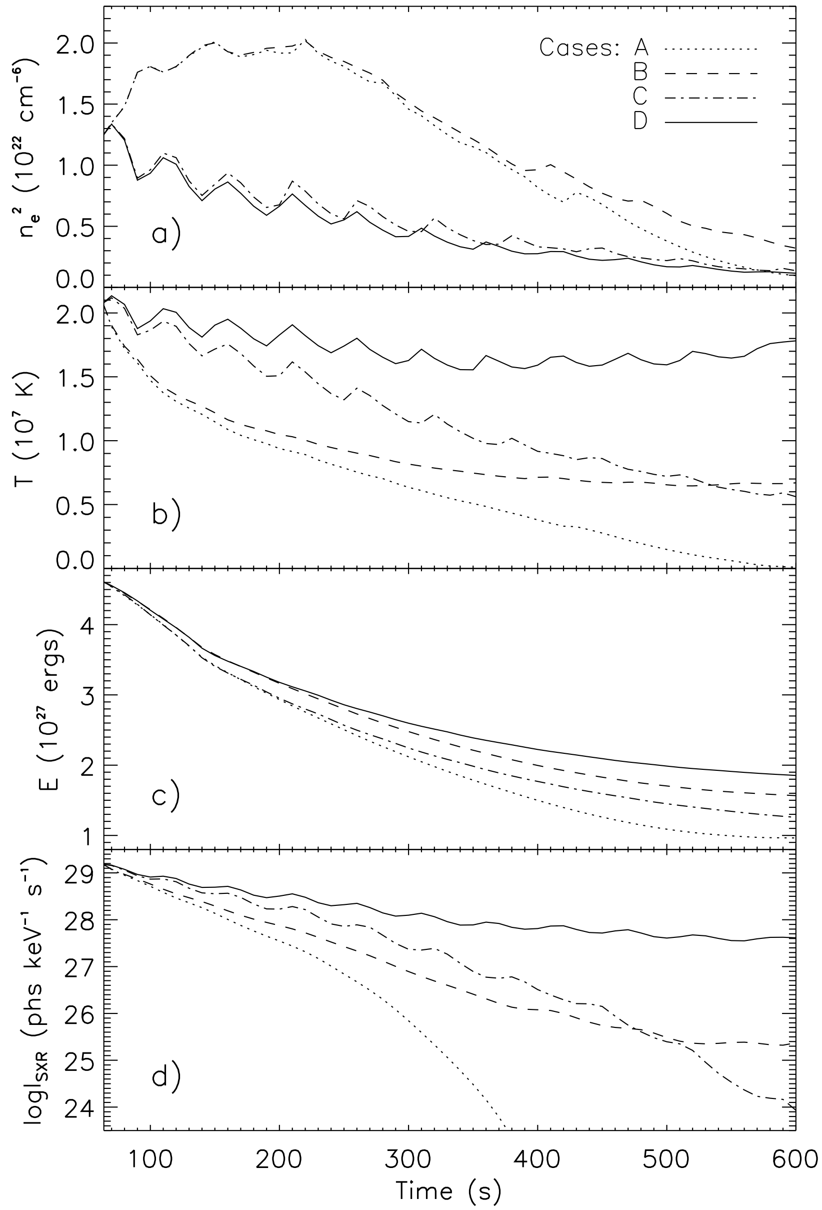

Figure 9.9: Comparison of decay of various quantities for Cases A-D. (*a*) and (*b*) Evolution of density squared n_e^2 and temperature, respectively, at the loop apex. (*c*) and (*d*) Total energy and thermal bremsstrahlung (at 6 keV) intensity $I_{\rm SXR}$, respectively, both integrated over the volume of the whole loop.

the hot, coronal portion of the loop, so radiative loss is small. Therefore, the only effective energy loss channel in their model is through conduction to transfer energy to the FPs. Contrastingly, here, we have plasma flow and traveling HD waves that act as another energy carrier. The energy input from the LT can be carried by plasma down to the transition region and the chromosphere and then be efficiently radiated away there.

9.4 Summary and Discussion

We have performed a HD simulation for the decay phase of solar flares, by inclusion of the fluid dynamics calculation and the chromosphere in the computational domain. This work improves on the previous work by Jiang et al. (2006) who assumed a hydrostatic condition and that by Antiochos & Sturrock (1978) who neglected radiative loss. In general, our result confirms the conclusions by Jiang et al. (2006):

1. Heating at/near the LT alone is not able to confine the LT source in a small region as seen in SXRs, although it could be invoked to explain observed energy decay rates.

2. Suppression of conduction localized near the LT is needed to produce a narrow temperature profile and thus a compact SXR source near the LT.

3. A combined heating and suppression of conduction is suggested to be present and to be localized near the LT region. Such a coexistence can explain both the reduced energy decay rates and spatially confined LT source.

Our calculation has also uncovered some new information not present in Jiang et al. (2006):

1. Different density profiles can modify the thermal XR emission profiles based on the corresponding temperature profile. Even in the presence of a compact temperature profile, a somewhat broad XR emission profile could be produced due to the interplay of the density and temperature distributions.

2. Plasma flow and/or waves can carry energy away from hot the LT region, and thus counteract the effects of heating and suppression of conduction. Therefore, an even larger factor of suppression would be required to explain the XR observations.

In this simple simulation study, the parameter space has not been fully explored. The width w for the Gaussian suppression profile, for example, is important in determining the effects of suppression, and in particular, the existence/growth of the traveling HD waves. The radiative loss calculation can also be improved, say, using the newly released CHIANTI package. We look forward to a future modeling development to carry out such tasks.

Chapter 10

Concluding Remarks

Now it is time to step back and review this work. Here we recapitulate our motivation and highlight our conclusions. We then comment on directions for future investigations.

10.1 Summary and Conclusions

We have carried out an investigation of acceleration and transport of particles in solar flares, and their thermal and nonthermal radiative signatures, using both HXR data analysis and combined Fokker-Planck and hydrodynamic (HD) modeling. This research focuses on solar flares because they provides a unique laboratory for us to understand particle acceleration mechanisms which have far-reaching implications, not only for solar and space physics in particular, but also for astrophysics in general. We summarize here our conclusions and their implications in the context of contemporary flare research as follows.

10.1.1 Hard X-ray Observations

Our observational efforts utilized HXR data obtained by the currently active *RHESSI* mission and focused on spatial, temporal, and spectral variations of the LT and FP emissions.

In the stochastic acceleration (SA) model, the LT emission comes directly from the accelerated electrons and the FP emission is produced by escaping electrons. The emissions of the two sources are related and can thus be used to constrain the SA model parameters. We have carried out a preliminary **statistical study** of 29 limb flares, which have minimal projection effects, and obtained the relative spectra and fluxes of the LT and FP sources.

As presented in *Chapter 2*, for the LT and FP sources, respectively, we find an average spectral index of $\bar{\gamma}_{\rm LT} = 6.84$ and $\bar{\gamma}_{\rm FP} = 3.35$, with a large difference which could, in principle, be explained by the SA model. However, the spectral indexes (of a given flare and from flare to flare) do not seem to be correlated. This is not expected, but not surprising either because of the complexity of the exact physical processes involved. This statistical study have also led us to identify four flares of special interest for further investigations, each of which presents *evidence* of particular aspects as well as imposes *challenges* for the classical reconnection model of solar flares.

In the classical flare model, magnetic reconnection takes place at lower altitudes first and then progresses to higher overlying loops. In this picture, one would expect that the FPs separate while the LT source moves up with time. However, such a **correlated motion** of the different sources was rarely observed *simultaneously* in the past, although either a rising LT or two separating FP sources have been reported. We have shown in *Chapter 3* an excellent example of such a picture. The 2003 November 03 X3.9 flare, unlike many other complex X-class flares, shows a very simple morphology with a well-defined LT and two FP sources. The almost monotonic upward motion of the LT source and the increase of separation between the two FPs at comparable speeds are exactly what are expected. In addition, we find that the source motions are relatively slower during the more active phases of HXR emission; the emission centroid of the LT source shifts toward higher altitudes with increasing energy; the separation between the LT emission centroids at two different photon energies is anti-correlated with the FP flux. Non-uniformity of the reconnecting magnetic fields could be a possible explanation of these features.

Outflow jets of high speed plasmas and associated turbulence, in the classical 2-D picture of magnetic reconnection, is present in opposite directions along the current sheet. Accelerated particles and heated plasmas are expected to be present in both directions as well. During the impulsive phase, we have commonly observed *one* LT source. A **double-coronal-source** structure has only been observed recently by *RHESSI* in a few flares (Sui & Holman, 2003; Sui et al., 2004; Veronig et al., 2006; Gan & Li, 2006) which show an additional, weaker source above the common LT source. Due to the faintness of the additional source, its spectrum has not been studied in these flares. We discovered another yet stronger case of such a double-source morphology in the 2002 April 30 flare, in which the upper source is relatively bright and long-lived, and imaging spectroscopy can be obtained to infer its spectrum and light curve. Another advantage of this event is that the FPs are occulted and thus they do not contaminate the LT emission at high energies. Analysis of this flare has been presented in *Chapter 4*. We find that the two coronal sources, closely spaced, co-exist for about 9 minutes during the impulsive and gradual phases of the flare. Their energy-dependent morphology reveals that higher-energy emissions of the two sources are closer together. (also see Sui & Holman, 2003; Sui et al., 2004). As energy further increases, an "X" shape of emission appears and a small distance of about $4''$ between the emission peaks is identified, which suggests that reconnection occurs within this small region. As time proceeds, both sources generally move together to high altitudes, with the upper one moving faster and thus their separation becomes larger. For each source, the separation of emission between different energies becomes smaller near the peak time of each HXR pulse and it becomes larger at other times, consistent with our earlier finding mentioned above (see Chapter 3). The light curves of the two sources are temporally correlated, and their spectra are very similar. This suggests that the two sources are produced by the same (or very similar) population of electrons, presumably heated and/or accelerated in the same acceleration region.

Magnetic field measurement in a flare region, in general, can provide clues of magnetic reconnection, while HXR data contains useful information of accelerated particles. Both types of observations, if available, can be combined and used to uncover the relationship between particle acceleration and magnetic reconnection development. In *Chapter 5*, we have examined the FP HXR emission together with the associated magnetic field in the 2003 October 29 X10 flare. This event occurred close to the disc center and thus had minimal projection effects for the line-of-sight magnetic field which can be obtained from *SOHO*/MDI. We find that there are two well-defined conjugate FPs showing **asymmetric characteristics**. One FP is about three times brighter in HXR flux than the other, and its associated magnetic field is about two times weaker, which is qualitatively consistent with the magnetic mirroring effect. As time proceeds, the two FPs move away from the magnetic neutral line, with the brighter one moving faster. At the same time, the inclination angle between the neutral line and the line connecting the two PFs increases and approaches 90°, indicating that the newly reconnected magnetic field lines (at higher altitudes) are less sheared. The magnetic fields of the two FPs generally decrease with time, and we find that the logarithm of the mean HXR flux of the two FPs correlates with the mean magnetic field, while the speeds of the FPs remain roughly constant. This means that the HXR production rate correlates with the magnetic field annihilation rate.

During this evolution, however, the HXR flux ratio of the two FPs cannot be quantitatively explained solely by the mirroring effect.

Chromospheric evaporation is a consequence of energy deposition by electrons in the lower atmospheres and it is usually observed by blue-shifted line emissions. Such observations, in a sense, are indirect evidence of chromospheric evaporation, because the mass motion is not directly imaged. The superior capabilities of *RHESSI* enabled us to remedy this shortcoming with the observation of the M1.7 flare of 2003 November 13, which shows some unusual spatial evolution and provides direct evidence for chromospheric evaporation. Analysis of this flare is presented in *Chapter 6*. We find that, as expected, the LT source dominates at low energies, while the FP sources dominate the high-energy emission. At intermediate energies, both the LT and FPs may be seen, but during certain intervals emission from the legs of the loop dominates, in contrast to the commonly observed LT and FP emission. The HXR emission tends to rise above the FPs and eventually merge into a single LT source. This evolution starts at low energies and proceeds to higher energies. The spectrum of the resultant LT source becomes more and more dominated by a thermal component with an increasing emission measure as the flare proceeds. The SXRs and HXRs show a Neupert-type behavior. With a nonthermal bremsstrahlung model, the brightness profile along the loop is used to determine the density profile and its evolution, which reveals a gradual increase of the gas density in the loop. These results are evidence for chromospheric evaporation and are consistent with the qualitative features of hydrodynamic simulations of this phenomenon. However, some observed source morphologies, such as the leg emission, and their evolution cannot be accounted for by previous models. This motivated us to carry our the following modeling efforts.

10.1.2 Combined Fokker-Planck and Hydrodynamic Modeling

We have started an investigation of combining our Fokker-Planck $\mathcal{F}lare$ code (Petrosian et al. 2001) with the NRL flux tube HD code (Mariska, Emslie, & Li 1989). The motivation is two-folded, one from the aforementioned new *RHESSI* observations and the other from theoretical demands which we describe as follows.

In solar flares, there are two important processes, one of which is the acceleration and transport of energetic particles, and the other of which is the HD response of the atmosphere heated via the particle energy deposition. The two processes are coupled together and can affect each other in a circular way. Variations of the acceleration rate and thus the spectrum of particles, for example, can alter the electron heating rate and thus affect the HD evolution. The chromospheric evaporation, as one form of the atmospheric response, can modify the density and temperature in the loop and possibly in the acceleration region as well. This, in turn, will change the acceleration process. The *circular nature* of the problem requires that the two processes should be studied together in a self-consistent way. However, because of the complexity of the subject, people in the past tended to separate them and focused on one process at a time, while making some simplified, yet not entirely accurate assumptions for the other. As progresses have been made on both sides over the past two decades, we are now in a position ready to break through previous imitations and conduct a combined study of both processes more accurately.

As described in *Chapter 7*, we use the Fokker-Planck code to calculate the electron distribution at each depth along the loop and thus obtain the spatial distribution of the electron energy loss rate (due to Coulomb collisions). Such energy loss is used as the heating function in the HD code and it drives the HD evolution. The updated density distribution is then fed back to the Fokker-Planck code to calculate the new heating rate. In this way, the two codes communicate in real time and keep tracking of the temporal evolution of the system. The heating rate calculated here is more accurate than the approximate, analytical ones (e.g., Emslie 1978) used in previous models. We also use more realistic electron spectra obtained from the recent SA model by Petrosian & Liu, S. (2004), which has a smooth transition from the quasi-thermal component at low energies to the nonthermal tail at high energies. Such a spectrum shape is consistent with that inferred from observed X-ray spectra, which can usually be fitted with a thermal plus power-law model. The previous models (e.g., Fisher et al. 1985a; Mariska et al. 1989), however, assumed a power-law spectrum with a low-energy cutoff (say 15 keV), thus essentially eliminating low-energy electrons from the distribution.

We now summarize our results from this newly combined Fokker-Planck and HD simulation. (1) One of the main findings is that inclusion of the more realistic electron spectrum from the SA model affects the spatial distribution of energy deposition and thus influences the HD evolution. The low-energy electrons in the quasi-thermal portion of the distribution produce more heating in the corona than the previous models (Mariska et al. 1989) which, rather, have more heating in the chromosphere. Because of the radiative loss function has its peak in the upper chromosphere, direct chromospheric heating results in a significant portion of the energy being radiated away and less energy left available to evaporate the plasma. Therefore, our new model generally drives chromospheric evaporation more efficiently than previous models. (2) Another finding is that variations of the acceleration rate are actually coupled with variations of the escape time $T_{\rm esc}$ and both factors can modify the escaping electron spectrum and thus the resulting HD response. In general, a higher acceleration rate produces a harder electron spectrum but smaller escaping electron flux, because stronger turbulence scatters particles more and traps them longer in the acceleration region. These two factors combine to produce less coronal heating and relatively more chromospheric heating. Therefore, for the same reason mentioned above, this results in a comparably weaker chromospheric evaporation for a harder electron spectrum.

From the same simulations, we have checked the empirical Neupert effect, as presented in *Chapter 8*. Here we use more rigorous calculations of the energy contents and thermal and nonthermal X-ray radiation than previous works, e.g., by Veronig et al. (2005). We find that a correlation of the SXR derivative and the HXR flux indeed exists. In addition, a more physical correlation between the SXR derivative and the thermal energy variation rate yields a better linear correlation. We point out that a simple *linear* correlation between the SXR derivative and the HXR flux is not expected, due to the many nonlinear processes involved.

As an extension of our studies on the flare impulsive phase, we have also carried out a simulation of the decay phase (*Chapter 9*). The motivation here is to test the effects of suppression of conduction and/or heating, presumably produced by turbulence (at a lower level during the decay phase), in the presence of HD flows. Our result confirms our earlier conclusion (Jiang et al. 2006) that suppression of conduction and/or heating is required to produce the observed low energy decay rate and the compact LT source seen in SXRs. The new conclusions include that plasma flow and/or waves can carry energy away from hot the LT region, and thus counteract the effects of heating and suppression of conduction. Therefore, an even larger factor of suppression would be required to explain the SXR observations.

10.2 Future Work

Now it is time to take an outlook for the future. As progresses were made in this work, we realized that many aspects of this research can be improved and we briefly discuss several important ones as follows.

Time-dependent Transport Code: The current particle transport code finds a steady state solution, while time-dependent solutions can be obtained with the particle acceleration and HD codes. One can upgrade the transport code to a time-dependent version and then the combined codes can make time advances in a more self-consistent manner. The upgrade can be done based on the time-dependent code of Hamilton, Lu, & Petrosian (1990). Once a fully time-dependent version is available, we can drop the constraints set by the current assumption of semi-time-dependent approach in which the heating rate is a function of column depth. These constraints include: (1) the loop must be uniform, i.e., no magnetic convergence or divergence; (2) synchrotron loss and diffusion must be neglected.

Warm-target Coulomb Collisions in the Transport Code: The current transport code assumes a cold ambient plasma, whose electron thermal velocities are negligibly small compared with those of the accelerated high-energy electrons. This is true for the chromospheric materials, as well as for the coronal plasma during the early stage of a flare. However, as the flare proceeds and as the chromospheric evaporation takes place, the plasma in the flaring loop is significantly heated and the thermal energy of the ambient electrons could be comparable to the kinetic energy of the accelerated electrons, particularly those in the low-energy portion of the spectrum. A modification to the Coulomb loss rate by taking into account the thermal energy of the background electrons is thus needed (e.g., Miller et al., 1996; Benz, 2002; Emslie, 2003). This has been done in the acceleration code, but has not yet been implemented into the transport code due to some technical difficulties. As an intermediate fix to this problem, one can stop the Fokker-Planck calculation once the energy of the beaming electrons degrades to the level of the thermal energy of background electrons. This is equivalent to the argument that such beaming electrons leave the nonthermal particle population and merge into the thermal background.

Angle-dependent Radiation Code: At present, the bremsstrahlung radiation is calculated using an angle-averaged cross-section for simplicity. A fully angle-dependent radiation code is available (McTiernan, 1989), but has not been implemented in the code yet. This would be included in the future development plan.

Momentum Deposition of Accelerated Particles: In the current model, momentum exchange between the accelerated particles and the background particles is not included in the HD equations. That is, the only contribution from the particles is the heating rate term in the energy equation. This is a valid approximation for electrons because of their small mass compared with that of the background protons. However, for accelerated protons (although less important in population than electrons), their momentum loss to the background plasma could be a significant portion of the system's momentum budget. This momentum, in addition to that produced by electron beam heating and the resulting overpressure, could be responsible for flaring seismic waves observed by helioseismological techniques (Kosovichev & Zharkova 1998). One of our future improvement would include the moment exchange term in the HD equation and we hope to combine this with the proton acceleration model (Petrosian & Liu, S., 2004).

Asymmetric Loop: The current HD model assumes a symmetric loop geometry and only calculates the evolution of one half of the loop. In reality, an asymmetric (to various extents) loop geometry is more general, which is indicated by commonly observed asymmetric HXR FP emissions (see *Chapter 5*). In such a configuration, on the side of the loop with a weaker magnetic field, the smaller convergence of the magnetic field results in a larger loss cone; this would allow more electrons to precipitate to the chromosphere, producing more heating and probably a stronger chromospheric evaporation upflow as well as a higher coronal density. However, such effects are counteracted by the larger cross-sectional area of the loop on this side and the energy deposited by electrons in a unit area may not be quite different from that on the other side. Another effect of an asymmetric loop geometry is that the evaporation upflow will not be symmetrically reflected at the loop apex and rather a stronger flow (higher velocity or density) on the one side will push a weaker flow on the other. The exact hydrodynamics will depend on the outcome of the interplay of such many factors and processes. A future direction would thus be to include the full loop in the combined HD and Fokker-Planck simulation. The NRL HD code is capable of a full-loop calculation, but the main challenge may come from making the acceleration and transport code work simultaneously in this manner and from setting proper boundary conditions. The simulation results can be checked against available HXR observations, particularly of those flares showing asymmetric FP emissions.

Appendix A

Miscellaneous *RHESSI* Data Analysis Tools and Notes

Since *RHESSI* is a relatively new mission and there is no comprehensive guideline published in the literature for necessary steps to take when analyzing *RHESSI* data of a flare, it is useful to document such steps and caveats. In addition, unlike many other missions, *RHESSI* provides only raw data and image reconstructions are handled on the ground by the users. This requires a high level of proficiency of the data analysis software, but the many options and control parameters, as well as the unstable software, make analyzing *RHESSI* data even more difficult. Here, we present a brief account of *RHESSI* data analysis notes, which were written and modified over the past four years, and can serve as a guideline for general *RHESSI* users.

A.1 *RHESSI* Data Analysis Flow Chart

We summarize here a flow chart used for the project of Imaging Spectroscopy Statistics, which includes the following four steps.

I. Initial Screening: In the very first step, we scan the online flare list and narrow down our search range gradually as follows.

1. We use the two criteria (as stated in Chapter 2), longitude ≥ 70 and peak count rate $\geq 30\,\mathrm{s}^{-1}\mathrm{detector}^{-1}$ in the 12–25 keV channel, to do the initial selection. We also want the highest energy band in which the flare is detected to be greater than

12 keV, in order to allow a sufficiently wide energy range for spectrum fitting.

2. Next we check various plots available online through the *RHESSI* data center to get a feeling of a flare selected. For each flare, the *Quicklook Browser* (by A. Y. Shih, http://sprg.ssl.berkeley.edu/~tohban/browser/) offers light curves, images, spectrograms (*RHESSI* and *WIND*) together with *GOES* light curves, and monitor rates. A spectrogram (by S. Krucker) shows the history of photon spectrum and can help distinguish between flare photons and those caused by radiation-belt particle events, which usually appear as a blob at high energies. When checking the images, one should pay attention to the flare location, source morphology, and the highest imageable energy band. Note that this browser only provides quicklook images (by J. McTiernan) of a single time interval in broad energy bands and may miss the HXR peak(s) and thus FP emissions. The image mosaics (time by energy), if available for a flare, at the HESSI Experimental Data Center (HEDC) at ETH Zurich (http://www.hedc.ethz.ch/www/quick_dp_search.html) are particularly useful for detailed inspection of images at separate times and energies. By examining these quicklook data sets, we can narrow down our focus to a sample of flares that show well-defined source structures, e.g., with clear LT and FP sources.

II. Preliminary Checking: Now one is ready to download the real flight data and do some more customized checks for each sample flare.

1. We can plot light curves through the *RHESSI* GUI widget and check various flags, including attenuator states, decimation (can be corrected since 2003/09/12), spacecraft night (eclipse), and South Atlantic Anomaly (SAA).

2. Some important information not shown in GUI can be obtained through J. McTiernan's quicklook flags (get_flist_flag.pro and get_flag.pro): (i) particle events; (ii) upper energy limit and weight of decimation; (iii) SC Transmitter (when it is on, detector 8 becomes noisy and should not be used); (iv) NMZ and SMZ flags (which are set in high magnetic latitude regions, where the background is higher and the rear segments are decimated — 3 out of 4 counts are discarded below 150 keV. For energies $\lesssim$ 200 kev, one should use front segments only in this case.)

3. One can also check the spin period, aspect solutions, and suspected roll solutions through chk_spin_aspect.pro and pmtras_analysis.pro. On the very early stage of the

mission, images should be integrated over a integer number of the spacecraft rotation period, but now this requirement is not necessary as long as the integration time is sufficiently long (at least half a spin, G. Hurford, private communication). However, bad aspect solutions or roll solutions would affect the accuracy of the positioning of images, and thus flares with this defect should generally not be included in our sample.

4. Pileup effects (see §6.2.1 for a detailed discussion) can be checked with hsi_check_pileup.pro (originally written by S. Krucker, using D. Smith's first order pileup correction). If the fraction of piled-up photons exceeds, say, the 10% level of the total photons in energy band where imaging spectroscopy will be conducted, one should exclude this flare from the sample, because pileup corrections for imaging are not yet available. The above steps (2)–(4) can all be done with pre_chk_batch.pro.

III. Imaging: For the flares remaining in the sample (after passing all the above evaluations), one must first reconstruct images from which spectra of individual sources can then be extracted from.

1. Preliminary images of wide time intervals, broad energy bins, large pixel sizes, and large field of views can be made with the Back-projection or CLEAN algorithms which are computationally fast. The purpose here is to obtain the flare morphology at different energies and its general evolution. This step can be omitted if such images are available online as mentioned above.

2. By checking the resulting images, one can identify a range in time, energy, and space in which there are well-define X-ray sources. Within these ranges, one may make more CLEAN images with finer time and energy bins. Another way to determine the upper limit of the energy range comes from checking the spatially integrated spectrum. Such a limit can be set at the energy where the spectrum turns flat (dominated by the background) or becomes noisy with large fluctuations.

3. Based on the above experience with the flare under study, the user now needs to determine the control parameters for the final images which will be used for imaging spectroscopy. There is no universal rules here, but the general considerations (particularly regarding photon statistics) of time ranges and energy bins can be found in §2.2. We shall emphasize that the number of energy bins should be large enough

for spectra fits, especially in the 10–30 keV range, in which the conjunction between thermal and non-thermal component appears. For example, one may take 16-20 logarithmic spaced energy bins in the 10–100 kev channel. Note that the selected image dimension (field of view) can be as small as possible to save computational time, but must be large enough to enclose *all* the sources (Hurford et al. 2002).

4. Now one is ready to use the above selected control parameters to make the final images. We used the PIXON algorithm because of its superior photometry and an error map, based on χ^2 estimates, can be obtained afterwards for each image. If using the CLEAN algorithm, we saved the component and residual maps, the latter of which can be used for error estimate (see §A.2 below).

IV. Imaging Spectroscopy: Once the images are reconstructed, we can proceed to obtain the spectra of individual sources.

1. We need to first identify the (LT and/or FPs) sources in the images. It is useful to superimpose *RHESSI* image on *TRACE* and *SOHO*/EIT EUV images, *SOHO*/MDI[1] magnetograms and/or white-light images, and *GOES*/SXI soft X-ray images, which help to identify the loop structure. However, oftentimes, we find a complex morphology and it is thus difficult to determine the source types (LT or FP) from images alone. Then, we will need to obtain additional information from the spectrum of each source (see below).

2. Once individual sources are identified, we can draw a box (or a circle or any arbitrary shape) around each source and integrate the photon flux enclosed. It is advised (Hurford et al. 2002) that one must integrate the photons of a source to obtain its spectrum, and a spectrum inferred from a portion of a source makes no sense due to *RHESSI*'s limited spatial resolution. The uncertainties (see §A.2 below) of the integrated flux should be calculated as well for each box.

3. Now that we have obtained the spectrum and its error of each source, one can fit a model (e.g., thermal plus power-law or double power-law) to the data. Note that the

---

[1] Conjugate FPs are usually located in magnetic fields of opposite polarities. For limb flares, large inclination angles (from line-of-sight) of magnetic field lines make it not very reliable to determine polarities from MDI magnetograms alone. However, if one overplots magnetograms and white-light maps together, one can identify individual sunspots and better estimate the polarities.

energy range that seriously suffers from pileup effects (as mentioned above) should be excluded (Emslie et al. 2003) for spectral fitting.

4. From the spectral fitting result, together with morphological information obtained above (item 1), we can determine the source types with more confidence now, because a LT source usually has a softer spectra and a stronger thermal component than the corresponding FP sources. This marks the end of the imaging spectroscopic analysis of one flare in the sample.

A.2 Technical Notes for Imaging Spectroscopy

Detector Selection: For spectroscopic images, the front segments of detectors 3, 4, 5, 6, and 8 were used by default (with a few exceptions). For broad band images (for inferring light curves of individual sources), detectors 3 through 8 were usually used. Detector 2 was deselected due to its threshold of about 25 keV and poor energy resolution of about 9 keV. Detector 7 was generally not included for spectroscopy either because of its threshold of 7 keV and resolution of about 3 keV. We did not use detector 1 because its $2.3''$ spatial resolution is smaller than most of the smallest features in our sample. Detector 9 should be excluded for most flares because it has a $3'$ FWHM resolution (pitch) and it is required that the distance from a source to the spin axis is greater than twice the FWHM of any detector used (G. Hurford, private communication Aug 07, 2003).

Background Estimate: Since *RHESSI* is non-shielded spacecraft, the background in the data is high (Smith et al. 2002). Various components contribute to *RHESSI* image background, falling into two categories: (1) Non-flare photon flux neither modulated by the grids nor by the spacecraft rotation, including cosmic diffuse x-ray background, secondary photons from cosmic ray interactions with Earth's atmosphere and the spacecraft, spacecraft radioactivity, and bremsstrahlung in the Earth's atmosphere and the spacecraft from electrons precipitating from the radiation belts, etc. These background components appear as an overall DC offset, to the extent that they remain uniform over the spin period, in the modulation pattern (Hurford et al. 2002) and in the reconstructed images. This background category constitutes on the order of 1% of the total flare photons (T. Metcalf 2003, private communication). (2) Flare-related flux not modulated by the grids but modulated by the spin period, i.e., flare photons that bypass the grids by Compton scattering at the spacecraft or Earth albedo, and flare photons that pass the grids but originate from large sources (which are larger than the FWHM resolution of the coarsest grid used, outside the imaging field-of-view (FOV), or of albedo photons reflected in the solar atmosphere and spreading in a large FOV (G. Hurford 2003, private communication). These fluxes form another category in image background which exhibit spatial structures and constitute on the order of 15% of the total flare flux (Aschwanden et al. 2003). A background model integrated in the PIXON (T. Metcalf 2003, private communication) and forward-fitting algorithms (Aschwanden et al. 2002) tries to remove (at least part of) the background flux of category (2) from images. The way such a model works is to fit a sinusoidal function with a period of one and one half spacecraft spin period, respectively, to the modulation pattern and subtract it. This background model was used for our PIXON images. We also took one more step in order to subtract the DC background flux of category (1). To do this, we simply selected a sufficiently large box to enclose all the flare sources. Next we took the averaged pixel value in the image excluding the selected box as the background contribution to each pixel. For a boxed source with N pixels, the background in the flux can be estimated as $b = \frac{N}{w} \times \frac{1}{M} \sum_{i=1}^{N} p_i$, where p_i is the individual pixel values (photons cm^{-2} s^{-1} arcsec^{-2}) in the image excluding the selected box, M is the corresponding number of pixels, and w is the width of the energy bin.

Error Estimate: The error estimate for *RHESSI* images was a research topic at the time of this study (as of May 2004) and we believe even now there is not yet a standard way to do this. Our first attempt was to take two different approaches for PIXON and CLEAN images. (1) For the former, we used the hsi_calc_image_error.pro routine (by T. Metcalf) in the *SSW* package to get an error map that contains the pixel by pixel error, σ_i, of an image. These errors are intended to provide a measure of how well constrained each pixel is by the data, given the image model derived from the reconstruction. The IDL routine determines how large a change in the image is required to make a one sigma change (based on χ^2) in the fit. The error for a source flux with N pixels and energy bin width w is $\sigma = \frac{A}{w} \left(\sum_{i=1}^{N} \sigma_i^2 \right)^{1/2}$, where A is area (in units of $''^2$) of each pixel. (2) For a CLEAN image, we use the rms of the residual map, $\sigma_{\rm rms}$, as the uncertainty of each pixel value. Similarly, the error for a source can then be calculated as $\sigma = \frac{A}{w} \left(N\sigma_{\rm rms}^2 \right)^{1/2} \frac{\rm FWHM}{\sqrt{A}}$, where the additional factor of $\frac{\rm FWHM}{\sqrt{A}}$ comes from the oversampling (or over-resolution) of pixels whose size $\sqrt{A}$ is usually selected (say, $1''$) to be smaller than the combined FWHM resolution of the detectors used. Such a correction is integrated in the hsi_calc_image_error.pro routine for PIXON (but not for CLEAN) images. From these estimates, the resulting errors are usually on the order of 10% at low energies (say, ~ 10 keV) and larger at high energies.

A.3 *RHESSI* Simulation and Its Applications

One of the advantages of the *RHESSI* software package is the inclusion of the simulation tools, developed and maintained by one of the *RHESSI* members, Jim McTiernan. A user can specify a model source morphology together with a photon spectrum, and use this model as an input to the simulation software. Then the software will generate images based on a user-specified image reconstruction algorithm (Hurford et al. 2002), taking into account the real instrument response, as if they were seen through the "eyes" of *RHESSI*. This can help user better understand observed flare morphology and distinguish reality from artifacts.

We have frequently used the simulation tools in our *RHESSI* data analysis. One of the examples was to simulate the emission profile along a loop in which thermal conduction is or is not suppressed and compare the results with the observed profile. Details of this study can be found in Jiang et al. (2006).

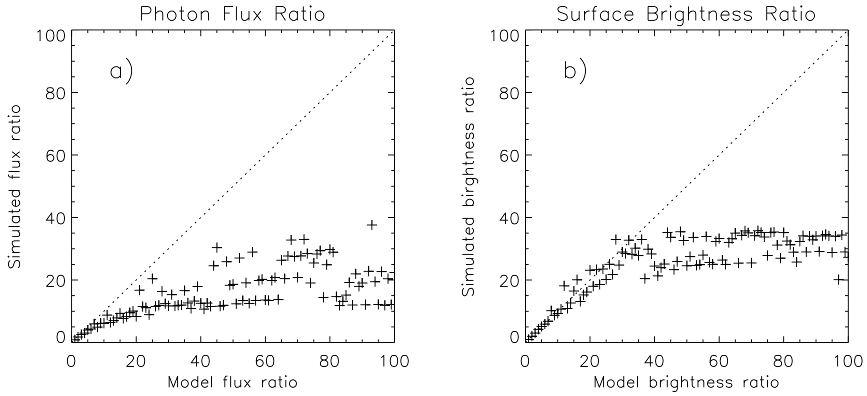

Figure A.1: (*a*) Simulated HXR photon flux ratio vs. input model flux ratio, obtained from the *RHESSI* simulation software. The dotted diagonal line indicates a perfect instrument response. (*b*) Same as (*a*) but for surface brightness.

Another example of simulation is testing the *RHESSI* dynamic range. Here we input an image with a size of $64'' \times 64''$ ($1''$ pixel), in which two $3'' \times 3''$ uniform sources were placed along the diagonal line, with their centers located at $x = 21''$ and $x = 46''$, respectively.

We then fixed the surface brightness of one source at 1 unit (arbitrary scale) and varied that of the other from 1 to 100 units, for each of which we ran the simulation software with the CLEAN algorithm to obtain an output image. Afterwards we calculated the ratio of the spatially integrated flux as well as the maximum surface brightness of the two sources. The simulated ratios (as of August 2003) are respectively plotted against the input (model) ratios in Figure A.1. As we can see, the surface brightness ratio can preserve the model input value up to about 30, beyond which the simulated value becomes flat. This simulation suggests a dynamic range of ~ 30 for surface brightness, higher than the nominal value of 10 as of 2003. The dynamic range for the integrated flux is slightly less than 10, because there are photons registered beyond the finite integration area in the image due the point spread function of the instrument.

Appendix B

On Energy Loss and Diffusion due to Coulomb Collisions With Warm Plasmas

B.1 Coulomb Loss in Warm Plasmas

In the previous SA model, the energy loss rate due to Coulomb collisions with the ambient plasma is calculated by assuming a cold-target scenario, in which the nonthermal electron velocity $v \gg v_{\mathrm{th}}$, where $v_{\mathrm{th}} = \sqrt{2kT/m_e}$ is the thermal velocity of the background electrons. This is a valid assumption in the high-energy regime, but it is not necessarily true for low-energy electrons whose velocity is comparable to or even less than the ambient electrons. In the latter case, the electrons may even gain energy from the ambient, rather than lose energy as is always the case in the cold-target scenario. More general treatment of Coulomb loss is therefore desired. Miller et al. (1996) has included such calculation in their electron acceleration model. Emslie (2003) also considered this effect when calculating particle transport and found that it can significantly reduces the inferred energy content of the injected electron distribution.

Here we briefly document how we improve on this in our current SA model. Since nonthermal electrons almost do not lose energy by collision with background protons or heavier ions, here we restrict ourselves to electron-electron collision only. The Coulomb energy loss rate for cold plasmas is:

$$\dot{E}_{\rm Coul}^{\rm cold} = 4\pi r_0^2 \ln \Lambda c n/\beta \,, \tag{B.1}$$

where $r_0 = e^2/(m_e c^2) = 2.8 \times 10^{-13}$ cm is the classical electron radius and $\ln \Lambda = 20$ is a reasonable value for solar flares (see, e.g., Leach, 1984). Following Miller et al. (1996, Eq. 2.5a)[1], we rewrite the general Coulomb loss rate (see also Benz, 2002, Eq. 2.6.28; Spitzer, 1962, p. 128–129) as

$$\dot{E}_{\rm Coul} = \dot{E}_{\rm Coul}^{\rm cold}[\psi(x) - \psi'(x)], \tag{B.2}$$

where we redefine $x = E m_e c^2/(kT)$, which is reduced to the definition of $\tilde{x} = (v/v_{\rm th})^2$ of Miller et al. (1996) at non-relativistic energies. In the relativistic regime, $x (\propto E)$ can approach ∞, which is mathematically more convenient than $\tilde{x}$ that has a finite upper limit of $(c/v_{\rm th})^2$.

$$\psi(x) = P(3/2, x) = \frac{1}{\Gamma(3/2)} \int_0^x t^{3/2-1} e^{-t} dt \tag{B.3}$$

is the incomplete gamma function (see Press et al., 1992, p. 160), where $\Gamma(a) = \int_0^\infty e^{-t} t^{a-1} dt$ is the common gamma function. Figure B.1 shows $\psi(x)$ and $\psi'(x)$, which approaches 1 and 0 very quickly, respectively, when x increases. Since

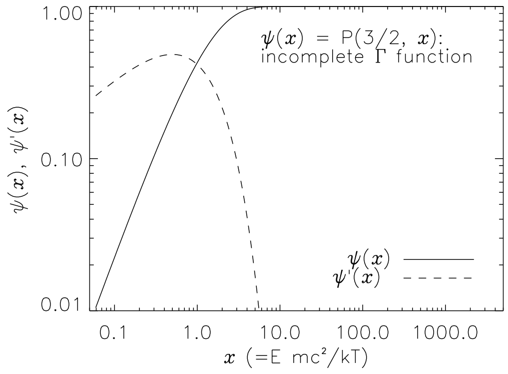

Figure B.1: Function $\psi(x)$ and its derivative.

---

[1] Note E in Miller et al. (1996) should be replaced with $\frac{1}{2} m_e v^2/(m_e c^2)$, *not* $\gamma - 1$, to make it valid in both non-relativistic and relativistic regimes, where $m_e c^2$ is used to make energy dimensionless. The same notation should be taken for Miller's Eq. (2.5b); see below.

$$P(a+1,x) = P(a,x) - \frac{x^a e^{-x}}{a\Gamma(a)},$$

one can rewrite

$$\psi(x) = P(3/2,x) = P(1/2,x) - 2\sqrt{\frac{x}{\pi}}e^{-x} = \mathrm{erf}(\sqrt{x}) - 2\sqrt{\frac{x}{\pi}}e^{-x}, \tag{B.4}$$

where

$$\mathrm{erf}(\sqrt{x}) = \frac{2}{\sqrt{\pi}}\int_0^x e^{-t^2}dt \tag{B.5}$$

is the error function. One can also readily obtain

$$\psi'(x) = 2\sqrt{\frac{x}{\pi}}e^{-x}. \tag{B.6}$$

Substituting equations B.4 and B.6 to B.2, we have

$$\dot{E}_{\mathrm{Coul}} = \dot{E}_{\mathrm{Coul}}^{\mathrm{cold}}\left[\mathrm{erf}(\sqrt{x}) - 4\sqrt{\frac{x}{\pi}}e^{-x}\right], \tag{B.7}$$

in terms of more commonly used error function. The absolute value of the Coulomb loss rate is shown in Figure B.2, together with its counterpart of cold-target approximation.

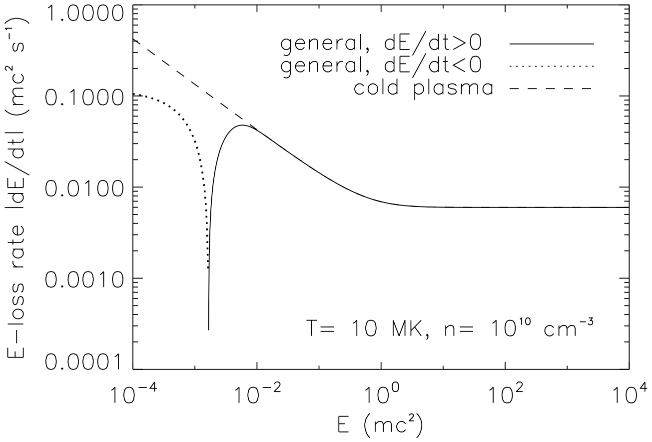

Figure B.2: Absolute value of Coulomb loss rate $\dot{E}_{\mathrm{Coul}}$ (*solid* and *dotted*) calculated for a typical background plasma condition for solar flares, $T = 10^7\,\mathrm{K}, n = 10^{10}\,\mathrm{cm}^{-3}$. Below the energy corresponding to the sharp "spike", $\dot{E}_{\mathrm{Coul}}$ turns to negative (*dotted*), meaning particle gaining energy. The cold-plasma loss rate $\dot{E}_{\mathrm{Coul}}^{\mathrm{cold}}$ (*dashed*) is shown for comparison.

As energy decreases, this Coulomb loss rate (solid line) first increases; it then decreases and becomes negative (gaining energy). The energy at which it turns negative is very close to (but slightly less than) the thermal energy of background electrons. As expected, the cold-target Coulomb loss rate (dashed line) deviates from the general loss rate at low energies but the two agree well at high energies.

B.2 Coulomb Diffusion in Warm Plasmas

Similarly, Coulomb collision also contributes to diffusion in energy. In general, one can split the diffusion coefficient $D(E)$ into two parts:

$$D(E) = D_{\mathrm{turb}}(E) + D_{\mathrm{Coul}}(E), \tag{B.8}$$

where $D_{\mathrm{turb}}(E)$ and $D_{\mathrm{Coul}}(E)$ are contributions by turbulence and by Coulomb collisions, respectively. At low energies, energy diffusion due to Coulomb collisions becomes important, while at high energies, diffusion would be dominated by the contribution from turbulence. However, the $D_{\mathrm{Coul}}(E)$ term was not included in the previous SA mode.

Following Miller et al. (1996, Eq. 2.5b)[2], we rewrite the Coulomb diffusion coefficient (see also Spitzer, 1962, p. 132)

$$D_{\mathrm{Coul}}(E) = \dot{E}_{\mathrm{Coul}}^{\mathrm{cold}} \left(\frac{kT}{m_e c^2}\right) \psi(x) = \dot{E}_{\mathrm{Coul}}^{\mathrm{cold}} \left(\frac{kT}{m_e c^2}\right) \left[\mathrm{erf}(\sqrt{x}) - 2\sqrt{\frac{x}{\pi}} e^{-x}\right]. \tag{B.9}$$

B.3 Implementation of Coulomb Loss and Diffusion

The F-P equation in some early works (Miller et al., 1996; Petrosian & Liu, S., 2004) was written as,

$$\frac{\partial f}{\partial t} = \frac{\partial^2}{\partial E^2}[D(E)f] - \frac{\partial}{\partial E}\{[A_1(E) - \dot{E}_{L1}]f\} - \frac{f}{T_{\mathrm{esc}}(E)} + Q(E)\,, \tag{B.10}$$

in a way which is slightly different from that of equation (1.1) used here. By substituting equation (B.8) one can rewrite this equation as

$$\frac{\partial f}{\partial t} = \frac{\partial}{\partial E}\left[D\frac{\partial f}{\partial E}\right] - \frac{\partial}{\partial E}\left\{\left[\left(A_1 - \frac{dD_{\mathrm{turb}}}{dE}\right) - \left(\dot{E}_{L1} + \frac{dD_{\mathrm{Coul}}}{dE}\right)\right] f\right\} - \frac{f}{T_{\mathrm{esc}}} + Q, \tag{B.11}$$

---

[2] Note $D(E)$ in Eq. B.10 here is equivalent to $D_C(E)/2$ in Eq. (2.5b) of Miller et al. (1996).

which can be directly compared this with equation (1.1). We then identify the following relationship between the two ways of writing the F-P equation:

$$A = A_1 - \frac{dD_{\rm turb}}{dE},^{3} \tag{B.12}$$

$$\dot{E}_L = \dot{E}_{L1} + \frac{dD_{\rm Coul}}{dE} = \dot{E}^{\rm eff}_{\rm Coul} + \dot{E}_{\rm synch}, \tag{B.13}$$

where we substitute equation B.13 and define the effective Coulomb loss rate

$$\dot{E}^{\rm eff}_{\rm Coul} = \dot{E}_{\rm Coul} + \frac{dD_{\rm Coul}}{dE}. \tag{B.14}$$

We must modify the energy loss rate accordingly using the above two equations, when we include Coulomb diffusion using equations B.9 and B.8.

Let us now derive $dD_{\rm Coul}/dE$ and $\dot{E}^{\rm eff}_{\rm Coul}$. Using equation B.9, we have

$$\frac{dD_{\rm Coul}}{dE} = D_{\rm Coul}\frac{d}{dE}\ln D_{\rm Coul} = D_{\rm Coul}\left[\frac{d}{dE}\ln \dot{E}^{\rm cold}_{\rm Coul} + \frac{d}{dE}\ln\psi(x)\right], \tag{B.15}$$

in which by equation B.1 and $E = \gamma - 1$ we note

$$\frac{d}{dE}\ln \dot{E}^{\rm cold}_{\rm Coul} = -\frac{d\ln\beta}{dE} = -\frac{1}{\beta}\frac{d\beta}{d\gamma} = -\frac{1}{\beta^2\gamma^3} = -\frac{1}{\gamma(\gamma^2-1)} = -\frac{1}{\gamma(\gamma+1)E},$$

and by $x = Em_ec^2/kT$ we have

$$\frac{d}{dE}\ln\psi(x) = \frac{\psi'(x)}{\psi(x)}\frac{dx}{dE} = \frac{\psi'(x)}{\psi(x)}\frac{m_ec^2}{kT}.$$

Plugging the above two expressions back to equation B.15 and noting equation (B.9), we obtain

$$\frac{dD_{\rm Coul}}{dE} = \dot{E}^{\rm cold}_{\rm Coul}\left[\psi'(x) - \frac{\psi(x)}{x}\frac{1}{\gamma(\gamma+1)}\right], \tag{B.16}$$

and the effective Coulomb loss rate

$$\dot{E}^{\rm eff}_{\rm Coul} = \dot{E}_{\rm Coul} + \frac{dD_{\rm Coul}}{dE} = \dot{E}^{\rm cold}_{\rm Coul}\psi(x)\left[1 - \frac{1}{x}\frac{1}{\gamma(\gamma+1)}\right]$$

---

[3] This notation conversion has already been taken care of in the code properly.

$$= \dot{E}^{\rm cold}_{\rm Coul}\left[\mathrm{erf}(\sqrt{x}) - 2\sqrt{\frac{x}{\pi}}e^{-x}\right]\left[1-\frac{1}{x}\frac{1}{\gamma(\gamma+1)}\right], \tag{B.17}$$

by using equation (B.2).

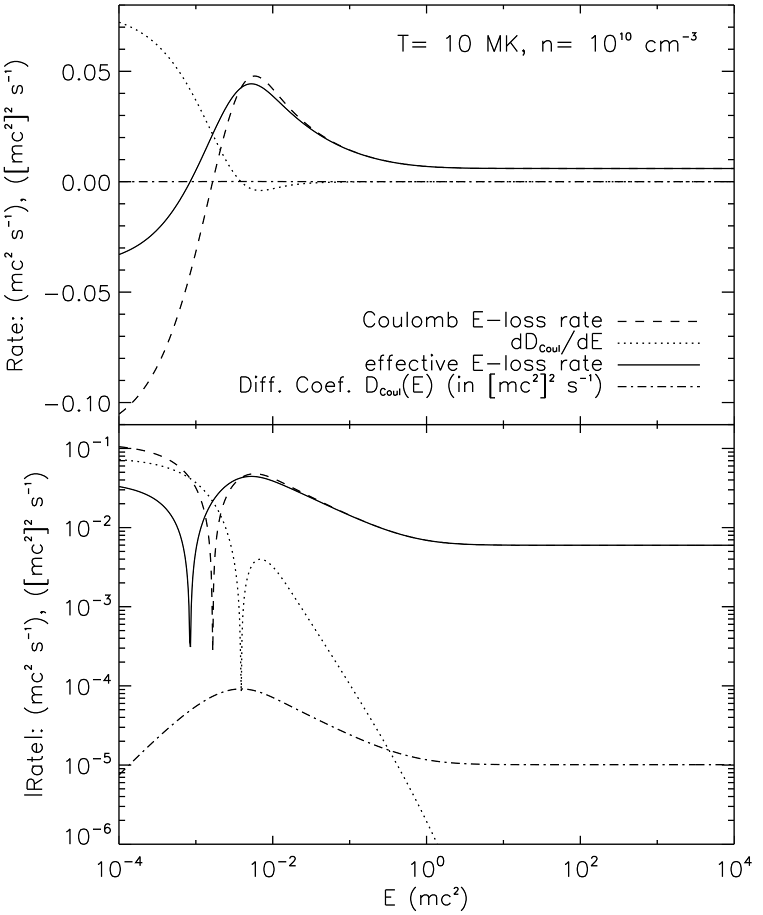

Figure B.3: Energy loss and diffusion rates due Coulomb collisions. *Top:* Coulomb energy loss rate $\dot{E}_{\rm Coul}$, diffusion coefficient $D_{\rm Coul}(E)$ and its derivative $dD_{\rm Coul}/dE$, and effective Coulomb energy loss rate $\dot{E}^{\rm eff}_{\rm Coul} = \dot{E}_{\rm Coul} + dD_{\rm Coul}/dE$. $D_{\rm Coul}(E)$ is in units of $(mc^2)^2\,{\rm s}^{-1}$ and the others are in units of $mc^2\,{\rm s}^{-1}$. *Bottom:* same as in the top panel but for the absolute values plotted in a logarithmic scale.

Figure B.3 shows the energy loss or diffusion rates calculated for the same background plasma condition as in Figure B.2. As can be seen, with decreasing energy, the Coulomb energy loss rate $\dot{E}_{\rm Coul}$ changes its sign from positive to negative at about the energy of the background electron thermal energy, while the Coulomb diffusion derivative $dD_{\rm Coul}/dE$

does the opposite. The addition of the two gives the effective Coulomb loss rate $\tau^{\rm eff}_{\rm Coul}$, which is mainly dominated by $\dot{E}_{\rm Coul}$ except at low energies. The energy at which $\tau^{\rm eff}_{\rm Coul}$ flips its sign is slightly (by a half decade) lower than that of $\dot{E}_{\rm Coul}$.

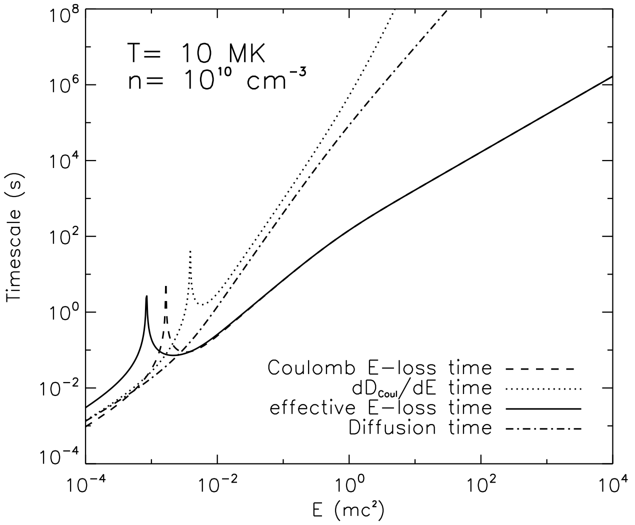

Figure B.4: Coulomb loss and diffusion timescales: $\tau_{\rm Coul}$, $\tau_{D'_{\rm Coul}}$, $\tau^{\rm eff}_{\rm Coul}(= [1/\tau_{\rm Coul} + 1/\tau_{D'_{\rm Coul}}]^{-1})$, and $\tau_{D_{\rm Coul}}$ (see text for definitions), corresponding to the rates plotted in Figure B.3. Note the spikes indicate infinite time and are located at the energy where the corresponding rate changes its sign (i.e., the rate equals zero). See the top panel of Figure B.3 for their signs.

It is convenient to define various timescales based on the above obtained coefficients:

$$\tau^{\rm cold}_{\rm Coul} = E/\dot{E}^{\rm cold}_{\rm Coul} = (\gamma - 1)\beta(4\pi r_0^2 \ln \Lambda c n)^{-1}, \tag{B.18}$$

$$\tau_{\rm Coul} = E/|\dot{E}_{\rm Coul}| = \tau^{\rm cold}_{\rm Coul}|\psi(x) - \psi'(x)|^{-1}, \tag{B.19}$$

$$\tau^{\rm eff}_{\rm Coul} = E/|\dot{E}^{\rm eff}_{\rm Coul}| = \tau^{\rm cold}_{\rm Coul}\left|1 - \frac{1}{x}\frac{1}{\gamma(\gamma+1)}\right|^{-1} /|\psi(x)|, \tag{B.20}$$

$$\tau_{D'_{\rm Coul}} = \frac{E}{|dD_{\rm Coul}/dE|} = \tau^{\rm cold}_{\rm Coul}\left|\psi'(x) - \frac{\psi(x)}{x}\frac{1}{\gamma(\gamma+1)}\right|^{-1}, \tag{B.21}$$

$$\tau_{D_{\rm Coul}} = E^2/D_{\rm Coul} = E^2[\dot{E}^{\rm cold}_{\rm Coul}(kT/m_e c^2)\psi(x)]^{-1} = \tau^{\rm cold}_{\rm Coul} x/\psi(x), \tag{B.22}$$

Figure B.4 shows these timescales, which is proportional to the inverse of the bottom panel of Figure B.3. We note that above $\sim$ 10 keV (about 10 times higher than the thermal energy of background electrons), both Coulomb diffusion time and the $dD_{\rm Coul}/dE$ time are sufficiently large that Coulomb diffusion can be neglected in the F-P calculation, as the previous SA model does.

B.4 Thermalization Test of Injected Distribution

We have tested the implementation of the new Coulomb loss and diffusion. We turned off acceleration by turbulence, but left Coulomb loss and diffusion on in the code. We injected a narrow gaussian (δ-function like) distribution of electrons with a mean energy of 1 keV into a background plasma of Maxwellian distribution with a temperature of 1 keV and a density of $n_e = 1.5 \times 10^{10}\,{\rm cm}^{-3}$. We then calculated the time-dependent spectrum of these electrons. Figure B.5 shows the evolution of the electron distribution in separate time intervals (*left*: 0–0.01 s, *middle*: 0.01–0.1 s, *right*: 0.1-1 s). The injected gaussian (*black*) and the background Maxwellian (*red*) distribution are plotted in all the panels as a reference. As can be seen, the distribution quickly thermalizes and approaches the background maxwellian distribution (overlapping with the final distribution at $t = 1\,{\rm s}$). From Figure B.4, we note that the Coulomb diffusion timescale $\tau_{D_{\rm Coul}}$ is about 0.1 s at $E = 1\,{\rm keV}$ in a plasma of $n_e = 1 \times 10^{10}\,{\rm cm}^{-3}$ (similar to the density here). The duration of 1 s in this calculation is thus about 10 times longer than the diffusion timescale, which allows sufficient time for the thermalization to happen.

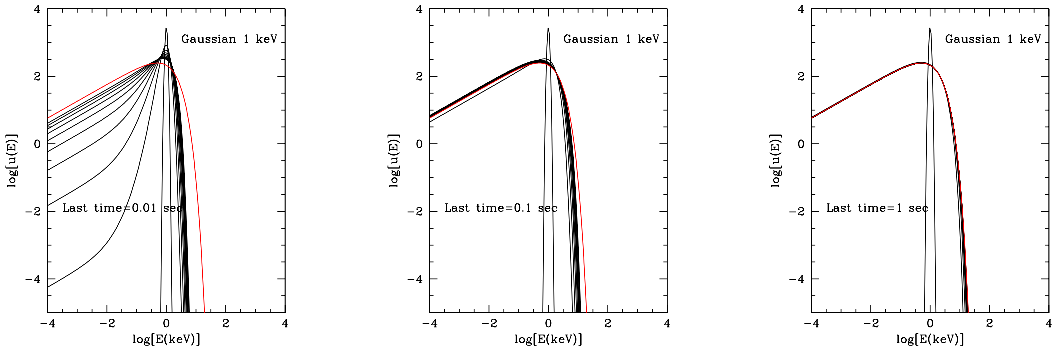

Figure B.5: Test against thermal distribution for injected gaussian distribution when Coulomb diffusion is included. The injected gaussian (*black*) and the background Maxwellian (*red*) distributions are fixed in each panel as a reference. The other curves (*black*, evenly spaced in time) in each panel show the temporal evolution on different stages *left*: 0–0.01 s, *middle*: 0.01–0.1 s, *right*: 0.1-1 s (Courtesy of William East).

Bibliography

Abbett, W. P. & Hawley, S. L. 1999, ApJ, 521, 906

Alexander, D. & Metcalf, T. R. 2002, Sol. Phys., 210, 323

Allred, J. C., Hawley, S. L., Abbett, W. P., & Carlsson, M. 2005, ApJ, 630, 573

Antiochos, S. K. & Sturrock, P. A. 1978, ApJ, 220, 1137

Antonucci, E., Alexander, D., Culhane, J. L., de Jager, C., MacNeice, P., Somov, B. V., & Zarro, D. M. 1999, in The Many Faces of the Sun: A Summary of the Results from NASA's Solar Maximum Mission, ed. K. T. Strong et al. (New York: Springer-Verlag), 345

Antonucci, E., Dodero, M. A., & Martin, R. 1990, ApJS, 73, 137

Antonucci, E., Gabriel, A. H., Acton, L. W., Leibacher, J. W., Culhane, J. L., Rapley, C. G., Doyle, J. G., Machado, M. E., et al. 1982, Sol. Phys., 78, 107

Antonucci, E., Gabriel, A. H., & Dennis, B. R. 1984, ApJ, 287, 917

Asai, A., Ishii, T. T., Kurokawa, H., Yokoyama, T., & Shimojo, M. 2003, ApJ, 586, 624

Aschwanden, M. J. 2002, Space Science Reviews, 101, 1

—. 2004, Physics of the Solar Corona. An Introduction (Physics of the Solar Corona)

Aschwanden, M. J., Brown, J. C., & Kontar, E. P. 2002, Sol. Phys., 210, 383

Benka, S. G. & Holman, G. D. 1994, ApJ, 435, 469

Benz, A. 2002, Plasma Astrophysics, second edition (Plasma Astrophysics. Kinetic Processes in Solar and Stellar Coronae, second edition. By A. Benz, Institute of Astronomy, ETH Zürich, Switzerland. Astrophysics and Space Science Library, Vol. 279, Kluwer Academic Publishers, Dordrecht, 2002.)

Brosius, J. W. 2003, ApJ, 586, 1417

Brosius, J. W. & Phillips, K. J. H. 2004, ApJ, 613, 580

Brown, J. C. 1971, Sol. Phys., 18, 489

—. 1973, Sol. Phys., 31, 143

Carmichael, H. 1964, in The Physics of Solar Flares, ed. W. N. Hess, 451

Chandran, B. D. G. & Cowley, S. C. 1998, Physical Review Letters, 80, 3077

Chernov, G. P., Yan, Y. H., Fu, Q. J., & Tan, C. M. 2005, A&A, 437, 1047

Crosby, N. B., Aschwanden, M. J., & Dennis, B. R. 1993, Sol. Phys., 143, 275

Culhane, J. L. & Acton, L. W. 1970, MNRAS, 151, 141

Dennis, B. R. 1985, Sol. Phys., 100, 465

Dennis, B. R., Veronig, A., Schwartz, R. A., Sui, L., Tolbert, A. K., Zarro, D. M., & Rhessi Team. 2003, Advances in Space Research, 32, 2459

Dennis, B. R. & Zarro, D. M. 1993, Sol. Phys., 146, 177

Dere, K. P., Moses, J. D., Delaboudinière, J.-P., Brunaud, J., Carabetian, C., Hochedez, J.-F., Song, X. Y., Catura, R. C., et al. 2000, Sol. Phys., 195, 13

Doschek, G. A., Feldman, U., Kreplin, R. W., & Cohen, L. 1980, ApJ, 239, 725

Doschek, G. A., Mariska, J. T., Strong, K. T., Bentley, R. D., Brown, C. M., Culhane, J. L., Lang, J., Sterling, A. C., et al. 1994, ApJ, 431, 888

Dung, R. & Petrosian, V. 1994, ApJ, 421, 550

Efron, B. & Petrosian, V. 1992, ApJ, 399, 345

—. 1995, ApJ, 449, 216

Emslie, A. G. 1978, ApJ, 224, 241

—. 2003, ApJ, 595, L119

Emslie, A. G., Kontar, E. P., Krucker, S., & Lin, R. P. 2003, ApJ, 595, L107

Feldman, U., Doschek, G. A., Kreplin, R. W., & Mariska, J. T. 1980, ApJ, 241, 1175

Fisher, G. H., Canfield, R. C., & McClymont, A. N. 1985a, ApJ, 289, 434

—. 1985b, ApJ, 289, 425

—. 1985c, ApJ, 289, 414

Fletcher, L. & Hudson, H. S. 2002, Sol. Phys., 210, 307

Forbes, T. G. & Acton, L. W. 1996, ApJ, 459, 330

Gallagher, P. T., Dennis, B. R., Krucker, S., Schwartz, R. A., & Tolbert, A. K. 2002, Sol. Phys., 210, 341

Gan, W. Q., Cheng, C. C., & Fang, C. 1995, ApJ, 452, 445

Gan, W. Q. & Fang, C. 1990, ApJ, 358, 328

Gan, W. Q. & Li, Y. P. 2006, Cosmic Particle Acceleration, 26th meeting of the IAU, Joint Discussion 1, 16-17 August, 2006, Prague, Czech Republic, JD01, #30, 1

Goff, C. P., Matthews, S. A., van Driel-Gesztelyi, L., & Harra, L. K. 2004, A&A, 423, 363

Grigis, P. C. & Benz, A. O. 2004, A&A, 426, 1093

Hamilton, R. J. 1990, Ph.D. Thesis, Stanford University

Hamilton, R. J., Lu, E. T., & Petrosian, V. 1990, ApJ, 354, 726

Hamilton, R. J. & Petrosian, V. 1992, ApJ, 398, 350

Hawley, S. L. & Fisher, G. H. 1994, ApJ, 426, 387

Hirayama, T. 1974, Sol. Phys., 34, 323

Holman, G. D. 1985, ApJ, 293, 584

Holman, G. D., Sui, L., Schwartz, R. A., & Emslie, A. G. 2003, ApJ, 595, L97

Hudson, H. S. 1991, BAAS, 23, 1064

Hurford, G. J., Schmahl, E. J., Schwartz, R. A., Conway, A. J., Aschwanden, M. J., Csillaghy, A., Dennis, B. R., Johns-Krull, C., et al. 2002, Sol. Phys., 210, 61

Hurford, G. J., Schwartz, R. A., Krucker, S., Lin, R. P., Smith, D. M., & Vilmer, N. 2003, ApJ, 595, L77

Isobe, H., Yokoyama, T., Shimojo, M., Morimoto, T., Kozu, H., Eto, S., Narukage, N., & Shibata, K. 2002, ApJ, 566, 528

Jiang, Y. W., Liu, S., Liu, W., & Petrosian, V. 2006, ApJ, 638, 1140

Jiang, Y. W., Liu, W., Petrosian, V., & McTiernan, J. 2003, in Bulletin of the American Astronomical Society, 840

Koch, H. W. & Motz, J. W. 1959, Reviews of Modern Physics, 31, 920

Kopp, R. A. & Pneuman, G. W. 1976, Sol. Phys., 50, 85

Kosovichev, A. G. 2006, Sol. Phys., 33

Kosovichev, A. G. & Zharkova, V. V. 1998, Nature, 393, 317

Krucker, S., Christe, S., Lin, R. P., Hurford, G. J., & Schwartz, R. A. 2002, Sol. Phys., 210, 445

Krucker, S., Fivian, M. D., & Lin, R. P. 2005, Advances in Space Research, 35, 1707

Krucker, S., Hurford, G. J., & Lin, R. P. 2003, ApJ, 595, L103

Krucker, S. & Lin, R. P. 2000, ApJ, 542, L61

Leach, J. 1984, Ph.D. Thesis, Stanford University

Leach, J. & Petrosian, V. 1981, ApJ, 251, 781

—. 1983, ApJ, 269, 715

Lee, T. T., Petrosian, V., & McTiernan, J. M. 1993, ApJ, 412, 401

—. 1995, ApJ, 448, 915

Li, J., Metcalf, T. R., Canfield, R. C., Wuelser, J.-P., & Kosugi, T. 1997, ApJ, 482, 490

Li, P., Emslie, A. G., & Mariska, J. T. 1993, ApJ, 417, 313

Lin, R. P., Dennis, B. R., Hurford, G. J., Smith, D. M., Zehnder, A., Harvey, P. R., Curtis, D. W., Pankow, D., et al. 2002, Sol. Phys., 210, 3

Lin, R. P., Krucker, S., Hurford, G. J., Smith, D. M., Hudson, H. S., Holman, G. D., Schwartz, R. A., Dennis, B. R., et al. 2003, ApJ, 595, L69

Liu, C., Lee, J., Deng, N., Gary, D. E., & Wang, H. 2006, ApJ, 642, 1205

Liu, Y. & Hayashi, K. 2006, ApJ, 640, 1135

Liu, S., Petrosian, V., & Mason, G. M. 2004a, ApJ, 613, L81

—. 2006, ApJ, 636, 462

Liu, S., Petrosian, V., & Melia, F. 2004b, ApJ, 611, L101

Liu, W., Jiang, Y. W., Liu, S., & Petrosian, V. 2004a, ApJ, 611, L53

Liu, W., Jiang, Y. W., Liu, S., & Petrosian, V. 2004b, in Bulletin of the American Astronomical Society, 739

Liu, W., Liu, S., Jiang, Y. W., & Petrosian, V. 2006, ApJ, 649, 1124

Lu, E. T. 1989, Ph.D. Thesis, Stanford University

MacKinnon, A. L. & Craig, I. J. D. 1991, A&A, 251, 693

Mariska, J. T., Doschek, G. A., Boris, J. P., Oran, E. S., & Young, Jr., T. R. 1982, ApJ, 255, 783

Mariska, J. T., Emslie, A. G., & Li, P. 1989, ApJ, 341, 1067

Masuda, S. 1994, Ph.D. Thesis, University of Tokyo

Masuda, S., Kosugi, T., & Hudson, H. S. 2001, Sol. Phys., 204, 55

McClements, K. G. 1992, A&A, 258, 542

McClements, K. G. & Alexander, D. 2005, ApJ, 619, 1153

McTiernan, J. M. 1989, Ph.D. Thesis, Stanford University

McTiernan, J. M. & Petrosian, V. 1990, ApJ, 359, 524

Metcalf, T. R., Hudson, H. S., Kosugi, T., Puetter, R. C., & Pina, R. K. 1996, ApJ, 466, 585

Metcalf, T. R., Leka, K. D., & Mickey, D. L. 2005, ApJ, 623, L53

Miller, J. A., Cargill, P. J., Emslie, A. G., Holman, G. D., Dennis, B. R., LaRosa, T. N., Winglee, R. M., Benka, S. G., et al. 1997, J. Geophys. Res., 102, 14631

Miller, J. A., Larosa, T. N., & Moore, R. L. 1996, ApJ, 461, 445

Miller, J. A. & Mariska, J. T. 2005, AGU Spring Meeting Abstracts, C2+

Milligan, R. O., Gallagher, P. T., Mathioudakis, M., Bloomfield, D. S., Keenan, F. P., & Schwartz, R. A. 2006, ApJ, 638, L117

Nagai, F. & Emslie, A. G. 1984, ApJ, 279, 896

Neupert, W. M. 1968, ApJ, 153, L59

Park, B. T. 1996, Ph.D. Thesis, Stanford University

Park, B. T. & Petrosian, V. 1996, ApJS, 103, 255

Park, B. T., Petrosian, V., & Schwartz, R. A. 1997, ApJ, 489, 358

Parker, E. N. 1963, ApJS, 8, 177

Peres, G. & Reale, F. 1993, A&A, 275, L13

Petrosian, V. 1973, ApJ, 186, 291

Petrosian, V. 1994, in Proceedings of Kofu Symposium, 239–242

Petrosian, V. 1996, in American Institute of Physics Conference Series, ed. R. Ramaty, N. Mandzhavidze, & X.-M. Hua, 445–+

—. 2001, ApJ, 557, 560

Petrosian, V. & Donaghy, T. Q. 1999, ApJ, 527, 945

Petrosian, V., Donaghy, T. Q., & Llyod, N. M. 2001

Petrosian, V., Donaghy, T. Q., & McTiernan, J. M. 2002, ApJ, 569, 459

Petrosian, V. & Liu, S. 2004, ApJ, 610, 550

Petschek, H. E. 1964, in The Physics of Solar Flares, ed. W. N. Hess, 425

Pick, M., Démoulin, P., Krucker, S., Malandraki, O., & Maia, D. 2005, ApJ, 625, 1019

Press, W. H., Teukolsky, S. A., Vetterling, W. T., & Flannery, B. P. 1992, Numerical recipes in FORTRAN. The art of scientific computing (Cambridge: University Press, —c1992, 2nd ed.)

Qiu, J., Ding, M. D., Wang, H., Gallagher, P. T., Sato, J., Denker, C., & Goode, P. R. 2001, ApJ, 554, 445

Qiu, J., Lee, J., & Gary, D. E. 2004, ApJ, 603, 335

Qiu, J., Lee, J., Gary, D. E., & Wang, H. 2002, ApJ, 565, 1335

Ramaty, R. 1979, in AIP Conf. Proc. 56: Particle Acceleration Mechanisms in Astrophysics, ed. J. Arons, C. McKee, & C. Max, 135–154

Ramaty, R. & Murphy, R. J. 1987, Space Science Reviews, 45, 213

Ryutova, M. & Shine, R. 2006, Journal of Geophysical Research (Space Physics), 111, 3101

Sakao, T. 1994, Ph.D. Thesis

Sakao, T., Kosugi, T., & Masuda, S. 1998, in ASSL Vol. 229: Observational Plasma Astrophysics : Five Years of YOHKOH and Beyond, ed. T. Watanabe & T. Kosugi (Boston: Kluwer), 273

Sato, J. 2001, ApJ, 558, L137

Scherrer, P. H., Bogart, R. S., Bush, R. I., Hoeksema, J. T., Kosovichev, A. G., Schou, J., Rosenberg, W., Springer, L., Tarbell, T. D., Title, A., Wolfson, C. J., Zayer, I., & MDI Engineering Team. 1995, Sol. Phys., 162, 129

Schlickeiser, R. 1989, ApJ, 336, 243

Schmahl, E. J. & Hurford, G. J. 2002, Sol. Phys., 210, 273

—. 2003, Advances in Space Research, 32, 2477

Schmieder, B., Hagyard, M. J., Guoxiang, A., Hongqi, Z., Kalman, B., Gyori, L., Rompolt, B., Demoulin, P., et al. 1994, Sol. Phys., 150, 199

Siarkowski, M. & Falewicz, R. 2004, A&A, 428, 219

Silva, A. V. R., Wang, H., Gary, D. E., Nitta, N., & Zirin, H. 1997, ApJ, 481, 978

Smith, D. M., Lin, R. P., Turin, P., Curtis, D. W., Primbsch, J. H., Campbell, R. D., Abiad, R., Schroeder, P., et al. 2002, Sol. Phys., 210, 33

Spicer, D. S. 1979, Sol. Phys., 62, 269

Spitzer, L. 1962, Physics of Fully Ionized Gases (New York: Interscience [2nd edition], 1962)

Sturrock, P. A. 1966, Nature, 211, 695

Su, Y., Gan, W. Q., & Li, Y. P. 2006, Sol. Phys., 51

Sui, L. & Holman, G. D. 2003, ApJ, 596, L251

Sui, L., Holman, G. D., & Dennis, B. R. 2004, ApJ, 612, 546

—. 2005, ApJ, 626, 1102

—. 2006, ApJ, 645, L157

Sui, L., Holman, G. D., Dennis, B. R., Krucker, S., Schwartz, R. A., & Tolbert, K. 2002, Sol. Phys., 210, 245

Švestka, Z. F., Fontenla, J. M., Machado, M. E., Martin, S. F., & Neidig, D. F. 1987, Sol. Phys., 108, 237

Sweet, P. A. 1958, in IAU Symp. 6: Electromagnetic Phenomena in Cosmical Physics, ed. B. Lehnert, 123

Syniavskii, D. V. & Zharkova, V. V. 1994, ApJS, 90, 729

Tomczak, M. & Ciborski, T. 2007, A&A

Tsuneta, S. 1996, ApJ, 456, 840

Tsuneta, S., Hara, H., Shimizu, T., Acton, L. W., Strong, K. T., Hudson, H. S., & Ogawara, Y. 1992, PASJ, 44, L63

Tsuneta, S., Masuda, S., Kosugi, T., & Sato, J. 1997, ApJ, 478, 787

Veronig, A. M., Brown, J. C., Dennis, B. R., Schwartz, R. A., Sui, L., & Tolbert, A. K. 2005, ApJ, 621, 482

Veronig, A. M., Karlický, M., Vršnak, B., Temmer, M., Magdalenić, J., Dennis, B. R., Otruba, W., & Pötzi, W. 2006, A&A, 446, 675

Vestuto, J. G., Ostriker, E. C., & Stone, J. M. 2003, ApJ, 590, 858

Wang, L., Lin, R. P., Krucker, S., & Gosling, J. T. 2006, Geophys. Res. Lett., 33, 3106

Watanabe, T. 1990, Sol. Phys., 126, 351

Winter, III, H. D. & Martens, P. C. 2006, AAS/Solar Physics Division Meeting, 37, 13.13

Wuelser, J.-P., Canfield, R. C., Acton, L. W., Culhane, J. L., Phillips, A., Fludra, A., Sakao, T., Masuda, S., et al. 1994, ApJ, 424, 459

Xu, Y., Cao, W., Liu, C., Yang, G., Jing, J., Denker, C., Emslie, A. G., & Wang, H. 2006, ApJ, 641, 1210

Xu, Y., Cao, W., Liu, C., Yang, G., Qiu, J., Jing, J., Denker, C., & Wang, H. 2004, ApJ, 607, L131

Yang, G., Xu, Y., Cao, W., Wang, H., Denker, C., & Rimmele, T. R. 2004, ApJ, 617, L151

Yokoyama, T. & Shibata, K. 2001, ApJ, 549, 1160

Zharkova, V. V., Brown, J. C., & Syniavskii, D. V. 1995, A&A, 304, 284